ORGANOANTIMONY LEWIS ACIDS AS FLUORIDE RECEPTORS AND LIGANDS TOWARDS TRANSITION METALS

A Dissertation

by

IOU-SHENG KE

Submitted to the Office of Graduate Studies of
Texas A&M University
in partial fulfillment of the requirements for the degree of

DOCTOR OF PHILOSOPHY

Chair of Committee,	François P. Gabbaï
Committee Members,	Marcetta Y. Darensbourg
	Timothy R. Hughbanks
	Mustafa Akbulut
Head of Department,	David H. Russell

August 2013

Major Subject: Chemistry

ABSTRACT

As part of our continuing interest in the chemistry of main group Lewis acids, we have now chosen to investigate the Lewis acidic behavior of organoantimony(V) species. In the first part of this thesis, we will describe some of the results obtained in pursuit of this quest including the use of the 9-anthryltriphenylstibonium cation for the fluorescence turn-on sensing of fluoride in water at ppm concentrations. This approach can also be extended to cationic transition metal complexes bearing triarylstibine ligands which readily interact with fluoride anions to afford the corresponding fluorostiboranyl palladium complex. The discovery that anion binding can take place at the antimony atom of coordinated stibine ligands has led us to speculate that the redox state of the metal could be used to control anion binding at antimony. Reaction of $(o\text{-}(Ph_2P)C_6H_4)_2SbPh$ with $(Et_2S)_2PtCl_2$ affords $[ClSb(Ph)PtCl(o\text{-}dppp)_2]$ (o-dppp = o-$(Ph_2P)C_6H_4$)) which further reacts with $PhICl_2$ to afford the tetravalent platinum complex $ClSb(Ph)PtCl_3(o\text{-}dppp)_2$. While the solid state structure of $[ClSb(Ph)PtCl(o\text{-}dppp)_2]$ and $[ClSb(Ph)PtCl_3(o\text{-}dppp)_2]$ show that the chloride anion is bound to antimony, solution studies indicate that $[ClSb(Ph)PtCl(o\text{-}dppp)_2]$ is very labile.

In addition, we will also present a number of fundamental results which show that electron deficient antimony(III) and antimony(V) centers can behave as σ-acceptor or Z-ligands toward electron rich transition metal centers. These unusual

ligative properties will be illustrated by the structural and computational study of complexes in which chlorostibine moiety is involved in a Au→Sb dative interaction.

DEDICATION

For My Grandparent

ACKNOWLEDGEMENTS

I would like to thank my M.S. advisor, Dr. Shiuh-Tzung Liu, who gave me a lot of supports in the organic chemistry. After retiring from the military service, he also helped me to apply the graduated program in the United States. In 5 years in Gabbaï's group, I feel really happy that I have such wonderful colleagues: Dr. Mitsukimi Tsunoda, Dr. Takeshi Matsumoto, Dr. Zureima Garcia Hernandez, Dr. Baofei Pan, Dr. Chris Dorsey, Dr. Youngmin Kim, Dr. Casey Wade, Dr. Haiyan Zhao, Dr. Tzu-Pin Lin, James Jones, Lauren Leamer, Masato Hirai, Kantapat Chansaenpak, Adriana Hampton, Haifeng Yang, Srobona Sen, Anna Marie DeLaRosa and Ahmed Ali. I also like to thank all of my Taiwanese friends who enjoy the life in College Station. Furthermore, I won't finish my PhD without my wife, Wen-Mei Chen, and two of my lovely sons, Charles Ke and Cliff Ke.

I would like to acknowledge my committee member, Prof. Marcetta Darensbourg, Prof. Timothy Hughbanks, Prof. Daniel Shantz and Prof. Mustafa Akbulut. Finally, I thank to my advisor Prof. François Gabbaï who spends 5 years teaching the knowledge in chemistry.

TABLE OF CONTENTS

Page

LIST OF FIGURES

Page

LIST OF TABLES

Page

CHAPTER I

INTRODUCTION TO LEWIS ACIDITY OF ANTIMONY AND GROUP 15 METAL-METAL BONDS

In this thesis, I will describe the results that I have obtained in two research areas. The first area deals with the use of Lewis acidic antimony compounds as receptors for small anions such as fluoride. The second area is concerned with the study of unusual binding interactions that can be formed between heavy group 15 elements including antimony and bismuth and late transition metals. Because these areas are quite different, this introductory chapter has been divided into two distinct sections in which I will provide the relevant background information.

1.1 Lewis acidity of antimony

Cationic boranes as anion receptors. Fluoride has found many uses in various industrial processes and in medical applications, especially in dental care.[1] On the other hand, excessive fluoride ingestion can result in fluorosis, urolithiasis, or even cancer.[2] Because of its considerable significance for health and environmental issues, fluoride is one of the most attractive targets for anion sensing. Moreover, the EPA (United States Environmental Protection Agency) has set the maximum contaminant level for fluoride at 4 ppm in drinking water. Fatal doses of this anion occur with exposures of only 700 mg (10 mg kg^{-1}) and can cause death in less than 30 minutes.[3] Sensing azide ions has become an important research field, although very few methods have been reported.[4,5]

Simple triarylboranes such as trimesitylborane or tris(9-anthryl)borane have been shown to bind fluoride in non-polar organic solvents to form the corresponding fluoride adducts with binding constants (K_F) in the 10^5 to 10^6 M^{-1} range.[6-15] Bidentate diboranes, in which fluoride binding is assisted by chelating effects, display binding constants which are increased by at least one order of magnitude (Figure 1).[16]

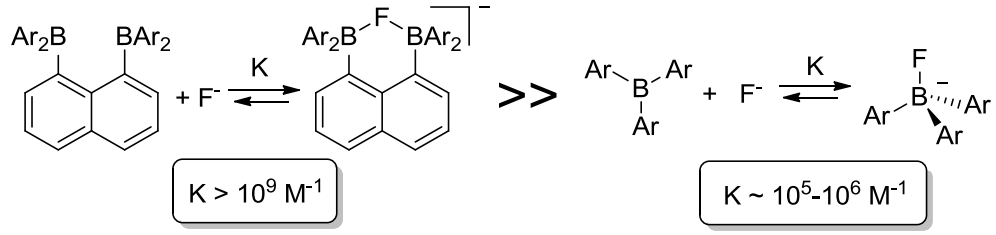

Figure 1. Fluoride binding constants of bidentate diborane and triarylborane.

To investigate the effects of the incorporation of cationic groups into triarylborane receptors, the phosphonium boranes $[\mathbf{1}]^+$ and $[\mathbf{2}]^+$ have been synthesized with the cationic moieties located at positions *ortho* and *para* to the boryl substituent (Figure 2, left).[16,17] In MeOH, the fluoride binding constant of $[\mathbf{2}]^+$ ($K_F > 10^6$ M^{-1}) exceeds the measurable range and is at least four orders of magnitude higher than that measured for the para-isomer $[\mathbf{1}]^+$ (K = 400 (±50) M^{-1}). The structure of the fluoride adduct **2**-F was confirmed by single crystal X-ray diffraction, and Natural Bond Orbital (NBO) analysis indicated the presence of a B-F→P donor-acceptor interaction involving a fluorine lone-pair and the σ* orbital of a P-C bond (Figure 2, right). Energetically, this interaction contributes 5.0 kcal/mol to the stability of the complex. Thus, $[\mathbf{2}]^+$ can be

regarded as a cationic bidentate Lewis acid, whose high fluoride affinity arises from both anion chelation and Coulombic attractions.

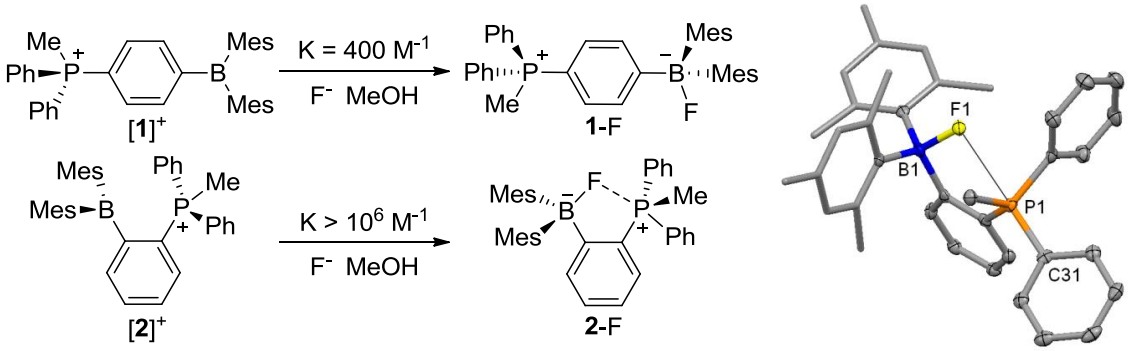

Figure 2. Fluoride binding by $[\mathbf{1}]^+$ and $[\mathbf{2}]^+$ and crystal structure of **2**-F.

Since it is predicted that the acidity of main group onium ions should increase on moving down to the 5th period, the Gabbaï group has synthesized the stibonium derivative $[\mathbf{3}]^+$ by the sequence of steps presented in Figure 3.[18] Competition experiments carried out with [*o*-(Ph_2MeP)(Mes_2FB)C_6H_4] (**2**-F) indicate that $[\mathbf{3}]^+$ exhibits a much higher fluoride affinity than its lighter phosphorus congener. Structural and computational analyses indicate that this enhanced fluoride affinity results from the formation of a Sb-F-B chelate motif characterized by a Sb-F bond of 15 kcal/mol according to NBO calculations.

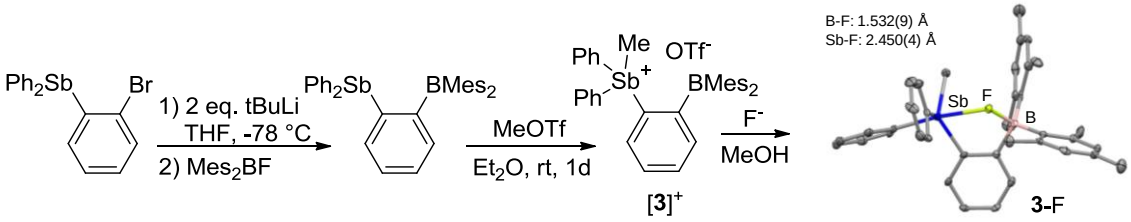

Figure 3. Synthesis of complex [**3**]$^+$ and the crystal structure of **3**-F.

Stibonium Lewis acids. The presence of a stabilizing B-F→Sb donor-acceptor interaction (5 kcal/mol) in **3**-F has led us to realize that heavier group 15 -onium Lewis acids may act as standalone anion receptors. A survey of the literature shows that stibonium cations tend to form covalent species with small anions.[19-26] This is, for example, the case of Ph_4SbF which has a trigonal bipyramidal (TBP) molecular structure,[27] while $[Ph_4Sb][ClO_4]$ is ionic.[23] In fact, the tetraphenylstibonium cation has been used for the extraction of fluoride ions from water into CCl_4 (Figure 4).[28,29] Examination of the Sb-X bonds in a series of tetraphenylstibonium halide ($SbPh_4X$) showed that the geometry around the antimony center can be presented as a resonance of the ionic form (tetrahedral) and covalent form (TBP). This ambiguous phenomenon can be confirmed by conductance data obtained in CH_3CN solution. The results indicate that for X = F, the compound is non-conducting in solution; for X = Br and I the compounds are fully ionized in solution while for X = Cl the conductance is intermediate suggesting an equilibrium between the ionic and covalent form. This suggested that the lower the basicity of the halide ion, the weaker the Sb-X bond and the closer the structure of the complex is to the ionic structure.[27] Such a property attests to the strength of the Sb-F interaction.

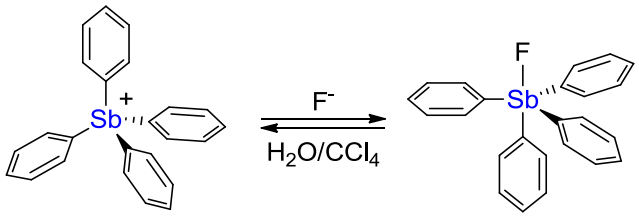

Figure 4. Extraction of fluoride ions by $SbPh_4^+$.

1.2 Group 15 metal-metal bonds

Unlike their lighter phosphine and arsine analogs, stibine ligands tend to form relatively labile complexes when coordinated to transition metals.[30-34] These properties can be correlated to the moderate donicity of the antimony-based lone pair which bears a large 5s character.[35] Despite these limitations, such ligands have been the subject of extensive investigations. In contrast to stibines which have enjoyed a wide precedent in coordination chemistry, few transition metal complexes possessing stiboranyl ligands have been isolated. The very first example which features R_2X_2Sb-TM (type I, Figure 5) was reported by Malisch in 1974.[36,37] Similar hypervalent pentacoordinate stiboranes with an Sb-group 6 element bond [$R_2R^fO_2Sb$-$MCp(CO)_3$ [{R^fO = o-$C_6H_4C(CF_3)_2O^-$, M = Cr, Mo, W}] were also synthesized (type II, Figure 5).[38-41] X-ray crystallographic analysis of those complexes showed that the geometry around the antimony atom is that of a distorted trigonal bipyramid (TBP) with the $CpM(CO)_3$ fragment at the equatorial site of the TBP. Although the metal-antimony bond of these complexes is largely covalent, it is conceivable that such systems could be described as resulting from the interaction of a stibonium ion with a reduced metal center. Stimulated by this possibility, the Gabbaï group decided to attempt the synthesis of such stiboranly complexes by

coordination of late transition metal fragments to Lewis acidic antimony centers. A brief overview of these investigations is provided in the following sections. Conceptually related results obtained with bismuth and tellurium compounds are also described.

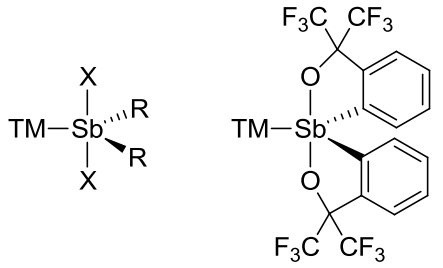

I **II**

Figure 5. Illustration of type **I** and type **II**.

Heavier Lewis acids in unusual donor-acceptor interactions with metals. In an unexpected outcome of this research grant, we have recently been able to synthesize a complex (**4**) in which a formally mercury(II) center acts as a donor toward a stibonium ion (Figure 6).[42] This complex was obtained by reaction of 1,8-dilithionaphthalene with Ph_3SbBr_2 and $HgBr_2$ in THF followed by exchange of the bromide by an iodide ligand. An examination of the crystal structure of **4** indicates the presence of a dinuclear core characterized by a short transannular Hg-Sb separation of 3.073(1) Å (Figure 3). This separation, which lies between the sum of the metallic (3.17 Å) and covalent radii (2.71 Å) of the two elements indicates that these two atoms are within bonding distance. The mercury adopts a distorted square planar coordination geometry with a very short Hg-I bond of 2.991(1) Å.

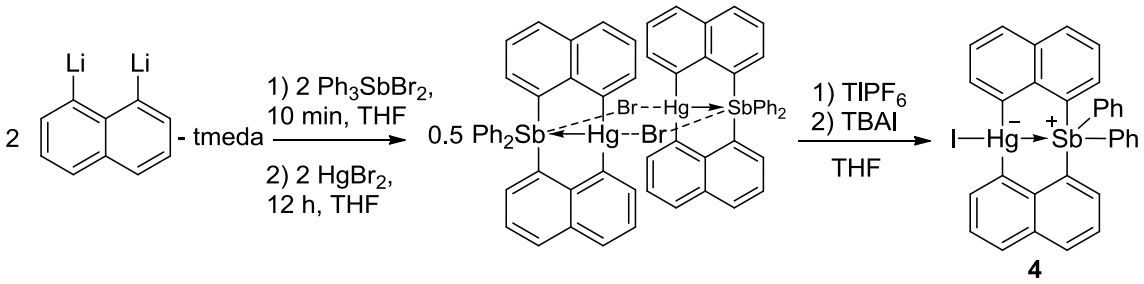

Figure 6. Synthesis of complex **4**.

To shed light on the nature of the Hg-Sb interaction present in **4**, the complex was subjected to DFT calculations and analyzed by a number of methods. The Electron Localization Function (ELF) shows a continuum of elevated values along the Hg→Sb vector in agreement with the presence of bonding electron density between the two elements (Figure 7). Further evidence for this phenomenon was derived from a Boys localization analysis (Figure 7). This analysis identifies a Hg lone pair, of d-character, that is clearly extended along the transannular vector toward the Sb atom. Altogether, these computational results show that the Hg→Sb present in **4** involves a polar covalent component which complements the strong mercurate-stibonium electrostatic interaction already present in this compound. These results are interesting because they show that the Hg center of **4** can act as a Lewis base, a phenomenon that had thus far only been observed for transition metals. In the case of **4**, this phenomenon is the result of a unique iodide push – stibonium pull effect which polarizes the diffuse "closed-shell" of the Hg atom thus promoting its engagement in a polar bonding interaction.

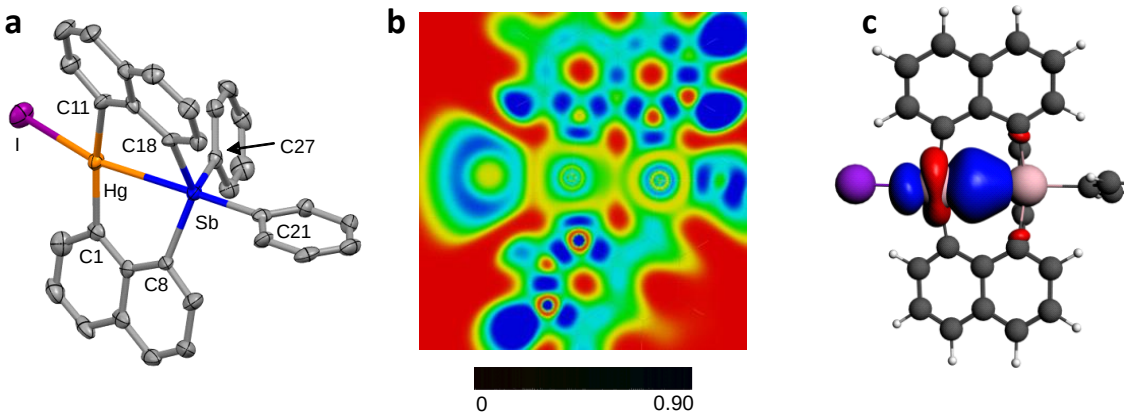

Figure 7. Crystal structure (a), ELF map (b) and gold-centered Boys (c) orbital in **4**.

Having observed that stibonium ions possess a high Lewis acidity toward small anions, we questioned whether such ions could also be used to engage transition metal fragments in unusual M→Sb interactions. Putting this new concept to a test, we targeted the stiboranyl-gold complex (**5**) which could be obtained by reaction of dilithionaphthalene with Ph_3SbBr_2 and, subsequently, AuCl(tht)/PPh_3 (Figure 8). The gold atom of this complex adopts a T-shaped geometry and is separated from the antimony center by only 2.76 Å. Surprisingly, the gold atom is also involved in an aurophilic interaction, a phenomenon typically only observed for monovalent gold complexes (Figure 9). This phenomenon indicates that the stiboranyl ligand possesses strong σ-donating properties making the trivalent gold atom of **5** electron rich. This view is supported by DFT calculations as well as Au L_3- and Sb K-edge XANES spectra which reveal that **5** may also be described as an aurate-stibonium derivative. In agreement with this view, complex **5** shows no reactivity toward the halides Cl^-, Br^-, and I^-. It does, however, rapidly react with F^- to form an unprecedented anionic aurate

fluorostiborane complex ([**5**-F]$^-$) which has been isolated as the tetra-*n*-butylammonium salt (Figure 5). The increased coordination number of the antimony center in this anionic complex ([**5**-F]$^-$) does not notably affect the Au–Sb separation (2.77 Å) or the geometry at the gold atom which remains T-shaped. Adopting the donor–acceptor formalism that has been recently popularized for late transition metals coordinated to Lewis acidic ligands, complex **5** can be described as a diarylaurate anion stabilized by partial electron donation to a Lewis acidic stibonium ligand. The same reasoning can be applied to [**5**-F]$^-$, which can be described as a diarylaurate anion intramolecularly stabilized by a Lewis acidic fluorostiborane.

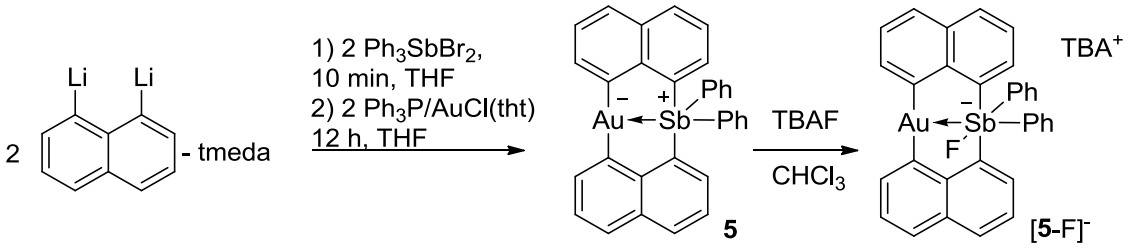

Figure 8. Synthesis of complex **5** and [**5**-F]$^-$.

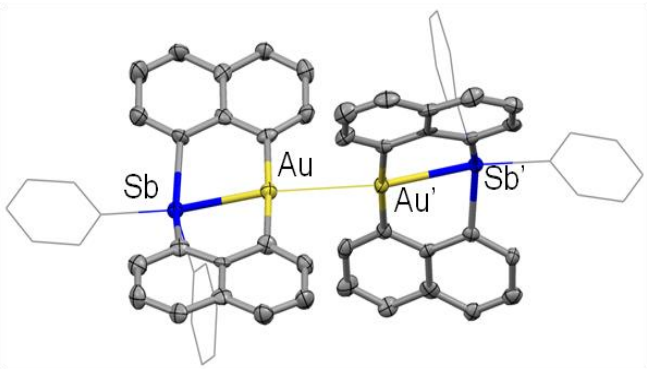

Figure 9. Crystal structure of **5** showing the presence of the aurophilic contact.

To test whether M→Sb(V) interactions could be supported by alternative ligand platforms, we turned our attention to the case of Sb/Au complexes that are featuring ortho-phenlylene-diphenylphosphino units as dinucleating ligands. To access such complexes, we decided to allow the triphosphanylstibine ligand (*o*-$(Ph_2P)C_6H_4)_3Sb$ to react with AuCl(tht) in CH_2Cl_2/acetone (Figure 10). This reaction afforded a stibine-gold complex (**6**) featuring a Sb→Au interaction of 2.8374(4) Å. Remarkably, this compound can be oxidized by reaction with $PhICl_2$ in CH_2Cl_2 to afford **7**. The dinuclear core of the structure shows a clear response to this oxidation reaction. In particular, the Au-Sb distance in **7** (2.7086(9) Å) is shorter than that measured for **6**. Changes are also observed in the coordination sphere of the metals which adopt a distorted octahedral and square planar geometry for antimony and gold, respectively. These changes, and in particular the square planar geometry of the gold atom, indicate that the latter is affected by oxidation as it transitions from a monovalent form in **6** to trivalent form in **7**. DFT calculations confirm this view and indicate that the gold atom is oxidized by partial electron donation to the antimony center. Altogether, these results show that addition of

a Cl_2 equivalent to the antimony center induces an umpolung of the Sb-Au dative bond which switches from Sb→Au in the reduced state to Au→Sb in the oxidized state.

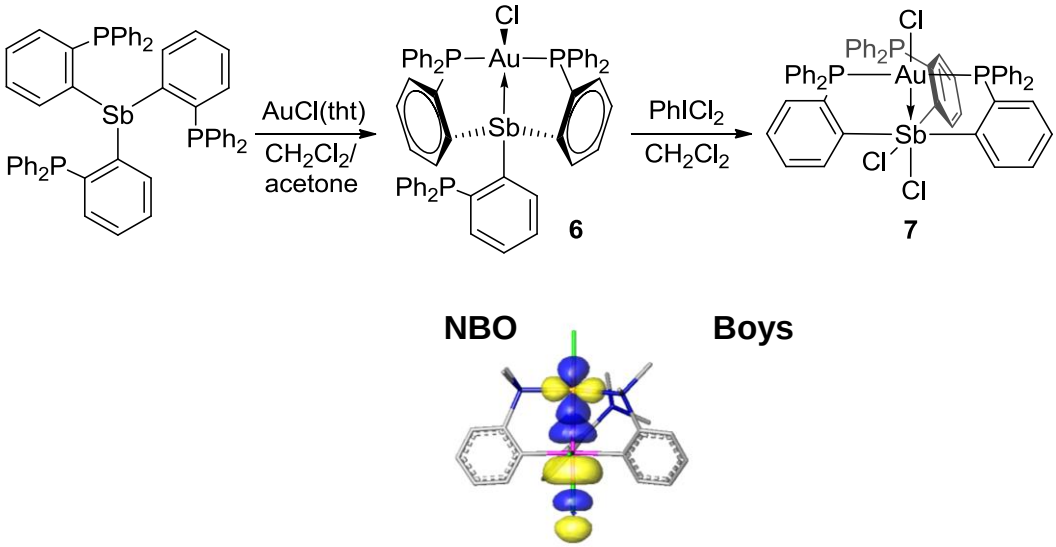

Figure 10. Top: Synthesis of **6** and **7**. Bottom: Natural Bond Orbitals involved in the Au→Sb present in **7**.

Anion complexation by antimony compounds. After establishing the potential that stibonium ions present in the field of anion binding, we investigated whether the strong Lewis acidic properties displayed by these species could also be expressed toward electron rich transition metal centers. With this in mind, we synthesized a series of compounds, including the Hg/Sb complex $\mathbf{8}^{+}$.[35,43] Using a combination of structural, spectroscopic, and computational methods, we showed that these complexes possess very unusual Hg→Sb donor-acceptor interactions, whose existence can be rationalized by considering resonance structures a and b (Figure 11). This interaction, which can be

viewed as involving a low lying antimony σ* orbital as the accepting orbital, is weak and does not lead to measurable changes in the Hg L_3-X-ray Absorption Near Edge Structure (XANES) spectrum. In agreement with the weakness of this interaction, we observed that the antimony center of the complex remains Lewis acidic and readily binds fluoride to form **8**-F.[42,44] Weaker interaction is observed with the larger halide anions. In this case, however, coordination occurs at mercury, leading to formation of **8**-Cl, **8**-Br and **8**-I whose stability constants in DMSO-d_6 are equal to 1890 (±10) M^{-1}, 500 (±10) M^{-1}, and 145 (±5) M^{-1}, respectively.

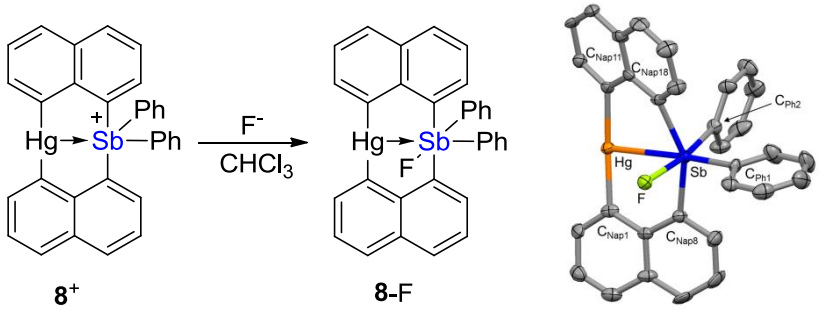

Figure 11. Structure and anion binding properties of **8**. The molecular structure of **8**-F is shown on the right.

Novel σ-acceptor ligands based on heavy main group elements. The structure of compounds such as **8**-F suggests that antimony(V) species are sufficiently Lewis acidic to engage electron rich metals in M→Sb donor acceptor interaction. Recently, however, we have started to question whether such a behavior could also be observed for group 15 species in the trivalent state. With this question as an incentive, we synthesized the complex [(*o*-$(Ph_2P)C_6H_4)_2$BiCl]AuCl (**9**) by reaction of the ligand Bi(*o*-

dppp)$_3$ (*o*-dppp = *o*–(Ph$_2$P)C$_6$H$_4$)) with AuCl(tht) (Figure 12). A careful analysis of the structure of this complex shows that the gold and bismuth atoms are involved in a Au→Bi donor acceptor interaction. This view is confirmed by a NBO analysis which describes the bonding as arising from a d(Au)→p(Bi) interaction.[45]

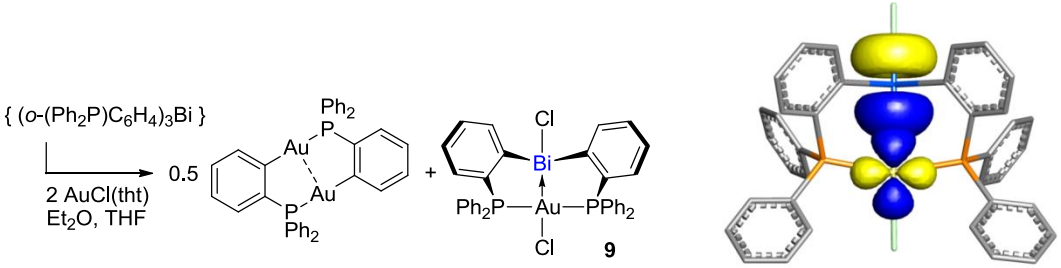

Figure 12. Synthesis of **9** (left) and NBO plot showing the Au→Bi interaction (right).

Having discovered that electron deficient bismuthines act as σ-acceptor ligands toward late transition metals, we decided to investigate whether a similar behavior would be observed for isolobal telluronium cations. As part of these studies, we synthesized the Te(IV)-bis(quinolyl) derivative **10** and found that it cleanly reacts with $Na_2Pd_2Cl_4$ in DMF in the presence of NaOH to afford the cationic complex **11**$^+$ as a 0.5 $PdCl_4^{2-}$ salt (Figure 13).[46] Examination of the structure of this complex shows that the telluronium ion engages the palladium center in an unusual Pd→Te donor acceptor interaction. As supported by computational studies, this interaction involves a d-elelctron pair from palladium and a σ*-orbital from tellurium. These results demonstrate that telluronium ions may behave as σ-acceptor ligands toward transition metals, a phenomenon that originates from the ability of tellurium to achieve an hypervalent configuration.

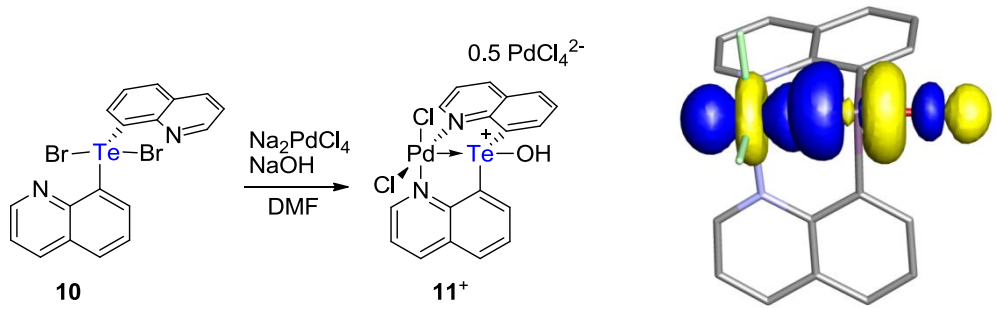

Figure 13. Synthesis (left) and NBO plot (right) of $\mathbf{11}^{+}$ showing the Pd→Te interaction.

Photoreductive elimination of chlorine from a dinuclear TePt platform. To explore the development of applications in the domain of solar energy storage, we have decided to probe whether dinuclear complexes containing a late transition metal element and a heavy main group element could sustain reversible and possibly photoinduced redox chemistry. With this idea as an objective, we synthesized the chloride salt of $[Te^{III}Pt^{I}Cl(o\text{–dppp})_2]^{+}$ ($\mathbf{12}^{+}$) and converted it into the oxidized derivative $ClTe^{III}Pt^{III}Cl_3(o\text{–dppp})_2$ (**13**, *o*-dppp = *o*-$(Ph_2P)C_6H_4$) by reaction with $PhICl_2$ (Figure 14). DFT and NBO calculations show that the central linkage of these complexes undergoes an umpolung from Te→Pt in $\mathbf{12}^{+}$ to Te←Pt in **13**.[47] This umpolung signals an increase in the electron releasing ability of the tellurium center upon switching from an eight–electron configuration in $\mathbf{12}^{+}$ to an hypervalent configuration in **13**. Thus, the tellurium atom acts as an electron reservoir which can alleviate, through increased σ–donation, the electron deficiency caused by oxidative addition of Cl_2. Crucial to the ability of tellurium to donate more extensively to platinum is also the ability of tellurium to accept a chloride anion as an inner sphere ligand *trans* from the platinum atom. Thus, the tellurium atom and its compatibility with a hypervalent configuration serves as a relay

for a "chloride–push/platinum–pull" effect that allows for a greater degree of electron–pair transfer to the platinum center.

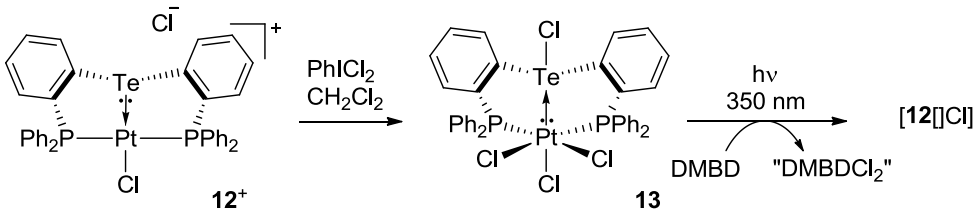

Figure 14. Oxidation of $\mathbf{12}^{+}$ into **13** and photoreductive elimination.

Remarkably, the two–electron redox chemistry displayed by this new dinuclear platform is reversible as shown by the photoreductive elimination of a Cl_2 equivalent when **13** is irradiated at 350 nm in the presence of a radical trap such as 2,3–dimethyl–1,3–butadiene (DMBD) (Figure 14). This photoreductive elimination, which affords [**12**][Cl] with a maximum quantum yield of 4.4%, is facilitated by the ability of tellurium to step back its donation toward platinum through dissociation of the chloride. Collectively, these results show that main group/late transition metal complexes can mimic the behavior of their transition metal–only analogs and, in particular, undergo halogen photoelimination from the oxidized state.

Finally, we have observed that **13** reacts with fluoride anions in methanol to afford an unprecendented telluroxanyl platinum complex **14** (Figure 15). Formation of this complex, which has been confirmed by single crystal X-ray diffraction, results from an internal redox reaction in which the two electron oxidative equivalent migrates from

platinum to tellurium. This internal redox reaction is driven by the preference of tellurium and platinum for hard and soft ligands, respectively.

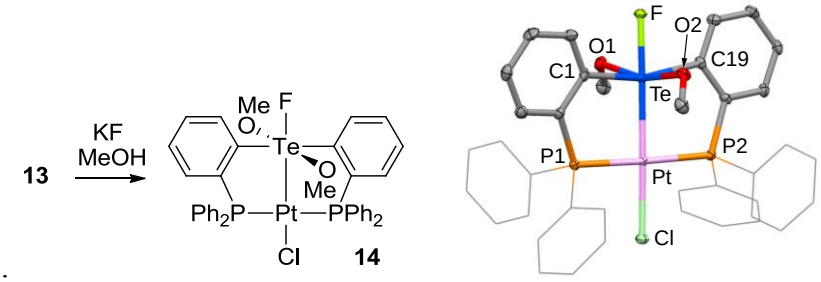

Figure 15. Synthesis (left) and crystal structure (right) of **14**.

1.3 Objective

As mentioned earlier, the anion affinity of main group Lewis acids can be increased by Coulombic attraction as in $[\mathbf{1}]^+$. In the case of $[\mathbf{2}]^+$, the phosphonium ion also acts as a Lewis acid thus enhancing the anion affinity of the receptor. Realizing that stibonium ions should be more Lewis acidic than their phosphonium ions, we have decided to investigate the use of the former as standalone cationic Lewis acidic receptors. As part of this objective, we will study how the nature of the antimony substituents affects the overall anion affinity of the stibonium ion. The knowledge derived from these studies will help us design antimony based anion receptors that are competent for ppm concentrations of fluoride ions in water. Another aspect of this project relates to the incorporation of appropriate reporting groups such as fluorophores that will be used to monitor the anion binding process.

The coordination chemistry of Sb and Bi ligands remains somewhat unexplored. To fill this knowledge gap, we have decided to investigate the synthesis of complexes containing antimony and a group 10 or 11 metal. The objective of these experiments was to 1) broaden the range of known complexes containing these heavy group 15 elements; 2) probe the possible σ-accepting character of the heavy group 15 element in these complexes. This second objective was prompted by the discovery that the antimony atom of complexes such as **9** and $\mathbf{11}^{+}$ behave σ-acceptor toward late transition metal atoms.

CHAPTER II

STIBONIUM IONS FOR THE FLUORESCENCE TURN-ON SENSING OF F^- IN DRINKING WATER AT PARTS PER MILLION CONCENTRATIONS*

2.1 Introduction

Fluoride anion salts are commonly added to drinking water supplies and toothpaste because of their beneficial effects in dental health. In the U.S., this practice has been the center of some discussions because of the adverse effects that excessive fluoride intake may trigger. The recent lowering of the U.S. Department of Health and Human Services recommended fluoride levels from 1.2 to 0.7 ppm[48] has sparked a renewed interest in Lewis acidic main-group compounds that can be used to sense low concentrations of this anion, especially in aqueous media.[49,50] Examples of such Lewis acidic compounds include cationic boron compounds[51-59] such as [**15**]$^+$ which react with fluoride ions to form the corresponding zwitterionic fluoroborates (Figure 16).[60,61] Although the fluoride ion affinity of these cationic boranes enables sensing at the parts per million level in aqueous media, the anion binding event is accompanied by a fluorescence turn-off response, thus limiting the analytical practicality of these derivatives.[60,61]

*Reprinted in part permission from, "Stibonium ions for the fluorescence turn-on sensing of F^- in drinking water at parts per million concentrations"; Ke, I. S.; Myahkostupov, M.; Castellano, F. N.; Gabbaï, F. P. *J. Am. Chem. Soc.* **2012**, *134*, 15309-15311. Copyright 2012 by American Chemical Society.

Some of these boranes also show evidence of slow decomposition in aqueous media. Because of these drawbacks, we are now searching for alternative fluoride ion binding platforms. Inspired by the emerging use of pnictogen-based Lewis acids in various areas of chemistry,[62-65] we have now turned our attention toward pnictonium ions ($[R_4Pn]^+$, Pn = pnictogen), which react with fluoride ions to form the corresponding fluoropnictoranes (R_4PnF). For example, tetraalkylphosphonium ions combine with fluoride ions to form fluorophosphoranes, albeit in strictly anhydrous and nonpolar media.[66-69] A higher fluoride ion affinity is displayed by stibonium ions such as $[Ph_4Sb]^+$ ($[\mathbf{16}]^+$), which, as documented in earlier reports, binds fluoride in biphasic water/CCl_4 mixtures (Figure 16).[28,29] Following a recent study in which we observed fluoride binding at the antimony center of cationic transition-metal stibine complexes,[70,71] we decided to investigate the use of organostibonium ions as water-compatible fluoride sensors (Figure 16). Another important objective of this study was the incorporation of a fluorescent turn-on reporter.

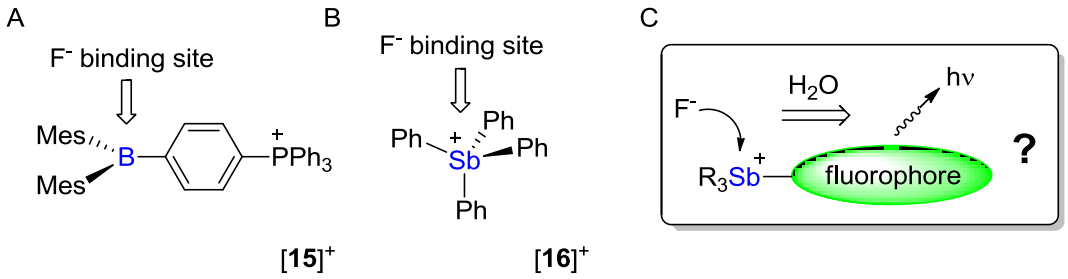

Figure 16. Illustration of **A**: cationic boron, **B**: tetraphenyl stibonium and **C**: organostibonium ions.

2.2 Experimental and computational studies of $[R_4Pn]^+$

With this in mind, we decided to survey the fluoride affinity of tetraphenylpnictogenium ions in acetonitrile. UV-vis titration experiments carried out by incremental addition of fluoride anions to solutions of Ph_4P^+ and Ph_4As^+ in MeCN indicate that these two cations do not associate with the fluoride anion under these conditions, which was also confirmed by ^1H NMR spectroscopy. In the case of Ph_4Sb^+, addition of fluoride anions results in a blue shift/quenching of the phenyl S2←S0 transition indicating formation of the Ph_4SbF. Fitting of these spectral data on the basis of a 1:1 binding isotherm affords a fluoride binding constant greater that 10^6 M^{-1} which indicates that Ph_4Sb^+ is a much stronger Lewis acid than its phosphorus or arsenic analog. The trend observed in the increasing Lewis acidity of these compounds is reminiscent of that observed in the chemistry of halogen-bonded (A) or chalcogen-bonded (B) complexes which become more stable as the group is descended. On the basis of this analogy, it can be proposed that the increased acidity observed on going from Pn = P to Sb originates from the increased polarizability and relative electropositivity of Sb when compared to P and As. The larger size of the element and its ability to accommodate more ligands in its coordination sphere may also be a contributing factor. A simple minded extension of the trend observed on going from the 3rd to the 5th period would suggest that the 6th period congeners would be the most Lewis acidic. A verification of this trend in the case of chalcogen-bonded and halogen-bonded complexes can however not be easily provided because of the nuclear instability of polonium and astatine, respectively. For this reason, we decided to investigate the Lewis

acidity of the Ph_4Bi^+ and compare it to that of its lighter congeners. ^1H NMR titration experiments carried out in d_3-MeCN indicate formation of Ph_4BiF with a stability constant of 1500(±150) M^{-1}. This binding constant is at least 3 orders of magnitude lower than that of the Sb derivative indicating that Ph_4Bi^+ is less Lewis acidic than Ph_4Sb^+ thus suggesting the following fluoride affinity trend: $Ph_4P^+ \sim Ph_4As^+ << Ph_4Bi^+ << Ph_4Sb^+$. To support these experimental findings by computational results, the structure the Ph_4Pn^+ cations and their respective fluoride complexes Ph_4PnF were optimized at the BP86 level of theory using the following mixed basis sets: 6-31G(d) for H and C; 6-31+G(d) for F, and CRENBL ECP for Pn, PCM/MeCN. Form these computational results, the enthalpy change of the reaction depicted in eqn 1 was calculated (Table 1).

$$Ph_4PF + Ph_4Pn^+ \rightarrow Ph_4P^+ + Ph_4PnF \text{ (eqn 1)}$$

Table 1. Enthalpy change for the reaction depicted in eqn 1.

Pn	P	As	Sb	Bi
ΔH (kcal/mol)	0	-7.3	-23.2	-21.1

These calculations indicate that the fluoride affinity of these derivatives increases from P to As to Sb and then decreases on going to Bi, showing a perfect agreement with our experimental results. The observation that Ph_4Bi^+ is less fluorophilic than Ph_4Sb^+ merits comments. While we do not pretend to fully understand these effects, we will note that the onset of strong relativistic effects on moving from Sb to Bi lead to a

"smaller-than-expected" increase in the electropositivity of the element (χ(Sb) = 2.05, χ(Bi) = 2.02). Accordingly, the Pn-F bond may only benefit from a minute increase in electrostatic stabilization. The small magnitude of this increase may not be sufficient to overcome the longer Pn-F bond length (Sb-F = 2.0530(8) for Ph_4SbF[72] and Bi-F = 2.218(3) for Ph_4BiF[73]) nor a weakening of the covalent contribution caused by the increased diffuseness of the 6s/6p orbitals of Bi. Altogether, these results show that stibonium ions are the strongest Lewis acids of the pnictogenium series.

2.3 Synthesis, characterization and photophysical property of stibonium

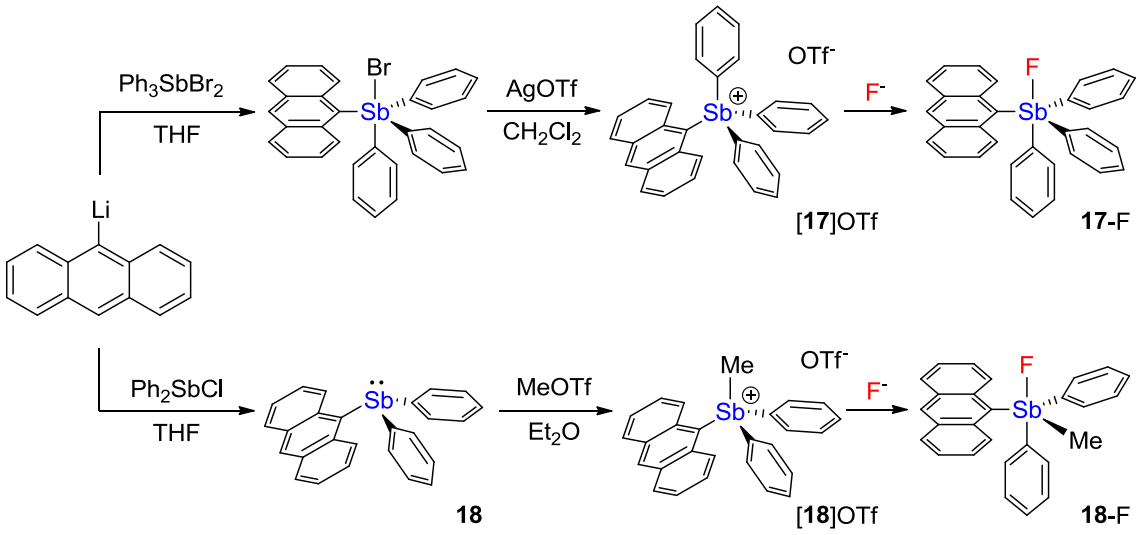

Figure 17. Reactions of [**17**]OTf and [**18**]OTf with KF to form **17**-F and **18**-F.

Following this initial survey, we considered the incorporation of a fluorescence reporter that would turn on upon anion binding. Inspired by the pioneering work of

Yamaguchi and Tamao, who showed a fluorescence turn-on response upon conversion of Ant_3P and Ant_3SiF into Ant_3PF_2 and $[Ant_3SiF_2]^-$ (Ant = 9-anthryl), respectively,[74,75] we prepared the triflate salt of 9-anthryltriphenylstibonium ion, [**17**]OTf. In another approach, anthryldiphenylantimony **18** was synthesized by reaction of Ph_2SbCl with 9-lithioanthracene and converted into [**18**]OTf by reaction with MeOTf in CH_2Cl_2. These salts were characterized by ^1H and ^{13}C NMR spectroscopy, elemental analysis, and single-crystal X-ray diffraction, which revealed that the stibonium cations adopt a tetrahedral structure comparable to those reported for other tetraarylstibonium ions. Treatment of [**17**]OTf and [**18**]OTf with KF in methanol afforded an essentially quantitative yield of the corresponding fluorostiborane, **17**-F and **18**-F, which were also fully characterized. The presence of a Sb-F bonds were confirmed by the detection of a ^{19}F NMR resonance at -75.8 ppm for **17**-F and -78.4 ppm for **18**-F in $CDCl_3$, a value comparable to that for Ph_4SbF (-81.4 ppm in $CDCl_3$). The crystal structures of **17**-F and **18**-F were also determined and indicated that the more sterically demanding anthryl substituent occupies an equatorial site, while the fluoride anion adopts an axial position as in Ph_4SbF (Figure 22).[72] Having established the facile conversion of $[\mathbf{17}]^+$ into **17**-F, we decided to investigate the photophysical properties of each compound in the case of [**17**]OTf and **17**-F. The low-energy part of the absorption spectrum of $[\mathbf{17}]^+$ in $CHCl_3$ is dominated by absorption bands from the anthryl substituent, as confirmed by the characteristic vibronic progression (Figure 18). Interestingly, this compound is only weakly fluorescent, with an anthryl-based emission band at λ_{fluo} = 427 nm and a quantum yield of Φ = 0.7% for [**17**]OTf. Conversion of [**17**]OTf into **17**-F by addition of

TBAF induced a blue shift of the anthryl-based absorption as well as a drastic increase in the fluorescence intensity of the anthryl fluorophore from Φ = 0.7% for [**17**]OTf to Φ = 9.5% for **17**-F (λ_{ex} = 375 nm in $CHCl_3$) (Figure 18). However, no shifts in the emission spectra were observed, thus suggesting that the 0-0 transition energy is virtually the same in the two complexes. As summarized in Table 2, **17**-F becomes a brighter emitter primarily because of a decrease of the nonradiative decay channel (k_{nr}). These changes may result from (i) the decrease in chromophore-solvent interactions that would accompany the conversion of an inherently highly solvated cation ([**17**]$^+$) into a neutral compound (**17**-F) and (ii) the disappearance of any intramolecular anthryl → Sb charge transfer processes in **17**-F that would otherwise quench the excited state of the anthryl chromophore. It is also possible that changes in intramolecular aryl-aryl interactions may be involved, as previously invoked by Yamaguchi and Tamao.[74,75]

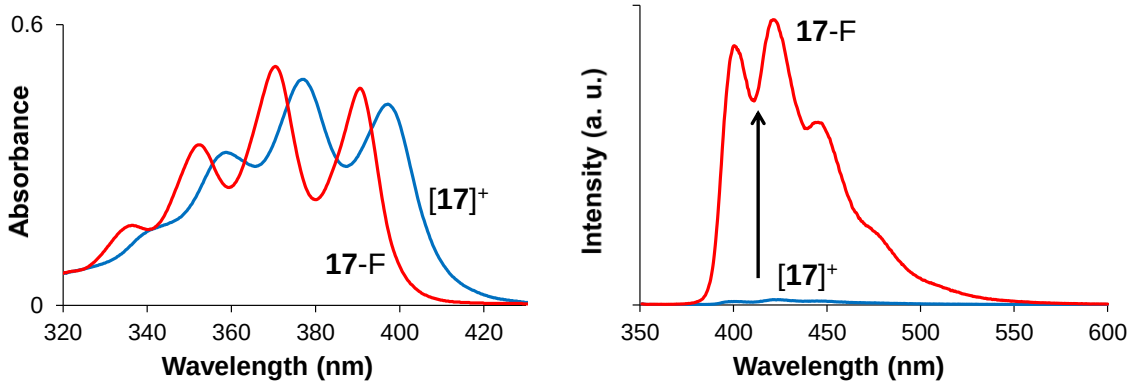

Figure 18. Left: absorption spectra for [**17**]OTf (blue) and **17**-F (red) in $CHCl_3$. Right: emission spectra of [**17**]OTf (blue) and **17**-F (red) in $CHCl_3$.

Table 2. Photophysical properties of [**17**]OTf, **17**-F, and anthracene (for Comparison) measured in $CHCl_3$

	τ (ns)	Φ (AQY)	k_r (s^{-1})	k_{nr} (s^{-1})
[**17**]OTf	<0.15	0.007	4.67×10^7	6.62×10^9
17-F	3.85	0.095	2.47×10^7	2.35×10^8
Ant	1.99	0.107	5.38×10^7	4.49×10^8

2.4 Fluoride binding study in aqueous environment

Initial evidence for the water compatibility of $[\mathbf{17}]^+$ was provided by the observation that addition of fluoride to a solution of [**17**]OTf in 9:1 (v/v) H_2O/dimethyl sulfoxide (DMSO) resulted in rapid precipitation of the fluoride complex. To prevent the formation of this precipitate and to study this reaction at equilibrium, we decided to use cetyltrimethylammonium bromide (CTAB) (10 mM) as an additive. As indicated by UV-vis spectroscopy, [**17**]OTf exists as the free cation up to pH 5. Above this pH, the UV-vis spectrum undergoes a distinct blue shift, suggesting binding of hydroxide anion to the antimony center. Similar results are observed in the case of [**18**]OTf which start becoming neutralized at pH 6.

To parametrize this phenomenon, an acid-base spectrophotometric titration was carried and afforded a pK_{R+} value[60] of 7.07 ± 0.05 for [**17**]OTf and 8.36 ± 0.05 for [**18**]OTf (Figure 19). These pK_{R+} values, which can be regarded as the pH at which the stibonium ions are 50% neutralized by hydroxide anions, indicates that [**17**]OTf and [**18**]OTf should serve as efficient fluoride anion sensors at slightly acidic pH. Indeed, a fluoride titration experiment carried out in 9:1 (v/v) H_2O/DMSO (CTAB, 10 mM) at pH

4.8 (pyridine buffer, 10 mM) indicated that [**17**]OTf binds fluoride anion with a binding constant of 12000 ± 1100 M^{-1}, making this compound compatible for the detection of fluoride in the parts per million range (Figure 18). [**18**]OTf was also investigated, but the titration revealed a significantly lower fluoride binding constant of 470(±30) M^{-1} under the same conditions. These results are therefore in perfect agreement with the acidity scale established on the basis of the pK_{R+} measurements. Gratifyingly and as observed in $CHCl_3$, an increase in the fluorescence intensity was also observed on going from [**17**]OTf to **17**-F, as indicated by Φ = 2.2% for [**17**]OTf and Φ = 14.1% for **17**-F (Figure 20) in aqueous solution. This assay is remarkably selective and does not produce any response to other anions such as Cl^-, Br^-, I^-, NO_3^-, N_3^-, HCO_3^-, and HSO_4^-. Because of this lack of interference, this compound can be used with untreated tap water. For example, this assay returned a value of 1.04 ± 0.01 ppm for a tap water sample (College Station, TX) and a value of 0.14 ± 0.01 ppm for bottled water (Evian, France). To confirm the accuracy of these measurements, the two samples were also tested independently using a fluoride-selective electrode, which returned comparable values (1.07 and 0.16 ppm for the tap and bottled water samples, respectively). Last but not least, the fluorescence turn-on response can be detected with the naked eye in under 1 min for concentrations of at least 1 ppm (Figure 20).

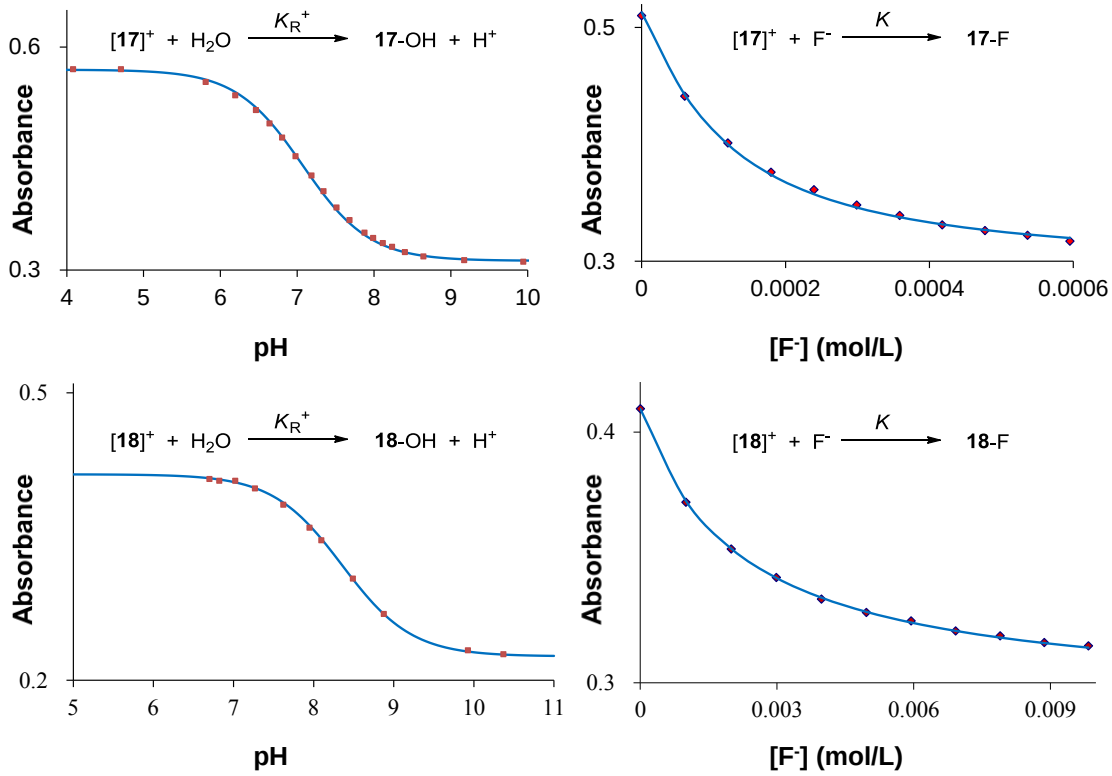

Figure 19. Top left: spectrophotometric acid-base titration curve for [**17**]OTf in a 9:1 (v/v) H_2O/DMSO solution containing CTAB (10 mM) and sodium phosphate (10 mM). The absorbance was measured at 381 nm and fitted to K_{R+} = [**17**-OH][H^+]/[[**17**]$^+$] with ε([**17**]OTf) = 8130 M^{-1} cm^{-1}, ε(**17**-OH) = 4460 M^{-1} cm^{-1}, and pK_{R+} = 7.07 ± 0.05. Top right: fluoride titration of [**17**]OTf in a 9:1 (v/v) H_2O/DMSO solution containing CTAB (10 mM) and pyridine (10 mM) at pH 4.8. The absorbance was monitored at 381 nm and fitted to a 1:1 binding isotherm with K = 12000 ± 1100 M^{-1}, ε([**17**]OTf) = 8130 M^{-1} cm^{-1}, and ε(**17**-F) = 4850 M^{-1} cm^{-1}. Bottom left: spectrophotometric acid-base titration curve for [**18**]OTf in a 9:1 (v/v) H_2O/DMSO solution containing CTAB (10 mM) and sodium phosphate (10 mM). The absorbance was measured at 380 nm and fitted to K_{R+} = [**18**-OH][H^+]/[[**18**]$^+$] with ε([**18**]OTf) = 9100 M^{-1} cm^{-1}, ε(**18**-OH) = 5300 M^{-1} cm^{-1}, and pK_{R+} = 8.36 ± 0.05. Bottom right: fluoride titration of [**18**]OTf in a 9:1 (v/v) H_2O/DMSO solution containing CTAB (10 mM) and pyridine (10 mM) at pH 4.8. The absorbance was monitored at 381 nm and fitted to a 1:1 binding isotherm with K = 470 ± 30 M^{-1}, ε([**18**]OTf) = 9100 M^{-1} cm^{-1}, and ε(**18**-F) = 5400 M^{-1} cm^{-1}.

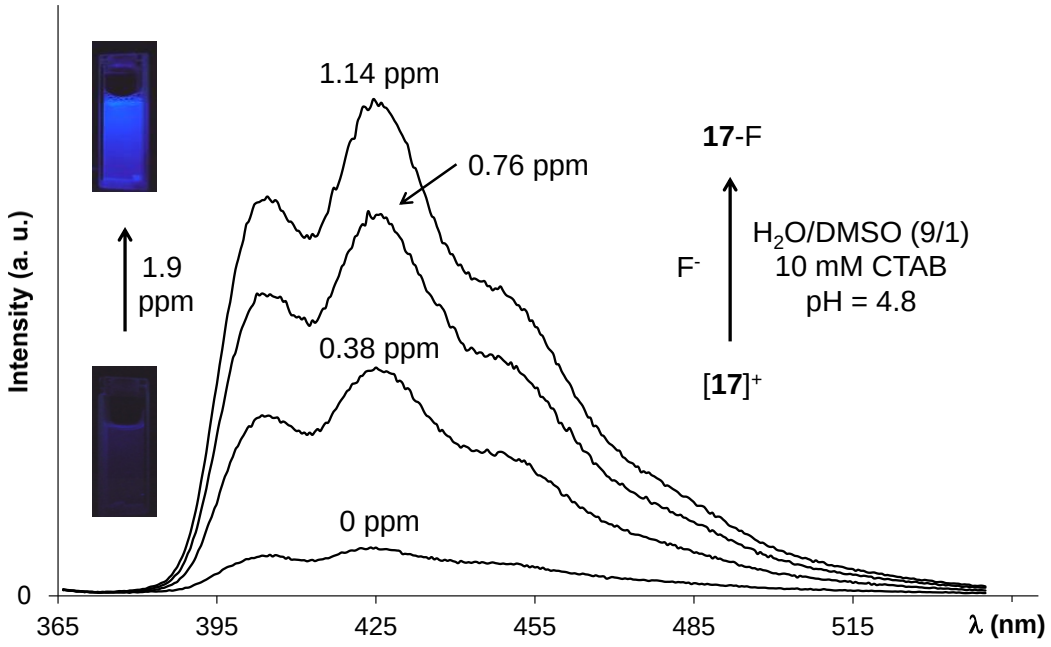

Figure 20. Fluorescence spectra of [**17**]OTf (5.0 μM) in 9/1 (v/v) H_2O/DMSO at pH 4.8 (10 mM CTAB/pyridine buffer) before and after addition of fluoride. The inset shows the visible fluorescence changes (under a hand-held UV lamp) accompanying the addition of 1.9 ppm F^-.

2.5 Conclusions

In conclusion, we have described an original approach to the detection of aqueous fluoride anions in water at the parts per million level. This approach is based on the discovery that stibonium ions are sufficiently fluorophilic to bind fluoride anions in highly competing solvents such as water. The stability, selectivity, and optical turn-on response of this new sensor should make it especially useful for analytical applications.

2.6 Experimental

General considerations. Antimony compounds are toxic and should be handled cautiously. Ph_3SbBr_2 was prepared by following the known method.[76] KF and TBAF were purchased from Alfa Aesar, 9-bromoanthracene from TCI and silver triflate from Strem Chemicals. All preparations were carried out without any special precautions to exclude oxygen. Solvents were dried by passing through an alumina column (toluene) or by refluxing under N_2 over Na/K (Et_2O and THF). UV-vis spectra were recorded on an Ocean Optics USB4000 spectrometer with an Ocean Optics ISS light source. Steady-state fluorescence measurements were carried out by using a PTI, QuantaMaster spectrofluorimeter. Time-resolved fluorescence measurements were carried out in capped 1 cm^2 quartz cuvettes at room temperature on freshly prepared air-saturated optically dilute solutions in $CHCl_3$. Photoluminescence lifetimes (τ_{FL}) were measured using the gated second-harmonic (4 MHz repetition rate, ~1 nJ/pulse) output of a tunable ultrafast Ti-Sapphire oscillator (Coherent, ~120 fs) as an excitation source and a time-correlated single photon counting (TCSPC) detection system (LifeSpec II, Edinburgh Instruments, ~150 ps IRF). The excited state lifetimes were obtained from the first-order decay fit of single wavelength emission transients using Origin 8.0 software. Fluorescence quantum yields (τ_{FL}) were measured on absolute PL quantum yield spectrometer (C11347, Hamamatsu). The radiative (k_r) and non-radiative (k_{nr}) excited state decay rate constants were calculated as follows:

$$k_r = \frac{\Phi_{FL}}{\tau_{FL}} \qquad k_{nr} = \frac{1}{\tau_{FL}} - k_r$$

Elemental analyses were performed by Atlantic Microlab (Norcross, GA). The pH measurements were carried out with a Radiometer PHM290 pH meter equipped with a VWR SympHony electrode. NMR spectra were recorded on Varian Inova 300 FT NMR (299.96 MHz for ^{1}H) and Varian Unity Inova 400 FT NMR (399.59 MHz for ^{1}H, 375.99 MHz for ^{19}F, 100.45 MHz for ^{13}C) spectrometers at ambient temperature. Chemical shifts δ are given in parts per million and are referenced against external $BF_3 \cdot Et_2O$ (^{19}F).

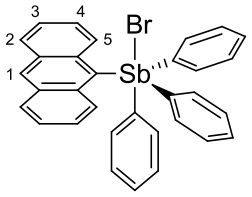

Synthesis of 17-Br. ^{n}BuLi (0.83 ml, 2.33 mmol, 2.8 M in hexane) was added into the solution of 9-bromoanthracene (0.5 g, 1.94 mmol) in 15 ml THF at -78^{o}C. After stirring the reaction mixture for 30 min, 9-lithioanthracene was slowly transferred into a solution of triphenylantimony dibromide (1 g, 1.94 mmol, in 20 ml Et_2O and 10 ml THF) at -78^{o}C. The solution was stirred overnight at room temperature. The solvent was removed under vacuum and the residue extracted with dichloromethane (20 mL). The resulting solution was filtered through Celite to remove LiBr. The filtrate was evaporated to dryness and re-dissolved in MeOH (20 ml). The solution was filtered through Celite again and evaporated to dryness. The residue was recrystallized from Et_2O/CH_2Cl_2 to afford pale-yellow powder **17**-Br (829 mg, 70% yield). ^{1}H NMR (399.59 MHz, $CDCl_3$): δ 8.67 (s, 1H; H_1), 8.45 (d, J = 8.00 Hz, 2H; H_2 or H_5), 8.09 (d, J = 8.00 Hz, 2H; H_2 or H_5), 7.86 (m, 6H; SbPh), 7.45 (m, 11H; SbPh + H_3 + H_4), 7.31 (t, J = 7.24

Hz, 2H; equi-*para*-SbPh). ^{13}C NMR (100.45 MHz, $CDCl_3$): δ139.74, 137.54, 135.92, 132.79, 132.18, 131.38, 131.03, 129.58, 129.39, 127.99, 127.47, 125.57. Elemental analysis calculated (%) for $C_{32}H_{24}BrSb + 0.5CH_2Cl_2$: C, 59.81; H, 3.86. Found: C, 60.57; H, 3.87 (approx. 0.5 eq. of CH_2Cl_2 was lost in drying).

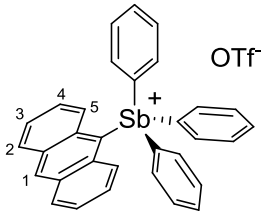

Synthesis of [17]OTf. 17-Br (500 mg, 0.82 mmol) was allowed to react with AgOTf (211 mg, 0.82 mmol) in dichloromethane (10 mL). The resulting mixture was stirred at room temperature for 3h. The solvent was removed under vacuum and the resiude extracted with MeOH (10 mL). The resulting solution was filtered through Celite to remove AgBr. The filtrate was evaporated to dryness and the residue recrystallized from Et_2O/CH_2Cl_2 to afford [**17**]OTf as a pale-yellow powder (507 mg, 91% yield). ^{1}H NMR (399.59 MHz, $CDCl_3$): δ 8.91 (s, 1H; H_1), 8.19 (d, J = 8.82 Hz, 2H; H_2 or H_5), 7.96 (d, J=8.82 Hz, 2H; H2 or H5), 7.72 (m, 6H; SbPh), 7.68 (m, 3H; SbPh), 7.60 (m,6H; SbPh), 7.54 (t, J = 7.21 Hz, 2H; H_3 or H_4), 7.35 (t, J = 7.21 Hz, 2H; H_3 or H_4). ^{13}C NMR (100.45 MHz, $CDCl_3$): δ136.53, 135.30, 133.41, 132.21, 131.17, 130.34, 129.07, 127.16, 126.54, 126.11. ^{19}F NMR (375.97 MHz, $CDCl_3$): δ -78.10 (triflate). Elemental analysis calculated (%) for $C_{33}H_{24}F_3O_3SSb$: C, 58.34; H, 3.56. Found: C, 58.19; H, 3.49.

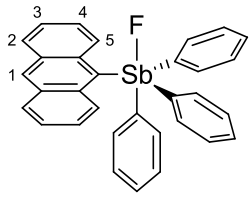

Synthesis of 17-F. [**17**]OTf (200 mg, 0.29 mmol) was dissolved in MeOH (5 mL) and treated with an excess of KF (84 mg, 1.45 mmol). After 10 min., the solvent was removed under vacuum and the residue extracted with dichloromethane (10 mL). The resulting solution was filtered through Celite to remove KOTf. The filtrate was evaporated to dryness and the residue recrystallized from hexane/toluene to afford **17**-F as white powder (105 mg, 65% yield). ^{1}H NMR (399.59 MHz, $CDCl_3$): δ 8.59 (s, 1H; H_1), 7.20 (t, J = 7.53 Hz, 2H; H_3 or H_4), 8.53 (d, J = 8.55 Hz, 2H; H_2 or H_5), 8.13 (m, 6H; SbPh), 8.04 (d, J = 8.55 Hz, 2H; H_2 or H_5), 7.50 (m, 9H; SbPh), 7.39 (t, J = 7.53 Hz, 2H; H_3 or H_4). ^{13}C NMR (100.45 MHz, $CDCl_3$): δ136.36, 135.89, 134.52, 131.83, 130.88, 130.31, 129.77, 129.33, 128.87, 128.57, 126.79, 125.26. ^{19}F NMR (375.97 MHz, $CDCl_3$): δ -75.76 (Sb-F). Elemental analysis calculated (%) for $C_{32}H_{24}FSb$: C, 67.97; H, 4.40. Found: C, 68.52; H, 4.47.

Synthesis of 18. ^{n}BuLi (1.44 ml, 4.02 mmol, 2.8 M in hexane) was added into the solution of 9-bromoanthracene (0.94 g, 3.66 mmol) in 10 ml THF at -78^{o}C. After stirring the reaction mixture for 30 min, diphenylantinomy chloride (1.14g, 3.66 mmol) in 5 ml THF was transfered into the solution. The reaction mixture was warmed to room temperature and stirred overnight. The solvent was removed by *vacuo* and solids were extracted with dichloromethane (20 mL) and filtered through Celite to remove LiCl. The filtrate was evaporated to dryness and the residue recrystallized from MeOH to afford

pale-yellow powder **18** (1.28 g, 77% yield). ^{1}H NMR (400 MHz, acetone-d_6) δ 8.73 (s, 1H), 8.54 (d, J = 8.4 Hz, 2H), 8.12 (d, J = 8.4 Hz, 2H), 7.53 (m, 4H), 7.46 (t, J = 8.4 Hz, 2H), 7.29 (m, 8H); ^{13}C NMR (100 MHz, $CDCl_3$) δ 125.03, 125.49, 128.32, 128.82, 129.33, 130.48, 131.43, 131.87, 135.59, 137.54, 137.82, 138.09. Elemental analysis calculated (%) for $C_{26}H_{19}Sb$: C, 68.91; H, 4.23. Found: C, 68.66; H, 4.19.

Synthesis of [18]OTf. 9-anthracenyldiphenylstibine (0.7889 g, 1.74 mmol) was allowed to react with methyl triflate (0.3 mL, 2.61 mmol) in dichloromethane (2 mL). The resulting mixture was stirred for 3 hours and afforded the pale-yellow precipitate. The solid was filtered, washed with Et_2O (2 × 5 mL) and pentane (2 × 5 mL), and dried under *vacuo* to afford [**18**]OTf (0.9809 g, 91.32% yield). ^{1}H NMR (400 MHz, $CDCl_3$) δ 8.79 ppm (s, 1H; ant-CH), 8.13 (d, J = 7.6 Hz, 2H; ant-CH), 7.87 (d, J = 7.6 Hz, 2H; ant-CH), 7.65 (d, J = 7.2 Hz, 4H; phenyl-CH), 7.59 (t, J = 7.6 Hz, 2H; ant-CH), 7.50 (t, 6H; J = 7.2 Hz, phenyl-CH), 7.41 (t, J = 7.6 Hz, 2H; ant-CH), 2.83 (s, 3H; Sb-CH_3); ^{13}C NMR (100 MHz, $CDCl_3$) δ 9.91, 125.81, 126.38, 128.67, 128.92, 130.15, 130.63, 131.99, 132.64, 134.284, 134.87, 135.94; ^{19}F NMR (375.97 MHz, $CDCl_3$): δ -78.42. Elemental analysis calculated (%) for $C_{28}H_{22}F_3O_3SSb$: C, 54.48; H, 3.59. Found: C, 54.06; H, 3.91.

Synthesis of 18-F. [**18**]OTf (200 mg, 0.32 mmol) was dissolved in MeOH (5 mL) and treated with excess of KF for 10 min. The solvent was removed by *vacuo* and solids were extracted with dichloromethane (10 mL) and filtered through Celite to remove KOTf. The filtrate was evaporated to dryness and the residue recrystallized from hexane/toluene to afford white powder **18-F** (81 mg, 51% yield). ^{1}H NMR (400 MHz, $CDCl_3$) δ 8.70 ppm (s, 1H; ant-CH), 8.12 (d, J = 8.56 Hz, 2H; ant-CH), 8.04 (d, J = 8.56

Hz, 2H; ant-CH), 7.57 (d, J = 7.22 Hz, 4H; phenyl-CH), 7.48 (t, J = 7.22 Hz, 2H; ant-CH), 7.50 (m, 8H phenyl-CH+ant-CH), 2.67 (s, 3H; Sb-CH_3); ^{13}C NMR (100 MHz, $CDCl_3$) δ 11.87, 125.16, 125.33, 126.84, 128.15, 128.41, 128.99, 129.43, 130.51, 131.86, 135.18, 135.88; ^{19}F NMR (375.97 MHz, $CDCl_3$): δ -78.42. Elemental analysis calculated (%) for $C_{27}H_{22}FSb$: C, 66.56; H, 4.55. Found: C, 65.11; H, 4.55.

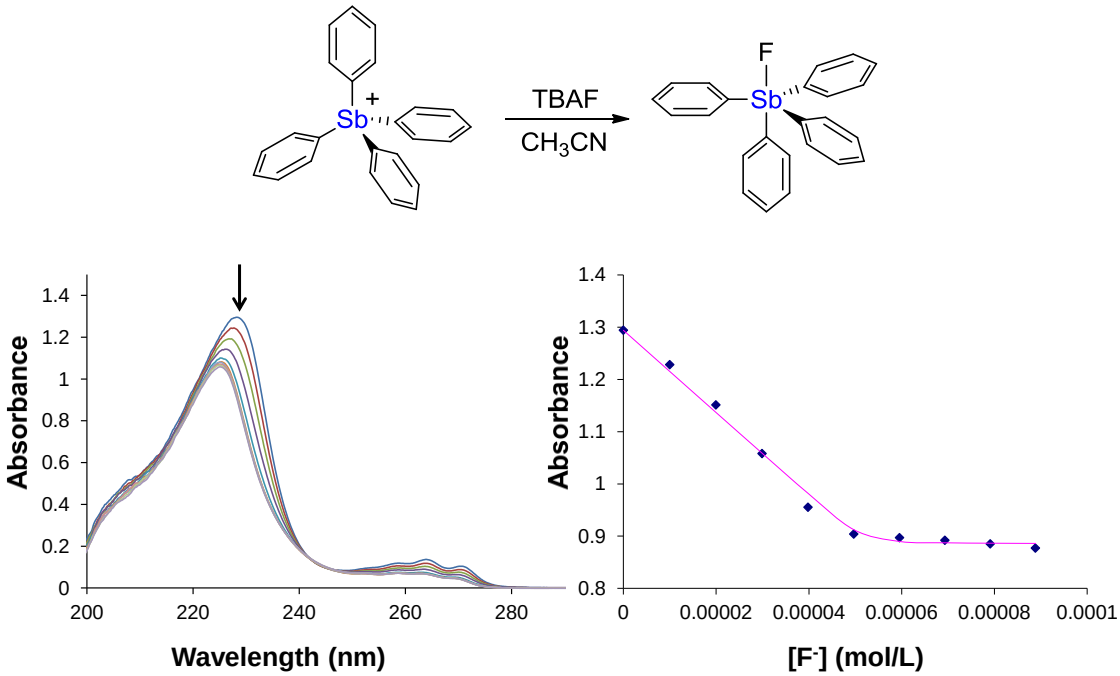

Figure 21. Spectral changes in the UV-vis absorption spectra of $[Ph_4Sb]^+$ (5.17×10^{-5} M) in CH_3CN upon incremental addition of a TBAF solution (6.0×10^{-3} M, CH_3CN). The isotherms are plotted based on the absorbance at 230 nm, and the line indicates the fit to the calculated 1:1 binding isotherm. The fluoride binding constant was calculated to be > 10^6 M^{-1}.

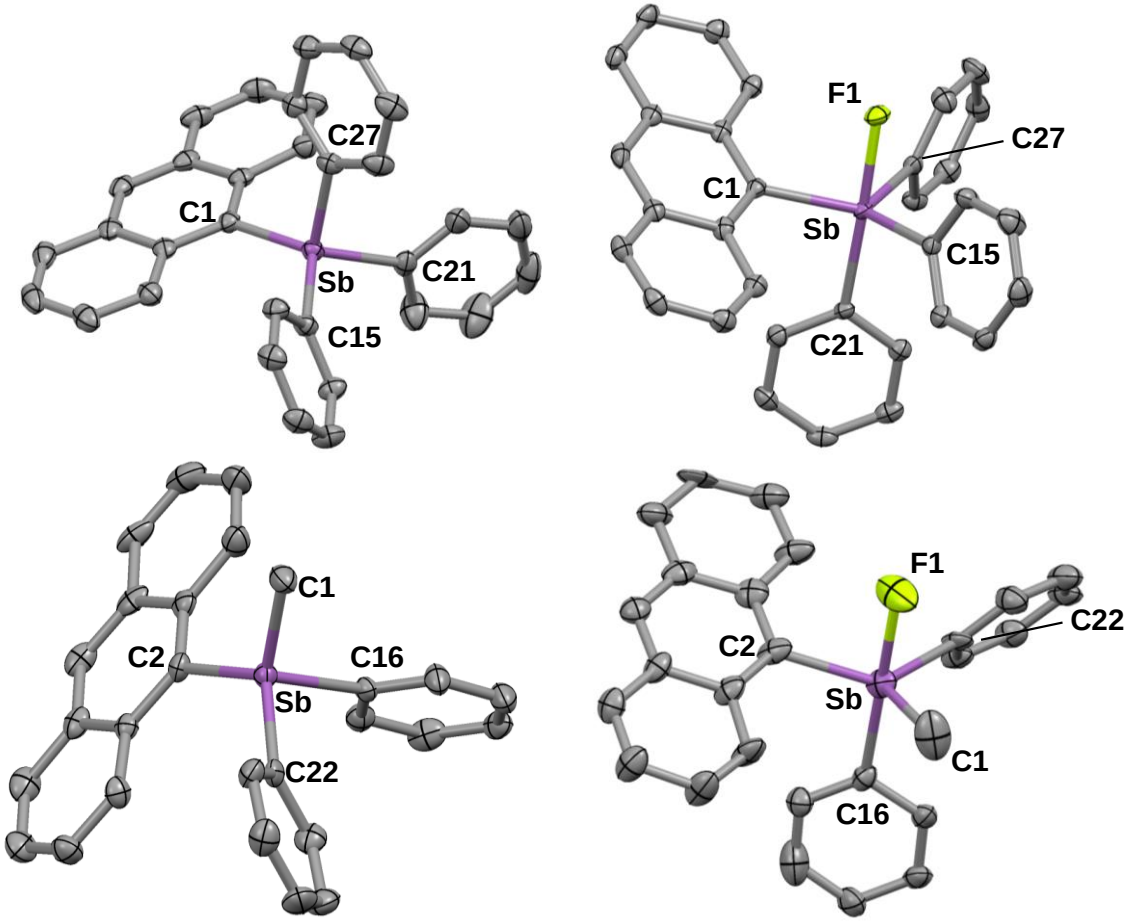

Figure 22. Structure of [**17**]OTf (top left), **17**-F (top right), [**18**]OTf (bottom left) and **18**-F (bottom right). Displacement ellipsoids are scaled to the 50% probability level. Interstitial solvent molecules, OTf^- and hydrogen atoms are omitted for clarity. Selected bond lengths (Å) and angles (deg) for: [**17**]OTf: Sb-C1 2.112(2), Sb-C15 2.112(2), Sb-C21 2.113(2), Sb-C27 2.111(2); C1-Sb-C27 102.27(8), C1-Sb-C15 121.88(8), C27-Sb-C15 102.02(8), C1-Sb-C21 116.36(8). **17**-F: Sb-F 2.0363(17), Sb-C1 2.160(3), Sb-C15 2.140(3), Sb-C21 2.180(3), Sb-C27 2.142(3); F1-Sb-C21 177.90(8), C27-Sb-C15 114.99(11), C15-Sb-C1 118.97(11), C27-Sb-C1 122.33(11).

Table 3. Crystal data, data collections, and structure refinements for [**17**]OTf and **17**-F

Crystal data	[**17**]OTf	**17**-F
Formula	$C_{33}H_{24}S_3O_3SSb$	$C_{32}H_{24}FSb$
Mr	679.33	549.29
Crystal size (mm^3)	0.45 x 0.35 x 0.20	0.15 x 0.13 x 0.08
Crystal system	Triclinic	Monoclinic
Space group	P-1	P2(1)/n
a (Å)	9.545(2)	9.622(4)
b (Å)	11.803(3)	16.820(6)
c (Å)	13.848(4)	14.0745(6)
α (°)	94.664(3)	90
β (°)	107.251(2)	92.461(4)
γ (°)	106.439(3)	90
V ($Å^3$)	1405.6(6)	2384.1(15)
Z	2	4
ρ_{calc} (g cm^{-3})	1.605	1.463
μ (mm^{-1})	1.110	1.181
F(000)	680	1008
T/K	110(2)	110(2)
Scan mode	ω, φ	ω, φ
hkl Range	-11 → +11	-12 → +12
	-14 → +14	-22 → +22
	-16 → +16	-19 → +19
Measd reflns	13411	29089
Unique reflns [R_{int}]	4927 [0.0203]	6002 [0.0600]
Reflns used for refinement	4927	6002
Refined parameters	370	307
GooF	1.035	1.036
$R1$,[a] $wR2$[b] (all data)	0.0226, 0.0523	0.0588, 0.0752
ρ_{fin} (max/min.) ($eÅ^{-3}$)	0.514, -0.295	0.594, -0.710

[a] $R_1 = \Sigma||Fo| - |Fc||/\Sigma|Fo|$. [b] $wR_2 = [[\Sigma w(Fo^2 - Fc^2)^2]/[\Sigma w(Fo^2)^2]]^{1/2}$.

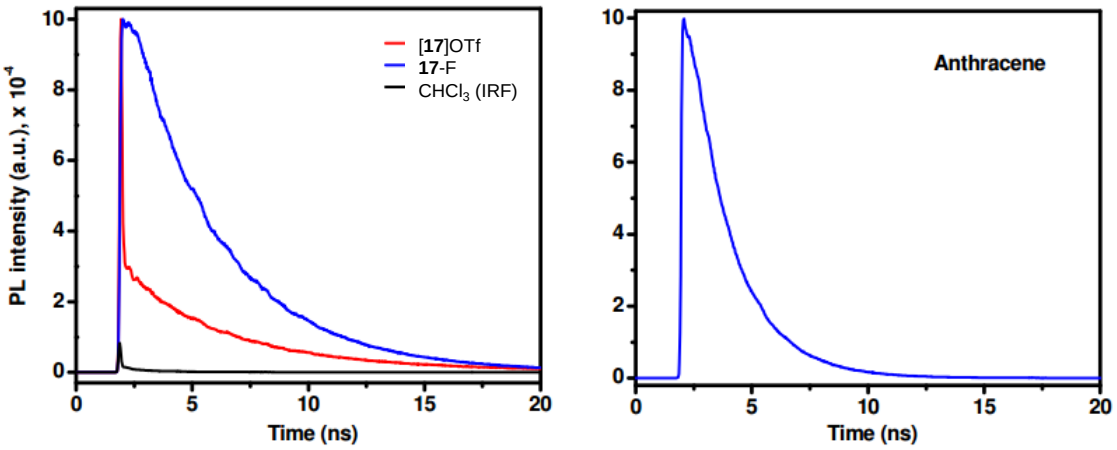

Figure 23. Photoluminescence intensity decays of [**17**]OTf, **17**-F (λ_{ex} = 390 nm) and anthracene (λ_{ex} = 375 nm, for comparative purposes) measured in $CHCl_3$.

Titration of [17]OTf with fluoride in 9/1 H_2O/DMSO. A solution of [**17**]OTf (3.0 mL, 5.0 x 10^{-5} M, H_2O/DMSO (9/1, v/v) at pH 4.8 (10 mM CTABr pyridine buffer) was titrated with incremental amounts of fluoride by addition of a 0.06 M solution of KF in H_2O. The changes in the absorption spectra were fitted to a 1:1 binding isotherm to provide fluoride binding constant of 12000 (±1100) M^{-1} (using ε([**17**]OTf) = 8130 M^{-1} cm^{-1}, ε(**17**-F) = 4850 M^{-1} cm^{-1}).

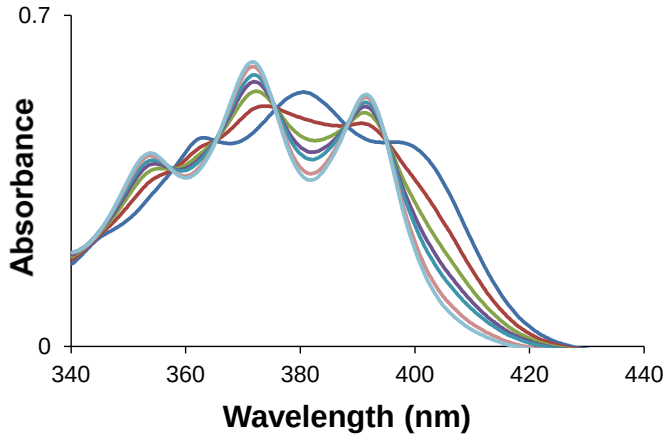

Figure 24. Changes in the absorption spectrum of [**17**]OTf after successive additions of fluoride anions.

Tap water fluoride concentration test:

1. Standard curve: In a fluorescence cell, a DMSO solution of [**17**]OTf (0.3 ml, 7.0 x 10^{-5} M) was combined with i) an aqueous CTAB (cetyltrimethylammonium bromide, 10mM) solution (1.7 ml) buffered at pH 4.8 (pyridine buffer, 10 mM), ii) H_2O (1ml). The resulting solution was titrated by incremental addition of a solution of KF (0.0072 M) in water. The experiment was monitored by fluorescence spectroscopy. The fluorescence intensity at 425 nm was used to establish a standard curve (Figure 25).

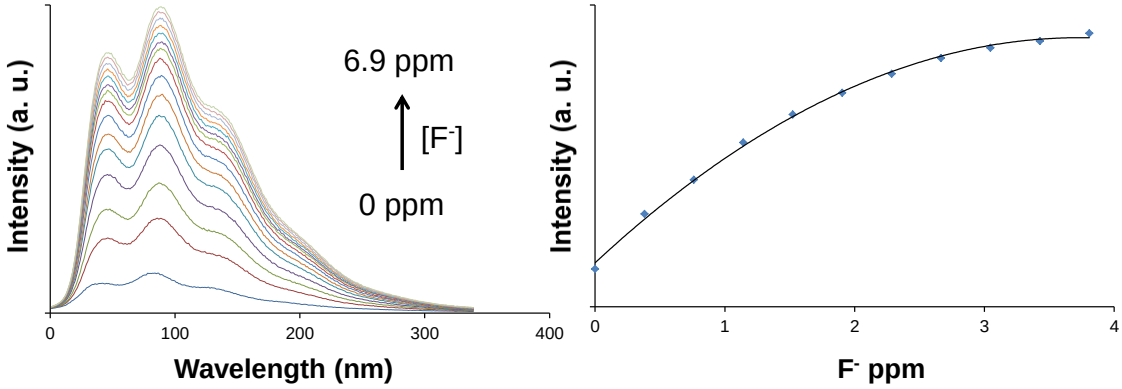

Figure 25. (left) Changes in the emission spectrum of [**17**]OTf after successive additions of fluoride anions; (right) The emission was measured at 425 nm.

The fluoride binding constant could also be calculated using the fluorescence data which was fitted to the following equation:

$$I = I_{Sb} + (I_{SbF} - I_{Sb})\frac{X}{C_o}$$

In this equation, C_o is the initial [**17**]OTf concentration and $\mathbf{I}_{Sb}$ and $\mathbf{I}_{SbF}$ are the intensities for the free and bound state of the sensor, respectively.[77] A full derivation of the equation (including the expression defining X) is provided below. Fitting of the experimental data afforded K = 12000 (±1100) M^{-1} ($\mathbf{I}_{Sb}$ = 340000 and $\mathbf{I}_{SbF}$ = 1400000), the same value as that determined by UV-vis spectroscopy.

$$\underset{C_o - X}{[Sb]^+} + \underset{F_o - X}{F^-} \longrightarrow \underset{X}{Sb\text{-}F}$$

Equation 1. Chemical distribution after of fluoride addition to a solution of [**17**]OTf.

$$K_a = \frac{X}{(C_o - X)(F_o - X)} \qquad [Sb]^+ = \frac{X}{(F_o - X)\,K_a} \qquad [Sb\text{-}F] = K_a\,(C_o - X)(F_o - X)$$

$$X = K_a\,(C_o - X)(F_o - X)$$

$$K_aX^2 - (C_oK_a + F_oK_a + 1)X + C_oF_oK_a = 0$$

$$X = \frac{A - (A^2 - 4C_oF_o)^{1/2}}{2} \qquad \text{where } A = C_o + F_o + \frac{1}{K_a}$$

Equation 2. Relationship between the observed concentration with respect to the amount of fluoride added and to the binding constant K_a.

$$I = I_{Sb}X_{Sb} + I_{SbF}X_{SbF} \qquad X_{Sb} + X_{SbF} = 1 \Longrightarrow X_{Sb} = 1 - X_{SbF}$$

$$= I_{Sb}(1 - X_{SbF}) + I_{SbF}X_{SbF}$$

$$= I_{Sb}\left(1 - \frac{K_a\,(C_o - X)(F_o - X)}{C_o}\right) + I_{SbF}\left(\frac{K_a\,(C_o - X)(F_o - X)}{C_o}\right)$$

$$= I_{Sb}\left(1 - \frac{X}{C_o}\right) + I_{SbF}\left(\frac{X}{C_o}\right) \qquad \text{replace } X = K_a\,(C_o - X)(F_o - X)$$

$$= I_{Sb} + (I_{SbF} - I_{Sb})\frac{X}{C_o}$$

Equation 3. Relationship between the observed fluorescence intensity with respect to the amount of fluoride added and to the binding constant K_a (X_{Sb} and X_{SbF} are the mole fraction of [**17**]OTf and **17**-F, respectively).

2. Tap water sample test: In a fluorescence cell, a DMSO solution of [**17**]OTf (0.3 ml, 7.0 x 10^{-5} M) was combined with i) an aqueous CTAB (cetyltrimethylammonium bromide, 10 mM) solution (1.7 ml) buffered at pH 4.8 (pyridine buffer, 10 mM). To this solution was added 1 ml of a water sample to analyze. The solution was stirred for two minutes prior to the fluorescence measurement. The resulting fluorescence data are listed in the following Table 4. The samples were also analyzed by Soil, Water, and Forage Testing Laboratory (345 Heep Center, College Station, TX 77843-2474) using a fluoride electrode.

Table 4. The resulting fluorescence data of tap and Evian water.

Sample	Em_{425}	F^- ppm (by $[\mathbf{17}]^+$)	F^- ppm (by F^- electrode)
Tap water	520600	1.045 (±0.011)	1.070
Evian water	368650	0.144 (±0.009)	0.164

(The tap water sample was collected on 10/18 2010 in College Station, TX. The Evian sample was purchased on the same day from the supermarket HEB, College Station, TX)

Crystallography. All crystallographic measurements were performed at 110(2) K using a Bruker SMART APEX II diffractometer with a CCD area detector (graphite monochromated Mo Kα radiation, λ = 0.71073 Å, ω-scans with a 0.5˚ step in ω) at 110K. In each case, a specimen of suitable size and quality was selected and mounted onto a nylon loop. The semi-empirical method SADABS was applied for absorption correction. The structures were solved by direct methods and refined by the full-matrix least-square

technique against F^2 with the anisotropic temperature parameters for all non-hydrogen atoms. All H atoms were geometrically placed and refined in riding model approximation. Data reduction and further calculations were performed using the Bruker SAINT+ and SHELXTL NT program packages.[78]

Computational details. Density functional theory (DFT) structural optimizations were performed on the pnictonium Ph_4Pn^+ and pnictoranes Ph_4Pn-F (Pn = P, As, Sb) using the Gaussian 03 program[79] (BP86[80,81] with 6-31g(d) for H, C, F; Stuttgart relativistic large core (RLC) 1997 ECP for P, As and Sb).[82-85] Frequency calculations, which were carried out on the optimized structure of the compounds, confirmed the absence of any imaginary frequencies. All energies, expressed in hartrees, are reported for standard conditions, 298 K and 1 atm., and include the vibrational and S11thermodynamic correction. For each structure, the numbering of the atoms follows their order of appearance in the Cartesian coordinate list. The energies corrected to enthalpy (ΔH) for $[Ph_4Pn]^+$ and Ph_4Pn-F are provided in the following Table 5. These energies were used to calculate the difference in fluoride affinities provided in the text.

$$Ph_4P\text{-}F + [Ph_4Sb]^+ \longrightarrow [Ph_4P]^+ + Ph_4Sb\text{-}F \qquad \Delta H = -23.2 \text{ kcal/mol}$$

$$Ph_4As\text{-}F + [Ph_4Sb]^+ \longrightarrow [Ph_4As]^+ + Ph_4Sb\text{-}F \qquad \Delta H = -15.9 \text{ kcal/mol}$$

Table 5. The energies corrected to enthalpy (ΔH) for $[Ph_4Pn]^+$ and Ph_4Pn-F.

	$[Ph_4P]^+$	$[Ph_4As]^+$	$[Ph_4Sb]^+$
Energy (Hartrees)	-932.5504073	-932.2293282	-931.442397
	Ph_4P-F	Ph_4As-F	Ph_4Sb-F
Energy (Hartrees)	-1032.5127863	-1032.2033128	-1031.4416037

CHAPTER III

CATIONIC STIBINE-PALLADIUM COMPLEX FOR FLUORIDE ANION SENSING

3.1 Introduction

The advent of triarylboranes as anion receptors has led to a number of positive developments including the discovery of water-compatible sensors for the potentially toxic fluoride anion.[52-54,86,87] The success of this approach lies in the ability of triarylboranes to form a covalent bond with the anionic guest (case **A**, Figure 26) and respond to its presence via a photophysical property change. As part of our interest in fundamental aspects of main group chemistry, we have recently questioned whether alternative fluoride sensing platforms based on main group Lewis acids could be envisaged.[74,88,89] With this idea in mind, we were drawn by the reported ability of $[Ph_4Sb]^+$ to react with fluoride anions in CCl_4/H_2O and generate the corresponding fluorostiborane Ph_4SbF (case **B**, Figure 26).[18,28,29] While this observed reactivity attests to the strength of the Sb-F bond, the absence of major photophysical changes accompanying the formation of the fluorostiborane limits the development of any anion sensing application.

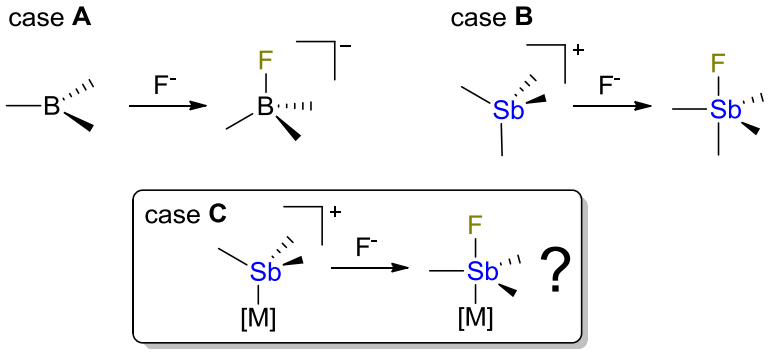

Figure 26. Illustration of fluoride sensors. Case **A**: boron, **B**: stibonium and **C**: transition metal-stibonium.

Cationic triarylstibine transition metal complexes have been previously reported.[33,90] Like stibonium ions, such species possess a four coordinate antimony atom. On the basis of this simple structural analogy, we speculated: i) that the antimony atom of such complexes may be reactive toward fluoride; ii) that anion binding at the antimony center may affect the properties of the transition metal center, leading to an easily detectable optical signal (case **C**, Figure 26). In this communication, we report a series of results which provide an initial validation of this approach.

3.2 Synthesis and characterization of [**19**]BPh_4

To prevent an anion-induced cleavage of the M-Sb bond, we decided to focus on a family of complexes in which the M-Sb bond is supported by auxiliary chelating ligands. With this prerequisite in mind, we decided to synthesize the pincer-type bisphosphanylphenyl antimony ligand [(*o*-$(Ph_2P)C_6H_4)_2PhSb$, referred to as L^2] which can be prepared by directly adding 2 equiv of *o*-$(Ph_2P)LiC_6H_4$ to the solution of $PhSbCl_2$.

Reaction of this ligands with $PdCl_2(cod)$ (cod = 1,5-cyclooctadiene), and subsequent treatment with 1 equiv. of $NaBPh_4$ in CH_2Cl_2/EtOH, afforded high yields of the cationic palladium complexes $[L^2PdCl]^+$ ($[\mathbf{19}]^+$) as the BPh_4^- salts (Figure 27). The $^{31}P\{^1H\}$ NMR spectra in $CDCl_3$ display a single resonance at δ = 53.81 ppm for $[\mathbf{19}]^+$. The crystal structure of [**19**]BPh_4 shows that the d^8 metal center in each complex adopts a square planar geometry with the two coordinated phosphine arms in a trans arrangement (Figure 29). The Pd(1)-Sb(1) bond distance of 2.4816(6) for [**19**]BPh_4 is slightly shorter than those measured in the square planar triarylstibine palladium complexes *trans*-(*o*-$Tol_3Sb)_2PdCl_2$ (Pd-Sb = 2.5658(3) Å) and *trans*-$(Ph_3Sb)_2Pd(Ph)Cl$ (Pd-Sb = 2.5568(5) Å), suggesting tight coordination of the antimony ligand.

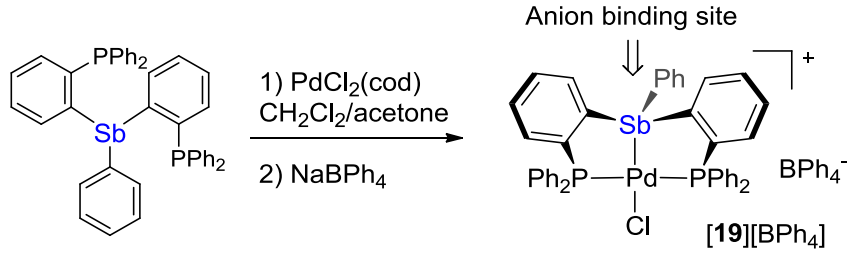

Figure 27. Synthesis of [**19**]BPh_4.

3.3 Fluoride binding studies and characterization of **19**-F

With this cationic complex in hand, we sought to determine if they would exhibit reactivity similar to tetraorganostibonium ions and form fluorostiboranes in the presence of fluoride ions.[18,28,29] To this end, solutions of [**19**]BPh_4 in CH_2Cl_2 were allowed to react with *n*-tetrabutylammonium fluoride (TBAF). The color of this solution retained a

pale yellow color. To gain insight into their course, these reactions were monitored by NMR spectroscopy. Formation of the fluoride complex **19**-F was supported by detection of a doublet resonance (64.06 ppm, $^{3}J_{F\text{-}P}$ = 26.7 Hz) in the $^{31}P\{^{1}H\}$ NMR spectrum of the reaction mixture (Figure 28). Consistent with this observation, the ^{19}F NMR spectrum showed the appearance of a quartet resonance ($^{3}J_{F\text{-}P}$ = 26.7 Hz) at -124.61 ppm.

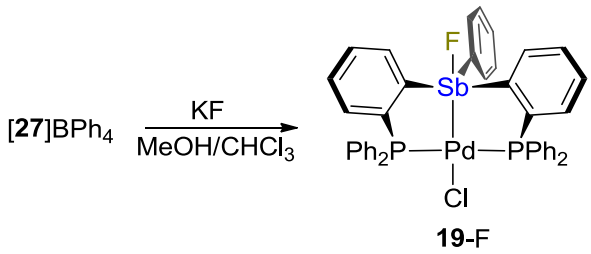

19-F

Figure 28. Synthesis of **19**-F.

To confirm that the fluoride anions in **19**-F is bound to antimony and not palladium, the structures of these complexes were determined using single crystal X-ray diffraction. In accordance with our original hypothesis, the structures show coordination of the fluoride anion to the antimony atom via a 2.0511(19) for **19**-F (Figure 29). This distance is close to that observed in the fluorostiborane Ph_4SbF (2.0530(8) Å),[72] thus attesting to the presence of a strong interaction. Finally, the Pd(1)-Sb(1) bonds in the fluoride complexes (2.5855(10) Å for **19**-F) are slightly longer than those measured in their cationic precursors (2.4816(6) Å for [**19**]BPh_4), a trend that we assign to the change in the antimony coordination geometries. Thus, **19**-F constitutes a rare example of stiboranyl complex, which prior to this work had not been observed with palladium.[36-

[42,64] This complex can also be classified as metallametallatranes[91-97] and are especially reminiscent of the metalla-silatranes and -stannatranes with hypervalent group 14 centers.[98-102]

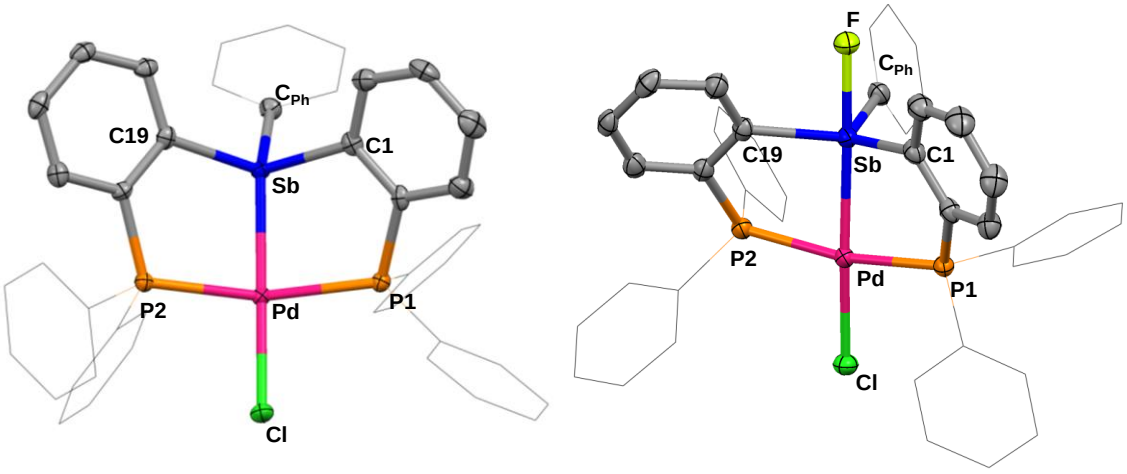

Figure 29. Crystal structures of [**19**]BPh_4 (left) and **19**-F (right). Thermal ellipsoids are drawn at the 50% probability. Phenyl groups are drawn in wireframe and hydrogen atoms, solvents and BPh_4^- for [**19**]BPh_4 are omitted for clarity. Selected bond lengths (Å) and angles (˚) for [**19**]BPh_4: Sb-Pd 2.4816(6), Pd-Cl1 2.3379(10), Pd-P1 2.3224(10), Pd-P2 2.3101(9); Cl1-Pd-Sb 176.69(2), P2-Pd-P1 164.52(3); C19-Sb-C37 105.24(12), C19-Sb-C1 115.21(12), C37-Sb-C1 101.68(12). **19**-F: Pd-Cl1 2.4062(12), Sb-Pd 2.5855(10), Pd-P1 2.2903(11), Pd-P2 2.3050(11), Sb-F1 2.0511(19); Cl1-Pd-Sb 173.43(2), F1-Sb-Pd 177.93(5), C37-Sb-C1 121.19(12), C37-Sb-C19 113.10(11), C1-Sb-C19 121.54(11).

Having confirmed that fluoride binds to the antimony center of this complex, we turned our attention to studying the fluoride binding by UV-vis spectrum. The UV-Vis spectrum of [**19**]BPh_4 in CH_2Cl_2 displays an absorption band at λ_{max} = 361 nm, which tails off beyond 390 nm (Figure 30). This low energy band is attributed to mixed MLCT and ligand-centered transitions typically observed for square planar Pd complexes.[103,104] UV-Vis monitoring of the conversion of [**19**]BPh_4 into **19**-F upon incremental addition of fluoride anions shows a progressive quenching of the band at 361 nm, accompanied

by the appearance of new absorption bands centered at 320 nm. The binding constant measurement was performed in 9/1 vol. MeOH/CH_2Cl_2 by incremental addition of KF in MeOH. Fitting of the resulting data affords a fluoride binding constant of 1.2(±0.2) x 10^4 M^{-1} (Figure 31).

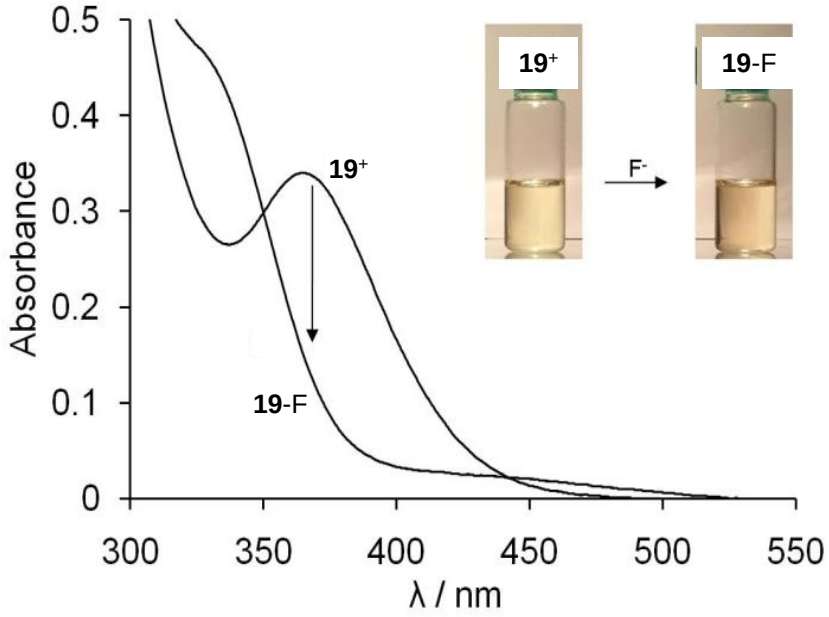

Figure 30. Absorption spectra of [**19**]BPh_4 and **19**-F (4.8×10^{-5} M) in CH_2Cl_2. The pictures in the insets show the colorimetric response associated to the formation of the fluoride derivatives at a concentration of 5×10^{-4} M.

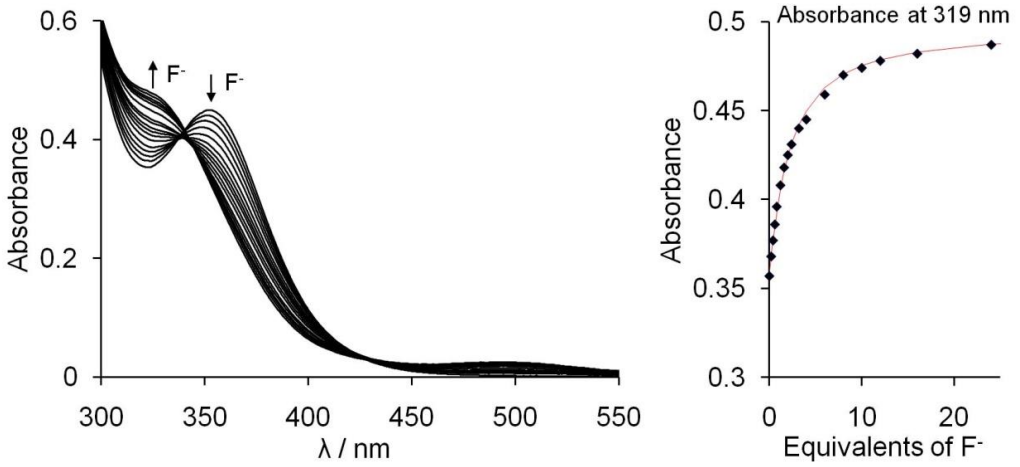

Figure 31. Spectral changes in the UV-Vis absorption spectra of [**19**]BPh_4 (5.0×10^{-5} M) in 9/1 vol. MeOH/CH_2Cl_2 upon incremental addition of 6.1×10^{-3} M and 6.1×10^{-2} M solutions of KF in MeOH. The isotherms are plotted based on the absorbance at 319 nm, and the line indicates the fit to the calculated 1:1 binding isotherm. The fluoride binding constant was calculated to be $1.2(0.2) \times 10^4$ M^{-1}.

3.4 Conclusions

In summary, we report a cationic bisphosphanylstibine-palladium complex ([**19**]BPh_4) which acts as a fluoride anion sensor. The sensing properties of this complex result from the formation of a hypervalent fluorostiboranyl motif coupled with a coordination geometry change of the palladium center. This fluoride sensor can bind fluoride in 90% MeOH/10% CH_2Cl_2 with the binding constant of $1.2(0.2) \times 10^4$ M^{-1}.

3.5 Experimental

General considerations. Antimony compounds are highly toxic and should be handled cautiously. $PdCl_2(cod)$[105] was prepared according to the reported procedures. All preparations were carried out without any special precautions to exclude oxygen.

Solvents were dried by passing through an alumina column (pentane and CH_2Cl_2) or refluxing under N_2 over Na/K (Et_2O, *n*-hexane, and THF). All other solvents were used as received. KF and TBAF were purchased from Alfa Aesar. Ambient temperature NMR spectra were recorded on a Varian Unity Inova 400 FT NMR (399.59 MHz for ^{1}H, 375.99 MHz for ^{19}F, 161.74 MHz for ^{31}P, 100.45 MHz for ^{13}C) spectrometer. Low temperature ^{31}P NMR spectra were recorded on a Varian Inova 300 FT NMR spectrometer (121.42 MHz for ^{31}P). Chemical shifts (δ) are given in ppm and are referenced against residual solvent signals (^{1}H, ^{13}C) or external BF_3•Et_2O (^{19}F) and H_3PO_4 (^{31}P). UV-Vis spectra were recorded on an Ocean Optics USB4000 spectrometer with an Ocean Optics ISS light source. Elemental analyses were performed at Atlantic Microlab (Norcross, GA).

Synthesis of (*o*-(Ph_2P)C_6H_4)$_2$PhSb. ^{n}BuLi (1.35 ml, 3.51 mmol, 2.60 M in hexane) was added into the solution of *o*-(Ph_2P)C_6H_4Br (1.00 g, 2.93 mmol) in Et_2O (10 mL) at room temperature. The reaction was allowed to stir for 30 min before adding solution of $PhSbCl_2$ (0.39g, 1.46 mmol) in THF (5 mL). The resulting mixture was stirred overnight at room temperature. The solvent was removed *in vacuo*, and the resulting solid was extracted with dichloromethane (20 mL) and filtered through Celite to remove LiCl. The filtrate was evaporated to dryness, and the residue was recrystallized from MeOH to afford (*o*-(Ph_2P)C_6H_4)$_2$PhSb as a white powder (0.88 g, 84% yield). ^{1}H NMR (499.43 MHz, $CDCl_3$): 7.09 (d, 2H, *o*-P(Sb)C_6H_4, $^{3}J_{H\text{-}H}$ = 7.00 Hz), 7.12-7.15 (m, 7H, PPh-C*H*), 7.16-7.25 (m, 22H, *o*-P(Sb)C_6H_4 + PPh-C*H*), 7.31 (d, 2H, Ph-C*H*, $^{3}J_{H\text{-}H}$ = 7.00 Hz). $^{13}C\{^{1}H\}$ NMR (125.58 MHz, $CDCl_3$): 127.99, 128.21,

128.25, 128.28, 128.38, 128.54, 128.73, 129.54, 133.63 (pseudo-quart, *o*-P(Sb)C_6H_4, $J_{C\text{-}P}$ = 18.33 Hz), 133.97, 136.76, 136.92, 137.11, 144.65. $^{31}P\{^1H\}$ NMR (202.16 MHz; $CDCl_3$): δ -6.64 (s). Elemental analysis calculated (%) for $C_{42}H_{33}P_2Sb$: C, 69.92; H, 4.61. Found: C, 69.46; H, 4.42.

Synthesis of [19]BPh_4. A solution of $PdCl_2$(cod) (cod = 1,5-cyclooctadiene) (20 mg, 0.07 mmol) in CH_2Cl_2 (2 mL) was added to a solution of (*o*-$C_6H_4P(PPh_2)$)$_2$SbPh (50 mg, 0.07 mmol) in CH_2Cl_2 (5 mL) and the resulting red/orange solution was allowed to stir for 12 hrs at room temperature. $NaBPh_4$ (24 mg, 0.07 mmol) in CH_2Cl_2 (5 mL) was added dropwise and the mixture was allowed to stir for 2 hrs. The reaction mixture was filtered over Celite to remove NaCl. The filtrate was evaporated to dryness and the residue recrystallized from pentane to afford [**19**]BPh_4 as a yellow powder (75 mg, 91% yield). Single crystals of [**19**]BPh_4 suitable for X-ray diffraction were obtained by vapor diffusion of Et_2O into a solution of the compound in CH_2Cl_2. ^1H NMR (499.43 MHz; $CDCl_3$): δ 6.36 (t, 2H, *o*-P(Sb)C_6H_4, $^3J_{H\text{-}H}$ = 7.50 Hz), 6.76 (t, 4H, BPh, $^3J_{H\text{-}H}$ = 7.50 Hz), 6.91 (t, 8H, BPh, $^3J_{H\text{-}H}$ = 7.50 Hz), 7.03 (t, 2H, *o*-P(Sb)C_6H_4, $^3J_{H\text{-}H}$ = 7.50 Hz), 7.31 (t, 1H, SbPh-C*H*, $^3J_{H\text{-}H}$ = 7.50 Hz), 7.39-7.45 (m, 18H, PPh-C*H* + SbPh-C*H*), 7.49-7.54 (m, 8H, BPh), 7.56-7.60 (m, 6H, PPh-C*H*), 7.64 (t, 2H, *o*-P(Sb)C_6H_4, $^3J_{H\text{-}H}$ = 7.50 Hz), 7.69 (d, 2H, *o*-P(Sb)C_6H_4, $^3J_{H\text{-}H}$ = 7.50 Hz). $^{13}C\{^1H\}$ NMR (125.85 MHz; $CDCl_3$): δ 121.56 (s), 125.46 (m), 127.40 (s), 129.10 (m), 129.71 (m), 130.11 (s), 131.09 (s), 131.93 (s), 132.17 (s), 132.31 (s), 133.16 (s), 133.35 (s), 133.73 (br), 134.59 (s), 134.69 (s), 136.33 (br), 137.15 (m), 164.27 (q, *J* = 62.92 Hz). $^{31}P\{^1H\}$ NMR (161.74 MHz; $CDCl_3$): δ

53.81 (s). ^{11}B NMR (128.2 MHz; $CDCl_3$): δ -6.78 (s). Elemental analysis calculated (%) for $C_{66}H_{53}BClPdP_2Sb + CH_2Cl_2$: C, 63.49 H, 4.37; found C, 63.23; H 4.45.

Synthesis of 19-F. A solution of [**19**]BPh_4 (50 mg, 0.042 mmol) in MeOH (2 mL) was treated with a solution of KF (4.87 mg, 0.084 mmol) in MeOH (1 mL). The reaction was stirred for 15 min. at room temperature before removing the solvent *in vacuo*. The resulting solid was extracted with CH_2Cl_2 (5 mL) and filtered over Celite. Evaporation of the solvent from the filtrate afforded 58 mg (95 %) of **19**-F as a orange solid. Single crystals of **19**-F suitable for X-ray diffraction were obtained by slow diffusion of Et_2O into a solution of the compound in CH_2Cl_2. **19**-F could also be prepared *in situ* by the addition of 1 equiv. of TBAF to a solution of **[19]**[BPh_4] in $CHCl_3$. Multinuclear NMR experiments confirmed quantitative conversion to the fluorostiborane species. ^{1}H NMR (499.43 MHz; $CDCl_3$): δ 6.64 (t, 2H, *o*-P(Sb)C_6H_4, $^3J_{H\text{-}H}$ = 7.50 Hz), 6.81 (t, 1H, SbPh-C*H*, $^3J_{H\text{-}H}$ = 7.00 Hz), 7.15 (t, 4H, PPh-C*H*, $^3J_{H\text{-}H}$ = 7.50 Hz), 7.21 (t, 2H, SbPh-C*H*, $^3J_{H\text{-}H}$ = 7.00 Hz), 7.28-7.30 (m, 2H, SbPh-C*H*), 7.38 (m, 2H, *o*-P(Sb)C_6H_4), 7.41-7.52 (m, 16H, PPh-C*H* + SbPh-C*H*), 7.64 (t, 2H, *o*-P(Sb)C_6H_4, $^3J_{H\text{-}H}$ = 7.50 Hz), 8.92 (d, 2H, *o*-P(Sb)C_6H_4, $^3J_{H\text{-}H}$ = 7.50 Hz). ^{13}C{^{1}H} NMR (125.58 MHz; $CDCl_3$): δ 127.92 (s), 128.48 (t, *J* = 5.40 Hz), 128.62 (t, *J* = 5.40 Hz), 129.13 (s), 130.30 (s), 130.79 (s), 130.84(s), 131.50(s), 133.08 (t, *J* = 6.90 Hz), 134.31 (t, *J* = 6.90 Hz), 134.41(s), 135.76(s), 137.88(t, *J* = 11.43 Hz), 152.85 (br). ^{31}P{^{1}H} NMR (161.74 MHz; $CDCl_3$): δ 64.06 (s). ^{19}F NMR (469.93 MHz; $CDCl_3$): δ -124.61 (br). Elemental analysis calculated (%) for $C_{42}H_{33}ClFP_2PdSb$: C, 57.17 H, 3.77; found C, 51.66; H 3.65.

Crystallographic measurements. All crystallographic measurements were performed at 110(2) K using a Bruker SMART APEX II diffractometer with a CCD area detector (graphite monochromated Mo Kα radiation, λ = 0.71073 Å, ω-scans with a 0.5˚ step in ω) at 110K. In each case, a specimen of suitable size and quality was selected and mounted onto a nylon loop. The semi-empirical method SADABS was applied for absorption correction. The structures were solved by direct methods and refined by the full-matrix least-square technique against F^2 with the anisotropic temperature parameters for all non-hydrogen atoms. All H atoms were geometrically placed and refined in riding model approximation. Data reduction and further calculations were performed using the Bruker SAINT+ and SHELXTL NT program packages.[78]

Table 6. Crystal data, data collections, and structure refinements for [**19**]BPh_4 and **19**-F

Crystal data	[**19**]$BPh_4 \cdot CH_2Cl_2$	**19**-F
Formula	$C_{67}H_{55}BCl_3P_2PdSb$	$C_{42}H_{33}ClFP_2PdSb$
Mr	1267.31	882.27
Crystal size (mm^3)	0.20 x 0.20 x 0.15	0.30 x 0.30 x 0.20
Crystal system	Triclinic	Triclinic
Space group	P 1	P -1
a (Å)	10.278(3)	11.614(6)
b (Å)	12.296(3)	11.864(6)
c (Å)	13.006(3)	14.198(7)
α (°)	64.328(2)	80.752(5)
β (°)	69.420(2)	70.005(5)
γ (°)	83.402(2)	75.521(5)
V ($Å^3$)	2384.1(15)	1773.8(15)
Z	1	2
ρ_{calc} (g cm^{-3})	1.519	1.652
μ (mm^{-1})	1.057	1.470
F(000)	640	876
T/K	110(2)	110(2)
Scan mode	ω, φ	ω, φ
hkl Range	-13 → +13	-14 → +14
	-16 → +16	-14 → +14
	-17 → +17	-17 → +17
Measd reflns	17238	18301
Unique reflns [R_{int}]	13147 [0.0210]	6936 [0.0282]
Reflns used for refinement	13147	6936
Refined parameters	676	433
GooF	1.002	1.029
$R1$,[a] $wR2$[b] (all data)	0.0324, 0.0636	0.0364, 0.0693
ρ_{fin} (max/min.) ($eÅ^{-3}$)	0.471, -0.365	0.758, -0.415

[a] $R_1 = \Sigma||Fo| - |Fc||/\Sigma|Fo|$. [b] $wR_2 = [[\Sigma w(Fo^2 - Fc^2)^2]/[\Sigma w(Fo^2)^2]]^{1/2}$.

CHAPTER IV

ANION-INDUCED INTERNAL REDOX SWITCHING OF A HETEROBIMETALLIC COMPLEX-APPLICATION TO THE PPM LEVEL SENSING OF FLUORIDE ANIONS

4.1 Introduction

The design of metal-based anion responsive platforms is gaining increasing interest because of new applications in the domain anion sensing[106-108] and anion actuated mechanical devices[109]. In most cases, anion binding to such platforms induces an electronic and/or structural response which can be monitored to infer the presence of an anionic analyte. Examples of such platforms include ferrocenylboranes which have been used for the recognition of the toxic fluoride and cyanide anions.[110] For such complexes, anion binding to the boron units lowers the FeII/III redox couple of the ferrocene unit, allowing for its oxidation to occur spontaneously in air or in the presence of mild oxidants. An approach that has thus far not been described is one in which anion binding would trigger an internal redox process that could occur in the absence of an external oxidizing or reducing agent.

As part of our exploratory program in main group chemistry, we have initiated a study on the anion binding properties of stibine metal complexes such as A and observed that fluoride anion coordination readily occurs at antimony. In an extension of this study, we now report a novel Pt/Sb complex which can be switched between two distinct redox states through a reversible fluoride/chloride exchange reaction.

4.2 Synthesis and characterization of **[20][**Cl**]** and **21**

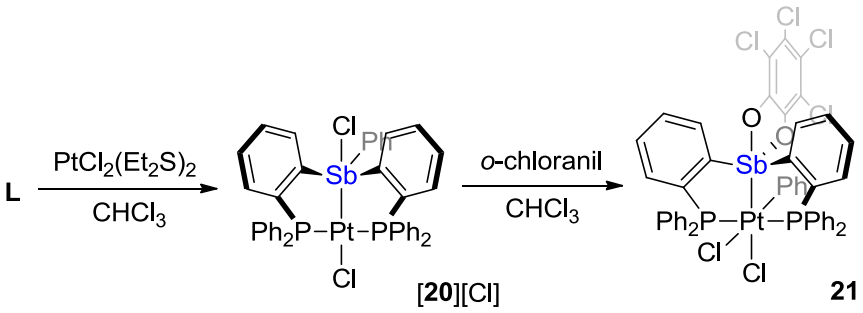

Figure 32. Synthesis of [**20**][Cl] and **21**.

Reaction of the bis(phosphanyl)stibine ligand **L** ($\delta(^{31}P)$ -6.6 ppm) with $(Et_2S)_2PtCl_2$ in chloroform proceeded over the course of 12 hours to afford a complex ([**20**][Cl]) characterized by a ^{31}P NMR resonance at 53.9 ppm showing coupling to the ^{195}Pt nucleus ($^1J_{Pt\text{-}P}$ = 2706 Hz) (Figure 32). The crystal structure of this complex, which confirms coordination of the two phosphines to the platinum center also reveals insertion of the Sb atom into one of the Pt-Cl bonds, leading to a species which can be formally described as a Sb(IV)-Pt(I) complex. The Pt(1)-Sb(1) bond of this complex (2.5380(8) Å) is slightly longer than that in *cis*-$[PtCl_2(SbPh_3)_2]$ (2.50 Å (av.))[111], a difference which may be assigned to the penta- raher than tetra-coordination of the antimony atom in [**20**][Cl] (Figure 33). The Sb(1)-Cl(2) bond of 2.7532(18) Å exceeds the sum of the covalent radii of the two elements by 14.2%-15.2%,[112,113] as observed for partially ionic chlorostiborane such as Ph_4SbCl (2.740(6) Å).[114,115] Finally, despite the constraints imposed by the rigid ligand backbone, the divalent platinum center adopts the expected

square planar geometry (P(1)-Pt(1)-P(2) = 170.01(6)°, Pt(1)-Sb(1)-Cl(1) = 180°). Complex [**20**][Cl] is air and moisture stable but quickly reacts with *o*-chloranil (*o*-$O_2C_6Cl_4$) in $CHCl_3$ to afford a complex (**21**) which can be formally described as a Sb(IV)-Pt(III) species. The ^{31}P NMR spectrum of **21** in $CDCl_3$ shows a signal at 45.51 ppm ($^1J_{Pt\text{-}P}$ = 2192 Hz) indicating coordination of the phosphines to the platinum center. When compared to [**20**][Cl] ($^1J_{Pt\text{-}P}$ = 2706 Hz), the $J_{Pt\text{-}P}$ value of **21** appears to be notably reduced, a phenomenon that is commonly observed for phosphine-platinum complexes upon oxidation.[116-118] A final elucidation of the structure of this complex was derived from an X-ray diffraction study which reveals that the oxidation reaction induces a migration of a chloride and phenyl ligand from Sb to Pt along with coordination of the tetrachlorocatecholate to the antimony atom. As a result of these ligand redistribution reactions, the platinum atom adopts an octahedral geometry characteristic of its tetravalent state while the antimony remains trigonal bipyramidal as in [**20**][Cl]. These changes are accompanied by a slight elongation of the Pt(1)-Sb(1) bond from 2.5380(8) Å in [**20**][Cl] to 2.5906(5) Å in **21**, which can be assigned to the higher coordination number of the platinum atom.

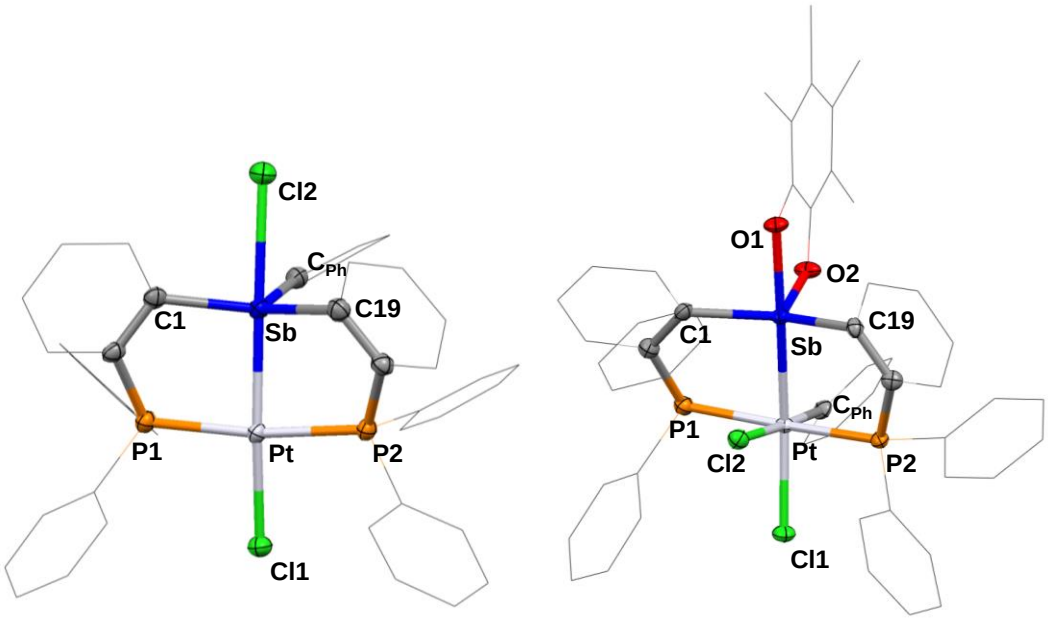

Figure 33. Crystal structures of and [**20**][Cl] (left) and **21** (right). Thermal ellipsoids are drawn at the 50% probability level. Phenyl groups are drawn in wireframe. Hydrogen atoms and solvents are omitted for clarity. Selected bond lengths (Å) and angles (˚) for [**20**][Cl]: Sb-Pt 2.5380(8), Pt-Cl1 2.3851(16), Sb-Cl2 2.7532(18); P1-Pt-P2 170.01(6), Cl2-Sb-Pt 178.06(4), Sb-Pt-Cl1 172.36(4), C1-Sb-C19 124.2(2), C19-Sb-C_{Ph} 108.6(2), C_{Ph}-Sb-C1 122.3(2). **21**: Sb-Pt 2.5906(5), Pt-Cl1 2.4235(11), Pt-Cl2 2.4608(12), Sb-O1 2.1239(3), Sb-O2 2.002(3); P1-Pt-P2 170.71(4), Cl2-Pt-C_{Ph} 177.99(13), Sb-Pt-Cl1 167.77(3), O1-Sb-Pt 176.12(8), C1-Sb-C19 133.47(17), C19-Sb-O2 110.84(16), O2-Sb-C1 111.02(16).

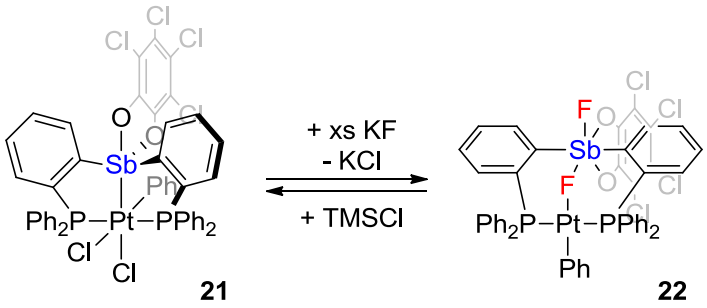

Figure 34. Synthesis of **22**.

A $CHCl_3$ solution of complex **21** quickly reacts with 10 equivalents KF in water to afford the Sb(V)-Pt(II) (complex **22**) (Figure 35). The color of the biphasic solution changed from yellow to orange immediately. The reaction could be conveniently followed by ^{31}P NMR spectroscopy which clearly indicates formation of a new species featuring a sharp resonance at 26.3 ppm with a strong ^{195}Pt coupling ($^1J_{Pt\text{-}P}$ = 3048 Hz). In addition, the appearance of two signals at -77.4 and -97.6 ppm in the ^{19}F NMR spectrum indicate the two distinguishable fluoride atoms in complex **22**. Formation of **22** is, however, chemically reversible. Indeed, **22** reacts with TMSCl (trimethylsilyl chloride) to produce **21** as well as TMSF. Fortunately, slow diffusion of Et_2O into a solution of **22** in $CHCl_3$ afforded light-yellow crystal which was suitable for X-ray diffraction (Figure 35). The structure reveals a normal square planar coordination about Pt and a octahedral geometry around Sb center as shown by P(1)-Pt(1)-P(2) and F(2)-Pt(1)-C(37) angles of 171.25(8)° and 178.3(3)°, respectively, and a F(2)-Sb(1)-O(1) angle of 165.2(2)°. A significant expansion of the Pt-Sb distance from 2.5906(5) Å in **21** to 3.1025(9) Å in **22** is indicative with the absence of a direct Pt-Sb interaction.

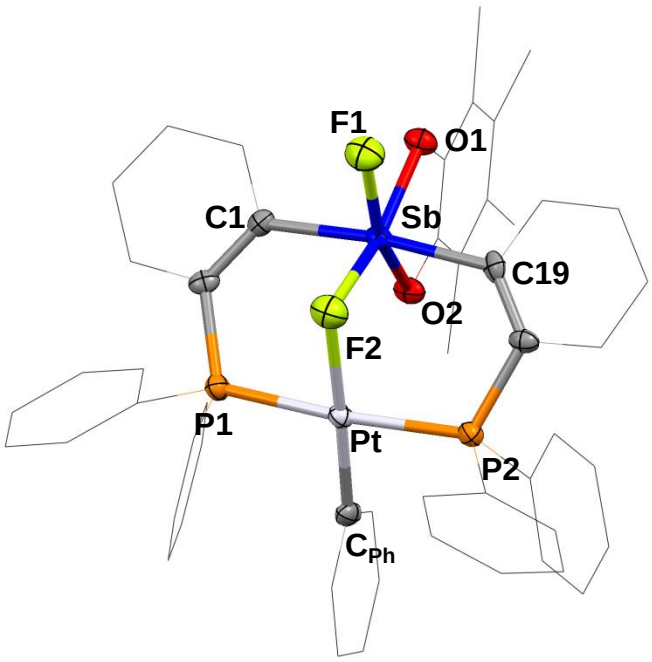

Figure 35. Structure of **22**. Displacement ellipsoids are scaled to the 50% probability level. Solvents and hydrogen atoms are omitted for clarity. Selected bond lengths (Å) and angles (deg) for: **22**: Sb-F1 1.988(5), Sb-F2 2.064(5), Pt-F2 2.142(5), Sb-O1 2.062(6), Sb-O2 2.117(6); P1-Pt-P2 171.25(8), F2-Pt-C_{Ph} 178.3(3), F2-Sb-O1 165.2(2), F1-Sb-O2 159.0(2), C1-Sb-C19 173.3(3), Sb-F2-Pt 95.0(2), O1-Sb-O2 78.9(2), F1-Sb-F2 85.2(2).

4.3 Computational studies of [**20**][Cl], **21** and **22**

To better understand the bonding configurations of these complexes, the structures of complexes [**20**][Cl] and **21** have been subjected to DFT calculations using the ADF program (BP86/TZP with ZORA). The optimized structures of these which complexes closely those determined experimentally were subjected to a Boys localization analysis which identifies a Sb-Pt σ-bond for both complexes. The elevated contributions of both antimony and platinum atomic orbitals (Pt: 32.7%/Sb: 31.9% in [**20**][Cl]; Pt: 35.3.7%/Sb: 33.4% in **21**) to the Sb-Pt σ-bonding orbital (Figure 36). The

presence of this bonding interaction supports the formal description of [**20**][Cl] as a Sb(IV)-Pt(I) and **21** as a Sb(IV)-Pt(III) complex. The Pt-Sb bond in **22** has also been investigated using a natural bond orbital (NBO) analysis (Figure 42). This analysis reveals a very weak $lp_{Pt} \rightarrow \sigma^*_{Sb\text{-}C}$ interaction with Pt as a donor and Sb as acceptor. Deletion calculation indicated that this interaction only provide 23.18 kcal mol^{-1} between these two atoms.

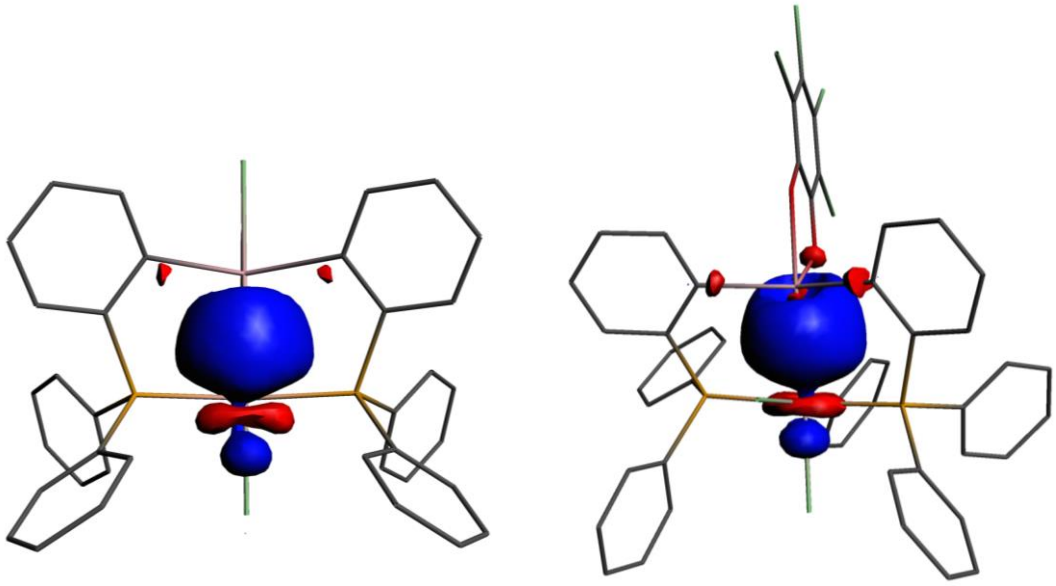

Figure 36. Boys orbitals (isovalue = 0.04) of the Sb-Pt bond in [**20**][Cl] and **21** obtained from ADF analysis. Hydrogen atoms are omitted for clarity.

4.4 X-ray absorption spectroscopy

To gather additional information about the electronic structure of [**20**][Cl], **21** and **22**, we decided to study the atomic properties of the platinum nucleus in [**20**][Cl], **21**

and **22** by measuring their room temperature, solid state Pt L3-X-ray Absorption Near Edge Structure (XANES) spectrum. XANES has been used to provide information about the oxidation states of metal complexes in a number of systems. However, few X-ray absorption fine structure (XAFS) analyses or XANES investigations of Pt compounds have been reported, and only few of them have been reported for Pt(IV).[119] The XANES spectra of Pt(II) and Pt(IV) differ in the height of their edges, with that for Pt(IV) being substantially greater. This is independent of the coordination sphere.

The change in the oxidation state of the platinum center is supported by the L3-edge XANES spectrum which shows a marked increase in the intensity of the white band in the case of **21** (Figure 37). As previously argued, this intensity increase observed upon oxidation results from a lower occupancy of the 5d shell which increases the oscillator strength of the $2p_{3/2} \rightarrow 5d$ transition observed at this edge. In Figure 37, the XANES spectrum clearly indicated that complex **21** has a higher white line intensity than [**20**][Cl] and **22**. The L3 edge energies also suggest that **21** (11566.6 eV) has a Pt atom in a higher oxidation state than [**20**][Cl] (11566.1 eV) and **22** (11566.3 eV).

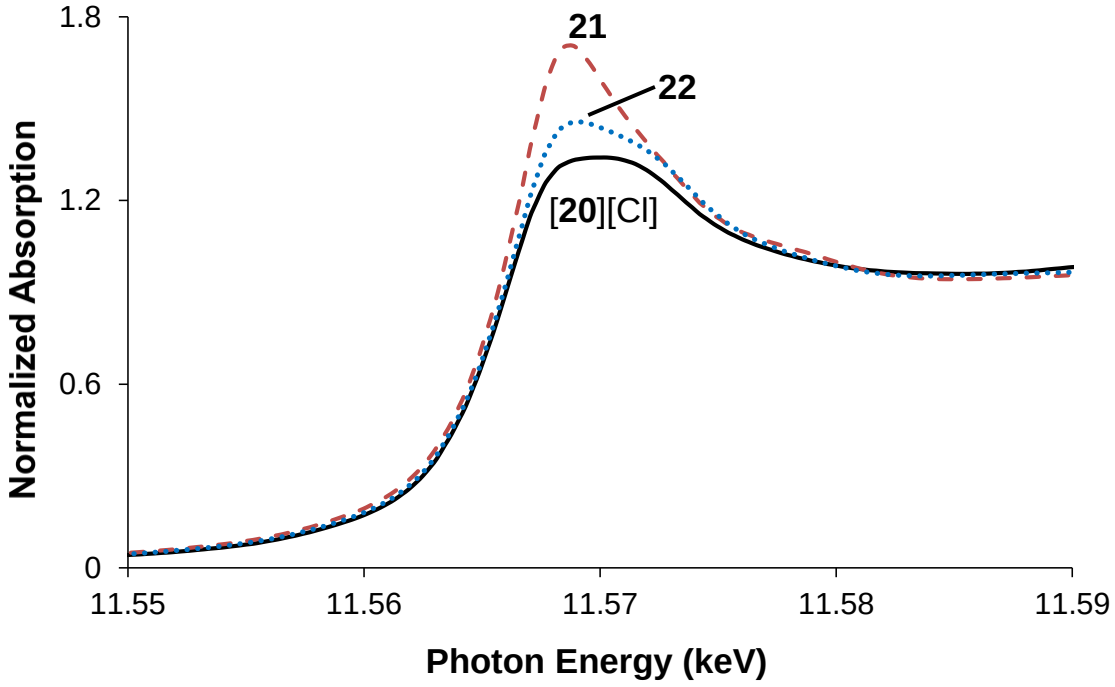

Figure 37. Solid-State XANES (Pt L_3-esge) spectrum of [**20**][Cl], **21** and **22**.

4.5 Fluoride binding studies

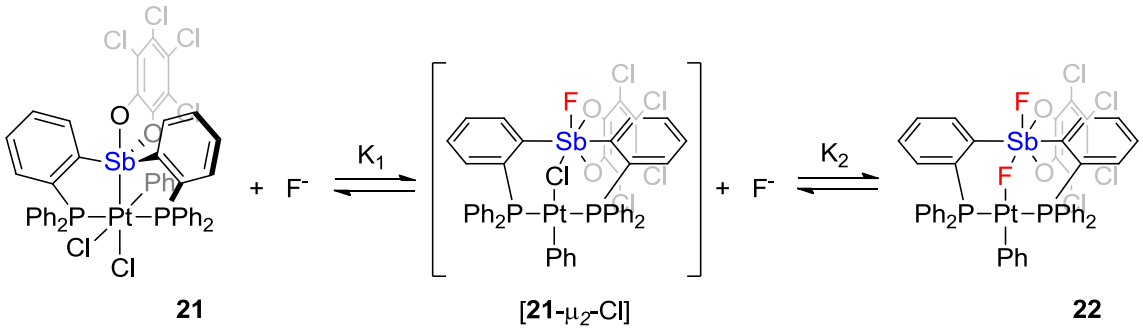

Figure 38. Fluoride binding process of **21**.

In order to understand the fluoride binding process, an NMR titration experiment has been performed (Figure 38). Addition of the first equivalent of TBAF to a $CDCl_3$ solution of **21**, leads to [**21**-μ_2-Cl] which displays a ^{31}P NMR resonance at 35.4 ppm with a strong ^{195}Pt coupling ($^1J_{Pt\text{-}P}$ = 2848 Hz). Consistent with this observation, the ^{19}F NMR spectrum showed the appearance of a resonance at -77.4 ppm. Unfortunately the 1:1 adduct [**21**-μ_2-Cl] could not able to be isolated. DFT (Gaussian: BP86 with 6-31g for H,C; 6-311g(d) for P, Cl, F; and CRENBS ECP for Sb, Pt) computational study carried out on the mono-fluoride adduct Cl-bridge over F-bridge (Figure 39). By adding a second equivalent of TBAF into the solution, the presence of **22** could be easily confirmed by the ^{31}P and ^{19}F NMR spectra which show signals of 26.3 ppm for ^{31}P and -77.4 and -97.6 ppm for ^{19}F. The electronic absorption spectrum of **21** in $CHCl_3$ displays a broad band spanning the 250-350 nm range (Figure 41). This low energy feature is attributed to a transition from the *o*-chloranil based HOMO to the LUMO which bears a significant contribution from Pt-Cl, Sb-O and Sb-C_{Ph} σ^* orbitals (Figure 40). The LUMO orbital also indicated that the first equivalent of fluoride was bound onto the five-coordinated antimony center. Further insights into the fluoride binding behavior of **21** were gained from UV-vis titration studies in $CHCl_3$. The addition of TBAF to a $CHCl_3$ solution of **21** (ε_{287} = 22340 M^{-1} cm^{-1}) results in a decrease of the absorbance at 287 nm caused by fluoride binding on the antimony center (Figure 41). Interestingly, addition of up to one equivalent of fluoride anion leads to a linear decrease of the absorbance. At exactly one equivalent of added fluoride, the isotherm shows a distinct break and addition of over 1 equivalent of fluoride leads to another decrease of the

absorbance around 302 nm. These observations can be rationalized based on the following argument. Addition of the first equivalent of TBAF essentially leads to the quantitative formation of the 1:1 adduct [**21**-μ_2-Cl] (ε_{302} = 12020 M^{-1} cm^{-1}). Addition of a second fluoride anion to produce complex **22** is much less favorable explaining the less progressive decrease of the absorbance. Because fluoride binding to **22** occurs in two very distinct areas, the fluoride binding constants can be evaluated independently. The first fluoride binding constant K_1 exceeds the value of 10^6 M^{-1} measurable by a UV-vis titration. Fitting of the data obtained above 1 equivalent of added fluoride affords K_2 = 4500 (± 200) M^{-1}.

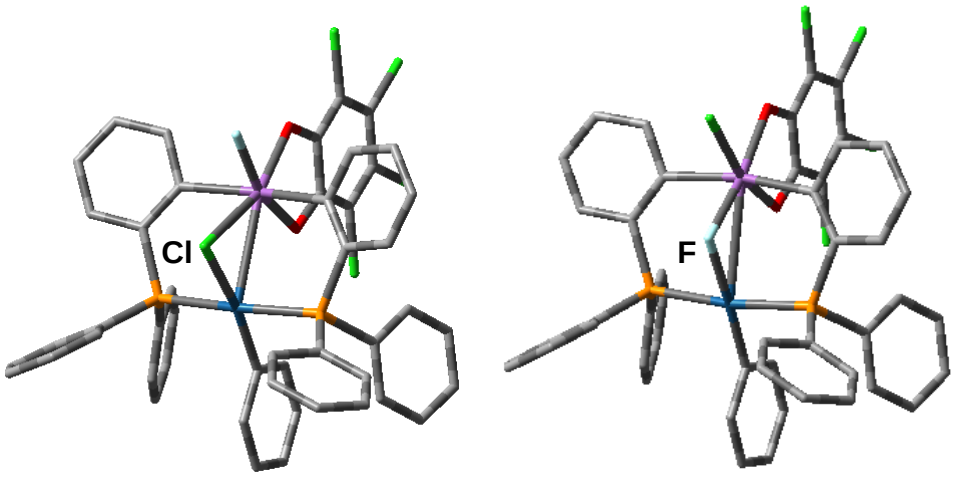

Cl-bridge
(-5443.4215 Hartree)

F-bridge
(-5443.0581 Hartree)

Figure 39. Optimized structures of Cl-bridge and F-bridge complexes

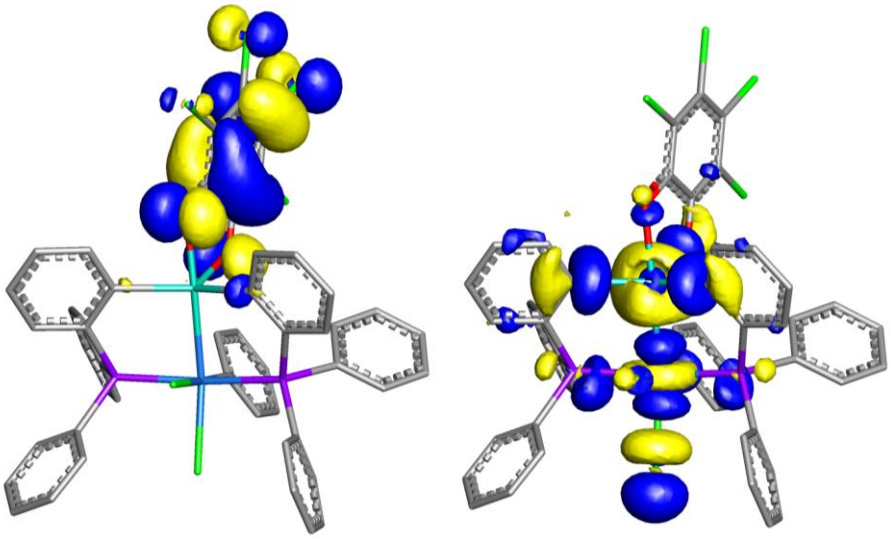

Figure 40. Plots of the HOMO (-0.17607 eV) and LUMO (-0.11280 eV) of **21** (at 0.03 isosurface value).

Encouraged by these results, we decided to investigate the use of **21** as a fluoride sensor in the protic solvents such as water. While attempts to use **21** in pure water were unsuccessful because of the insolubility of the complex, even at low concentrations, we found that **21** could be used under biphasic conditions for the detection of ppm concentrations of fluoride anions. Solutions of **21** in $CDCl_3$ (1.15×10^{-3} M) were layered with aqueous solutions containing 8 ppm (10 ml, 4×10^{-4} M TBAF in H_2O, 7.3 eq. of TBAF) and 4 ppm (10 ml, 2×10^{-4} M TBAF in H_2O, 3.7 eq. of TBAF) of fluoride anions. Upon shaking, the generation of **22** was confirmed by ^{31}P NMR measurement, which showed a 100 % conversion for **21** solutions layered with aqueous solutions containing 4 ppm and 8 ppm of fluoride anions. We also tried to layer solution of **21** in $CDCl_3$ (1.15×10^{-3} M) with 8 ppm (6 ml, 4×10^{-4} M TBAF in H_2O, 2.2 eq. of TBAF) of

fluoride anions. Under this condition, the aqueous solution only provides 2.2 equivalent of fluoride anion. By shaking the solution, ^{31}P NMR showed a conversion of approximately 42% for [**21**-μ_2-Cl] and 58% for **22** (Figure 43). No obvious change in ^{31}P NMR was observed in the presence of common interferents, including Cl^-, Br^-, OAc^-, NO_3^-, and $H_2PO_4^-$, thus indicating that this new sensor is highly selective for fluoride anions.

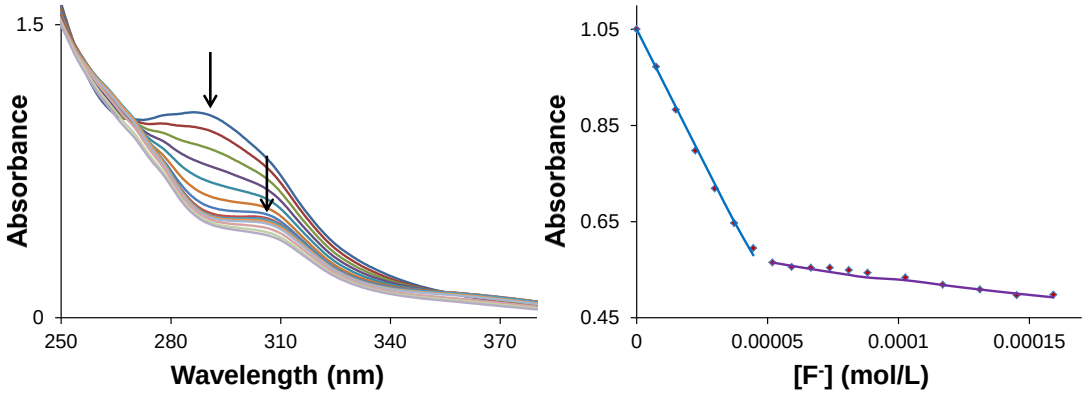

Figure 41. Left: Spectral changes in the UV-Vis absorption spectra of **21** (4.72×10^{-5} M) in $CHCl_3$ upon incremental addition of a TBAF solution (4.5×10^{-3} M, $CHCl_3$). Right: The isotherms are plotted based on the absorbance at 287 nm and 302 nm, and the line indicates the fit to the calculated 1:1 binding isotherm. The fluoride binding constant was calculated to be $k_1 > 10^6$ M^{-1} and $K_2 = 4500$ (± 200) M^{-1}.

4.6 Conclusions

In summary, we report that the Sb(IV)-Pt(I) coordination complex [**20**][Cl] is readily oxidized by *o*-chloranil to afford the corresponding Sb(IV)-Pt(III) complex **21**. This oxidative addition reaction resulted in migration of the phenyl ring to the Pt atom to generate a Pt(III) complex. By adding 2 equivalents of KF into a solution of **21**, we

show that the fluoride trigger an internal redox process to afford the new Sb(V)-Pt(II) complex. The oxidation states of the Pt center are not only confirmed by the computational results but also supported by the XANES Pt L3-edge spectrum. This internal redox process, however, is chemically reversible through addition of TMSCl. Finally, the fluoride affinity of complex **21** is also investigated by layering the dilute of aqueous fluoride solutions.

4.7 Experimental

General considerations. Antimony compounds are toxic and should be handled cautiously. $SbCl_3$ and KF were purchased from Alfa Aesar. *o*-chloranil and TMSCl were purchased from Aldrich and used as received. *cis*-$PtCl_2(Et_2S)_2$[120] and $PhICl_2$[121] were prepared according to the reported procedures. Solvents were dried by passing through an alumina column (*n*-pentane and CH_2Cl_2) or by reflux under N_2 over Na/K (Et_2O and THF). All other solvents were used as received. Ambient temperature NMR spectra were recorded on a Varian Unity Inova 400 FT NMR (399.59 MHz for ^1H, 100.45 MHz for ^{13}C, 375.89 MHz for ^{19}F, 161.74 MHz for ^{31}P) spectrometer. Chemical shifts (δ) are given in ppm and are referenced against residual solvent signals (^1H, ^{13}C) or external BF_3-Et_2O (^{19}F) and H_3PO_4 (^{31}P). Elemental analyses were performed at Atlantic Microlab (Norcross, GA).

Synthesis of [**20**][Cl]**.** A solution of $(Et_2S)_2PtCl_2$ (62 mg, 0.14 mmol) in CH_2Cl_2 (2 mL) was added to a solution of ligand **L** (100 mg, 0.14 mmol) in CH_2Cl_2 (10 mL) and the resulting yellow solution was allowed to stir for 12 hrs at room temperature. The

reaction mixture was concentrated to ca. 5 mL under vacuo and the product precipitated by addition of pentane (10 mL). The product was filtered and washed with pentane (3 × 5 mL) to afford 112 mg (82% yield) as a yellow solid. Single crystals of [**20**][Cl] suitable for X-ray diffraction were obtained by vapor diffusion of Et_2O into a solution of the compound in CH_2Cl_2. ^{1}H NMR (499.43 MHz; $CDCl_3$): δ 9.89 (d, 2H, *o*-P(Sb)C_6H_4, $^3J_{H\text{-}H}$ = 9.50 Hz), 7.80 (t, 2H, *o*-P(Sb)C_6H_4, $^3J_{H\text{-}H}$ = 9.50 Hz), 7.37-7.56 (m, 18H, PPh-CH + SbPh-CH), 7.29-7.33 (m, 6H, PPh-CH), 6.90 (t, 1H, SbPh-CH, $^3J_{H\text{-}H}$ = 9.00 Hz), 6.78 (d, 2H, *o*-P(Sb)C_6H_4, $^3J_{H\text{-}H}$ = 9.50 Hz), 6.68 (t, 2H, *o*-P(Sb)C_6H_4, $^3J_{H\text{-}H}$ = 9.50 Hz). ^{13}C{^{1}H} NMR (125.58 MHz; $CDCl_3$): δ139.51(t, *J* = 9.54 Hz), 133.97-134.10 (bm, 2C), 135.21(s), 133.91(s), 133.85(s), 133.77(s), 133.51(s), 133.15(s), 132.08 (s), 131.61 (s), 129.65 (s), 129.20 (t, *J* = 6.66 Hz), 128.58 (s). ^{31}P{^{1}H} NMR (161.74 MHz; $CDCl_3$): δ 53.95 (s, $^1J_{P\text{-}195Pt}$ = 2706 Hz). Elemental analysis calculated (%) for $C_{42}H_{33}Cl_2P_2PtSb$ + 0.5CH_2Cl_2: C, 49.56 H, 3.33; found C, 47.16; H 3.02 (approx. 1eq. of CH_2Cl_2 was lost in drying).

Synthesis of 21. A solution of *o*-chloranil (32 mg, 0.13 mmol) in $CHCl_3$ (2 mL) was added dropwise to a solution of [**20**][Cl] (130 mg, 0.13 mmol) in $CHCl_3$ (2 mL) at room temperature. The resulting orange solution was allowed to stir for 12 hrs before adding pentane (10 mL) upon which a yellow precipitate was formed. The solid was filtered, washed with pentane (3 × 3 mL) and dried under vacuo to afford 99 mg (62 %) of **21**. Single crystals of **21** suitable for X-ray difraction were obtained by slow diffusion of Et_2O into a solution of the compound in THF. ^{1}H NMR (499.43 MHz; $CDCl_3$): δ8.94 (d, 2H, *o*-P(Sb)C_6H_4, $^3J_{H\text{-}H}$ = 8.50 Hz), 7.78-7.82 (m, 2H, *o*-P(Sb)C_6H_4), 7.62-7.68 (m,

4H, PPh-CH), 7.37-7.48 (m, 12H, PPh-CH), 7.17 (t, 4H, PPh-CH, $^3J_{H-H}$ = 7.00 Hz), 6.94-6.97 (m, 2H, SbPh-CH), 7.10-7.12 (m, 2H, *o*-P(Sb)C_6H_4), 6.75 (d, 1H, SbPh-CH, $^3J_{H-H}$ = 7.00 Hz), 6.53 (t, 1H, SbPh-CH, $^3J_{H-H}$ = 7.00 Hz), 6.46 (d, 2H, *o*-P(Sb)C_6H_4, $^3J_{H-H}$ = 8.50 Hz), 5.96 (t, 1H, SbPh-CH, $^3J_{H-H}$ = 7.00 Hz). ^{13}C NMR (125.58 MHz; $CDCl_3$): δ153.17 (t, *o*-P(Sb)C_6H_4, $^3J_{C-P}$ = 17.83 Hz), 145.87 (s), 143.02 (s), 136.55 (m), 136.32 (m), 135.94 (t, J_{C-P} = 5.27 Hz), 133.69 (t, J_{C-P} = 5.27 Hz), 132.31 (s), 131.75 (s), 130.77 (s), 128.06 (t, J_{C-P} = 5.40 Hz), 127.65 (t, J_{C-P} = 5.40 Hz), 126.97 (s), 126.61 (s), 126.50 (s), 126.24 (s), 126.01 (s), 125.76 (s), 125.54 (s, $O_2C_6Cl_4$), 123.67 (s, $O_2C_6Cl_4$), 120.23 (s, $O_2C_6Cl_4$), 116.75 (s, $O_2C_6Cl_4$). ^{31}P{^{1}H} NMR (161.74 MHz; $CDCl_3$): δ 45.51 (s, $^1J_{P-195Pt}$ = 2192 Hz). Elemental analysis calculated (%) for $C_{48}H_{33}Cl_6O_2P_2PtSb$: C, 46.75 H, 2.70; found C, 47.01 H 2.71.

Synthesis of 22. Solutions of **21** (50 mg, 41 mmol) in 10 ml $CHCl_3$ were layered and stirred with 10 ml aqueous solutions containing KF (48 mg, 820 mmol) for 20 min. After separation of the layers, organic layer was dried with $MgSO_4$ and filtered over Celite. The solvent was removed under vacuo to afford 43 mg (87 %) of **22**. Single crystals of **22** suitable for X-ray difraction were obtained by slow diffusion of Et_2O into a solution of the compound in $CHCl_3$. ^{1}H NMR (499.43 MHz; $CDCl_3$): δ 8.95 (d, 2H, *o*-P(Sb)C_6H_4, $^3J_{H-H}$ = 7.80 Hz), 7.67 (t, 2H, *o*-P(Sb)C_6H_4, $^3J_{H-H}$ = 7.94 Hz), 7.53-7.40 (m, 16H, PPh-CH), 7.31-7.29 (m, 6H, PPh-CH), 7.23 (t, 2H, PPh-CH, $^3J_{H-H}$ = 7.28 Hz), 7.17 (t, 2H, PPh-CH, $^3J_{H-H}$ = 7.28 Hz), 6.83 (t, 1H, *p*-PhCH, $^3J_{H-H}$ = 7.28 Hz), 6.66 (t, 2H, $^3J_{H-H}$ = 7.28 Hz). ^{13}C NMR (125.58 MHz; $CDCl_3$): δ146.32 (s), 145.28 (s), 138.03 (s), 137.10 (s), 136.88 (s), 134.97 (t, J_{C-P} = 5.45 Hz), 134.33 (s), 133.99 (t, J_{C-P} = 6.97 Hz),

132.93 (t, $J_{C\text{-}P}$ = 5.38 Hz), 132.68 (t, $J_{C\text{-}P}$ = 5.37 Hz), 132.43 (s), 131.99 (s), 131.55 (s), 130.20 (s), 129.97 (s), 129.74 (s), 129.25 (t, $J_{C\text{-}P}$ = 5.30 Hz), 129.13 (t, $J_{C\text{-}P}$ = 5.30 Hz), 128.36 (s), 121.76 (s, $O_2C_6Cl_4$), 120.25 (s, $O_2C_6Cl_4$), 119.69 (s, $O_2C_6Cl_4$), 118.95 (s, $O_2C_6Cl_4$), 118.03 (s, $O_2C_6Cl_4$). $^{31}P\{^1H\}$ NMR (161.74 MHz; $CDCl_3$): δ 26.29 (s, $^1J_{P\text{-}195Pt}$ = 3048 Hz). Elemental analysis calculated (%) for $C_{48}H_{33}Cl_4F_2O_2P_2PtSb$: C, 48.03 H, 2.77; found C, 48.02; H, 2.80.

Crystallography. All crystallographic measurements were performed at 110(2) K using a Bruker SMART APEX II diffractometer with a CCD area detector (graphite monochromated Mo K_α radiation, λ = 0.71073 Å) at 110 K. In each case, a specimen of suitable size and quality was selected and mounted onto a nylon loop. The semi-empirical method SADABS was applied for absorption correction. The structures were solved by direct methods and refined by the full-matrix least-square technique against F^2 with the anisotropic temperature parameters for all non-hydrogen atoms. All H atoms were geometrically placed and refined in riding model approximation. Data reduction and further calculations were performed using the Bruker SAINT+ and SHELXTL NT program packages.[78]

Theoretical calculations. Density functional theory (DFT) calculations (full geometry optimization) were carried out on [**20**][Cl], **21** and **22** starting from the crystal structure geometries with Gaussian09[122] program (BP86[80,81] with 6-31g(d) for H, C, O; 6-311+g(d) for P, Cl; Stuttgart relativistic large core (RSC) 1997 ECP for Pt[123]; Stuttgart relativistic small core (RLC) 1997 ECP for Sb[124]). Frequency calculations were also carried out on the optimized geometry, showing no imaginary frequencies. The

optimized structures, which are in excellent agreement with the solid-state structures, were subjected to a NBO analysis.[125] The resulting Natural Localized Molecular Orbitals (NLMOs) were visualized and plotted in Jimp 2 program.[126]

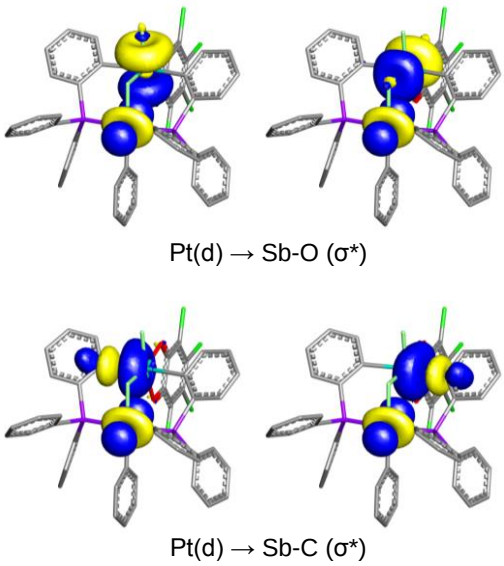

Figure 42. Superposition of the donor and acceptor orbitals according to NBO analysis, which contribute mainly to the Pt-Sb interactions. Hydrogen atoms are omitted for clarity (isovalue=0.05).

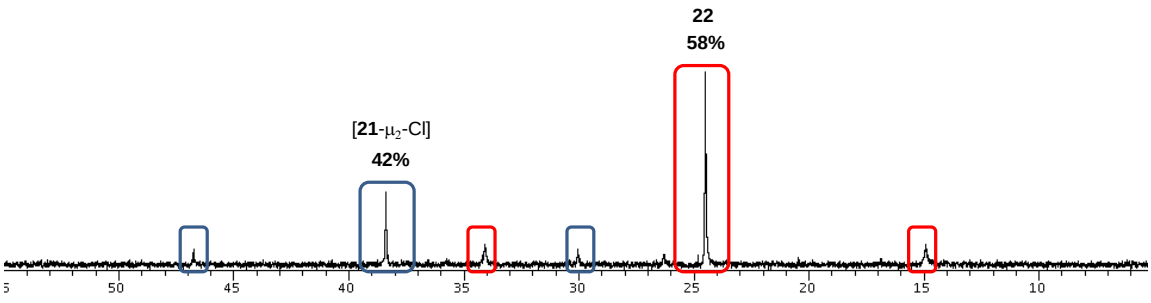

Figure 43. $^{31}P\{^{1}H\}$ NMR spectra of **21** in $CDCl_3$ after layering with distilled water and 8 ppm aqueous fluoride solutions.

Table 7. Crystal data, data collections, and structure refinements for [**20**][Cl] and **21**

Crystal data	[**20**][Cl]·1/2(CH_2Cl_2)	**21**·THF
Formula	2($C_{42}H_{33}Cl_2P_2PtSb$)·CH_2Cl_2	$C_{48}H_{33}Cl_6O_2P_2PtSb$·THF
Mr	2057.64	1305.33
Crystal size (mm^3)	0.21 x 0.14 x 0.11	0.10 x 0.08 x 0.08
Crystal system	Triclinic	Monoclinic
Space group	P-1	P2(1)/c
a (Å)	11.844(4)	20.768(4)
b (Å)	11.882(4)	11.824(2)
c (Å)	14.723(5)	20.679(4)
α (°)	78.783(4)	90
β (°)	71.597(4)	106.813(2)
γ (°)	72.713(4)	90
V ($Å^3$)	1865.6(11)	4860.9(17)
Z	1	4
ρ_{calc} (g cm^{-3})	1.832	1.784
μ (mm^{-1})	4.801	3.870
F(000)	996	2552
T/K	110(2)	110(2)
Scan mode	ω, φ	ω, φ
hkl Range	-14 → +14	-27 → +27
	-14 → +14	-15 → +15
	-18 → +18	-27 → +27
Measd reflns	19131	58051
Unique reflns [R_{int}]	7288 [0.0419]	12120 [0.0683]
Reflns used for refinement	7288	12120
Refined parameters	451	586
GooF	1.038	1.035
$R1$,[a] $wR2$[b] (all data)	0.0480, 0.0917	0.0635, 0.0898
ρ_{fin} (max/min.) ($eÅ^{-3}$)	2.375, -1.612	1.910, -1.475

[a] $R_1 = \Sigma||Fo| - |Fc||/\Sigma|Fo|$. [b] $wR_2 = [[\Sigma w(Fo^2 - Fc^2)^2]/[\Sigma w(Fo^2)^2]]^{1/2}$.

Table 8. Crystal data, data collections, and structure refinements for **22**

Crystal data	**22**·2Et_2O·$CHCl_3$
Formula	2($C_{48}H_{33}Cl_4F_2O_2P_2PtSb$)·2($C_4H_{10}O$)·$CHCl_3$
Mr	2668.26
Crystal size (mm^3)	0.06 x 0.05 x 0.05
Crystal system	Monoclinic
Space group	P2(1)/c
a (Å)	28.589(9)
b (Å)	20.547(7)
c (Å)	18.242(6)
α (°)	90
β (°)	107.073(4)
γ (°)	90
V ($Å^3$)	3510(3)
Z	4
ρ_{calc} (g cm^{-3})	1.730
μ (mm^{-1})	3.655
F(000)	5224
T/K	110(2)
Scan mode	ω, φ
hkl Range	-35 → +35
	-25 → +25
	-22 → +22
Measd reflns	105339
Unique reflns [R_{int}]	20137 [0.1148]
Reflns used for refinement	20137
Refined parameters	1195
GooF	1.059
*R*1,[a] *wR*2[b] (all data)	0.0961, 0.1316
ρ_{fin} (max/min.) ($eÅ^{-3}$)	3.455, -1.534

[a] $R_1 = \Sigma||Fo| - |Fc||/\Sigma|Fo|$. [b] $wR_2 = [[\Sigma w(Fo^2 - Fc^2)^2]/[\Sigma w(Fo^2)^2]]^{1/2}$.

CHAPTER V

A REDOX ACTIVE PTSB PLATFORM WITH DIFFERENTIAL CHLORIDE ANION AFFINITY

5.1 Introduction

Because of its impact on various areas ranging from separation science to intracellular ion delivery, strategies for the controlled release of an ion using light has been the topic of interest. Such strategies rest on the design of a photocage, which typically consists of a photolabile or photoswitchable chelator coordinated to the ion of interest. Irradiation of such a complex triggers a photochemical reaction or structural change within the chelators, resulting in the release of the caged ion to the medium. While this elegant approach has been convincingly employed for a number of cations,[127-144] its extension to the controlled release of anions is much more ephemeral, with only a handful of systems studied to date.[145-151] Current efforts in this area of research have been dedicated to the chloride anion[147-151] because of its role in biological processes.[152] The most successful approaches for the controlled release of this anion are based on photo-isomerizable azobenzene-[147,148] or ethene-based[149,150] receptors which interact with the anion via hydrogen bonds. While these systems present the undeniable advantage of reversibility, the weakness of the interactions between the hydrogen bond donor groups and the anionic guest limits the chloride concentration range that these systems can regulate. In search of systems that could be used for the photogated release

of chloride anions, we have now turned our attention toward main group-based photocages for chloride anions.

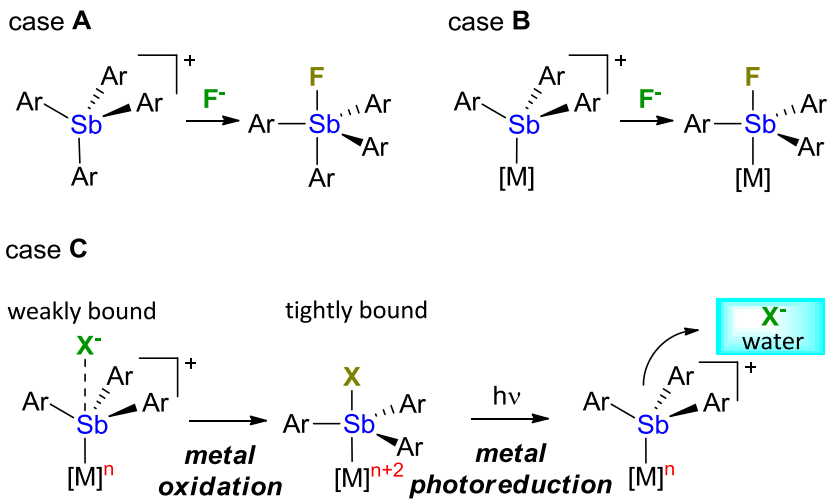

Figure 44. Illustration of case **A**, **B** and **C**.

We have shown recently that stibonium ions are powerful Lewis acids[18,44] which can be used in aqueous environments for the capture of fluoride anions (**A**).[153] We have also shown that anion coordination occurs at the antimony center of transition metal stibine complexes (**B**).[71] In this chapter, we now present a series of results which indicate that the anion affinity of such transition metal stibine complexes can be modulated by the redox state of the metal (**C**).

5.2 Synthesis and characterization of [**20**][Cl] and **23**-Cl

As a starting point for our studies, we decided to work with a metal that is amenable to facile light-induced redox changes. These considerations led us to consider

platinum which is known to undergo photoreduction when in the tetravalent state. Reaction of the bis(phosphanyl)stibine ligand **L** ((^{31}P) -6.6 ppm)[71] with $(Et_2S)_2PtCl_2$ in chloroform proceeded over the course of 12 hours to afford complex [**20**][Cl]. This complex could be oxidized with $PhICl_2$ to afford complex **23**-Cl as a yellow solid (Figure 45). The $^{31}P\{^1H\}$ NMR spectra of these two compounds display a peak at 53.9 ppm for [**20**][Cl] in $CDCl_3$ and 34.8 ppm for **23**-Cl in CD_2Cl_2, flanked in both cases by platinum satellites ($^1J_{Pt\text{-}P}$ = 2706 Hz for [**20**][Cl] and 1954 Hz for **23**). The decrease $^1J_{Pt\text{-}P}$ coupling constant observed upon conversion of [**20**][Cl] into **23**-Cl is consistent with oxidation of the platinum center.[116-118,154]

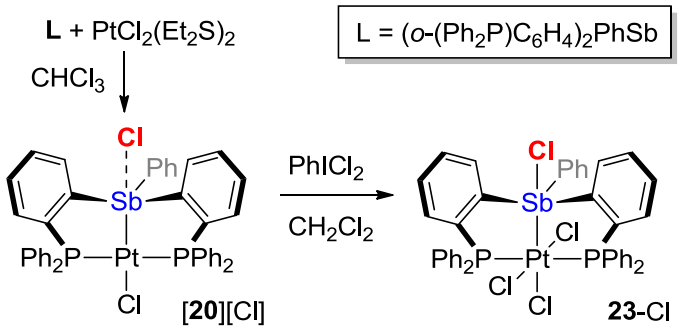

Figure 45. Synthesis of the Sb-Pt complexes [**20**][Cl] and **23**-Cl

Both of these complexes have been fully characterized and their crystal structure determined. The structure of [**20**][Cl] shows formal insertion of the antimony atom into a Pt-Cl of the square platinum unit. As a result, the antimony atom adopts a distorted trigonal bipyramidal geometry with a chloride ion and a platinum atom at the axial position (Cl(2)-Sb(1)-Pt(1) = 178.06(4)^o) (Figure 46). The resulting Sb(1)-Cl(2) bond of

2.7532(18) Å is rather long; it exceeds the sum of the covalent radii of the two elements by 14.2%-15.2% and iscomparable to that of partially ionic chlorostiboranes such as Ph_4SbCl (2.740(6) Å).[114,115] This structural features suggest that this chloride ligand is loosely bound to antimony and possibly poised to release once in solution (*vide infra*). Examination of the structure of **23**-Cl shows oxidative addition of a Cl_2 equivalent to the platinum center which adopts an octahedral geometry. This oxidation induces an elongation of the Sb-Pt bond distance from 2.5380(8) Å in [**20**][Cl] to 2.6563(5) Å in **23**-Cl. It also induces a notable contraction of the Sb(1)-Cl(2) distance from 2.7532(18) Å in [**20**][Cl] to 2.6202(18) Å in **23**-Cl, thus suggesting a tighter coordination of the chloride anion to antimony in **23**-Cl. This change can be rationalized by invoking an increase in the electronegativity and negative inductive (-I) effect of the platinum moiety upon oxidation.

5.3 Computational studies of [**20**][Cl] and **23**-Cl

To further support this argument, the structures of [**20**][Cl] and **23**-Cl have also been studied computationally using the Gaussian 09 program[122] (functional, BP86;[80,81] mixed basis sets: Sb/Pt, VTZ-PP cc-pVTZ-PP; P/Cl, 6-311+g(d); C/H, 6-31g(d))[123,124] and analysed using the Natural Bond Orbital method (Figure 46). This analysis reveals that the orbital contribution of Sb–Pt bonding pair changes from Sb, 45.6%/Pt, 54.4% in [**20**][Cl] to Sb, 20.6%/Pt, 79.4% in **23**. The increased platinum character of this bonding pair in **23** corroborates the conclusion of our structural studies and further illustrates the increased -I effect of the tetravalent platinum moiety.

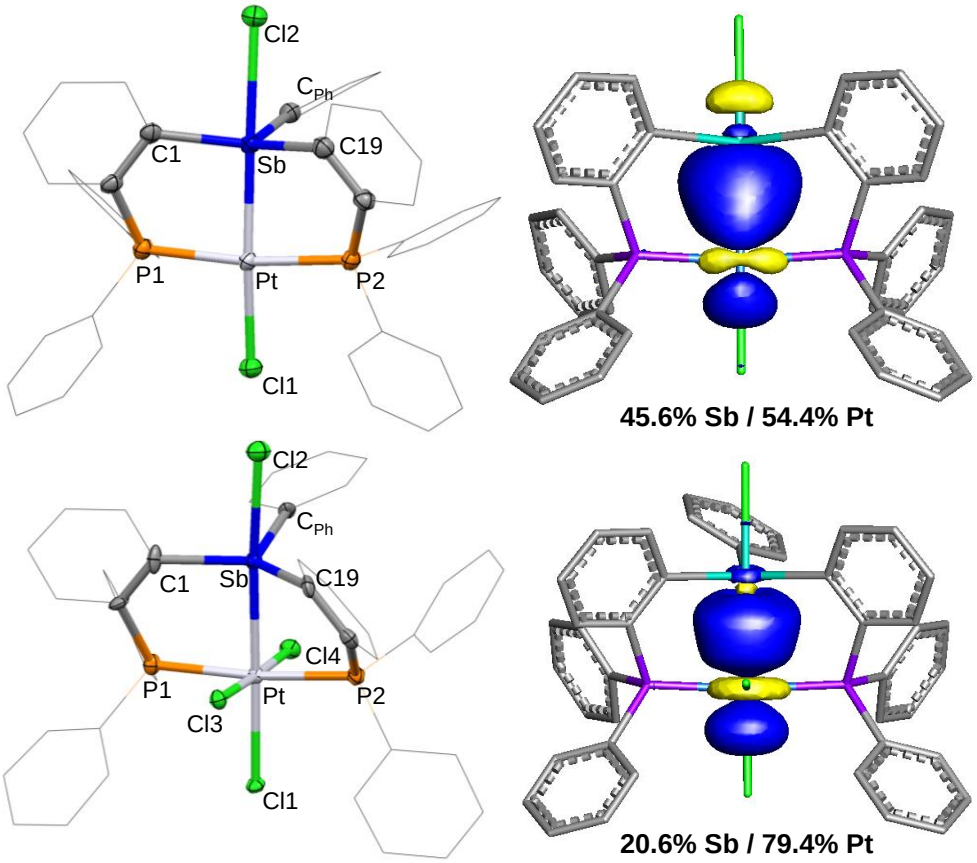

Figure 46. Left: Crystal structures of [**20**][Cl] and **23**-Cl. Thermal ellipsoids are drawn at the 50% probability level. Phenyl groups are drawn in wireframe. Pertinent metrical parameters can be found in the text. Right: NLMO plot (isovalue = 0.04) of the Sb-Pt bond in [**20**][Cl] and **23**-Cl obtained from NBO analysis. Hydrogen atoms are omitted for clarity. Selected bond lengths (Å) and angles (˚) for [**20**][Cl]: Sb-Pt 2.5380(8), Pt-Cl1 2.3851(16), Sb-Cl2 2.7532(18); P1-Pt-P2 170.01(6), Cl2-Sb-Pt 178.06(4), Sb-Pt-Cl1 172.36(4), C1-Sb-C19 124.2(2), C19-Sb-C_{Ph} 108.6(2), C_{Ph}-Sb-C1 122.3(2). **23**-Cl: Sb-Pt 2.6563(5), Pt-Cl1 2.4877(16), Pt-Cl3 2.3508(16), Pt-Cl4 2.3088(16), Sb-Cl2 2.6202(18); P1-Pt-P2 170.84(6), Cl3-Pt-Cl4 178.40(6), Sb-Pt-Cl1 177.75(4), Cl2-Sb-Pt 174.71(4), C1-Sb-C19 120.2(3), C19-Sb-C_{Ph} 111.7(3), C_{Ph}-Sb-C1 125.4(3).

5.4 Chloride binding studies

With the photoinduced release of chloride as the main objective of this work, it became important to measure the strength of the Sb-Cl interaction in [**20**][Cl] and **23**-Cl. We first tested the stability of **23**-Cl under various conditions. Addition of $NaBPh_4$ to a solution of **23**-Cl in CH_2Cl_2 does not result in the precipitation of NaCl. The absence of a reaction is further supported by ^{31}P NMR spectroscopy which shows no changes of the resonance of at 34.8 ppm. Compound **23**-Cl also fails to react when treated with an equivalent of 9-anthryltriphenylstibonium ([**17**]OTf), a cation that binds chloride in $CHCl_3$ with a binding constant of 10^5 M^{-1} (Figure 52). This lack of reaction suggests that the effective stability constant of **23**-Cl must be at least equal to 10^6 M^{-1}. Altogether, these experiments show that chloride is effectively caged in compound **23**-Cl. By contrast, [**20**][Cl] quickly reacts with $NaBPh_4$ in CH_2Cl_2 to afford the cationic platinum complex [**20**][BPh_4] which could be isolated in 93% yield. The $^{31}P\{^1H\}$ NMR resonance of [**20**][BPh_4] in $CDCl_3$ at 51.35 ppm ($^1J_{Pt\text{-}P}$ = 2426 Hz), which is close to the value recorded for [**20**][Cl] in the same solvent. The crystal structures of [**20**][BPh_4] shows that the d^8 metal center adopts a square-planar geometry with the two coordinated phosphine arms in a trans arrangement (Figure 53). As indicated by the average C-Sb-C bond angle of 111.5°, the antimony atom adopts a tetrahedral geometry and forms a shorter Pt-Sb bond (2.4834(5) Å) than in [**20**][Cl] (Sb-Pt = 2.5380(8) Å). Next we decided to measure the stability constant of [**20**][Cl]. To this end, a $CDCl_3$ solution of $[\mathbf{20}]^+$ was titrated with an incremental amount of TBACl ([*n*-Bu_4N]Cl). Monitoring of the titration using ^1H NMR spectroscopy indicates a progressive upfield shift of the

phenylene hydrogen nuclei positioned ortho from the antimony atom (H_{Ph}). Fitting of the resulting titration data to a 1:1 binding isotherm affords a stability constant of 910 (±30) M^{-1} for [**20**][Cl] (Figure 47). These measurements indicate that the stability constants of [**20**][Cl] and **23**-Cl differ by at least five orders of magnitude. Thus, while **23**-Cl shows no measured tendency toward chloride release, [**20**][Cl] is partly ionized in solvents such as $CHCl_3$. For example, it can be calculated that a 1 mM solution of [**20**][Cl] in $CHCl_3$ would be 64 % ionized leading to substantial release of chloride to the medium.

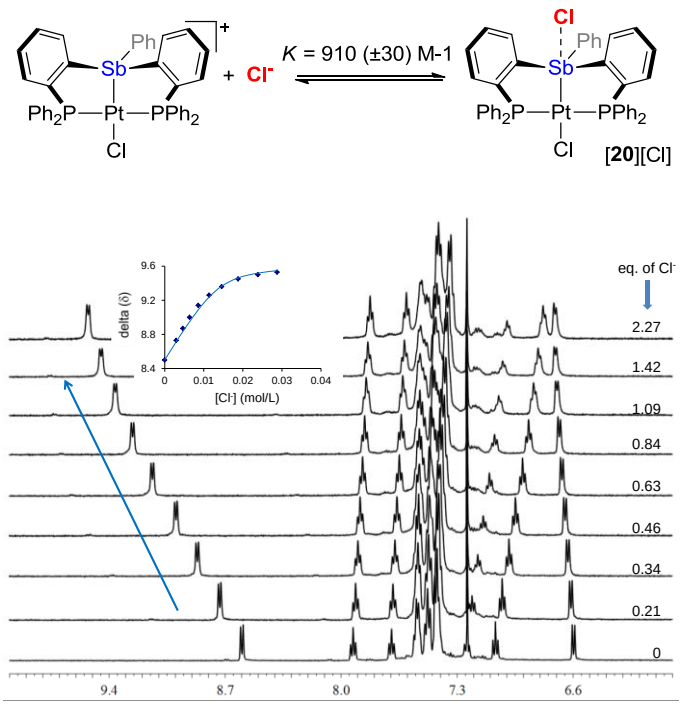

Figure 47. Top: Solution equilibria studied by ^{1}H NMR spectroscopy. Botton: Overlaid ^{1}H NMR spectra obtained during the titration of [**20**][Cl] with TBACl in $CDCl_3$. The concentration of [**20**][Cl] remained constant during the titrations (0.014 M). The inset shows experimental data and calculated 1:1 binding isotherm with K = 910 (±30) M^{-1}.

Given the markedly different stability constant of [**20**][Cl] and **23**-Cl, we decided to investigate the photoreductive conversion of **23**-Cl into [**20**][Cl] as a means to achieve chloride anion release. The UV-is spectrum of **23**-Cl features an intense absorption band at 310 nm (ε_{310} = 23900), which, as indicated by TD-DFT calculations, results from electronic excitation from filled orbitals into the LUMO and LUMO+1. Since both of the LUMO and LUMO+1 have strong Pt-Cl antibonding character, irradiation into this band is expected to induce chlorine atom elimination as already observed for other tetravalent chloroplatinum complexes. We monitored the photolysis of **23**-Cl by ^{31}P NMR and found that it gave a photoproduct with a resonance at 51.55 ppm ($^{1}J_{Pt\text{-}P}$ = 2580 Hz) along with other unidentified species. This experiment shows that **23**-Cl does not convert back into [**20**][Cl] thus invalidating our approach toward the photorelease of chloride ions.

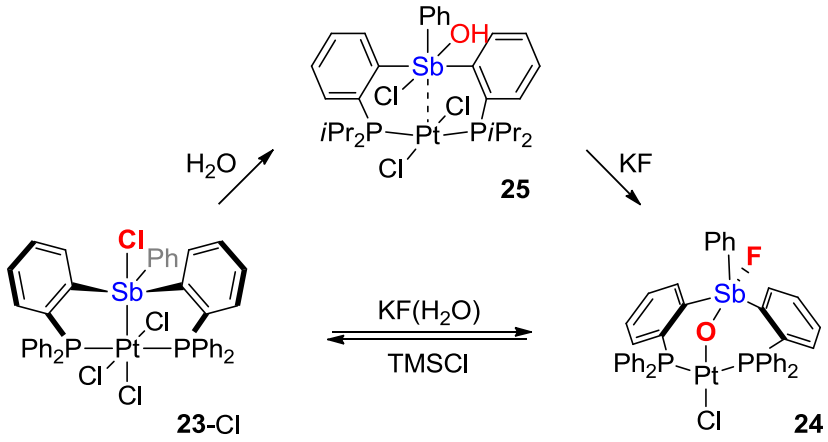

Figure 48. Synthesis of **24** and **25**.

5.5 Internal redox switch

To investigate the anion trigger interal redox switch properties, a $CHCl_3$ solution of complex **23**-Cl quickly reacts with 10 equivalents KF in methanol to afford Sb(V)-Pt(II) (**24**) (Figure 48). The reaction could be conveniently followed by ^{31}P NMR spectroscopy which clearly indicates formation of a new species featuring a sharp resonance at 28.5 ppm with a strong ^{195}Pt coupling ($^{1}J_{Pt\text{-}P}$ = 2544 Hz). In addition, the appearance of the signal at -98.3 ppm in the ^{19}F NMR spectrum indicated the fluoride atom in complex **24**. Formation of **24** is, however, chemically reversible. Indeed, **24** reacts with TMSCl (trimethylsilyl chloride) to produce **23**-Cl. Fortunately, slow diffusion of Et_2O into a solution of **24** in $CHCl_3$ afforded light-yellow crystal which was suitable for X-ray diffraction (Figure 49). The structure reveals a normal square planar coordination around Pt atom and a distorted trigonal bypyramidal geometry around Sb center as shown by P(1)-Pt(1)-P(2) and O(1)-Pt(1)-Cl(1) angles of 157.49(12)° and 177.8(3)°, respectively, and a F(1)-Sb(1)-O(1) angle of 173.1(4)°. These platinum and antimony atoms are separated by the oxygen atom. A significant expansion of the Pt-Sb distance from 2.6563(5) Å in **23**-Cl to 3.344 Å in **24** is indicative of the absence of a direct Pt-Sb interaction. The structure also shows coordination of the fluoride anion to the antimony atom with Sb(1)-F(1) bond length of 2.024(9) Å for **24**. This bond length is close to that observed in the fluorostiboranes Ph_4SbF (2.0530(8) Å)[72] and $AntPh_3SbF$ (2.0363(17) Å)[155], thus attesting to the presence of a strong interaction. In order to better understanding the internal redox process, the intermediate complex **25** has been synthesized by layering neutral water with the solution of **23**-Cl in CH_2Cl_2. The ^{31}P

NMR of **25** shows a single peak at 30.5 ppm with platinum satellite 2703 Hz. The X-ray crystal structure of **25** shows a distorted square planar coordination around Pt atom with a Sb-Pt separation of 3.1003(9) Å (Figure 49). The d(z^2) orbital of Pt atom is not invoved in any bonding except having a weak interaction with the σ*(Sb-C_{Ph}). Around the Sb atom, a distorted octahedral geometry was observed with the hydroxide bound at an equatorial position. Furthermore, the complex **25** can be converted into **24** in the presence of KF.

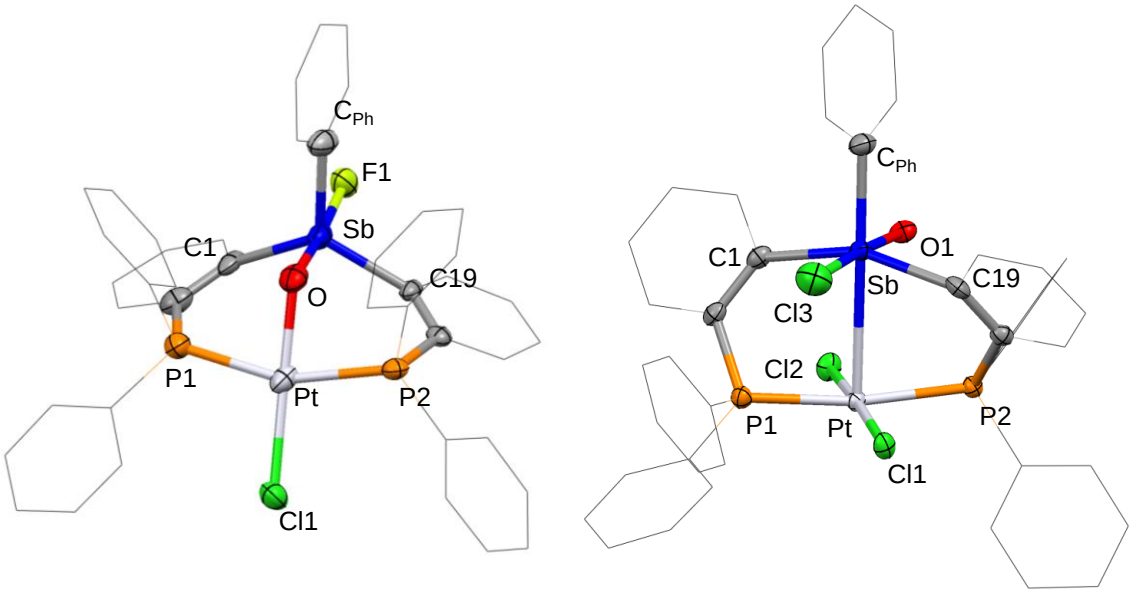

Figure 49. Crystal structures of and **24** (left) and and **25** (right). Thermal ellipsoids are drawn at the 50% probability level. Phenyl groups are drawn in wireframe. Hydrogen atoms and solvents are omitted for clarity. Selected bond lengths (Å) and angles (˚) for **24**: Sb-Pt 3.344, Pt-Cl1 2.330(3), Pt-P1 2.275(3), Pt-P2 2.267(3), Pt-O 2.028(10), Sb-F1 2.024(9), Sb-O 1.939(10); P1-Pt-P2 157.49(12), O-Pt-Cl1 177.8(3), F1-Sb-O 173.1(4), C19-Sb-C_{Ph} 119.5(5), C19-Sb-C1 120.0(4), C_{Ph}-Sb-C1 118.7(5). For **25**: Sb-Pt 3.1003(9), Pt-Cl1 2.2951(13), Pt-Cl2 2.3154(14), Pt-P1 2.3202(14), Pt-P2 2.3238(14), Sb-Cl3 2.409(2), Sb-O1 2.061(4); Cl1-Pt-Cl2 174.52(5), P2-Pt-P1 170.33(5), Pt-Sb-C_{Ph} 175.11(15), C1-Sb-C19 156.83(19), Cl3-Sb-O1 176.72(11).

To further evaluate the nature of the Sb-Pt bond in **25**, DFT structural optimization was performed using the same program and basis sets as previously described. The optimized structure of **25** is very close to solid state structure. Second-order perturbative NBO analyses of **25** also provided evidence for a very weak Pt→Sb very weak dative interaction, with NBO delocalization energies of about 5.21 $kcalmol^{-1}$ (Figure 50). This result also reconfirmed the absence of a significant Pt-Sb interaction.

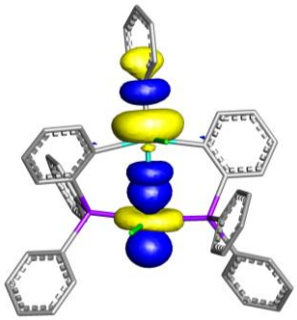

Figure 50. Superposition of the donor and acceptor orbitals according to NBO analysis, which contribute mainly to the Pt→Sb interactions in **25**. Hydrogen atoms are omitted for clarity (isovalue=0.05).

First, is can be recognized that the charge of the binuclear core in [**20**][Cl] increase from 5^+ to 7^+ upon conversion into **23**-Cl. Since conversion of **23**-Cl into **24** is not a redox reaction, the two elements still share total charge of 7^+. These considerations lead us to propose the assignment charge in Figure 51. This formal view is supported by the computed NBO charge shown in Figure 51.

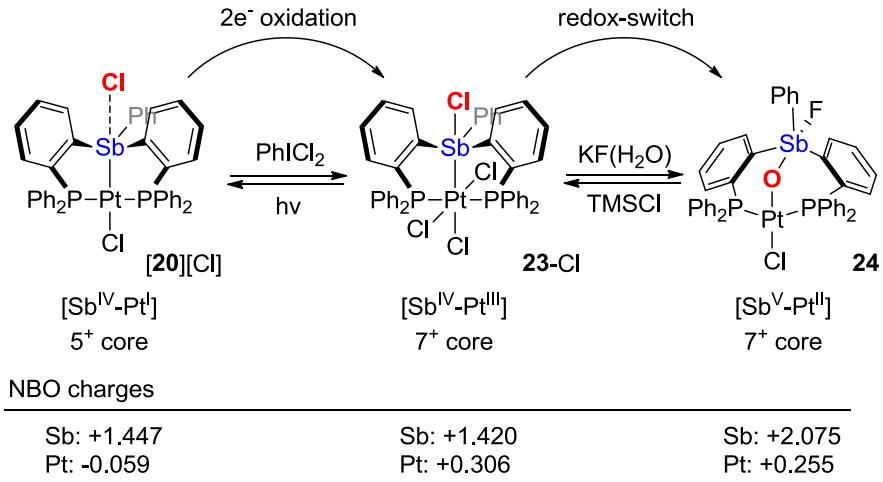

Figure 51. The oxidation and interal redox switch between [**20**][Cl], **23**-Cl and **24** and NBO charges.

5.6 Conclusions

The results presented in this study show that the chloride affinity of the antimony atom in the title platinum stibine complexes is controlled by the redox state of the metal center. When the latter is oxidized as in **23**-Cl, the Lewis acidity of the antimony atom increases, leading to a tighter coordination of the anion. Conversely, in [**20**][Cl], the chloride is loosely bound and readily liberated to the medium.

5.7 Experimental

General considerations. (*o*-$(Ph_2P)C_6H_4)_2PhSb$ ligand **L**,[71] *cis*-$PtCl_2(Et_2S)_2$[120] and $PhICl_2$[121] were prepared according to procedures reported in the literature. TMSCl and KF were purchased from Aldrich and used as received. 2,3-dimethyl-1,3-butadiene (DMBD) and *n*-Bu_4NCl (TBACl) were purchased from Alfa Aesar and used as received. Solvents were dried by passing through an alumina column (*n*-hexane, CH_2Cl_2) or refluxing under N_2 over Na/K (Et_2O and THF). $CHCl_3$ and $CDCl_3$ were dried by refluxing under N_2 over P_2O_5. All other solvents were ACS reagent grade and used as received. Air-sensitive compounds were handled under a N_2 atmosphere using standard Schlenk and glovebox techniques. UV-vis spectra were recorded on an Ocean Optics USB4000 spectrometer with an Ocean Optics ISS light source. Elemental analyses were performed at Atlantic Microlab (Norcross, GA). NMR spectra were recorded on Varian Unity Inova 400 FT NMR (399.59 MHz for ^1H, 375.99 MHz for ^{19}F and 161.74 MHz for ^{31}P) and Varian Inova 500 FT NMR (125.58 MHz for ^{13}C) spectrometer at ambient temperature unless otherwise stated. Chemical shifts are given in ppm, and are referenced against external Me_4Si (^1H, ^{13}C), BF_3•Et_2O (^{19}F) and H_3PO_4 (^{31}P).

Synthesis of [**20**]**[**BPh_4**].** To a CH_2Cl_2 (5 mL) solution of [**20**][Cl] (50 mg, 0.051 mmol) was added a MeOH (5 mL) solution of $NaBPh_4$ (17 mg, 0.051 mmol) at ambient temperature for 2 hrs. The mixture turned from a yellow to orange solution immediately. The reaction mixture was filtered over Celite to remove NaCl. The filtrate was evaporated to dryness and the residue recrystallized from pentane to afford [**20**][BPh_4] as a yellow powder (60 mg, 93% yield). Single crystals of [**20**][BPh_4] suitable for X-ray

diffraction were obtained by vapor diffusion of Et_2O into a solution of the compound in $CHCl_3$. ^{1}H NMR (399.9 MHz; $CDCl_3$): δ 6.42 (d, 2H, o-P(Sb)C_6H_4, $^3J_{H\text{-}H}$ = 7.54 Hz), 6.76 (t, 4H, BPh, $^3J_{H\text{-}H}$ = 7.29 Hz), 6.91 (t, 8H, BPh, $^3J_{H\text{-}H}$ = 7.29 Hz), 6.99 (t, 2H, *o*-P(Sb)C_6H_4, $^3J_{H\text{-}H}$ = 7.64 Hz), 7.13 (t, 1H, SbPh-C*H*, $^3J_{H\text{-}H}$ = 7.54 Hz), 7.39-7.45 (m, 18H, PPh-C*H* + SbPh-C*H*), 7.35-7.40 (m, 8H, BPh), 7.49-7.58 (m, 8H, PPh-C*H* + *o*-P(Sb)C_6H_4), 7.91 (d, 2H, *o*-P(Sb)C_6H_4, $^3J_{H\text{-}H}$ = 7.54 Hz). ^{13}C{^{1}H} NMR (125.85 MHz; CDCl3): δ 121.62 (s), 125.48 (m), 127.18 (s), 127.91 (m), 128.77 (s), 129.01 (m), 129.74 (s), 130.27 (s), 130.60 (s), 132.30 (s), 132.50 (s), 133.36 (s), 133.50 (s), 133.86 (br), 134.73 (s), 136.42 (s), 137.09 (br), 164.31 (q, $J_{C\text{-}P}$ = 50.41 Hz). ^{31}P{^{1}H} NMR (161.74 MHz; $CDCl_3$): δ 51.35 (s, $^1J_{P-195Pt}$ = 2426 Hz). ^{11}B NMR (128.2 MHz; $CDCl_3$): δ -6.78 (s). Elemental analysis calculated (%) for $C_{66}H_{53}BClP_2PtSb$ + $CHCl_3$: C, 60.01 H, 4.05; found C, 59.62; H 4.22.

Synthesis of 23-Cl. A solution of [**20**][Cl] (50 mg, 0.051 mmol) in CH_2Cl_2 (2 mL) was added to a solution of $PhICl_2$ (14 mg, 0.051 mmol) in CH_2Cl_2 (2 mL) at ambient temperature. A yellow precipitate was formed immediately. After the mixture was stirred for 2 hrs, 10 mL of Et_2O was added. The resulting yellow precipitate was collected by filtration and dried under vacuum, to afford **23**-Cl (49 mg, 91% yield). Yellow crystals of **23**-Cl suitable for X-ray diffraction analysis were obtained from diffusing Et_2O into a CH_2Cl_2 solution of **23**-Cl. ^{1}H NMR (399.9 MHz; CD_2Cl_2): δ 6.54 (d, 2H, *o*-SbPh-C*H*, $^3J_{H-H}$ = 8.16 Hz), 6.69 (pseudo-t, 2H, m-SbPh-C*H*, $^3J_{H-H}$ = 8.16 Hz), 6.97 (t, 1H, p-SbPh-C*H*, $^3J_{H-H}$ = 8.16 Hz), 7.42-7.59 (m, 18H, PPh-CH), 7.63 (pseudo-t, 2H, m-P(Sb)C_6H_4, $^3J_{H-H}$ = 8.20 Hz), 7.81-7.90 (m, 6H, PPh-C*H* + SbPh-C*H*), 9.54 (d, 2H, *o*-

P(Sb)C_6H_4, $^3J_{H-H}$ = 8.10 Hz). $^{13}C\{^1H\}$ NMR (125.58 MHz; CD_2Cl_2): δ 126.59 (s), 127.50 (s), 127.71 (t, J_{C-P} = 5.11 Hz), 128.96 (t, J_{C-P} = 5.11 Hz), 128.83 (s), 130.84(s), 131.45(s), 131.97(d, J_{C-P} = 6.17 Hz), 132.22(s), 135.32(s), 136.07(s), 137.02(s), 139.22(s), 143.55(s). $^{31}P\{^1H\}$ NMR (161.74 MHz; CD_2Cl_2): δ 34.8 (s, $^1J_{P-195Pt}$ = 1954 Hz). Elemental analysis calculated (%) for $C_{42}H_{33}Cl_4P_2PtSb$: C, 47.67 H, 3.14; found C, 47.40; H 3.23.

Synthesis of 24. A solution of **23**-Cl (30 mg, 0.028 mmol) in CH_2Cl_2 (3 mL) was treated with a solution of KF (16.2 mg, 0.28 mmol) in MeOH (1 mL). The reaction was stirred for 30 min. at room temperature before removing the solvent in vacuo. The resulting solid was extracted with CH_2Cl_2 (5 mL) and filtered over Celite. Evaporation of the solvent from the filtrate afforded 26.5 mg (96 %) of **24** as a yellow solid. Single crystals of **24** suitable for X-ray diffraction were obtained by slow diffusion of Et_2O into a solution of the compound in CH_2Cl_2. ^1H NMR (399.9 MHz; $CDCl_3$): δ 6.98 (pseudo-t, 2H, *m*-SbPh-C*H*, $^3J_{H-H}$ = 7.57 Hz), 6.13 (pseudo-t, 2H, *m*-P(Sb)C_6H_4, $^3J_{H-H}$ = 7.57 Hz), 7.20 (t, 1H, *p*-SbPh-C*H*, $^3J_{H-H}$ = 7.57 Hz), 7.31-7.46 (m, 18H, PPh-C*H*), 7.75 (m, 6H, PPh-C*H* + SbPh-C*H*), 8.07 (d, 2H, *o*-P(Sb)C_6H_4, $^3J_{H-H}$ = 7.57 Hz), 8.84 (pseudo-t, 2H, *m*-P(Sb)C_6H_4, $^3J_{H-H}$ = 7.73 Hz). $^{13}C\{^1H\}$ NMR (125.58 MHz; $CDCl_3$): δ 127.89 (s), 128.05 (s), 128.35 (t, J_{C-P} = 6.27 Hz), 129.08 (s), 130.07 (s), 130.27(s), 130.45(s), 130.55(s), 130.88(s), 131.20(s), 134.57(t, J_{C-P} = 6.10 Hz), 135.10(s), 136.35(t, J_{C-P} = 6.10 Hz), 136.95(s). $^{31}P\{^1H\}$ NMR (161.74 MHz; $CDCl_3$): δ 28.5 (s, $^1J_{P-195Pt}$ = 2544 Hz). ^{19}F NMR (469.93 MHz; $CDCl_3$): δ -98.3 (br). Elemental analysis calculated (%) for $C_{42}H_{33}ClFOP_2PtSb$: C, 51.11 H, 3.37; found C, 50.83; H 3.23.

Photolysis reactions and quantum yield measurements. Photolysis reactions were performed using 310 nm light generated from a 75 W xenon lamp with a PTI model 101 monochromator integrated in a PTI QuantaMaster 40 fluorescence spectrometer. Potassium ferrioxalate was freshly prepared as a standard actinometer to determine the photon flux.[156-158]

Crystallography. All crystallographic measurements were performed at 110(2) K using a Bruker SMART APEX II diffractometer with a CCD area detector (graphite monochromated Mo K_α radiation, λ = 0.71073 Å) at 110 K. In each case, a specimen of suitable size and quality was selected and mounted onto a nylon loop. The semi-empirical method SADABS was applied for absorption correction. The structures were solved by direct methods and refined by the full-matrix least-square technique against F^2 with the anisotropic temperature parameters for all non-hydrogen atoms. All H atoms were geometrically placed and refined in riding model approximation. Data reduction and further calculations were performed using the Bruker SAINT+ and SHELXTL NT program packages.[78]

Theoretical calculations. Density functional theory (DFT) calculations (full geometry optimization) were carried out on [**20**][Cl], [**20**][BPh_4], **23**-Cl and **24** starting from the crystal structure geometries with Gaussian09[122] program (BP86[80,81] with 6-31g(d) for H, C, O; 6-311+g(d) for P, Cl; Stuttgart relativistic large core (RSC) 1997 ECP for Pt[123]; Stuttgart relativistic small core (RLC) 1997 ECP for Sb[124]). Frequency calculations were also carried out on the optimized geometry, showing no imaginary frequencies. The optimized structures, which are in excellent agreement with the solid-

state structures, were subjected to a NBO analysis.[125] The resulting Natural Localized Molecular Orbitals (NLMOs) were visualized and plotted in Jimp 2 program.[126]

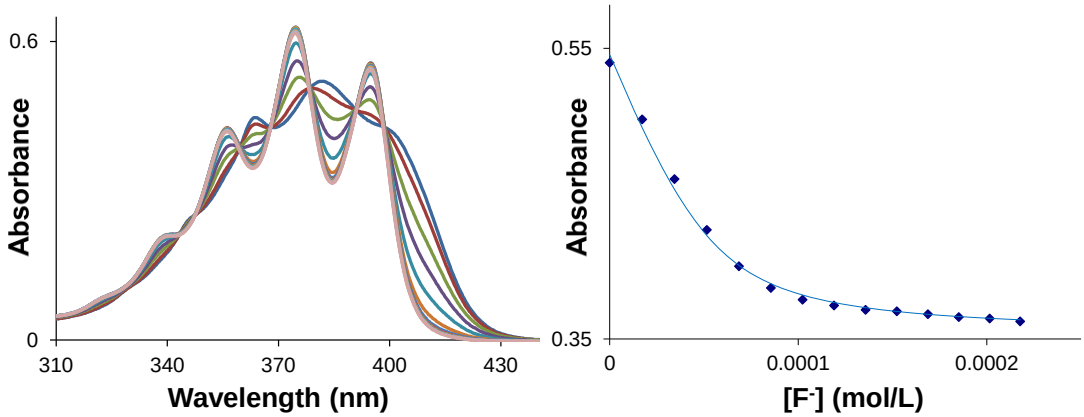

Figure 52. Spectral changes in the UV-vis absorption spectra of [**17**]OTf (5.35×10^{-5} M) in $CHCl_3$ upon incremental addition of a TBACl solution (6.5×10^{-3} M, $CHCl_3$). The isotherms are plotted based on the absorbance at 382 nm, and the line indicates the fit to the calculated 1:1 binding isotherm. The fluoride binding constant was calculated to be 1.08×10^5 ($\pm$7000) M^{-1}.

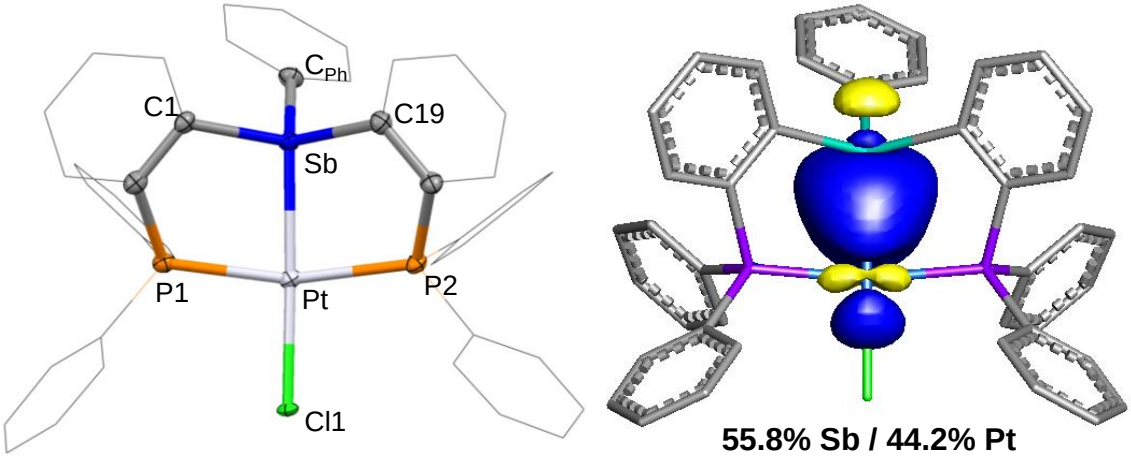

Figure 53. Left: Crystal structures of [**20**][BPh_4]. Thermal ellipsoids are drawn at the 50% probability level. Phenyl groups are drawn in wireframe. Pertinent metrical parameters can be found in the text. Right: NLMO plot (isovalue = 0.04) of the Sb-Pt bond in [**20**][BPh_4] obtained from NBO analysis. Hydrogen atoms are omitted for clarity. Selected bond lengths (Å) and angles (˚) [**20**][BPh_4]: Sb-Pt 2.4834(5), Pt-Cl1 2.3603(9), Pt-P1 2.3083(11), Pt-P2 2.3070(11); P1-Pt-P2 165.57(3), Sb-Pt-Cl1 175.19(2), C1-Sb-C19 114.93(14), C19-Sb-C_{Ph} 113.87(14), C_{Ph}-Sb-C1 105.85(14).

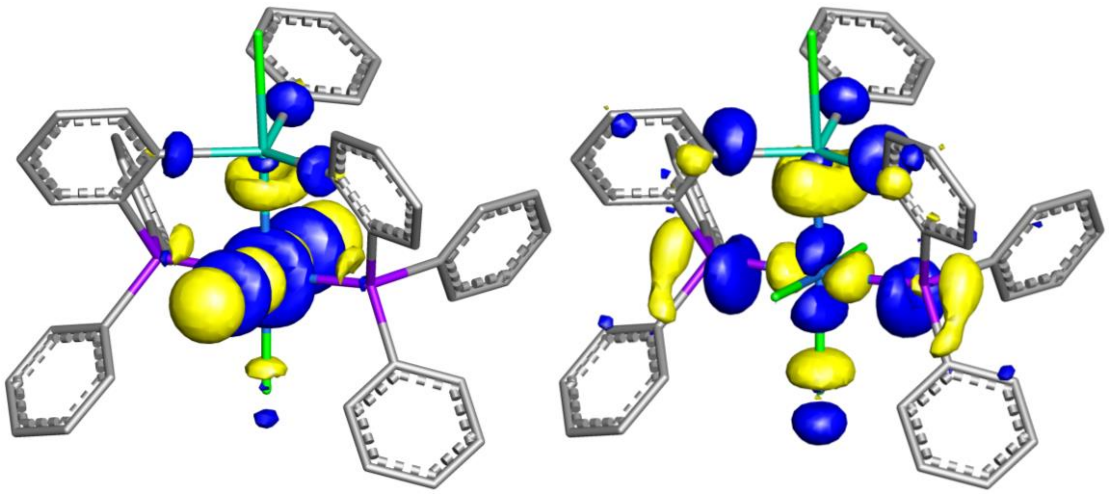

Figure 54. Plots of the LUMO (-0.09481 eV) and LUMO+1 (-0.07633 eV) of **23**-Cl (at 0.04 isosurface value).

Table 9. TD-DFT calculation output showing the nature of the low energy excitations for **23**-Cl.

Excitation (Energy)	Oscillator strength	MO→MO transition	Contributions
4.1185 eV (301.04 nm)	0.2762	199→213 206→214 208→213 209→213 210→213 211→213	0.10120 -0.26630 0.47913 0.25980 0.22031 -0.18370

Table 10. Crystal data, data collections, and structure refinements for [**20**][BPh_4] and **23**-Cl

Crystal data	[**20**][BPh_4]·$CHCl_3$	**23**-Cl
Formula	$C_{66}H_{53}BClP_2PtSb·CHCl_3$	$C_{42}H_{33}Cl_4P_2PtSb$
Mr	1390.49	1058.35
Crystal size (mm^3)	0.38 x 0.19 x 0.14	0.15 x 0.12 x 0.09
Crystal system	Monoclinic	Orthorhombic
Space group	P2(1)/c	P2(1)2(1)2(1)
a (Å)	17.206(4)	12.1954(10)
b (Å)	17.397(4)	14.8621(12)
c (Å)	19.382(5)	22.6398(18)
α (°)	90	90
β (°)	90.955(3)	90
γ (°)	90	90
V ($Å^3$)	5801(2)	4103.4(6)
Z	4	4
ρ_{calc} (g cm^{-3})	1.592	1.713
μ (mm^{-1})	3.156	4.432
F(000)	2752	2048
T/K	110(2)	110(2)
Scan mode	ω, φ	ω, φ
hkl Range	-23 → +23	-15 → +15
	-23 → +23	-18 → +18
	-25 → +25	-27 → +27
Measd reflns	71058	42790
Unique reflns [R_{int}]	14570 [0.0781]	8055 [0.0567]
Reflns used for refinement	14570	8055
Refined parameters	685	451
GooF	1.049	1.088
*R*1,[a] *wR*2[b] (all data)	0.0547, 0.0812	0.0350, 0.0808
ρ_{fin} (max/min.) ($eÅ^{-3}$)	1.393, -1.440	1.815, -0.992

[a] $R_1 = \Sigma||Fo| - |Fc||/\Sigma|Fo|$. [b] $wR_2 = [[\Sigma w(Fo^2 - Fc^2)^2]/[\Sigma w(Fo^2)^2]]^{1/2}$.

Table 11. Crystal data, data collections, and structure refinements for **24** and **25**

Crystal data	**24**	**25**·Et_2O
Formula	$C_{42}H_{33}ClFOP_2PtSb$	$C_{42}H_{34}Cl_3OP_2PtSb \cdot Et_2O$
Mr	986.91	1113.94
Crystal size (mm^3)	0.25 x 0.13 x 0.11	0.31 x 0.28 x 0.11
Crystal system	Triclinic	Monoclinci
Space group	P-1	P2(1)/c
a (Å)	11.5409(13)	12.335(3)
b (Å)	12.9818(14)	20.297(6)
c (Å)	14.1093(16)	16.933(5)
α (°)	68.0480(10)	90
β (°)	66.7740(10)	92.915(3)
γ (°)	85.1010(10)	90
V ($Å^3$)	1796.9(3)	4234(2)
Z	2	4
ρ_{calc} (g cm^{-3})	1.824	1.748
μ (mm^{-1})	4.842	4.242
F(000)	956	2184
T/K	110(2)	110(2)
Scan mode	ω, φ	ω, φ
hkl Range	-16 → +16	-16 → +16
	-14 → +14	-27 → +26
	-29 → +29	-22 → +22
Measd reflns	18751	52040
Unique reflns [R_{int}]	7019 [0.0272]	10573 [0.0712]
Reflns used for refinement	7019	10573
Refined parameters	442	496
GooF	1.105	1.032
$R1$,[a] $wR2$[b] (all data)	0.0922, 0.2065	0.0590, 0.0920
ρ_{fin} (max/min.) ($eÅ^{-3}$)	11.322, -3.919	1.103, -1.558

[a] $R_1 = \Sigma||Fo| - |Fc||/\Sigma|Fo|$. [b] $wR_2 = [[\Sigma w(Fo^2 - Fc^2)^2]/[\Sigma w(Fo^2)^2]]^{1/2}$.

CHAPTER VI

σ-DONOR/ACCEPTOR-CONFUSED LIGANDS: THE CASE OF A CHLOROSTIBINE*

6.1 Introduction

Unlike their lighter phosphine and arsine analogs, stibine ligands tend to form relatively labile complexes when coordinated to transition metals.[30,31,33,34,90] These properties can be correlated to the moderate donicity of the antimony-based lone pair which bears a large 5s character.[35] As part of our current interest in the chemistry of such ligands, we have recently investigated the redox properties of late transition metal-stibine complexes such as **A** (Figure 55) and showed that the stibine could be oxidized in the coordination sphere of the transition metal center to afford stiborane-gold complex (**B**)[35] in which the stiborane acts as a σ-acceptor.[91-96,159-162] This switch in the ligative behavior of the antimony ligand is accompanied by an umpolung of the Sb-Au bond from Sb→Au in the reduced state to Au→Sb in the oxidized state. An initial conclusion of these studies was that the σ-accepting properties of antimony ligand may be exclusive to the pentavalent state.[42,64,70,71] Recently, however, we have started to question whether such a behaviour could also be observed for antimony species in the trivalent state.

*Reprinted in part permission from, "σ-Donor/acceptor-confused ligands: The case of a chlorostibine"; Ke, I. S.; Gabbaï, F. P. *Inorg. Chem.* **2013**, in press, DOI: 10.1021/ic400736b. Copyright 2013 by American Chemical Society.

This revision of our thinking was prompted by the realization that antimony(III) species substituted by electronegative ligands form Lewis adducts when in the presence of Lewis basic substrates as in compound **C** (Figure 55).[163,164] An elegant contribution of Reid also demonstrated that halostibine ligands of general formula $SbMe_{3-n}Br_n$ display increased π-acceptor properties as the number of bromine atoms increases.[165] Thus, we have now decided to determine if halostibine ligands could behave as pure Lewis acidic, σ-acceptor ligands. This possibility was reinforced by the very recent discovery that chlorobismuthine ligands show Z-ligand behavior when in the coordination of electron rich metals.[63,166]

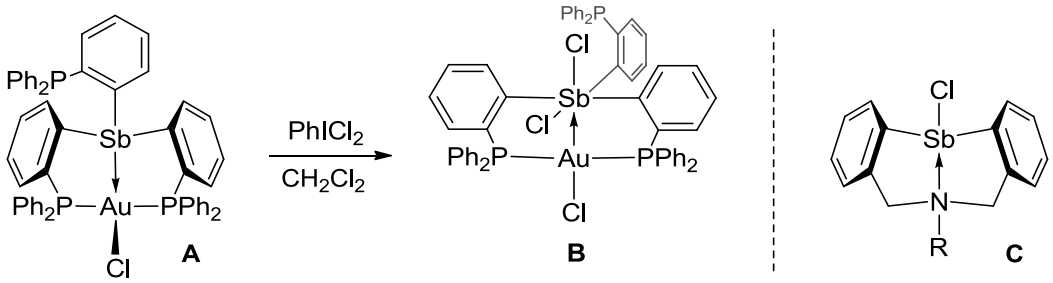

Figure 55. Illustration of **A** and **B**: Sb-Au complexes and **C**: Lewis adducts of halostibine.

6.2 σ-Accepting properties of diarylhalostibines

To test the aforementioned hypothesis, we chose to employ a simple SbP_2 ligand system amenable to variation of one of the antimony substituents. With this objective in mind, we first targeted (*o*-(*i*Pr_2P)$_2C_6H_4)_2$SbPh) as a triarylstibine ligand (referred to as L^{Ph}). This ligand, which was synthesized using a similar strategy as that adopted for its diphenylphosphino analog,[71] reacts with (tht)AuCl (tht = tetrahydrothiophene) to afford L^{Ph}AuCl (**26**). Next we targeted the chlorostibine analog of **26**. The ligand (*o*-(*i*Pr_2P)$C_6H_4)_2$SbCl (L^{Cl}) was generated by co-proportionation of neat $SbCl_3$ and (*o*-(*i*Pr_2P)$C_6H_4)_3$Sb at 90°C and was allowed to react, without isolation or purification, with (tht)AuCl in CH_2Cl_2 to afford L^{Cl}AuCl (**27**) (Figure 56). Complexes **26** and **27** are air stable and readily soluble in organic solvents such as THF, CH_2Cl_2 and acetone. They have been fully characterized. Their ^{31}P NMR spectra display a peak at 69.18 ppm for **26** and 64.18 ppm for **27** corresponding to the coordinated phosphine groups. These two complexes also feature a downfield ^{1}H NMR resonance at 7.92 ppm for **26** and 8.53 ppm for **27** corresponding to the phenylene proton positioned *ortho* from the antimony atom.

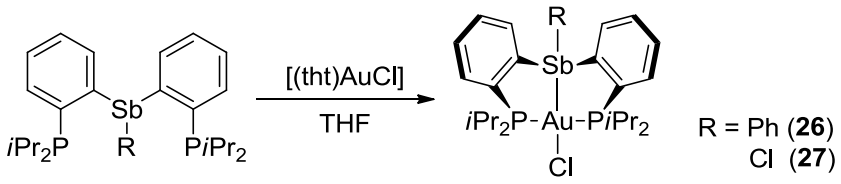

Figure 56. Reaction of L^{Ph} and L^{Cl} with (tht)AuCl.

To gain a greater insight into the nature of these complexes, their structure has been determined using single crystal X-ray diffraction. Complex **26** crystallizes in the monoclinic space group $P2_1/c$ as a THF solvate with one molecule in the asymmetric unit (Figure 57). The coordination geometry of the gold atom of **26** is trigonal pyramidal, with the chloride and two phosphine ligands defining the base (P1-Au-P2 = 149.23(3)^o, P1-Au-Cl1 = 104.72(3)^o, P2-Au-Cl1 = 105.96(3)^o; and Σ = 359.91^o) and the antimony atom, the apex (Sb-Au-P1 = 84.69(2)^o, Sb-Au-P2 = 84.54(2)^o, Sb-Au-Cl1 = 115.09(2)^o). The Au–Sb separation of 2.8669(4) Å exceeds the sum of the covalent radii of the two elements (2.64-2.75 Å) by only 4.3%-8.6%.[112,113] It is comparable to that found in stibine gold(I) complexes including $[Au(SbPh_3)_4][ClO_4]$ (2.656–2.658 Å)[167] and $[Au(\mu_2\text{-}1,8\text{-}(C_{10}H_6))_2SbPh_2]$ (2.76 Å av.)[64] and slightly longer than the Au-Sb distance observed in the related complex $[(o\text{-}(Ph_2P)C_6H_4)_3Sb]AuCl$ (2.8374(4) Å).[35] Last, with a Au-Sb-C_{Ph} angle of 171.07(8)^o, the stibine adopts a seesaw rather than a tetrahedral geometry. Complex **27** crystallizes in the monoclinic space group $P2_1/c$ with one molecule in the asymmetric unit (Figure 57). Although the structure of **27** resembles that of **26**, a close inspection reveals a number of notable differences. In particular, the sum of the P1-Au-P2 (153.14(6)^o), P1-Au-Cl1 (105.72(6)^o) and P2-Au-Cl1 (97.89(7)^o) of 356.75^o indicates a small but measurable displacement of the gold atom from the plane defined by the three primary ligands. The Sb-Au-Cl1 angle (141.73(4)^o) is also markedly larger than the The Sb-Au-Cl angle (115.09(2)^o) in **26**. Altogether, these structural peculiarities suggest the presence of a Au→Sb interaction leading to an hypervalent configuration at antimony. In line with this conclusion, the Sb-Cl2 bond distance (2.519(2) Å) in **27** is

intermediate between that observed for Ph_2SbCl (2.409 Å) [168] and $[Ph_2SbCl_2]^-$ (2.619 Å av.).[169] Also, the antimony center of **27** adopts a seesaw geometry analogous to that of $[Ph_2SbCl_2]^-$.

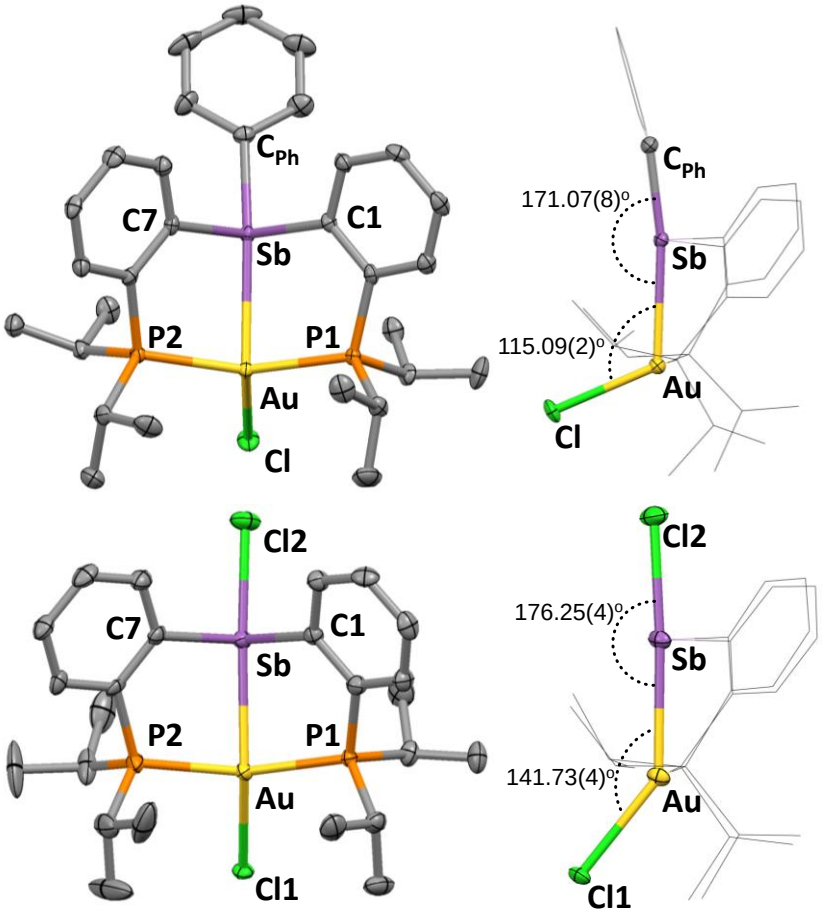

Figure 57. Structure of **26** (top) and **27** (bottom). Displacement ellipsoids are scaled to the 50% probability level. Interstitial solvent molecules and hydrogen atoms omitted for clarity. Selected bond lengths (A˚) and angles (deg) for: **26**: Au-Sb 2.8669(4), Au-Cl 2.6080(8), Au-P1 2.3224(9), Au-P2 2.3244(9); P1-Au-P2 149.23(3), Cl-Au-Sb 115.09(2), Au-Sb-C_{Ph} 171.07(8), C1-Sb-C7 98.28(12). **27**: Au-Sb 2.7937(13), Au-Cl1 2.5836(16), Au-P1 2.3364(19), Au-P2 2.3386(18), Sb-Cl2 2.519(2); P1-Au-P2 153.14(6), Cl1-Au-Sb 141.73(4), Au-Sb-Cl2 176.25(4), C1-Sb-C7 99.5(2).

To shed light on the bonding present in these compounds, the structures of **26** and **27** were optimized using DFT methods (Gaussian09: BP86 with 6-31g for H, C; Stuttgart relativistic small core (RSC) 1997 ECP for Au; Stuttgart relativistic large core (RLC) ECP for P, Cl, Sb) and subjected to NBO calculations. The level of theory chosen for these calculations was first validated by a geometry optimization that produced structures very close to those determined experimentally (Table 12). The NBO analysis decomposes the Au-Sb interactions in two distinct components (Figure 58). The first component is a lp(Sb)→6p(Au) interaction in which the stibine ligands plays its expected role of donor toward the gold atom. The second component is a more unexpected lp(Au)→5p(Sb) interaction, with the roles of the two atoms inverted. To estimate the magnitude of these interactions, we resorted to deletion calculations, which are carried out by zeroing the Kohn–Sham matrix elements corresponding to the interaction of interest. The resulting deletion energies (E_{del}(lp(Sb)→6p(Au)) = 9.4 kcal/mol and E_{del}(lp(Au)→5p(Sb)) = 9.2 kcal/mol) indicate that these two interactions contribute almost equally to the stability of the complex. The opposite directionality of these two interactions as well as their essentially equal contribution to the stability of the complex indicate that the gold and antimony atoms are connected by a weak (E_{del}(lp(Sb)→6p(Au) + (lp(Au)→5p(Sb)) = 18.5 kcal/mol) and non-polar interaction.

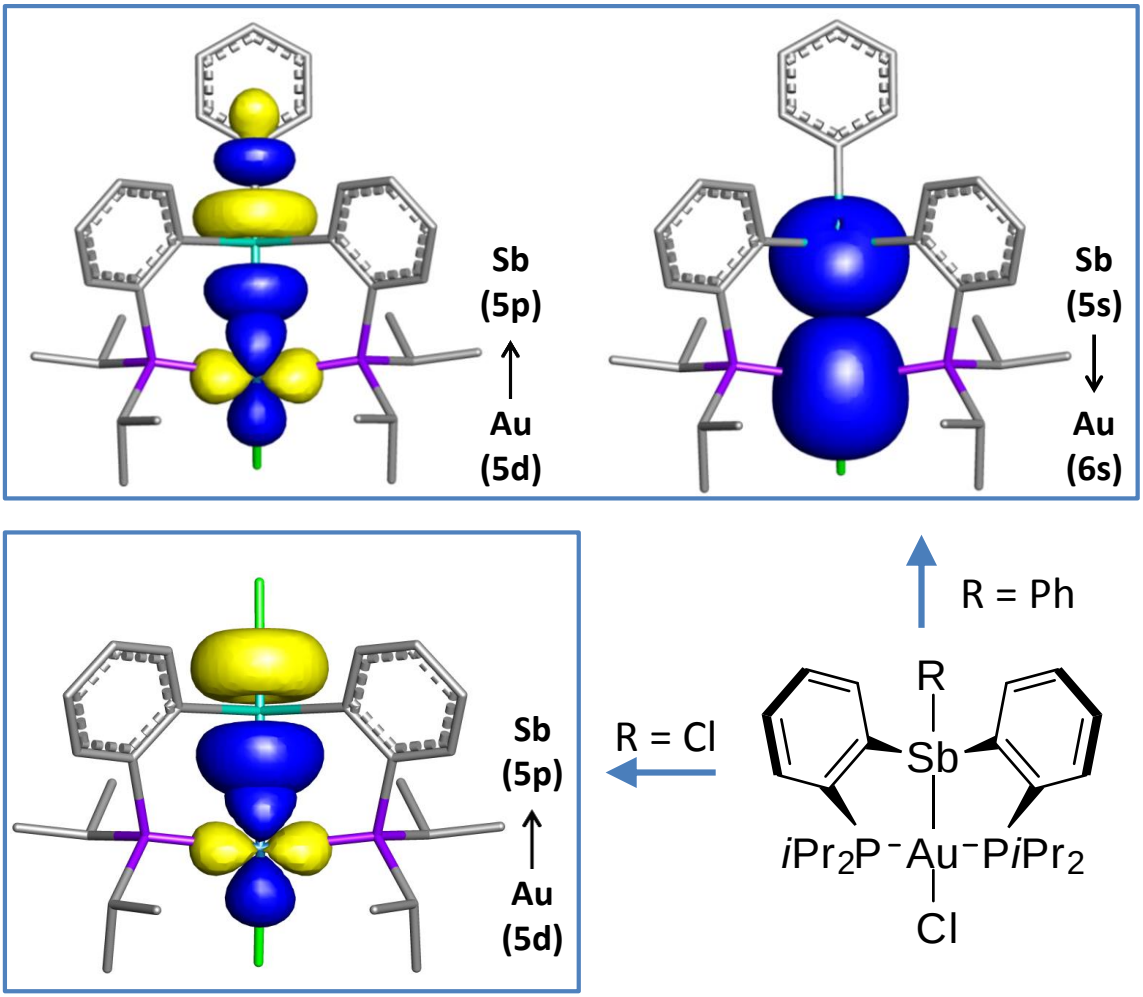

Figure 58. Superposition of the donor and acceptor orbitals according to NBO analysis, which contribute mainly to the antimony–gold interactions in **26** (above) and **27** (below). Hydrogen atoms are omitted for clarity (isovalue=0.05).

Table 12. Selected bond lengths (Å) and angles (°) for complexes as determined crystallographically (**26**, **27**, **28** and **29**) and optimized computationally (**26***, **27***, **28*** and **29***).

	E-Au[a] (Å)	Au-Cl (Å)	P-Au-P (°)	E-Au-Cl[a] (°)	Σ_αAu (°)
26	2.8669(4)	2.6080(8)	149.23(3)	115.09(2)	379.91
26*	2.946	2.654	151.481	136.381	372.75
27	2.7937(13)	2.5836(16)	153.14(6)	141.73(4)	372.93
27*	2.845	2.636	157.877	151.632	367.69
28	2.892(2)	2.561(2)	151.96(7)	140.67(6)	373.35
28*	2.950	2.640	157.357	150.770	367.56
29	2.309(8)	2.522(2)	160.2(1)	168.7(2)	362.2
29*	2.3544	2.6486	158.48	171.23	362.36

[a]E = Sb for **26**, **27**; E = Bi for **28**; E = B for **29**

For complex **27**, the NBO analysis treats the antimony-bound chloride as an independent unit that interacts with the antimony atom by a strong lp(Cl)→5p(Sb) interaction. This interaction may be viewed as a dative bond resulting from the donation of a chloride lone pair into a vacant antimony p orbital (Figure 2). More significantly, the same 5p orbital is involved in a 5d(Au)→5p(Sb) interaction, indicating that the gold atom donates to the antimony center by one of its filled d orbitals. A donation in the reverse direction, *ie* from antimony to gold, is not observed indicating that the donor/acceptor ambiguity noted in **26** is no longer present. Hence, according to NBO, the antimony atom of **27** acts as a pure σ-acceptor or Z-ligand toward the transition

metal. Finally, a deletion calculation show that the 5d(Au)→5p(Sb) interaction stabilizes the complex by E_{del}, = 24.4 kcal/mol.

6.3 Comparison of complex **27** with its halobismuthine analog

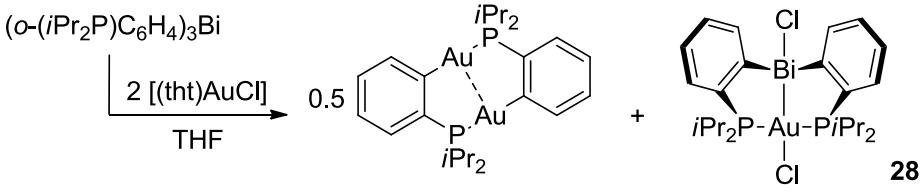

Figure 59. Reaction of $(o\text{-}(i\text{Pr}_2\text{P})\text{C}_6\text{H}_4)_3\text{Bi}$ with (tht)AuCl.

The bonding situation observed in **26** is reminiscent of that recently described for the chlorobismuthine gold complex $[(o\text{-}(\text{Ph}_2\text{P})\text{C}_6\text{H}_4)_2\text{BiCl}]\text{AuCl}$.[63,166] Given this relationship, we set out to determine which of antimony or bismuth would be the strongest σ-acceptor. To carry out a comparison that is exempt of phosphorus substituent effects, we have now synthesized and characterized the isopropyl derivative $[(o\text{-}(i\text{Pr}_2\text{P})\text{C}_6\text{H}_4)_2\text{BiCl}]\text{AuCl}$. This compound was prepared by reactions of the newly prepared ligand $(o\text{-}(i\text{Pr}_2\text{P})\text{C}_6\text{H}_4)_3\text{Bi}$ with [(tht)AuCl] (Figure 59). The ^{31}P NMR spectrum of the reaction mixtures shows two singlets at 57.05 ppm and 55.33 ppm integrating in a 2:1 intensity ratio (Figure 76). The species giving rise to a resonance at 55.33 ppm is tentatively assigned to the by-product $[\{o\text{-}(i\text{Pr}_2\text{P})\text{C}_6\text{H}_4\text{Au}\}_2]$ resulting from transfer of an *o*-phenylenephosphino group from bismuth to gold. The second peak is assigned to the chlorobismuthine gold complex **28**. This assignment has been confirmed by the isolation

and full characterization of **28**. Similarly to the chlorostibine analog, this complex features a ^{1}H NMR resonance at 9.18 ppm corresponding to the phenylene proton positioned *ortho* from the bismuth atom. A single crystal X-ray diffraction analysis has also been carried out (Figure 60). Compound **28** is essentially isostructural with **27**, as indicated by the minute differences observed in the cell parameters. This isostructural relationship is confirmed by the molecular structure of **28** and its close relationship to that of **27**. Key metrical parameters include the Au-Bi distance (2.892(2) Å) as well as the Bi-Au-Cl1 (140.67(6)^{o}) P1-Au-P2 (151.96(7)^{o}), and Au-Bi-Cl2 (178.45(5)^{o}) angles which deviate only slightly from their corresponding values in **27** (Sb-Au-Cl1 (141.73(4)^{o}) P1-Au-P2 (153.14(6)^{o}), and Au-Sb-Cl2 (176.25(4)^{o})).

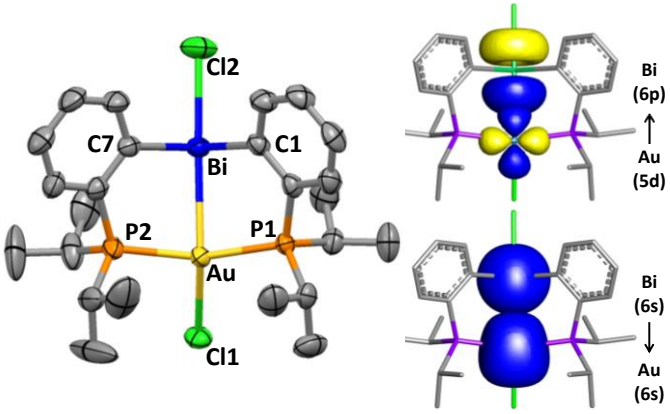

Figure 60. Left: Solid-state structure of **28**. Ellipsoids are set at 50 % probability; hydrogen atoms and non-coordinated solvent molecules are omitted for clarity. Pertinent metrical parameters can be found in the text. Selected bond lengths (A˚) and angles (deg) for **28**: Au-Bi 2.892(2), Au-Cl1 2.561(2), Au-P1 2.330(3), Au-P2 2.338(2), Bi-Cl2 2.613(3); P1-Au-P2 151.96(7), Cl1-Au-Bi 140.67(6), Au-Bi-Cl2 178.45(5), C1-Bi-C7 97.3(2). Right: Superposition of the donor and acceptor orbitals according to NBO analysis, which contribute mainly to the bismuth–gold interactions. Hydrogen atoms are omitted for clarity (isovalue=0.05).

For complex **28**, the NBO analysis identifies a 5d(Au)→6p(Bi) interaction which stabilizes the complex by E_{del} = 14.8 kcal/mol. A 6s(Bi)→6s(Au) is also observed. The deletion energy of this interaction (E_{del} = 5.1 kcal/mol to) is however relatively low, thus indicating that it makes a minor contribution to the bonding and that the Au-Bi bond is dominated by Au→Bi character. A comparison with the results of the NBO analysis of **27** indicates that the Au→Pn interaction (Pn = Sb, Bi) is stronger in the **27** than in **28**. We thus conclude that halostibines are more potent σ-accpetor ligand than their halobismuthine counterparts. This finding is in agreement with the experimentally established Lewis acidity scale which, shows that antimony(III) halides are more Lewis acidic than their bismuth(III) counterparts.[170]

6.4 Comparison of **27** with a related boron analog

Complex **27** is closely related to complex [(*o*-(*i*Pr_2P)C_6H_4)$_2$BPh]AuCl (**29**) which has been previously isolated by the group of Bourissou.[171] Complexes **27** and **29** both feature a short Au-E interaction (2.309(8) Å for E = B, 2.7937(13) Å for E =Sb) that exceeds the sum of the covalent radii (2.09-2.20 Å for E = B and 2.64-2.75 Å for E = Sb) by a relatively short margin of 1.6%-5.8% in the case of **27** and 5.0%-10.5% in the case of **29**.[112,113] This simple metrical analysis suggests that the stabilizing energy of these linkages may be of similar magnitude. To substantiate this view, we optimized the structure of **29** using the level of theory employed for **27** and carried out a NBO analysis. As suggested by the above structural comparison, we found that the stabilization energy of the 5d(Au)→2p(B) interaction (E_{del} = 26.2 kcal/mol) of **29** only slightly exceeds that

determined for the 5d(Au)→5p(Sb) (E_{del} = 24.4 kcal/mol) of **27**. This comparison suggests that the ClSb of **27** and the PhB moiety of **29** have a comparable Lewis acidity toward gold, a result that we did not originally anticipate.

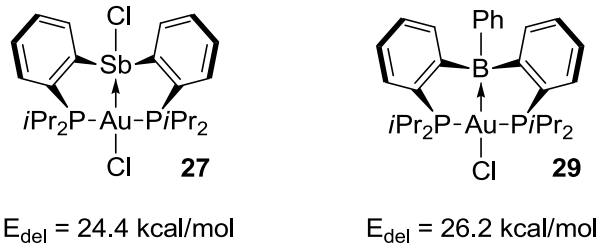

E_{del} = 24.4 kcal/mol E_{del} = 26.2 kcal/mol

6.5 Two electron-oxidation of complexes **26** and **27**.

We have previously demonstrated that stibine gold complexes may undergo oxidation in the presence of reagents such as $PhICl_2$ to afford dichlorostiborane gold complexes with a Au→Sb interactions.[35] By analogy with such reactions, we have decided to study the oxidation of **26** and **27** in the presence of *ortho*-chloranil, a two electron oxidant that has been previously shown to add to both triarylstibines and aryldichlorostibines.[172] To this end, these two derivatives were allowed to react with **26** equiv. of *o*-chloranil in CH_2Cl_2, leading to the precipitation of complexes **30** and **31** as light orange solids (Figure 61). Formation of this compounds show that both **26** and **27**, despite their different binding characteristics, are amenable to a clean two-electron oxidation. The $^{31}P\{^1H\}$ NMR spectrum of **30** and **31** in $CDCl_3$ shows a single resonance at 103.26 ppm for **30** and 108.63 ppm for **31**. These resonances are significantly downfield from those of **26** and **27**, signalling a more oxidized gold atom. Complex **30**

crystallizes in the rhombic space group *R*-3. The crystal structure of **30** confirms the oxidative addition of *o*-chloranil to the antimony atom which now features a tetrachlorocatecholate ligand bound in a κ^2-*O*,*O* fashion (Figure 62). Incorporation of this ligands leads to the formation of a six coordinate antimony atom that adopts a slightly distorted octahedral geometry (O1-Sb-Au = 162.13(8)^o, C1-Sb-C7 = 172.65(15)^o, C13-Sb-O2 = 173.8(2)^o). This oxidative addition reaction also affects the coordination environment of the gold atom. Indeed, there is a notable contraction of the Au-Sb bond (from 2.8669(4) Å in **26** to 2.6833(3) Å for **30**) pointing to the effect of oxidation on the bimetallic core of these complexes. Also, as indicated by the value of the Sb-Au-Cl (173.91(3)^o) and P-Au-P (174.09(5)^o) angles, the gold atom is no longer in a trigonal pyramidal geometry but rather in a distorted square planar geometry. These changes indicate that the oxidation is not limited to the antimony atom but also affects the gold atom whose square planar geometry is consistent with a trivalent configuration. Such structural changes parallel those observed upon oxidation of [(*o*-$(Ph_2P)C_6H_4)_3Sb$]AuCl with $PhICl_2$.[35] Single crystals of **31** suitable for X-ray diffraction could not be obtained but all spectroscopic data point to a structure similar to that of **30**.

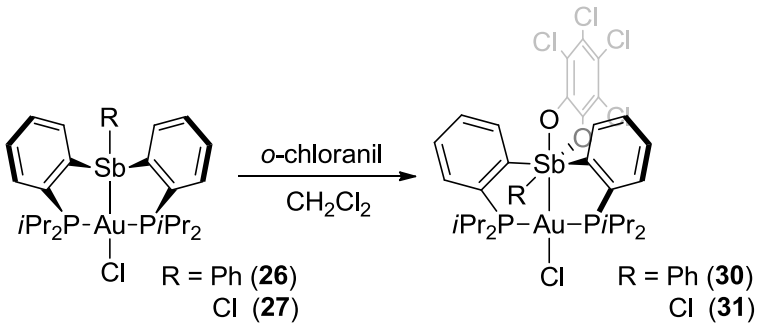

Figure 61. Two electron-oxidation of complexes **26** and **27** by *o*-chloranil.

Table 13. Selected bond lengths (Å) and angles (°) for complexes as determined crystallographically (**30**) and optimized computationally (**30*** and **31***).

	Sb-Au (Å)	Au-Cl (Å)	Sb-Au-Cl (°)	Σ_αAu (°)
30	2.6833(3)	2.4886(9)	173.91(3)	360.57(1)
30*	2.780	2.600	173.298	360.689
31*	2.733	2.567	176.326	360.010

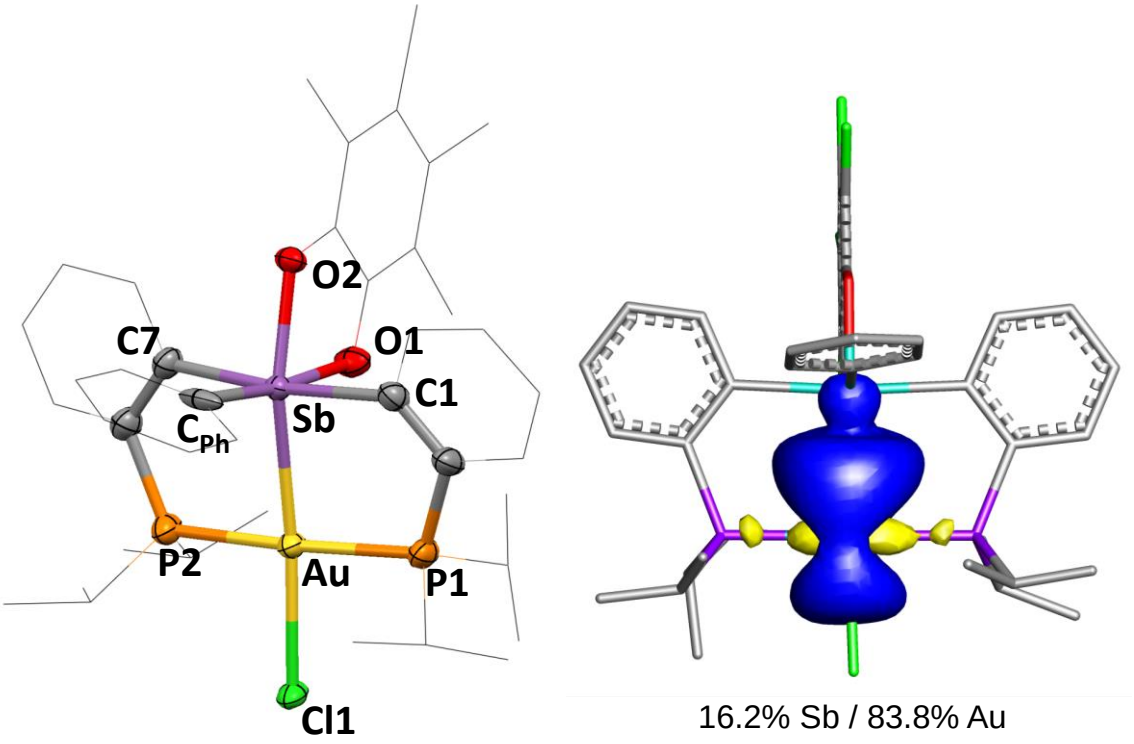

Figure 62. Left **:** Solid-state structure of **30**. Ellipsoids are set at 50 % probability; hydrogen atoms and non-coordinated solvent molecules are omitted for clarity. Pertinent metrical parameters can be found in the text. Right: Au-Sb Natural Localized Bond Orbital (NLMO, isovalue=0.03). Hydrogen atoms are omitted for clarity.

The structure of both **30** and **31** has been computationally optimized and analysed using NBO. The good match observed between the experimental and computed structure of **30** validates the adequacy of the level of theory employed for this complexes (Table 13). The strengthening of the Au-Sb interactions in **30** and **31** is reflected by the fact that NBO defines this linkage as a covalent one rather than as a second order donor acceptor interaction as for **26** and **27**. Analysis of the corresponding NLMO (Figure 62) shows that the Au-Sb bonding pair possesses a larger orbital contribution from the gold atom (Sb, 16.2%/Au, 83.8% for **30** and Sb, 16.3%/Au, 83.7% for **31**) in agreement with

a Au→Sb dative bond in both complexes. It is interesting to note the similarity that exists in the orbital contributions of the Au-Sb NLMOs of **30** and **31**. To explain this result, we propose that the antimony bound phenyl group (for **30**) or chloride ligand (for **31**) have little effect on the Au-Sb bond because of their *cis*-position with respect to the gold atom.

6.6 Complexation with Cu and Ag

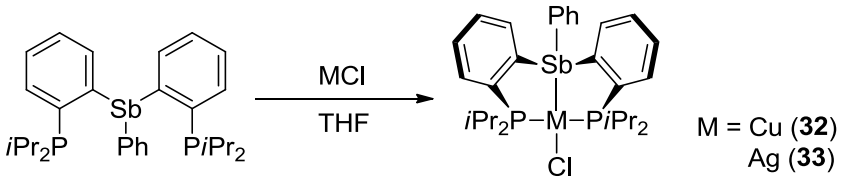

Figure 63. Reaction of L^{Ph} with CuCl and AgCl.

The copper and silver complexes **32** and **33** were prepared by adding 1 equiv of the L^{Ph} to a suspension of the corresponding metal(I) chloride in THF (Figure 63). In both cases, the reaction mixture immediately became homogeneous, and for copper, the solution turned yellow. After standard workup, complexes **32** and **33** were obtained in 84% and 89% yield, respectively. The ^{31}P NMR spectrum of **32** displays a unique signal at δ ^{31}P = 31.52 ppm, in agreement with the symmetric coordination of the two phosphorus atoms. The ^{31}P NMR spectrum of **33** exhibits a pair of doublets of almost equal intensity centered at 35.93 ppm. The coupling constants with the two silver isotopes are well-resolved [$^{1}J(^{109}Ag, ^{31}P)$ = 425 Hz and $^{1}J(^{107}Ag, ^{31}P)$ = 368 Hz] and

consistent with the $^{109}Ag/^{107}Ag$ gyromagnetic ratio. The ESI mass spectrum of this complexes show a peak at m/z 647.1016 and 693.0788 amu corresponding to the $[\mathbf{L}^{P2}Cu]^+$ and $[\mathbf{L}^{P2}Ag]^+$ ions, respectively.

To gain greater insight into the precise structure of these group 11 metal-stilbines, single crystals suitable for X-ray diffraction analyses were obtained by vapor diffusion of pentane into a solution of the compound in THF (Figure 64). For all complexes, the Cu and Ag metal centers are tetracoordinated. The two phosphane atoms span trans sites with a significantly bent P-M-P arrangement (135.09° and 128.61° for Cu and Ag), respectively. The Sb-Cu (2.6477(4) Å) bond length is shorter than the sum of the covalent radii of the two elements (2.52-2.71 Å for Sb-Cu)[112,113] by 1.2-5.1% %. This short separation suggests that there is strong dative interaction between Sb and Cu. Further inspection of the structure of **33** reveals a Sb-Ag separation of 2.9392(4) Å which only exceeds the sum of the covalent radii of the two elements (2.68-2.84 Å for Sb-Ag)[112,113] by 3.5%-9.8%. The separation of similar group 11 metal-stilbine complexes also can be found in the literature such as $CuCl(SbPh_3)_3$ (2.548-2.564 Å)[173] and $AgCl(SbPh_3)_3$ (2.705-2.786 Å)[174]. Other interesting features are the value of the M-Sb-Cl angle (160.11° and 163.37° for Cu and Ag) which indicates that the stibine ligand approaches the lighter group 11 atoms to achieve a seesaw rather than a tetrahedral geometry.

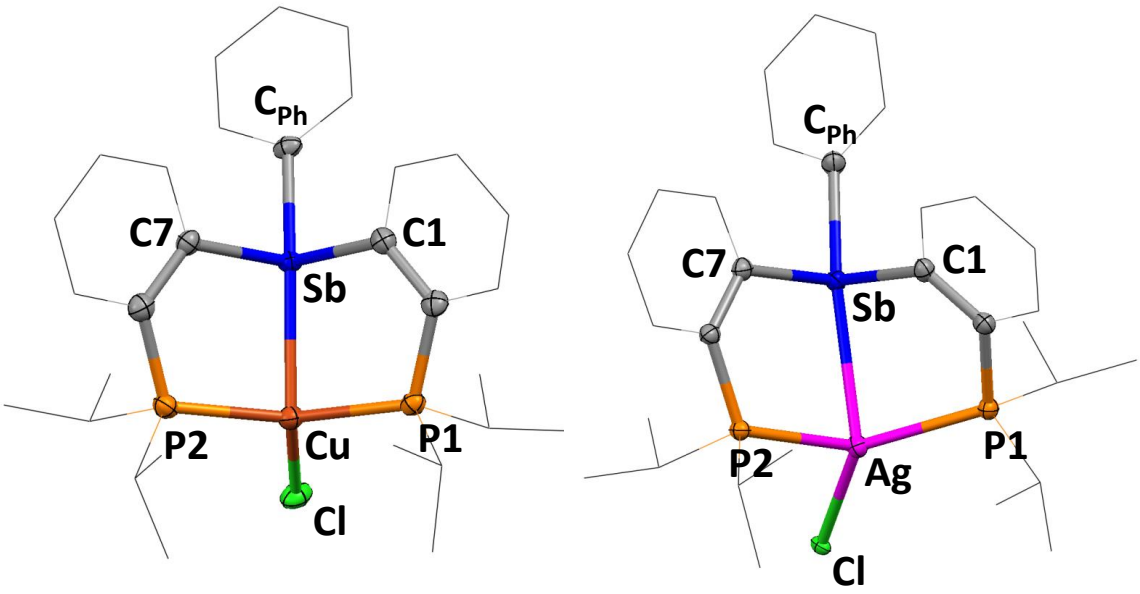

Figure 64. Crystal structures of **32** (left) and **33** (right). Thermal ellipsoids are drawn at the 50% probability. Phenyl groups are drawn in wireframe and hydrogen atoms, solvents are omitted for clarity. Pertinent metrical parameters can be found in the text.

To shed more light into the Sb→M interactions involved in metal-stilbine complexes **32** and **33**, the structures have been optimized using DFT methods (ADF: BP86/TZP) and subjected to a Boys localization analysis and an NBO analysis (Gaussian: BP86 with 6-31g for H, C; Stuttgart relativistic large core (RLC) ECP for P, Cl, Cu, Ag, Au and Sb). The optimized geometries fit closely with those determined experimentally, confirming the capability of the method in describing such complexes. For complexes **32** and **33**, the NBO analysis identifies a relatively weak 5s(Sb)→s(M) donor-acceptor interaction (E_{del} = 26.97 kcal mol^{-1} for Cu and 18.97 kcal mol^{-1} for Ag) as the primary interaction. Some backdonation d(M)→σ*(Sb-C) does occur in complexes **32** and **33**, but comparison of the corresponding stabilizing energies of 4.92

kcal mol^{-1} for Cu, 3.37 kcal mol^{-1} for Ag show that its contribution to the bonding is minor.

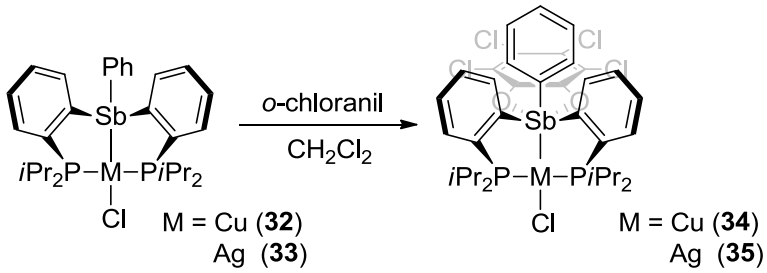

Figure 65. Two electron-oxidation of complexes **32** and **33** by *o*-chloranil.

With complexes **32** and **33** in hand, we sought to determine if the Sb-M core could sustain oxidation. To this end, complexes **32** and **33** were allowed to react with *o*-chloranil in CH_2Cl_2 resulting in the formation of complex **34** and **35** as an orange-yellow, air stable derivatives in 86% and 73% yield (Figure 65). All the ^{31}P NMR spectrums of **34** and **35** display a more downfield shift unique signal compared with **32** and **33**, in agreement with the symmetric coordination of the two phosphorus atoms. The ^{31}P NMR spectrum of **34** displays a unique signal at $\delta\ ^{31}P = 45.68$ ppm and **35** still exhibits a pair of doublets of almost equal intensity centered at 59.76 ppm. The coupling constants with the two silver isotopes are well-resolved [$^{1}J(^{109}Ag, ^{31}P)$ = 444 Hz and $^{1}J(^{107}Ag, ^{31}P)$ = 385 Hz] and consistent with the $^{109}Ag/^{107}Ag$ gyromagnetic ratio. Accordingly, the ^{13}C NMR ($CDCl_3$) exhibits three distinguishable *o*-chloranil peaks for the complexes **34** and **35**, but six distinguishable peaks in complex **30**. The different feature in ^{13}C NMR may result in the different geometries between complexes **34**, **35** and **30**. Fortunately, the

single crystal structures can be obtained by vapor diffusion of pentane into a solution of the compound in THF (Figure 66). In complexes **34** and **35**, the metal center is tetracoordinated and adopts a distorted octahedral geometry. The metal atom and phenyl ring define the apical axis, while the two phosphorus arms and *o*-chloranil occupy the basal positions. The two phosphane moieties span trans sites with a significantly bent P-M-P arrangement (139.0° for Cu and 138.0° for Ag). The Sb-M-Cl arrangements are 133.2° for Cu and 141.1° for Ag. The Sb-M distances (2.9905(6) Å for Sb-Cu and 3.0918(12) Å for Sb-Ag) are longer than those observed in complexes **32** and **33**, but fall within the sum of the van der Waals radii (3.40 Å for Sb-Cu and 3.72 Å for Sb-Ag).

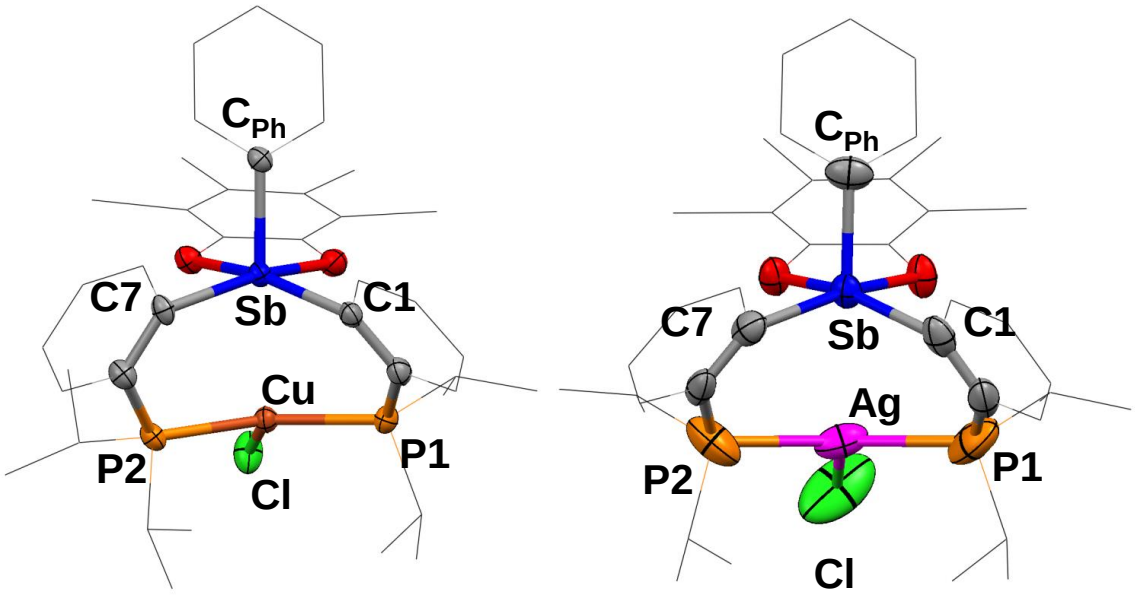

Figure 66. Crystal structures of **34** (left) and **35** (right). Thermal ellipsoids are drawn at the 50% probability. Phenyl groups are drawn in wireframe and hydrogen atoms, solvents are omitted for clarity. Pertinent metrical parameters can be found in the text.

To better understand the changes induced by oxidation, the structures of **34** and **35** have been optimized by using the same calculation method. These optimized structures, which are in good agreement with the X-ray diffraction results (d_{calc}(Sb-Cu) = 2.911 Å and d_{calc}(Sb-Ag) = 3.097 Å) were subjected to a NBO analysis. For both **34** and **35**, the NBO analysis treats the Cu and Ag as an independent unit that interact with the antimony atom by a d(M)→σ*(Sb-C) interaction. A deletion calculation carried out by concomitantly zeroing the Kohn–Sham matrix elements corresponding to the 3d(Cu)→σ*(Sb-C) and 4d(Ag)→σ*(Sb-C) interactions afford stabilization energies, E_{del}, of 20.52 kcal mol^{-1} for complex **34** and 13.74 kcal mol^{-1} for complex **35**, respectively.

6.7 Conclusions

The work reported in this paper show that chlorostibine ligands, when constrained to the appropriate geometry, may behave as pure σ-acceptor ligands toward late transition metals. This possibility is illustrated by the isolation of the chlorostibine gold complex **27** which possesses a Au→Sb dative interaction. This interaction leads to an hypervalent configuration at antimony reminiscent of that found in species such as $Ph_2SbCl_2^-$, a anion formed by coordination of a chloride anion to Ph_2SbCl. The results discussed in this paper also show that the Lewis acidity of chlorostibine ligands may exceed those of analogous chlorobismuthine ligands. This conclusion is in line with the documented greater Lewis acidity of antimony(III) halides when compared to bismuth(III) halide. Finally, we show that the antimony center of gold-stibine complexes undergo a clean oxidative cycloaddition in the presence *o*-chloranil. This

reaction which results in the formation of a rare aurated pentavalent antimony species, is accompanied by a contraction of Au-Sb core and a strengthening of the central Au-Sb bond.

6.8 Experimental

General considerations. [(tht)AuCl][175] (tht = tetrahydrothiophene) *o*-(*i*Pr_2P)C_6H_4Br[176] were prepared according to the reported procedures. Solvents were dried by passing through an alumina column (n-pentane and CH_2Cl_2) or by reflux under N_2 over Na/K (Et_2O and THF). All other solvents were used as received. $SbCl_3$, $BiCl_3$ and *o*-chloranil were purchased from Aldrich and used as received. All air and moisture sensitive manipulations were carried out under an atmosphere of dry N_2 employing either a glove box or standard Schlenk techniques. Ambient temperature NMR spectra were recorded on a Varian Unity Inova 400 FT NMR (399.59 MHz for ^{1}H, 100.45 MHz for ^{13}C, 161.74 MHz for ^{31}P) spectrometer. Chemical shifts (δ) are given in ppm and are referenced against residual solvent signals (^{1}H, ^{13}C) or external H_3PO_4(^{31}P). Elemental analyses were performed at Atlantic Microlab (Norcross, GA).

Synthesis of (*o*-(*i*Pr_2P)C_6H_4)$_2$SbPh. *n*-BuLi (4.50 ml, 11.72 mmol, 2.60 M in hexane) was added into the solution of *o*-(*i*Pr_2P)C_6H_4Br (2.67 g, 9.77 mmol) in Et_2O (10 mL) at room temperature. The reaction was allowed to stir for 30 min before adding solution of $PhSbCl_2$ (1.32g, 4.88 mmol) in THF (5 mL). The resulting mixture was stirred overnight at room temperature. The solvent was removed in vacuo, and the resulting solid was extracted with dichloromethane (20 mL) and filtered through Celite

to remove LiCl. The filtrate was evaporated to dryness, and the residue was recrystallized from MeOH to afford (*o*-(*i*Pr_2P)C_6H_4)$_2$SbPh as a white powder (1.53 g, 53% yield). ^{1}H NMR (499.43 MHz; $CDCl_3$): δ 7.44 (d, 2H, *o*-P(Sb)C_6H_4, $^3J_{H-H}$ = 7.50 Hz), 7.33 (d, 2H, SbPh-C*H*, $^3J_{H-H}$ = 7.50 Hz), 7.27 (pseudo-t, 2H, *o*-P(Sb)C_6H_4, $^3J_{H-H}$ = 7.50 Hz), 7.22 (pseudo-t, 2H, *o*-P(Sb)C_6H_4, $^3J_{H-H}$ = 7.50 Hz), 7.13-7.07 (m, 5H, *o*-P(Sb)C_6H_4 + PPh-C*H*), 2.08 (sept.d, 4H, $^3J_{H-H}$ = 4.10 Hz, $^2J_{H-P}$ = 29.03 Hz, C*H*CH_3), 1.07 (dd, 12H, $^3J_{H-H}$ = 3.40 Hz, $^3J_{H-P}$ = 14.51 Hz, CHC*H*$_3$), 0.80 (dd, 12H, $^3J_{H-H}$ = 3.40 Hz, $^3J_{H-P}$ = 14.51 Hz, CHC*H*$_3$). ^{13}C{^{1}H} NMR (125.58 MHz; $CDCl_3$): δ 153.72 (d, J_{C-P} = 13.82 Hz), 153.38 (d, J_{C-P} = 13.83 Hz), 143.22 (d, J_{C-P} = 8.68 Hz), 141.87 (t, J_{C-P} = 16.31 Hz), 137.31 (s), 136.75 (d, J_{C-P} = 13.84 Hz), 132.04 (s), 129.21 (s), 128.25 (s), 127.69 (s), 24.84 (dd, J_{C-P} = 13.81 Hz, J_{C-P} = 54.20 Hz), 20.22 (pseudo-t, J_{C-P} = 15.19 Hz), 19.66 (dd, J_{C-P} = 11.42 Hz, J_{C-P} = 40.21 Hz). ^{31}P{^{1}H} NMR (202.16 MHz; $CDCl_3$): δ 8.53 (s). Elemental analysis calculated (%) for $C_{30}H_{41}P_2Sb$: C, 61.56; H, 7.06. Found: C, 61.26; H, 6.97.

Synthesis of (*o*-(*i*Pr_2P)C_6H_4)$_3$Sb. *n*-BuLi (3.33 ml, 8.65 mmol, 2.60 M in hexane) was added into the solution of o-(*i*Pr_2P)C_6H_4Br (2.46 g, 7.21 mmol) in Et_2O (15 mL) at room temperature. The reaction was allowed to stir for 30 min before adding solution of $SbCl_3$ (0.55g, 2.40 mmol) in THF (5 mL). The resulting mixture was stirred overnight at room temperature. The solvent was removed in vacuo, and the resulting solid was extracted with dichloromethane (20 mL) and filtered through Celite to remove LiCl. The filtrate was evaporated to dryness, and the residue was recrystallized from MeOH to afford (*o*-(*i*Pr_2P)C_6H_4)$_3$Sb as a white powder (1.39 g, 64% yield). ^{1}H NMR

(399.59 MHz; $CDCl_3$): δ 7.37 (d, 3H, *o*-P(Sb)C_6H_4, $^3J_{H\text{-}H}$ = 7.72 Hz), 7.17 (pseudo-t, 3H, *m*-P(Sb)C_6H_4, $^3J_{H\text{-}H}$ = 7.72 Hz), 6.98 (pseudo-t, 3H, *m*-P(Sb)C_6H_4, $^3J_{H\text{-}H}$ = 7.72 Hz), 6.94 (d, 3H, *o*-P(Sb)C_6H_4, $^3J_{H\text{-}H}$ = 7.72 Hz), 2.02 (m, 6H, C*H*CH_3), 1.02 (br, 18H, CHC*H*$_3$), 0.78 (br, 18H, CHC*H*$_3$). $^{13}C\{^1H\}$ NMR (125.58 MHz; CDCl3): δ 155.68 (t, $J_{C\text{-}P}$ =14.21 Hz), 143.59 (d, $J_{C\text{-}P}$ = 10.40 Hz), 137.70 (d, $J_{C\text{-}P}$ = 14.52 Hz), 131.54 (s), 128.67 (s), 127.10 (s), 24.74 (br), 20.28 (d, $J_{C\text{-}P}$ = 11.97 Hz), 19.59 (br). $^{31}P\{^1H\}$ NMR (161.73 MHz; $CDCl_3$): δ 8.26 (s). Elemental analysis calculated (%) for $C_{36}H_{54}P_3Sb$: C, 61.64; H, 7.76. Found: C, 61.17; H, 7.80.

Synthesis of (*o*-(*i*Pr_2P)C_6H_4)$_3$Bi. *n*-BuLi (6.35 ml, 18.36 mmol, 2.89 M in hexane) was added into the solution of *o*-(*i*Pr_2P)C_6H_4Br (4.18 g, 15.30 mmol) in Et_2O (20 mL) at room temperature. The reaction was allowed to stir for 30 min before adding solution of $BiCl_3$ (1.61g, 5.10 mmol) in THF (10 mL). The resulting mixture was stirred overnight at room temperature. The solvent was removed in vacuo, and the resulting solid was extracted with dichloromethane (20 mL) and filtered through Celite to remove LiCl. The filtrate was evaporated to dryness, and the residue was recrystallized from MeOH to afford (*o*-(*i*Pr_2P)C_6H_4)$_3$Bi as a white powder (2.33 g, 58% yield). ^1H NMR (499.43 MHz; $CDCl_3$): δ 7.57 (d, 3H, *o*-P(Bi)C_6H_4, $^3J_{H\text{-}H}$ = 7.85 Hz), 7.49 (d, 3H, *o*-P(Bi)C_6H_4, $^3J_{H\text{-}H}$ = 7.85 Hz), 7.26 (pseudo-t, 3H, *m*-P(Bi)C_6H_4, $^3J_{H\text{-}H}$ = 7.85 Hz), 7.11 (pseudo-t, 3H, *m*-P(Bi)C_6H_4, $^3J_{H\text{-}H}$ = 7.85 Hz), 2.07 (m, 6H, C*H*CH_3), 1.05 (dd, 18H, $^3J_{H\text{-}H}$ = 6.82 Hz, $^3J_{H\text{-}P}$ = 14.56 Hz, CHC*H*$_3$), 0.81 (dd, 18H, $^3J_{H\text{-}H}$ = 6.82 Hz, $^3J_{H\text{-}P}$ = 14.56 Hz, CHC*H*$_3$). $^{13}C\{^1H\}$ NMR (125.58 MHz; $CDCl_3$): δ 176.66 (s), 143.92 (d, $J_{C\text{-}P}$ = 7.24 Hz), 139.75 (d, $J_{C\text{-}P}$ = 15.78 Hz), 132.92 (s), 131.54 (s), 131.19 (s), 126.35 (s), 24.47 (d, $J_{C\text{-}P}$

= 13.75 Hz, $C(CH_3)_2$), 20.39 (d, $J_{C\text{-}P}$ = 17.67 Hz, $CH_{3i\text{-}Pr}$), 19.47 (d, $J_{C\text{-}P}$ = 9.73 Hz, $CH_{3i\text{-}Pr}$). $^{31}P\{^1H\}$ NMR (202.16 MHz; $CDCl_3$): δ 8.68 (s). Elemental analysis calculated (%) for $C_{36}H_{54}P_3Bi$: C, 54.82; H, 6.90. Found: C, 54.52; H, 7.00.

Coproportionation of (*o*-(*i*Pr$_2$P)C$_6$H$_4$)$_3$Sb with SbCl$_3$: generation (*o*-(*i*Pr$_2$P)C$_6$H$_4$)$_2$SbCl. In the absence of solvent, a 2/1 molar mixture of (*o*-(*i*Pr$_2$P)C$_6$H$_4$)$_3$Sb and $SbCl_3$ rapidly liquefies at 90°C and the redistribution is complete in 3 hrs. The resulting (*i*Pr$_2$P)C$_6$H$_4$)$_2$SbCl is a pale-yellow viscous oil, which usually solidifies on standing at 0°C.[177,178] The coproportionation product was used without further purification. ^{31}P NMR showed 3 peaks corresponding to the (*i*Pr$_2$P)C$_6$H$_4$)$_3$Sb (8.26 ppm), (*i*Pr$_2$P)C$_6$H$_4$)$_2$SbCl (5.70 ppm, major peak) and (*i*Pr$_2$P)C$_6$H$_4$)$SbCl_2$ (0.25 ppm). (**Figure 77**)

Synthesis of 26. To a suspension of [(tht)AuCl] (27.4 mg, 0.086 mmol) in THF (2 mL) was added a solution of (*o*-(*i*Pr$_2$P)C$_6$H$_4$)$_2$PhSb (50 mg, 0.086 mmol) in THF (2 mL) at room temperature. After subsequent stirring for 10 minutes, volatiles were removed and the residue was washed with pentane (10 mL). Removal of the residual solvent afforded **26** (55 mg, 79% yield) as a white powder. X-ray quality crystals were obtained by slow diffusion of pentane into a solution of the compound in THF. ^1H NMR (499.43 MHz; $CDCl_3$): δ 7.92 (d, 2H, *o*-P(Sb)C$_6$H$_4$, $^3J_{H\text{-}H}$ = 7.50 Hz), 7.48 (br, 2H, *o*-P(Sb)C$_6$H$_4$), 7.37 (pseudo-t, 4H, *o*-P(Sb)C$_6$H$_4$, $^3J_{H\text{-}H}$ = 7.50 Hz), 7.30 (m, 5H, SbPh-C*H*), 2.84 (m, 4H, C*H*CH$_3$), 1.50 (dd, 6H, $^3J_{H\text{-}H}$ = 7.50 Hz, $^3J_{H\text{-}P}$ = 19.50 Hz, CHC*H*$_3$), 1.42 (dd, 6H, $^3J_{H\text{-}H}$ = 7.50 Hz, $^3J_{H\text{-}P}$ = 19.50 Hz, CHC*H*$_3$), 1.24 (dd, 6H, $^3J_{H\text{-}H}$ = 7.20 Hz, $^3J_{H\text{-}P}$ = 15.0 Hz, CHC*H*$_3$), 0.91 (dd, 6H, $^3J_{H\text{-}H}$ = 7.20 Hz, $^3J_{H\text{-}P}$ = 19.50 Hz, CHC*H*$_3$). $^{13}C\{^1H\}$

NMR (125.58 MHz; $CDCl_3$): δ 150.34 (t, $J_{C\text{-}P}$ = 16.32 Hz), 145.34 (t, $J_{C\text{-}P}$ = 11.90 Hz), 137.06 (t, $J_{C\text{-}P}$ = 6.81 Hz), 136.01 (s), 135.26 (t, $J_{C\text{-}P}$ = 21.31 Hz), 131.97 (br), 131.02 (s), 129.05 (s), 128.67 (t, $J_{C\text{-}P}$ = 3.12 Hz), 128.10 (s), 26.04 (pseudo-t, $J_{C\text{-}P}$ = 15.12 Hz, $C(CH_3)_2$), 24.13 (pseudo-t, $J_{C\text{-}P}$ = 12.65 Hz, $C(CH_3)_2$), 20.53 (s, $CH_{3i\text{-}Pr}$), 19.61 (s, $CH_{3i\text{-}Pr}$), 19.53 (s, $CH_{3i\text{-}Pr}$), 16.68 (s, $CH_{3i\text{-}Pr}$). $^{31}P\{^1H\}$ NMR (202.17 MHz; $CDCl_3$): δ 69.18. Elemental analysis calculated (%) for $C_{30}H_{41}AuClP_2Sb$: C, 44.06; H, 5.05. Found: C, 43.47; H, 5.15.

Synthesis of 27. (*o*-(*i*Pr_2P)$C_6H_4)_2SbCl$ (232.5 mg, 0.43 mmol) was prepared by stirring (*o*-(*i*Pr_2P)$C_6H_4)_3Sb$ (200.0 mg, 0.29 mmol) and $SbCl_3$ (32.5 mg, 0.14 mmol) for 3 h at 90°C under neat conditions. Then, the a suspension of [(tht)AuCl] (137.8 mg, 0.43 mmol) in THF (5 mL) was slowly added a solution of (*o*-(*i*Pr_2P)$C_6H_4)_2SbCl$ in THF (15 mL) at room temperature. After subsequent stirring for 30 minutes, volatiles were removed and the residue was washed with pentane (10 mL). Removal of the residual solvent afforded **27** (183.5 mg, 55% yield) as a yellow powder. X-ray quality crystals were obtained by slow diffusion of Et_2O into a solution of the compound in CH_2Cl_2. ^1H NMR (399.59 MHz; $CDCl_3$): δ 8.53 (d, 2H, *o*-P(Sb)C_6H_4, $^3J_{H\text{-}H}$ = 7.65 Hz), 7.61 (m, 2H, *m*-P(Sb)C_6H_4), 7.41 (br, 4H, *o*-P(Sb)C_6H_4 + *m*-P(Sb)C_6H_4), 3.05 (m, 2H, C*H*CH_3), 2.90 (m, 2H, C*H*CH_3), 1.59 (dd, 6H, $^3J_{H\text{-}H}$ = 8.25 Hz, $^3J_{H\text{-}P}$ = 18.55 Hz, CHC*H*$_3$), 1.37 (dd, 6H, $^3J_{H\text{-}H}$ = 8.25 Hz, $^3J_{H\text{-}P}$ = 18.55 Hz, CHC*H*$_3$), 1.27 (dd, 6H, $^3J_{H\text{-}H}$ = 8.25 Hz, $^3J_{H\text{-}P}$ = 18.55 Hz, CHC*H*$_3$), 0.94 (dd, 6H, $^3J_{H\text{-}H}$ = 8.25 Hz, $^3J_{H\text{-}P}$ = 18.55 Hz, CHC*H*$_3$). $^{13}C\{^1H\}$ NMR (125.58 MHz; $CDCl_3$): δ 152.69 (t, $J_{C\text{-}P}$ = 18.09 Hz), 135.49 (t, $J_{C\text{-}P}$ = 8.25 Hz), 133.33 (t, $J_{C\text{-}P}$ = 24.74 Hz), 132.46 (s), 131.91 (s), 128.89 (s), 26.21 (pseudo-t, $J_{C\text{-}P}$ = 14.11 Hz,

$C(CH_3)_2$), 25.29 (pseudo-t, $J_{C\text{-}P}$ = 14.11 Hz, $C(CH_3)_2$), 20.17 (s, $CH_{3i\text{-}Pr}$), 19.37 (s, $CH_{3i\text{-}Pr}$), 18.56 (s, $CH_{3i\text{-}Pr}$), 16.81 (s, $CH_{3i\text{-}Pr}$). $^{31}P\{^1H\}$ NMR (161.73 MHz; $CDCl_3$): δ 64.18. Elemental analysis calculated (%) for $C_{24}H_{36}AuCl_2P_2Sb$: C, 37.14; H, 4.68. Found: C, 37.08; H, 4.65.

Synthesis of 28. A THF solution (3 mL) of [(tht)AuCl] (56.0 mg, 0.16 mmol) was added dropwise to a THF solution (2 mL) of (*o*-(*i*Pr_2P)C_6H_4)$_3$Bi (70.0 mg, 0.08 mmol) at ambient temperature. The resulting mixture was allowed to stir for 12 hours. The solvent was then removed under reduced pressure to give a light yellow solid, which was washed with pentane (3 x 5 mL) to remove the [{*o*-(*i*Pr_2P)C_6H_4Au}$_2$] dimer complex. The resulting residue was drying under reduced pressure to afford light yellow solid (46.1 mg, 61% yield). Fractional crystallization from CH_2Cl_2/Et_2O afforded yellow crystals of **28**. ^1H NMR (499.43 MHz; $CDCl_3$): δ 9.18 (d, 2H, *o*-P(Bi)C_6H_4, $^3J_{H\text{-}H}$ = 7.31 Hz), 7.88 (pseudo-t, 2H, *m*-P(Bi)C_6H_4, $^3J_{H\text{-}H}$ = 7.83 Hz), 7.57 (br, 2H, *m*-P(Bi)C_6H_4), 7.53 (pseudo-t, 2H, *m*-P(Bi)C_6H_4, $^3J_{H\text{-}H}$ = 7.83 Hz), 3.15 (m, 2H, C*H*CH_3), 2.91 (m, 2H, C*H*CH_3), 1.60 (dd, 6H, $^3J_{H\text{-}H}$ = 7.80 Hz, $^3J_{H\text{-}P}$ = 19.80 Hz, CHC*H*$_3$), 1.33 (dd, 6H, $^3J_{H\text{-}H}$ = 7.80 Hz, $^3J_{H\text{-}P}$ = 19.80 Hz, CHC*H*$_3$), 1.25 (dd, 6H, $^3J_{H\text{-}H}$ = 7.80 Hz, $^3J_{H\text{-}P}$ = 19.80 Hz, CHC*H*$_3$), 1.03 (dd, 6H, $^3J_{H\text{-}H}$ = 7.80 Hz, $^3J_{H\text{-}P}$ = 19.80 Hz, CHC*H*$_3$). $^{13}C\{^1H\}$ NMR (125.58 MHz; $CDCl_3$): δ 179.59 (t, $J_{C\text{-}P}$ = 17.46 Hz), 138.09 (t, $J_{C\text{-}P}$ = 8.68 Hz), 137.23 (t, $J_{C\text{-}P}$ = 24.39 Hz), 136.05 (s), 135.52 (s), 127.93 (s), 26.15 (pseudo-t, $J_{C\text{-}P}$ = 14.23 Hz, $C(CH_3)_2$), 25.33 (pseudo-t, $J_{C\text{-}P}$ = 14.23 Hz, $C(CH_3)_2$), 20.66 (s, $CH_{3i\text{-}Pr}$), 19.54 (s, $CH_{3i\text{-}Pr}$), 18.78 (s, $CH_{3i\text{-}Pr}$), 17.01 (s, $CH_{3i\text{-}Pr}$). $^{31}P\{^1H\}$ NMR (202.16 MHz; $CDCl_3$): δ 57.05.

Elemental analysis calculated (%) for $C_{24}H_{36}AuCl_2P_2Bi$ + Et_2O: C, 35.87; H, 4.95. Found: C, 35.93; H, 4.58 (approx.. 1 equiv of ether was lost in drying).

Synthesis of 30. A solution of *o*-chloranil (12.0 mg, 0.049 mmol) in CH_2Cl_2 (1 mL) was added dropwise to a solution of **26** (40.0 mg, 0.049 mmol) in CH_2Cl_2 (5 mL) at ambient temperature. The reaction was stirred for 10 min. before removing the solvent in vacuo. The resulting yellow solid was washed with pentane (2 x 3 mL) and dried in vacuo to afford 42.1 mg (81 %) of **30** as an orange powder. Single crystals of **30** suitable for X-ray diffraction were obtained by vapor diffusion of pentane into a solution of the compound in THF. ^{1}H NMR (499.43 MHz; $CDCl_3$): δ 8.34 (d, 2H, *o*-P(Sb)C_6H_4, $^3J_{H\text{-}H}$ = 8.00 Hz), 7.75 (d, 2H, *o*-P(Sb)C_6H_4, $^3J_{H\text{-}H}$ = 8.00 Hz), 7.56 (t, 2H, *m*-P(Sb)C_6H_4, $^3J_{H\text{-}H}$ = 8.00 Hz), 7.47 (t, 2H, *m*-P(Sb)C_6H_4, $^3J_{H\text{-}H}$ = 8.00 Hz), 7.11 (t, 1H, *p*-SbPhC*H*, $^3J_{H\text{-}H}$ = 7.50 Hz), 7.01 (t, 2H, *o*-SbPhC*H* or *m*-SbPhC*H*, $^3J_{H\text{-}H}$ = 7.50 Hz), 6.87 (d, 2H, *o*-SbPhC*H* or *m*-SbPhC*H*, $^3J_{H\text{-}H}$ = 7.50 Hz), 3.41 (m, 4H, C*H*CH_3), 1.41 (dd, 6H, $^3J_{H\text{-}H}$ = 7.50 Hz, $^3J_{H\text{-}P}$ = 19.00 Hz, CHC*H*$_3$), 1.31 (dd, 6H, $^3J_{H\text{-}H}$ = 7.50 Hz, $^3J_{H\text{-}P}$ = 17.50 Hz, CHC*H*$_3$), 1.19 (dd, 6H, $^3J_{H\text{-}H}$ = 7.50 Hz, $^3J_{H\text{-}P}$ = 19.00 Hz, CHC*H*$_3$), 1.12 (dd, 6H, $^3J_{H\text{-}H}$ = 7.50 Hz, $^3J_{H\text{-}P}$ = 17.50 Hz, CHC*H*$_3$). ^{13}C{^{1}H} NMR (125.58 MHz; $CDCl_3$): δ 167.69 (t, $J_{C\text{-}P}$ = 28.88 Hz), 151.03 (s), 149.08 (s), 146.43 (s), 135.53 (t, $J_{C\text{-}P}$ = 10.93 Hz), 133.92 (s), 133.23 (s), 131.54 (t, $J_{C\text{-}P}$ = 5.78 Hz), 129.31 (s), 129.09 (t, $J_{C\text{-}P}$ = 3.52 Hz), 128.13 (s), 120.19 (s), 119.96 (s, $O_2C_6Cl_4$), 119.73 (s, $O_2C_6Cl_4$), 119.53 (s, $O_2C_6Cl_4$), 117.75 (s, $O_2C_6Cl_4$), 117.03 (s, $O_2C_6Cl_4$), 116.43 (s, $O_2C_6Cl_4$), 28.93 (pseudo-t, $J_{C\text{-}P}$ = 13.81 Hz), 27.39 (pseudo-t, $J_{C\text{-}P}$ = 13.81 Hz), 19.34 (s), 19.19 (s), 18.99 (s), 18.70 (s). ^{31}P{^{1}H}

NMR (202.17 MHz; $CDCl_3$): δ 103.26. Elemental analysis calculated (%) for $C_{36}H_{41}AuCl_5O_2P_2Sb$: C, 40.65; H, 3.89. Found: C, 39.04; H, 3.81.

Synthesis of 31. A solution of *o*-chloranil (15.8 mg, 0.064 mmol) in CH_2Cl_2 (1 mL) was added dropwise to a solution of **27** (50.0 mg, 0.064 mmol) in CH_2Cl_2 (5 mL) at ambient temperature. The reaction was stirred for 10 min. before removing the solvent in vacuo. The resulting yellow solid was washed with pentane (2 x 3 mL) and dried in vacuo to afford 57.5 mg (88 %) of **31** as an orange powder. ^{1}H NMR (499.43 MHz; $CDCl_3$): δ 8.69 (d, 2H, *o*-P(Sb)C_6H_4, $^3J_{H\text{-}H}$ = 8.20 Hz), 7.72 (m, 4H), 7.52 (t, 2H, *m*-P(Sb)C_6H_4, $^3J_{H\text{-}H}$ = 8.20 Hz), 3.44 (m, 4H, C*H*CH_3), 1.42 (m, 12H, CHC*H*$_3$), 1.35 (dd, 6H, $^3J_{H\text{-}H}$ = 8.36 Hz, $^3J_{H\text{-}P}$ = 19.03 Hz, CHC*H*$_3$), 1.25 (dd, 6H, $^3J_{H\text{-}H}$ = 8.36 Hz, $^3J_{H\text{-}P}$ = 19.03 Hz, CHC*H*$_3$). ^{13}C{^{1}H} NMR (125.58 MHz; $CDCl_3$): δ 147.18 (s), 146.71 (s), 134.89 (s), 134.16 (t, $J_{C\text{-}P}$ = 10.34 Hz), 130.50 (t, $J_{C\text{-}P}$ = 5.48 Hz), 130.22 (s), 119.83 (s, $O_2C_6Cl_4$), 119.64 (s, $O_2C_6Cl_4$), 118.40 (s, $O_2C_6Cl_4$), 117.13 (s, $O_2C_6Cl_4$), 115.13 (s, $O_2C_6Cl_4$), 114.88 (s, $O_2C_6Cl_4$), 28.77 (pseudo-t, $J_{C\text{-}P}$ = 15.10 Hz, *C*$(CH_3)_2$), 27.95 (pseudo-t, $J_{C\text{-}P}$ = 13.55 Hz, *C*$(CH_3)_2$), 19.09 (s, $CH_{3i\text{-}Pr}$), 19.02 (s, $CH_{3i\text{-}Pr}$), 18.96 (s, $CH_{3i\text{-}Pr}$), 18.65 (s, $CH_{3i\text{-}Pr}$). ^{31}P{^{1}H} NMR (202.17 MHz; $CDCl_3$): δ 108.63. Elemental analysis calculated (%) for $C_{30}H_{36}AuCl_6O_2P_2Sb$ + 0.6 THF: C, 36.53; H, 3.86. Found: C, 36.69; H, 3.92 (approx. 0.6 equiv of THF was lost in drying, **Figure 75**).

Synthesis of 32. To a suspension of CuCl (8.5 mg, 0.086 mmol) in THF (2 mL) was added a solution of (*o*-(*i*Pr$_2$P)C_6H_4)$_2$PhSb (50 mg, 0.086 mmol) in THF (2 mL) at room temperature. The solution turned yellow immediately. After subsequent stirring for 10 minutes, volatiles were removed and the residue was washed with pentane (10 mL).

Removal of the residual solvent afforded **32** (49 mg, 84% yield) as a yellow powder. X-ray quality crystals were obtained by slow diffusion of pentane into a solution of the compound in THF. ^{1}H NMR (399.59 MHz, $CDCl_3$): δ 7.71 (d, 2H, *o*-P(Sb)C_6H_4, $^{3}J_{H\text{-}H}$ = 7.20 Hz), 7.43 (m, 2H, SbPh-C*H*), 7.38-7.31 (m, 9H, *o*-P(Sb)C_6H_4 + PPh-C*H*), 2.60 (m, 4H, C*H*CH_3), 1.36 (pentet, 12H, $^{3}J_{H\text{-}H}$ = 7.6 Hz, CHC*H*$_3$), 1.13 (dd, 6H, $^{3}J_{H\text{-}H}$ = 6.8 Hz, $^{3}J_{H\text{-}P}$ = 14.4 Hz, CHC*H*$_3$), 0.91 (dd, 6H, $^{3}J_{H\text{-}H}$ = 7.2 Hz, $^{3}J_{H\text{-}P}$ = 16.8 Hz, CHC*H*$_3$). ^{13}C{^{1}H} NMR (125.58 MHz, $CDCl_3$): δ 150.0 (pseudo-t, *J*(C,P)=20.1 Hz), 139.1 (pseudo-t, *J*(C,P)=20.1 Hz), 137.2 (pseudo-t, *J*(C,P)=13.8 Hz), 136.1 (s), 135.8 (pseudo-t, *J*(C,P)=6.9 Hz), 131.8 (s), 130.6 (s), 129.1 (s), 128.6 (s), 25.4 (pseudo-t, *J*(C,P)=10.8 Hz), 22.2 (pseudo-t, *J*(C,P)=6.8 Hz), 20.2 (s; $CH_{3i\text{-}Pr}$), 19.6 (pseudo-t, *J*(C,P)=3.0 Hz), 19.5 (pseudo-t, *J*(C,P)=6.2 Hz), 16.5 (s; $CH_{3i\text{-}Pr}$), (1 *ipso*-C signal not observed). ^{31}P{^{1}H} NMR (161.73 MHz; $CDCl_3$): δ 31.52 (s). Elemental analysis calculated (%) for $C_{30}H_{41}ClCuP_2Sb$: C, 52.65; H, 6.04. Found: C, 52.39; H, 6.13. HRMS (ESI^+) calcd for $C_{30}H_{41}CuP_2Sb$: 647.1018, found: 647.1016.

Synthesis of 33. To a suspension of AgCl (12.2 mg, 0.086 mmol) in THF (2 mL) was added a solution of (*o*-(*i*Pr_2P)C_6H_4)$_2$PhSb (50 mg, 0.086 mmol) in THF (2 mL) at room temperature. After subsequent stirring for 10 minutes, volatiles were removed and the residue was washed with pentane (10 mL). Removal of the residual solvent afforded **33** (55 mg, 89% yield) as a white powder. X-ray quality crystals were obtained by slow diffusion of Et_2O into a solution of the compound in $CHCl_3$. ^{1}H NMR (499.43 MHz, $CDCl_3$): δ 7.70 (d, 2H, *o*-P(Sb)C_6H_4, $^{3}J_{H\text{-}H}$ = 7.50 Hz), 7.47 (d, 2H, *o*-P(Sb)C_6H_4, $^{3}J_{H\text{-}H}$ = 7.50 Hz), 7.37 (pseudo-t, 2H, *o*-P(Sb)C_6H_4, $^{3}J_{H\text{-}H}$ = 7.50 Hz), 7.43 (m, 2H, SbPh-C*H*),

7.33-7.30 (m, 7H, *o*-P(Sb)C_6H_4 + PPh-C*H*), 2.53 (m, 4H, C*H*CH_3), 1.39 (dd, 6H, $^3J_{H\text{-}H}$ = 7.0 Hz, $^3J_{H\text{-}P}$ = 19.0 Hz, CHC*H*$_3$), 1.30 (dd, 6H, $^3J_{H\text{-}H}$ = 7.0 Hz, $^3J_{H\text{-}P}$ = 19.5 Hz, CHC*H*$_3$), 1.17 (dd, 6H, $^3J_{H\text{-}H}$ = 6.5 Hz, $^3J_{H\text{-}P}$ = 15.0 Hz, CHC*H*$_3$), 0.84 (dd, 6H, $^3J_{H\text{-}H}$ = 7.0 Hz, $^3J_{H\text{-}P}$ = 19.0 Hz, CHC*H*$_3$). $^{31}P\{^1H\}$ NMR (202.17 MHz; $CDCl_3$): δ 35.93 ($^1J(^{107}Ag, P)$ = 368 Hz, $^1J(^{109}Ag, P)$ = 425 Hz); $^{13}C\{^1H\}$ NMR (125.58 MHz, $CDCl_3$): δ 149.8 (pseudo-t, *J*(C,P)=20.1 Hz), 139.9 (br), 137.5 (br), 136.9 (pseudo-t, *J*(C,P)=6.0 Hz), 136.2 (s), 131.9 (s), 130.7 (s), 129.1 (s), 128.7 (s), 128.6 (s), 26.6 (pseudo-t, *J*(C,P)=7.3 Hz), 23.0 (br), 20.3 (pseudo-t, *J*(C,P)=3.8 Hz), 20.0 (s; $CH_{3i\text{-}Pr}$), 19.9 (pseudo-t, *J*(C,P)=5.7 Hz), 17.9 (s; $CH_{3i\text{-}Pr}$). Elemental analysis calculated (%) for $C_{30}H_{41}ClAgP_2Sb$: C, 49.45; H, 5.67. Found: C, 49.27; H, 5.56. HRMS (ESI^+) calcd for $C_{30}H_{41}AgP_2Sb$: 693.0775, found: 693.0788.

Synthesis of 34. A solution of *o*-chloranil (14.4 mg, 0.058 mmol) in CH_2Cl_2 (1 mL) was added dropwise to a solution of **32** (40.0 mg, 0.058 mmol) in CH_2Cl_2 (5 mL) at ambient temperature. The reaction was stirred for 10 min. before removing the solvent in vacuo. The resulting yellow solid was washed with pentane (2 x 3 mL) and dried in vacuo to afford 46.8 mg (86 %) of **34** as an orange powder. Single crystals of **34** suitable for X-ray diffraction were obtained by vapor diffusion of pentane into a solution of the compound in THF. ^1H NMR (499.43 MHz, $CDCl_3$): δ 7.74 (d, 2H, *o*-P(Sb)C_6H_4, $^3J_{H\text{-}H}$ = 7.50 Hz), 7.62 (t, 2H, *m*-P(Sb)C_6H_4, $^3J_{H\text{-}H}$ = 7.50 Hz), 7.55 (t, 2H, *m*-P(Sb)C_6H_4, $^3J_{H\text{-}H}$ = 7.50 Hz), 7.50 (d, 2H, *o*-P(Sb)C_6H_4, $^3J_{H\text{-}H}$ = 7.50 Hz), 7.44 (t, 2H, *o*-SbPhC*H*, $^3J_{H\text{-}H}$ = 7.50 Hz), 7.35 (m, 3H, SbPh-C*H* and *p*-SbPhC*H*), 3.36 (br, 2H, C*H*CH_3), 2.76 (br, 2H, C*H*CH_3), 1.57 (dd, 6H, $^3J_{H\text{-}H}$ = 7.00 Hz, $^3J_{H\text{-}P}$ = 17.00 Hz, CHC*H*$_3$), 1.51 (dd, 6H, $^3J_{H\text{-}H}$ =

7.00 Hz, $^{3}J_{H\text{-}P}$ = 17.00 Hz, CHCH_3), 1.36 (dd, 6H, $^{3}J_{H\text{-}H}$ = 7.0 Hz, $^{3}J_{H\text{-}P}$ = 16.00 Hz, CHCH_3), 0.92 (dd, 6H, $^{3}J_{H\text{-}H}$ = 7.00 Hz, $^{3}J_{H\text{-}P}$ = 18.00 Hz, CHCH_3). $^{31}P\{^{1}H\}$ NMR (202.17 MHz; $CDCl_3$): δ 45.68. $^{13}C\{^{1}H\}$ NMR (125.58 MHz, $CDCl_3$): δ 156.50 (pseudo-t, *J*(C,P)=23.92 Hz), 144.08 (s), 135.22 (br), 133.81 (s), 133.70 (s), 133.05 (br), 131.82 (s), 131.01 (s), 130.59 (s), 130.10 (s), 128.81 (s), 120.47 (s, $O_2C_6Cl_4$), 116.55 (s, $O_2C_6Cl_4$), 28.96 (pseudo-t, *J*(C,P)=10.71 Hz), 26.13 (br), 21.54 (s), 20.82 (s), 19.94 (s), 17.47 (s). Elemental analysis calculated (%) for $C_{30}H_{41}ClCuP_2Sb$ + THF: C, 47.93; H, 4.93. Found: C, 47.91; H, 5.09.

Synthesis of 35. A solution of *o*-chloranil (13.5 mg, 0.055 mmol) in CH_2Cl_2 (1 mL) was added dropwise to a solution of **33** (40.0 mg, 0.055 mmol) in CH_2Cl_2 (5 mL) at ambient temperature. The reaction was stirred for 10 min. before removing the solvent in vacuo. The resulting yellow solid was washed with pentane (2 x 3 mL) and dried in vacuo to afford 39 mg (73 %) of **35** as an orange powder. Single crystals of **35** suitable for X-ray diffraction were obtained by vapor diffusion of pentane into a solution of the compound in THF. ^{1}H NMR (499.43 MHz, $CDCl_3$): δ 7.78 (d, 2H, *o*-P(Sb)C_6H_4, $^{3}J_{H\text{-}H}$ = 8.50 Hz), 7.68 (d, 2H, *o*-P(Sb)C_6H_4, $^{3}J_{H\text{-}H}$ = 7.00 Hz), 7.58 (t, 2H, *m*-P(Sb)C_6H_4, $^{3}J_{H\text{-}H}$ = 7.00 Hz), 7.48 (m, 4H, SbPh-C*H*), 7.39 (t, 1H, *p*-SbPhC*H*, $^{3}J_{H\text{-}H}$ = 6.50 Hz), 7.31 (t, 2H, *m*-P(Sb)C_6H_4, $^{3}J_{H\text{-}H}$ = 7.00 Hz), 3.28 (br, 2H, C*H*CH_3), 2.86 (br, 2H, C*H*CH_3), 1.65 (dd, 6H, $^{3}J_{H\text{-}H}$ = 7.00 Hz, $^{3}J_{H\text{-}P}$ = 17.00 Hz, CHCH_3), 1.59 (dd, 6H, $^{3}J_{H\text{-}H}$ = 8.50 Hz, $^{3}J_{H\text{-}P}$ = 21.50 Hz, CHCH_3), 1.38 (dd, 6H, $^{3}J_{H\text{-}H}$ = 7.0 Hz, $^{3}J_{H\text{-}P}$ = 14.5 Hz, CHCH_3), 0.90 (dd, 6H, $^{3}J_{H\text{-}H}$ = 7.5 Hz, $^{3}J_{H\text{-}P}$ = 18.5 Hz, CHCH_3). $^{31}P\{^{1}H\}$ NMR (202.17 MHz; $CDCl_3$): δ 59.76 ($^{1}J(^{107}Ag, P)$ = 385 Hz, $^{1}J(^{109}Ag, P)$ = 444 Hz). $^{13}C\{^{1}H\}$ NMR (125.58 MHz, $CDCl_3$): δ

156.7 (pseudo-t, *J*(C,P)=27.6 Hz), 143.9 (s), 136.2 (br), 135.2 (s), 135.1 (s), 134.6 (pseudo-t, *J*(C,P)=8.8 Hz), 133.6 (s), 131.3 (s), 130.8 (s), 130.4 (s), 129.0 (s), 121.0 (s, $O_2C_6Cl_4$), 116.6 (s, $O_2C_6Cl_4$), 29.7 (pseudo-t, *J*(C,P)=7.7 Hz), 24.3 (br), 23.0 (s), 21.0 (s), 19.8 (s), 16.3 (s). Elemental analysis calculated (%) for $C_{36}H_{41}AgCl_5O_2P_2Sb$: C, 44.37; H, 4.24. Found: C, 44.08; H, 4.28.

Crystallography. All crystallographic measurements were performed at 110(2) K using a Bruker SMART APEX II diffractometer with a CCD area detector (graphite monochromated Mo K_α radiation, λ = 0.71073 Å) at 110 K. In each case, a specimen of suitable size and quality was selected and mounted onto a nylon loop. The semi-empirical method SADABS was applied for absorption correction. The structures were solved by direct methods and refined by the full-matrix least-square technique against F^2 with the anisotropic temperature parameters for all non-hydrogen atoms. All H atoms were geometrically placed and refined in riding model approximation. Data reduction and further calculations were performed using the Bruker SAINT+ and SHELXTL NT program packages.[78]

Theoretical calculations. Density functional theory (DFT) calculations (full geometry optimization) were carried out on **26**, **27**, **28**, **29**, **30** and **31** starting from the crystal structure geometries with Gaussian09[122] program (BP86[80,81] with 6-31g for H, C, O; Stuttgart relativistic small core (RSC) 1997 ECP for Au;[179] Stuttgart relativistic large core (RLC) 1997 ECP for P,[84] Cl, Sb,[124] Bi)[180]. Frequency calculations were also carried out on the optimized geometry, showing no imaginary frequencies. The optimized structures, which are in excellent agreement with the solid-state structures, were

subjected to a NBO analysis.[125] The resulting Natural Localized Molecular Orbitals (NLMOs) were visualized and plotted in Jimp 2 program.[126]

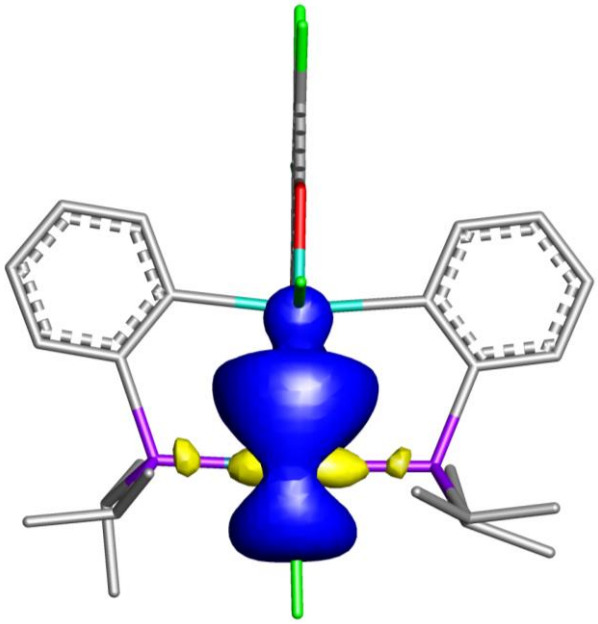

Figure 67. NLMO plot (isovalue = 0.03) of the Sb-Au bond in **31** obtained from NBO analysis. Hydrogen atoms are omitted for clarity.

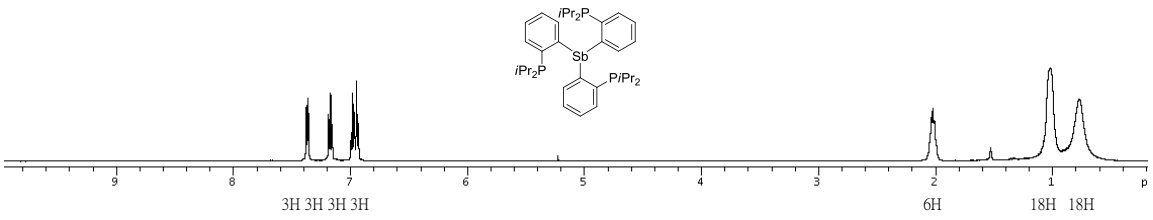

Figure 68. ^{1}H NMR spectrum of (*o*-(*i*Pr$_2$P)C$_6$H$_4$)$_2$SbPh in CDCl$_3$.

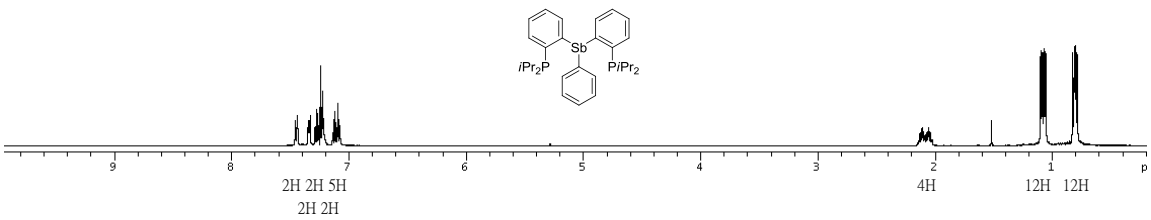

Figure 69. ^{1}H NMR spectrum of (*o*-(*i*Pr$_2$P)C$_6$H$_4$)$_3$Sb in CDCl$_3$.

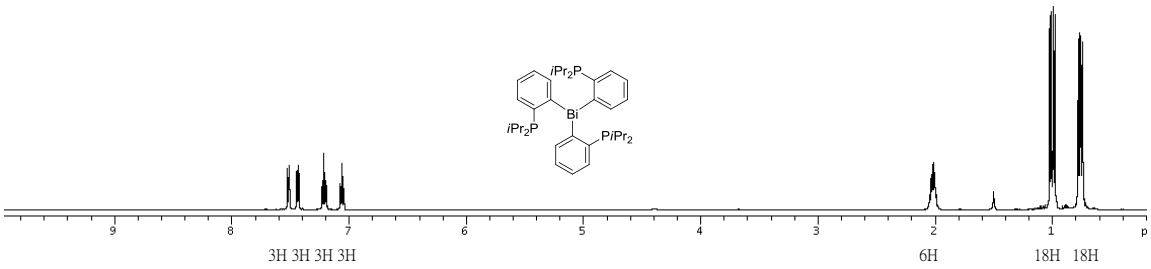

Figure 70. ^{1}H NMR spectrum of (*o*-(*i*Pr$_2$P)C$_6$H$_4$)$_3$Bi in CDCl$_3$.

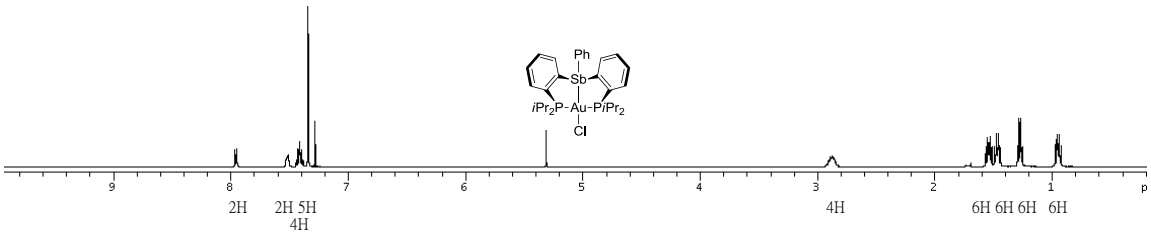

Figure 71. ^{1}H NMR spectrum of complex **26** in CDCl$_3$.

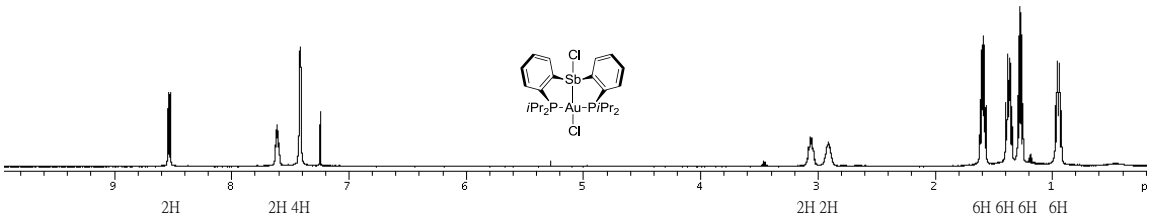

Figure 72. ^{1}H NMR spectrum of complex **27** in $CDCl_3$.

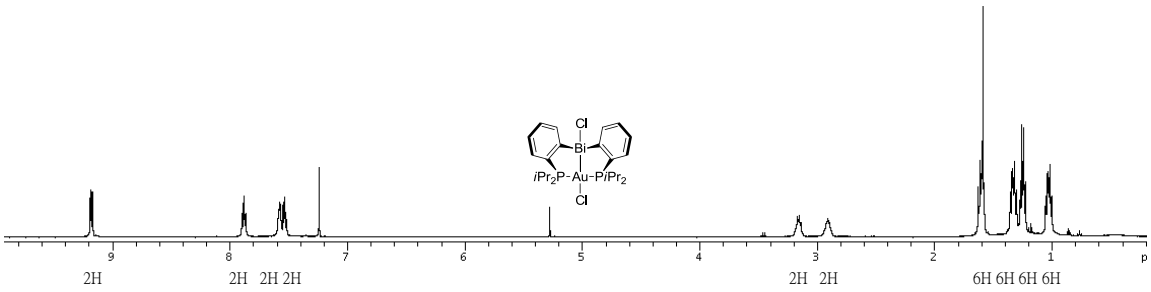

Figure 73. ^{1}H NMR spectrum of complex **28** in $CDCl_3$.

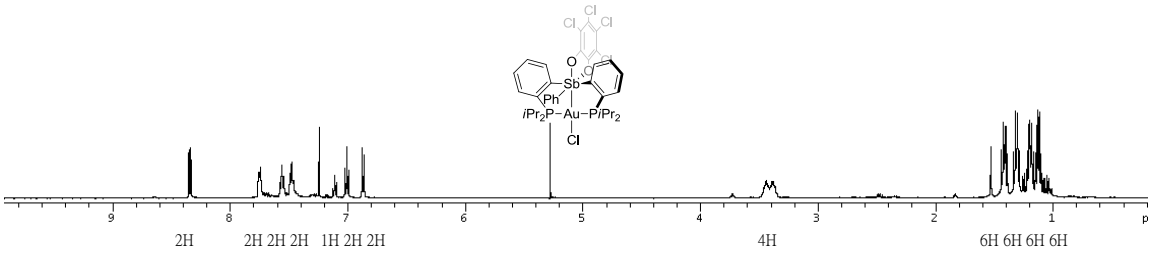

Figure 74. ^{1}H NMR spectrum of complex **30** in $CDCl_3$.

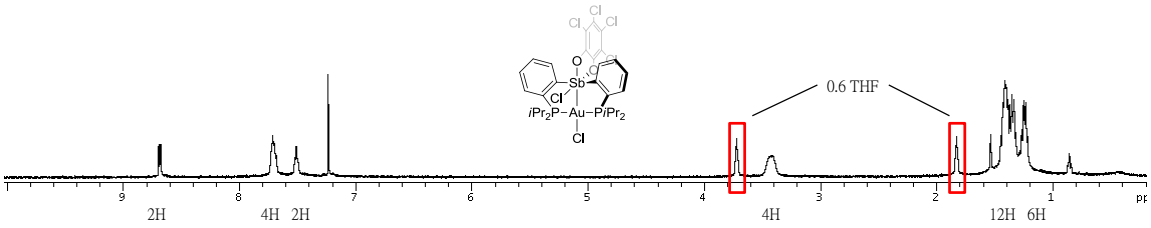

Figure 75. ^{1}H NMR spectrum of complex **31** in $CDCl_3$.

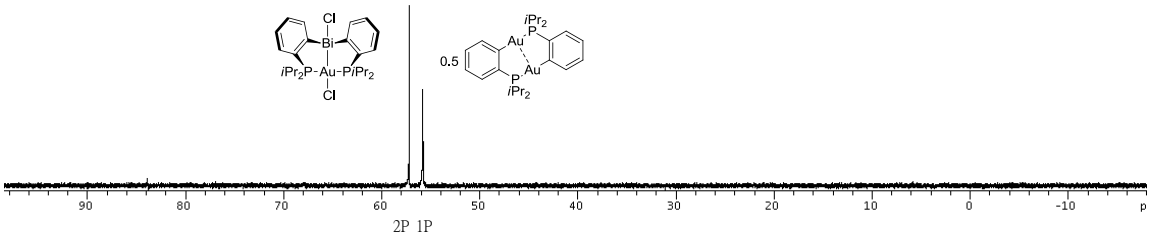

Figure 76. ^{31}P NMR spectrum of the mixture of [(tht)AuCl] and (*o*-(*i*Pr$_2$P)C$_6$H$_4$)$_3$Bi in $CDCl_3$.

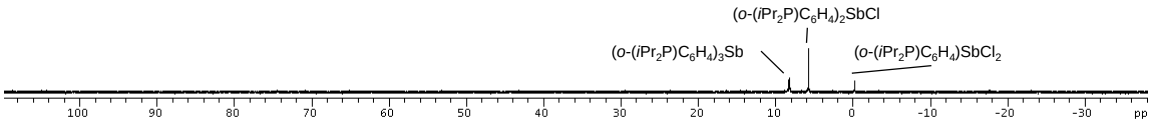

Figure 77. ^{31}P NMR spectrum of the co-proportionation of neat $SbCl_3$ and (*o*-(*i*Pr$_2$P)C$_6$H$_4$)$_3$Sb in $CDCl_3$.

Table 14. Crystal data, data collections, and structure refinements for **26** and **27**

Crystal data	**26**·THF	**27**
Formula	$C_{30}H_{41}OAuClP_2Sb$·THF	$C_{24}H_{36}AuCl_2P_2Sb$
Mr	889.89	776.08
Crystal size (mm^3)	0.30 x 0.18 x 0.14	0.24 x 0.21 x 0.15
Crystal system	Monoclinic	Triclinic
Space group	P2(1)/c	P2(1)/c
a (Å)	11.3055(19)	11.368(7)
b (Å)	14.066(2)	17.732(10)
c (Å)	22.146(4)	14.713(8)
α (°)	90	90
β (°)	98.752(2)	109.889(6)
γ (°)	90	90
V ($Å^3$)	4436(2)	2789(3)
Z	4	4
ρ_{calc} (g cm^{-3})	1.698	1.848
μ (mm^{-1})	5.180	6.539
F(000)	1752	1496
T/K	110(2)	110(2)
Scan mode	ω, φ	ω, φ
hkl Range	-15 → +15	-14 → +15
	-18 → +18	-23 → +23
	-29 → +29	-19 → +19
Measd reflns	42290	31196
Unique reflns [R_{int}]	8743 [0.0553]	6831 [0.0904]
Reflns used for refinement	8743	6831
Refined parameters	349	271
GooF	1.036	1.025
$R1$,[a] $wR2$[b] (all data)	0.0367, 0.0553	0.0428, 0.1007
ρ_{fin} (max/min.) ($eÅ^{-3}$)	0.951, -0.624	1.050, -1.643

[a] $R_1 = \Sigma||Fo| - |Fc||/\Sigma|Fo|$. [b] $wR_2 = [[\Sigma w(Fo^2 - Fc^2)^2]/[\Sigma w(Fo^2)^2]]^{1/2}$.

Table 15. Crystal data, data collections, and structure refinements for **28** and **30**

Crystal data	**28**	**30**
Formula	$C_{24}H_{36}AuBiCl_2P_2$	$C_{36}H_{41}AuCl_5O_2P_2Sb$
Mr	863.31	1063.59
Crystal size (mm^3)	0.21 x 0.16 x 0.15	0.41 x 0.33 x 0.20
Crystal system	Monoclinic	Rhombic
Space group	P2(1)/c	R -3
a (Å)	11.354(12)	36.851(3)
b (Å)	17.910(19)	36.851(3)
c (Å)	14.814(16)	15.665(3)
α (°)	90	90
β (°)	109.852(12)	90
γ (°)	90	120
V ($Å^3$)	2833(5)	18423(4)
Z	4	18
ρ_{calc} (g cm^{-3})	2.024	1.726
μ (mm^{-1})	11.685	4.674
F(000)	1624	9324
T/K	110(2)	110(2)
Scan mode	ω, φ	ω, φ
hkl Range	-14 → +14	-49 → +49
	-22 → +22	-49 → +49
	-18 → +18	-20 → +20
Measd reflns	29028	75780
Unique reflns [R_{int}]	5568 [0.0535]	10220 [0.0660]
Reflns used for refinement	5568	10220
Refined parameters	271	479
GooF	1.042	1.074
$R1$,[a] $wR2$[b] (all data)	0.0433, 0.0627	0.0479, 0.0905
ρ_{fin} (max/min.) ($eÅ^{-3}$)	0.554, -0.746	1.281, -0.884

[a] $R_1 = \Sigma||Fo| - |Fc||/\Sigma|Fo|$. [b] $wR_2 = [[\Sigma w(Fo^2 - Fc^2)^2]/[\Sigma w(Fo^2)^2]]^{1/2}$.

CHAPTER VII

A DIPHOSPHANYLSTIBINE GOLD COMPLEX: SYNTHESES, STRUCTURES, BONDING, AND REACTIVITY

7.1 Introduction

While a great number of gold(I)-phosphine and Au(I)-arsine adducts are known[181-183] Au(I)-stibine complexes constitute a rather limited family of compounds.[35,64,167,184-188] Although the first Sb-Au(I) complex, [PhC≡CAu($SbEt_3$)], was reported in 1962, the chemistry of gold(I)-stibine complexes has been developing very slowly.[189] A few years ago, the synthesis and crystal structure of the salts [Au($SbPh_3$)$_4$]X (X = [Au(C_6F_5)$_2$]$^{-}$[187] and ClO_4^{-}[167]) (Figure 78, **A**) was reported. Regardless of the nature of the counter anion, the [Au($SbPh_3$)$_4$]$^{+}$ cations show an almost tetrahedral coordination geometry about the gold center, with Sb-Au-Sb bond angles between 107.8^{o} and 111.0^{o} and Au-Sb bond lengths between 2.585(1) and 2.669(1) Å. More recently, the use of stibines with increasing bulk has been shown to afford salts with both linear ([Au($SbMes_nPh_{3-n}$)$_2$]ClO_4) and trigonal planar of ([Au($SbMesPh_2$)$_3$]ClO_4) stibine-Au(I) cations (Figure 78, **B**).[188] As part of our ongoing effort to develop the chemistry of metallated hypervalent antimony compounds, we recently synthesized a stiborane-Au complex (Figure 78, **C**) which was obtained by oxidation of the corresponding stibine-gold complex with $PhICl_2$.[35] Formation of such a complex, which is made possible by the use of pendent phosphine ligands, results in an unusual Au→Sb interaction in which the gold donates two of its d-electrons to the Lewis acidic stiborane. In a continuation of

these studies, we have now decided to target related structures in which the gold atom is formally a cationic center.(**D**).

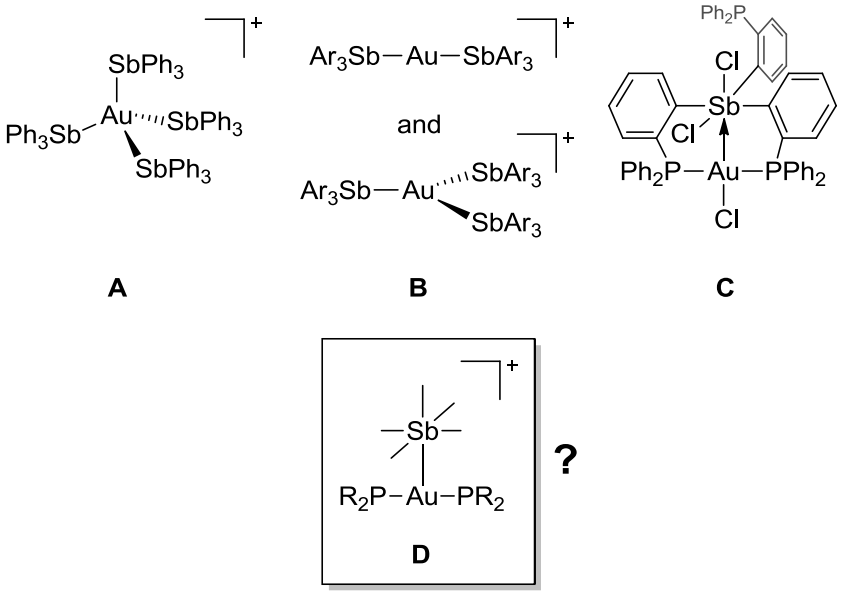

Figure 78. Illustration of **A**: tetra-coordinated Au(I) cation, **B**: linear and trigonal planar Au(I) cation **C**: tri-valence Sb-Au complex.

7.2 Synthesis and characterization of the gold-stiborane complexes

In this study, we chose to use the Sb-Au complex **26** which features diisopropylphosphine substituents. Complex **26** was allowed to react with one equivalent of $PhICl_2$ in THF resulting in the formation of complex **36** in 91% yield as a yellow, air stable derivative (Figure 79). The ^{31}P NMR spectrum of complex **36** exhibited a single signal at δ = 130.7 ppm, indicating symmetric coordination of the phosphorus atoms. The resonance is significantly downfield from complex **26**, signalling a more oxidized gold atom. The precise structure of **36** was established by an X-ray diffraction study

(Figure 80). The gold center is tetracoordinated with a slightly distorted square planar coordination geometry (sum of angles (ΣAu_α) = 364.89°). The two phosphine moieties span trans sites with a significantly bent P-Au-P arrangement (166.03(3)°). The value of the Sb-Au-Cl1 angle (160.217(18)°) confirms that the gold atom adopts a moderately distorted square-planar geometry characteristic of the trivalent state. The separation of the Sb and Au atoms is 2.8651(4) Å, which is slightly longer than the sum of the covalent radii of the two elements (2.64-2.75 Å). This distance is comparable to that found in related complexes such as [(*o*-(Ph_2P)C_6H_4)$_3SbCl_2$]AuCl (2.7086(9) Å) and slightly longer than that in stibine gold(I) complexes such as [$Au(SbPh_3)_4$][ClO_4] (2.656–2.658 Å)[167] and [Au(μ_2-1,8-($C_{10}H_6$))$_2SbPh_2$] (2.76 Å av.)[64]. The antimony center is located in a distorted octahedral geometry as indicated by the Au-Sb-C_{Ph}, Cl2-Sb-Cl3 and C1-Sb-C7 angles of 169.52(8)°, 170.84(3)° and 171.78(11)°, respectively. The short Sb-Cl2 (2.4846(8) Å) and Sb-Cl3 (2.4757(8) Å) bonds are comparable to those observed for other hexavalent antimony species with similar Sb-Cl linkages. For example a comparison can be made with (Toyl)$_2$(*o*-(CH_2NMe_2)C_6H_4)$SbCl_2$ which features Sb-Cl bonds with an average value of 2.49 Å.[190]

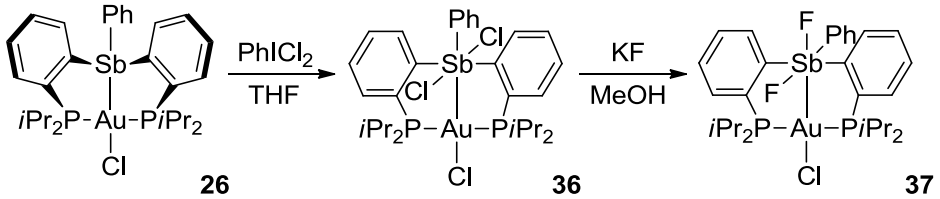

Figure 79. Synthesis of **36** and **37**.

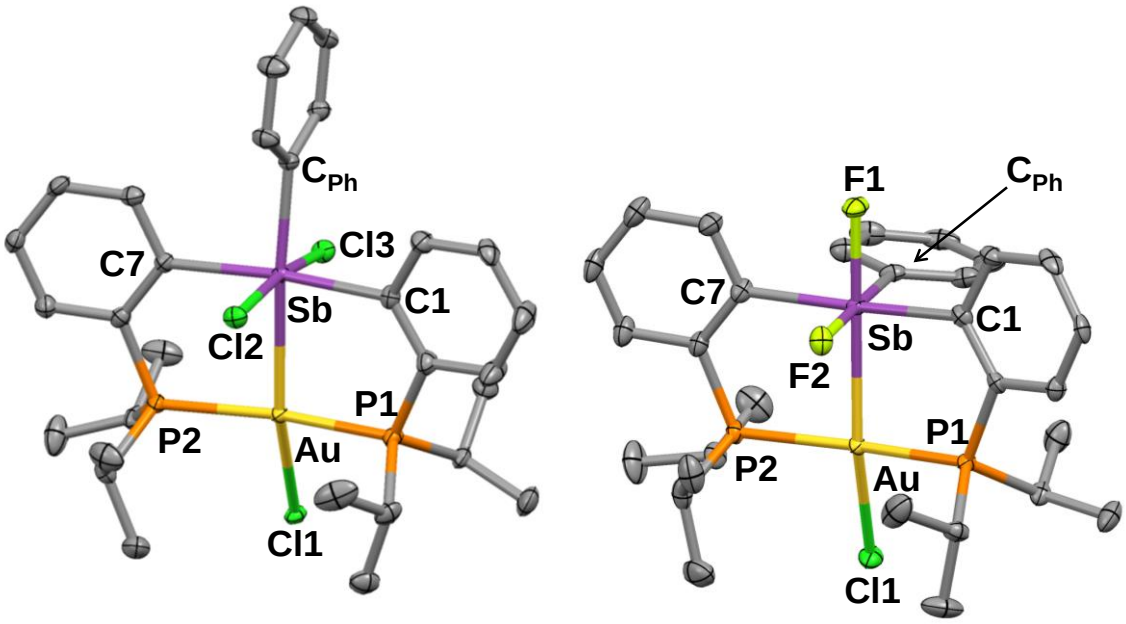

Figure 80. Structure of **36** (left) and **37** (right). Displacement ellipsoids are scaled to the 50% probability level. Interstitial solvent molecules and hydrogen atoms are omitted for clarity. Selected bond lengths (Å) and angles (deg) for: **36**: Au-Sb 2.8651(4), Au-Cl1 2.5946(8), Sb-Cl2 2.4757(8), Sb-Cl3 2.4846(8); P1-Au-P2 166.03(3), Cl1-Au-Sb 160.217(18), Au-Sb-C_{Ph} 169.52(8), Cl2-Sb-Cl3 170.84(3), C1-Sb-C7 171.78(11). **37**: Au-Sb 2.7450(14), Au-Cl1 2.5190(18), Sb-F1 2.968(3), Sb-F2 1.994(3); P1-Au-P2 163.82(5), Cl1-Au-Sb 164.18(3), Au-Sb-F1 178.70(9), F2-Sb-C_{Ph} 177.53(15), C1-Sb-C7 165.93(17).

With compound **36** in hand, we sought to investigate its stability upon exchange of the chloride ligands with other halides. To this end, compound **36** was allowed to react with 4 equivalent of KF in MeOH resulting in the formation of complex **37** as a colorless, air stable derivative (Figure 79). The ^{31}P NMR signal at 93.1 ppm appears as a doublet because of coupling to one of the fluorine nucleus ($J_{P\text{-}F}$ = 15.0 Hz). The ^{19}F NMR spectrum of **37** in $CDCl_3$ displays two signals of equal intensity at -20.7 and -147.3 ppm. The first signal is a simple doublet arising from the non-equivalence of the two fluorine nuclei ($J_{F\text{-}F}$ = 31.5 Hz). The second signal is a doublet of triplet ($J_{F\text{-}F}$ = 31.5

Hz and $J_{P\text{-}F}$ = 15.0 Hz) (Figure 81). The upfield chemical shifts and $J_{P\text{-}F}$ coupling of the signals suggests unsymmetrical coordination of the two fluorine atoms to the Sb atom. Upon further inspection of the ^{19}F NMR spectrum, the peak at -20.7 ppm was assigned to the equatorial fluorine atom (F_{eq}) which only coupled with the apical fluorine atom (F_a) with a coupling constant $J_{F\text{-}F}$ = 31.5 Hz. The other upfield peak at -147.3 ppm corresponding to F_a is not only coupled with the F_{eq} but also with two phosphorus atoms resulting in a doublet of triplet. These two significant ^{19}F NMR signals are comparable to the *cis*-(M-Sb-F) complexes (M = Au, -41 ppm; M = Hg, -43.3 ppm) and *trans*-(M-Sb-F) complex (M = Pd, -129.7 ppm) which we reported previously.[64,70,71] Complex **37** crystallizes in the space group $P2_1/c$ with one molecule in the asymmetric unit (Figure 80). The structure of **37** shows two fluorine atoms coordinated to the antimony center with an average Sb-F bond distance of 1.980(3) Å (Figure 80). This Sb-F distance is similar to that observed in Ph_4SbF (2.0530(8) Å)[72] or $AntPh_3SbF$ (2.0530(8) Å).[155] Fluoride coordination results in a nearly octahedral geometry about the antimony atom with angles of 177.48(16)° for F2-Sb-C_{Ph}, 178.66(10)° for F1-Sb-Au, and 166.00(19)° for C1-Sb-C7. To the best of our knowledge, this is the first structure of an hexacoordinated antimony complex with the two fluorine atoms located in a *cis*-position. Also of interest is the Au-Sb distance of **37** (2.7449(14) Å) which is shorter than that measured for **36**. The value of the Sb-Au-Cl1 angle (164.17(3)°) in **37** is more linear than that in **36** (160.217(18)°). Altogether, these structural peculiarities suggest a strengthening of the of the Au→Sb interaction upon conversion of **36** into **37**.

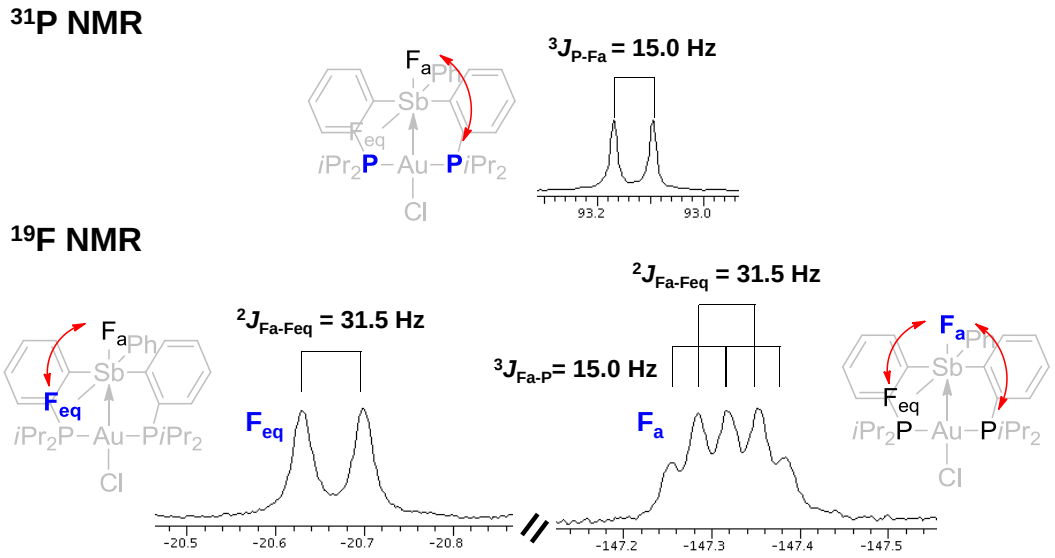

Figure 81. ^{31}P NMR (above) and ^{19}F NMR (below) spectrum of **37** in $CDCl_3$.

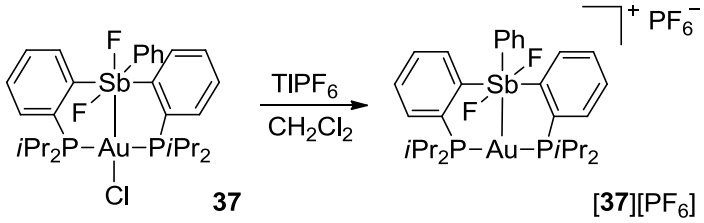

Figure 82. Synthesis of the cationic stiboranyl-gold complex [**37**][PF_6].

To test the idea of a cationic gold-stiborane complex introduced at the beginning of this chapter, we targeted the cationic stiboranyl-gold complex [**37**][PF_6]. Chloride abstraction from the neutral complex **37** was readily achieved with 1 eq. of $TlPF_6$ in dichloromethane at room temperature within 30 minutes (Figure 82). After standard workup, complex [**37**][PF_6] was isolated in 80% yield as a white powder. The ^{31}P NMR spectrum of [**37**][PF_6] in $CDCl_3$ consists of a resonance at 78.8 ppm, shifted to higher

field by about 15 ppm (from δ ^{31}P = 93.1 ppm in **37**) and a PF_6^- resonance (δ -144.2 ppm, $J_{P\text{-}F}$ = 712.73 Hz) with a half intensity ratio . In addition to a PF_6^- resonance at -96.9 ppm, the ^{19}F NMR spectrum of the [**37**][PF_6] shows a peak at -73.3 ppm corresponding to the two fluorine atoms bound to the antimony center. Single crystals of [**37**][PF_6] were obtained by slow vapor diffusion of Et_2O into a solution of the compound in CH_3CN. The crystallographic measurement of [**37**][PF_6] was performed at 253(2) K due to loss of crystallinity at lower temperature. This salt crystallizes in the triclinic space group P-1 with one independent molecule and one PF_6^- counter anion in the asymmetric unit (Figure 83). The shortest contact between [**37**]$^+$ and PF_6^- (2.685 Å between a hydrogen atom of a isopropyl group and a fluorine atom of PF_6^-) unambiguously established the ion pair character of [**37**][PF_6]. The Sb-Au bond is elongated (from 2.7450(14) Å in **37**, to 3.0708(13) Å in [**37**][PF_6]) but remains noticeably shorter than the sum of the van der Waals radii (4.3 Å).[191] A further examination of the structure indicates that the F1 and F2 atoms are placed in *trans*-position, which is consistent with the observation of the identity of one fluorine signal in the ^{19}F NMR spectrum of [**37**]$^+$. The Sb-F1 and Sb-F2 bond lengths of 1.953(7) Å and 1.955(6) Å, respectively, are close to those observed in the difluorostiboranes such as Ph_3SbF_2 (1.974 Å av.),[192] (*p*-$(NMe_2)C_6H_4)_3SbF_2$ (2.272 Å av.)[193] and Me_3SbF_2 (1.997 Å av.).[194] The gold atom adopts a T-shaped geometry as confirmed by the average P-Au-Sb and P1-Au-P2 angles of 89.96^o and 178.70(11)^o, respectively. Accordingly, the antimony atom displays a distorted octahedral geometry with the Au-Sb-C_{Ph}, F1-Sb-F2 and C1-Sb-C7 angles equal to 177.9(3)^o, 171.4(3)^o and 162.3(4)^o, respectively.

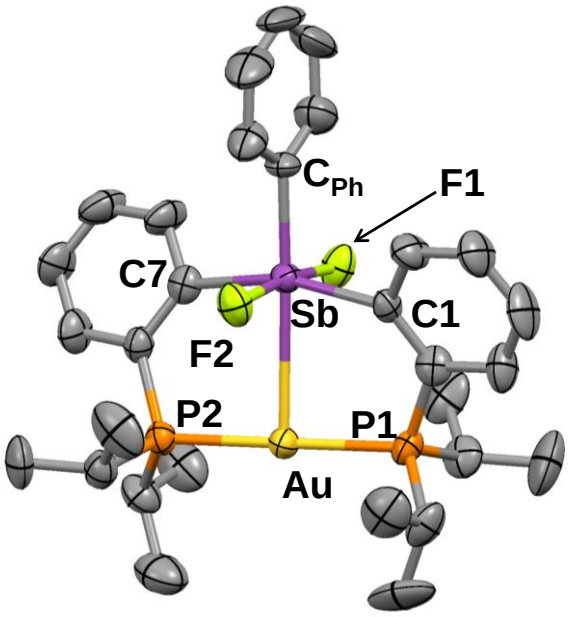

Figure 83. Structure of [**37**]$^{+}$. Displacement ellipsoids are scaled to the 50% probability level. Counter anion PF_6^- and hydrogen atoms are omitted for clarity. Selected bond lengths (Å) and angles (deg) for: [**37**]$^{+}$: Au-Sb 3.0708(13), Sb-F1 1.953(7), Sb-F2 1.955(6), Au-P1 2.293(3) ,Au-P2 2.291(3); P1-Au-P2 178.70(11), Au-Sb-C_{Ph} 177.9(3), F2-Sb-F1 171.4(3), C1-Sb-C7 162.3(4).

7.3 Computational studies

To study the Au→Sb interactions possibly present in this family of derivatives, the structures of **36**, **37** and [**37**][PF_6] have been optimized using DFT methods (Gaussian09: BP86 with 6-31g for H, C; Stuttgart relativistic small core (RSC) 1997 ECP for Au; Stuttgart relativistic large core (RLC) ECP for P, Cl, Sb) and subjected to NBO calculations. For each complex **36**, **37** and [**37**][PF_6], the optimized structures are in good agreement with those determined crystallographically. The largest deviation in the Sb-Au bond is 0.106 Å and is observed in the case of complex **38**. The Sb-Au bond lengths are listed in Table 16. In complex **36**, the NBO analysis identifies a lp(Au)→σ*(Sb-C_{Ph}) donor-acceptor interaction (E_{del} = 15.6 kcal mol^{-1}) as the primary

interaction (Figure 84). After the halide exchange reaction by fluoride, the NBO analysis treats two of the antimony-bound fluorides (F_a and F_{eq}) and the chloride on gold as three independent units. The fluoride which is located on the apical position interacts with the antimony atom by a strong lp(F)→5p(Sb) interaction. This interaction may be viewed as a dative bond resulting from the donation of a fluoride lone pair into a vacant antimony 5p orbital. Accordingly, the same p orbital is involved in a 5d(Au)→5p(Sb) interaction, indicating that the gold atom donates to the antimony center by one of its filled d orbitals. Further investigation of this donor-acceptor interaction gives a deletion energy of 53.7 kcal mol^{-1}. A comparison shows that complex **37** has a stronger Au→Sb interaction than **36**, a phenomenon rationalized the presence of an apical fluoride atom trans to the gold atom. These results of these NBO studies are also consistent with what we observed in the solid state structures of **36** and **37**. Comparison of the neutral gold stiborane **37** with its cationic analog [**37**]$^+$ obtained by chlorine abstraction gives more insight into the influence of the charge of the metal center. The Sb-Au bond significantly elongates upon cationization (from 2.7450(14) Å in **37** to 3.0708(13) Å in [**37**][PF_6]), suggesting a noticeable weakening of the Au→Sb interaction. This was confirmed by second-order NBO analysis. The interactions identified include a lp(Au)→σ*(Sb-C_{Ph}) interaction, whose deletion of 2.4 kcal mol^{-1} is now very small.

Table 16. Selected bond lengths (Å) and angles (°) for complexes as determined crystallographically (**36**, **37**, [**37**]$^+$ and **38**) and optimized computationally (**36***, **37***, [**37**]$^+$* and **38***).

	Sb-Au (Å)	P-Au-P (°)	Sb-Au-X[a] (°)	Σ_αAu (°)
36	2.8651(4)	166.03(3)	160.217(18)	364.89
36*	2.86283	175.017	167.831	361.053
37	2.7450(14)	163.82(5)	164.18(3)	364.13
37*	2.80172	171.868	167.645	361.617
[37]$^+$	3.0708(13)	178.70(11)	-	-
[37]$^+$*	2.98693	178.116	-	-
38	2.6886(5)	171.84(5)	177.14(19)	360.17
38*	2.79422	170.493	179.997	360.000

[a]X = Cl for **36**, **37**; X = C_{Ph} for **38**

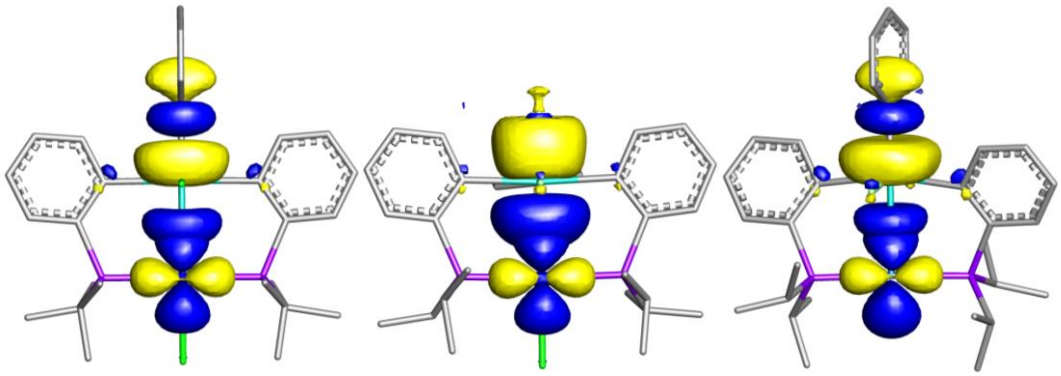

Figure 84. Superposition of the donor and acceptor orbitals according to NBO analysis, which contribute mainly to the Sb-Au interactions in **36** (left), **37** (middle) and [**37**]$^+$ (right). Hydrogen atoms are omitted for clarity (isovalue=0.04).

7.4 Fluoride affinity of cationic Sb-Au complex

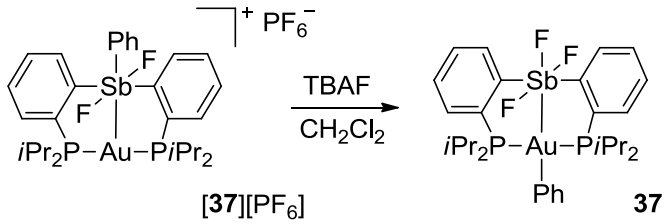

[**37**][PF_6] **37**

Figure 85. Reaction **37** with TBAF.

Fluoride complexes of the late transition metals raise interesting questions in bonding and display unusual reactivity. The fluoride ion, according to hard/soft acid/base theory,[195] is mismatched with cations formed by late transition metals in low oxidation state. Until now, only three gold-fluoride complexes have been synthesized.[196-198] With this cationic T-shaped gold stiborane in hand, we decided to test the addition of fluoride. The corresponding fluoride adduct was prepared by adding 1 equiv. of the tetra-*n*-butylammonium fluoride (TBAF) to a solution of [**37**][PF_6] in CH_2Cl_2 for 12 hours (Figure 85). After the addition of TBAF, we monitored the reaction by ^{19}F NMR which gave rise to a mutiplet signal at around -203.6 ppm (Figure 86). After standard work-up, a fluoride adduct (**38**) was isolated in 67% yield as a white powder. The ^{31}P NMR spectrum of **38** displays a unique doublet signal at δ 107.3 ppm with a coupling constant $J_{P\text{-}F}$ = 18.8 Hz. (Figure 87). The ^{19}F NMR spectrum exhibits two signals at -83.4 ppm and -121.6 ppm in a 2:1 intensity ratio suggesting 2 fluorine atoms sitting at equatorial position and another one at the apical position. Further examination of the splitting of the ^{19}F NMR signals leads to the following assignment: the peak at -83.4 ppm is

assigned to the 2 F_{eq} atoms with a coupling constant $J_{F\text{-}F}$ = 20.6 Hz to the F_a; the signal at -121.6 ppm, which features a pseudo-quintet$_a$ ($J_{F\text{-}F}$ = 20.6 Hz, $J_{P\text{-}F}$ = 18.8 Hz) atoms, is assigned to F_a. Single crystal of **38** was grown by vapor diffusion of Et_2O into a concentrated CH_2Cl_2 solution (Figure 88). Complex **38** crystallizes in the rhombic space group *R*-3. The solid state structure shows that the three fluorine atoms are attached to the antimony center and that the phenyl ring migrated to the gold atom, a result that we did not originally anticipate (Figure 88). The Sb-Au bond length (2.6886(5) Å) is shorter than in complexes **36** (2.8651(4) Å), **37** (2.7450(14) Å) and [**37**][PF_6] (3.0708(13) Å). Formation of this new Sb-F3 bond leads to a distorted octahedral geometry about the antimony atom as indicated by the angles of 177.17(10)^o for Au-Sb-F3, 176.77(13)^o for F1-Sb-F2, and 165.2(2)^o for C1-Sb-C7. The Au-C_{Ph} distance (2.149(6) Å) is slightly longer than those observed for *t*Bu_3PAuPh (2.044(4) Å)[199] and *t*Bu_3PAu($C_6F_3H_2$) (2.053(4) Å).[200] Phenyl coordination to the gold center results in a distorted square-planar geometry (P1-Au-P2 171.84(5)^o and C_{Ph}-Au-Sb 177.14(19)^o) reminiscent of that observed for **36** and **37**.

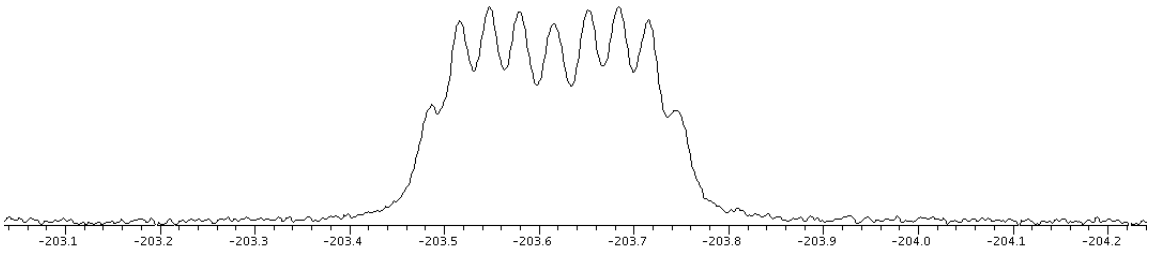

Figure 86. ^{19}F NMR spectrum of Au-F complex in $CDCl_3$.

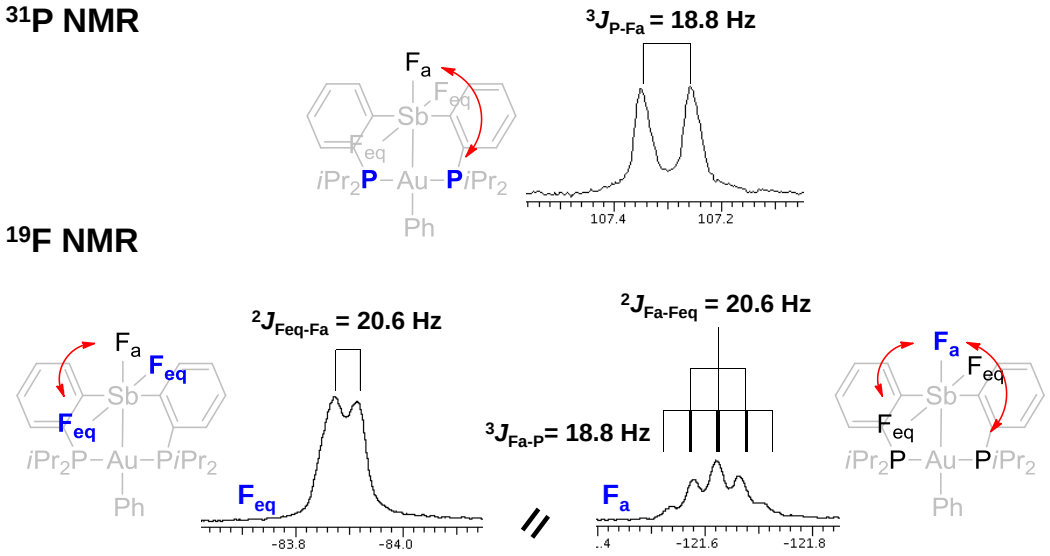

Figure 87. ^{31}P NMR (above) and ^{19}F NMR (below) spectrum of **38** in $CDCl_3$.

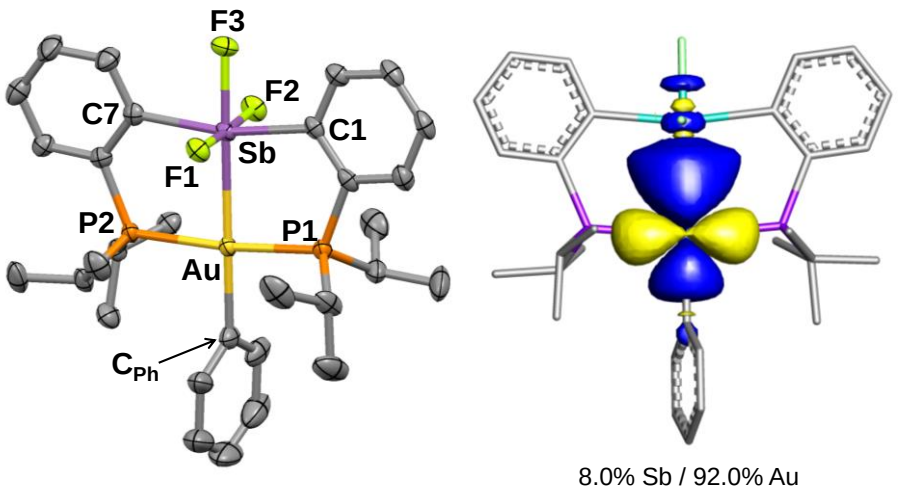

Figure 88. Left: Structure of **38**. Displacement ellipsoids are scaled to the 50% probability level. Hydrogen atoms are omitted for clarity. Selected bond lengths (Å) and angles (deg) for: **38**: Au-Sb 2.6886(5), Au-C_{Ph} 2.149(6), Sb-F1 1.997(3), Sb-F2 1.983(3), Sb-F3 1.973(3); P1-Au-P2 171.84(5), C_{Ph}-Au-Sb 177.14(19), Au-Sb-F3 177.17(10), F1-Sb-F2 176.77(13), C1-Sb-C7 165.2(2). Right: Sb-Au Natural Localized Bond Orbital (NLMO, isovalue=0.02). Hydrogen atoms are omitted for clarity.

In order to better understand the Au-Sb bonding interaction of complex **38**, the structure of **38** was computationally optimized and analyzed using NBO. The good match observed between the experimental and computed structure of **38** validates the adequacy of the level of theory (BP86[80,81] with 6-31g(d) for H, C, F; 6-311+g(d) for P, Cl; Stuttgart relativistic small core (RSC) 1997 ECP for Au[179]; Stuttgart relativistic large core (RLC) 1997 ECP for Sb[180]) employed for this complexes (Table 16). The strengthening of the Au-Sb interaction in **38** is reflected by the fact that NBO defines this linkage as a covalent one rather than as a second order donor acceptor interaction as for **36**, **37** and [**37**][PF_6]. Analysis of the corresponding NLMO (Figure 88) shows that the Au-Sb bonding pair possesses a larger orbital contribution from the gold atom (Sb, 8.0%/Au, 92.0% for **38**) in agreement with a Au→Sb dative character of this linkage.

7.5 Conclusions

In summary, we have described the synthesis of a series of complexes featuring a gold(I) center flanked by a stiborane group. The structural and computational result point to the existence of a Au→Sb interaction which is stronger when the gold(I) center is substituted by an anionic ligand. We also find that this interaction is stronger when the Lewis acidity of the antimony atom is made stronger by presence of antimony bound fluorine substituents. Finally, we show that the cationic complex [**37**]+ reacts with fluoride to afford a transient Au-F complex which rearranges via an internal ligand exchange reaction to afford **38**, an aurated trifluoroantimonate species.

7.6 Experimental

General considerations. [(tht)AuCl][175] (tht = tetrahydrothiophene) *o*-(*i*Pr$_2$P)C$_6$H$_4$Br[176] were prepared according to the reported procedures. Solvents were dried by passing through an alumina column (n-pentane and CH_2Cl_2) or by reflux under N_2 over Na/K (Et_2O and THF). All other solvents were used as received. $SbCl_3$, $BiCl_3$ and *o*-chloranil were purchased from Aldrich and used as received. All air and moisture sensitive manipulations were carried out under an atmosphere of dry N_2 employing either a glove box or standard Schlenk techniques. Ambient temperature NMR spectra were recorded on a Varian Unity Inova 400 FT NMR (399.59 MHz for ^{1}H, 100.45 MHz for ^{13}C, 161.74 MHz for ^{31}P) spectrometer. Chemical shifts (δ) are given in ppm and are referenced against residual solvent signals (^{1}H, ^{13}C) or external H_3PO_4(^{31}P). Elemental analyses were performed at Atlantic Microlab (Norcross, GA).

Synthesis of 36. A solution of $PhICl_2$ (17 mg, 0.06 mmol) in CH_2Cl_2 (1 mL) was added dropwise to a solution of **26** (50 mg, 0.06 mmol) in CH_2Cl_2 (5 mL) at ambient temperature. The reaction was stirred for 10 min. before removing the solvent in vacuo. The resulting yellow solid was washed with pentane (2×3 mL) and dried in vacuo to afford 49 mg (91 %) of **36** as a yellow powder. Single crystals of **36** suitable for X-ray diffraction were obtained by vapor diffusion of pentane into a solution of the compound in $CHCl_3$. ^{1}H NMR (499.43 MHz, $CDCl_3$): δ 8.51 (dd, 2H, $^3J_{H\text{-}H}$ = 7.00 Hz, $^3J_{H\text{-}P}$ = 2.33 Hz, *o*-P(Sb)C$_6$H$_4$), 7.79 (m, 2H, *o*-P(Sb)C$_6$H$_4$), 7.56 (m, 3H, SbPh-C*H*), 7.41 (pseudo-t, 2H, $^3J_{H\text{-}H}$ = 7.00 Hz, *o*-P(Sb)C$_6$H$_4$), 7.32 (d, 2H, $^3J_{H\text{-}H}$ = 8.38 Hz, *o*-SbPh-C*H*), 7.23 (pseudo-t, 2H, $^3J_{H\text{-}H}$ = 7.00 Hz, *o*-P(Sb)C$_6$H$_4$), 3.46 (m, 4H, C*H*CH$_3$), 1.41 (dd, 12H, $^3J_{H\text{-}}$

$_H$ = 7.00 Hz, $^3J_{H\text{-}P}$ = 18.26 Hz, CHC*H*$_3$), 1.30 (dd, 12H, $^3J_{H\text{-}H}$ = 7.00 Hz, $^3J_{H\text{-}P}$ = 18.26 Hz, CHC*H*$_3$). $^{31}P\{^1H\}$ NMR (202.17 MHz; $CDCl_3$): δ 103.68. $^{13}C\{^1H\}$ NMR (125.58 MHz, $CDCl_3$): δ 178.59 (pseudo-t, $J_{C\text{-}P}$ = 29.05 Hz), 142.09 (s), 136.21 (s), 133.02 (s), 131.72 (pseudo-t, $J_{C\text{-}P}$ = 9.32 Hz), 131.22 (pseudo-t, $J_{C\text{-}P}$ = 5.45 Hz), 129.58 (s), 129.03 (s), 116.27 (pseudo-t, $J_{C\text{-}P}$ = 27.15 Hz), 27.75 (pseudo-t, $J_{C\text{-}P}$ = 14.40 Hz), 19.55 (s; $CH_{3i\text{-}Pr}$), 19.03 (s; $CH_{3i\text{-}Pr}$). Elemental analysis calcd (%) for $C_{30}H_{41}AuCl_3P_2Sb$: C 40.55, H 4.65; found: C 38.09, H 4.45.

Synthesis of 37. A solution of KF (10 mg, 0.20 mmol) in MeOH (1 mL) was added to a solution of **36** (40 mg, 0.05 mmol) in THF (3 mL) and stirred at ambient temperature for 30 min. resulting in the precipitation of a white solid. The solvent was removed in vacuo, and the residue extracted with CH_2Cl_2 (5 mL). The resulting mixture was filtered over Celite and concentrated to ca. 1 mL. Addition of pentane (5 mL) resulted in precipitation of a white powder that was filtered, washed with MeOH (3 × 3 mL), and dried in vacuo to afford 33 mg (85%) of **37**. Single crystals of **37** suitable for X-ray diffraction were obtained by slow evaporation of the compound in CH_2Cl_2/Et_2O (1/1). ^1H NMR (499.43 MHz, $CDCl_3$): δ 8.74 (d, 2H, $^3J_{H\text{-}H}$ = 7.84 Hz, *o*-P(Sb)C_6H_4), 7.76 (m, 2H, *m*-P(Sb)C_6H_4), 7.69 (pseudo-t, 2H, $^3J_{H\text{-}H}$ = 7.84 Hz, P(Sb)C_6H_4), 7.54 (pseudo-t, 2H, $^3J_{H\text{-}H}$ = 6.39 Hz, P(Sb)C_6H_4), 7.03 (pseudo-t, 1H, $^3J_{H\text{-}H}$ = 6.39 Hz, *p*-SbPh-C*H*), 6.95 (pseudo-t, 2H, $^3J_{H\text{-}H}$ = 6.39 Hz, *m*-SbPh-C*H*), 6.76 (d, 2H, $^3J_{H\text{-}H}$ = 6.39 Hz, *o*-SbPh-C*H*), 3.40 (br, 2H, C*H*CH_3), 3.26 (br, 2H, C*H*CH_3), 1.34 (dd, 12H, $^3J_{H\text{-}H}$ = 7.35 Hz, $^3J_{H\text{-}P}$ = 20.05 Hz, CHC*H*$_3$), 1.21 (dd, 12H, $^3J_{H\text{-}H}$ = 7.35 Hz, $^3J_{H\text{-}P}$ = 20.05 Hz, CHC*H*$_3$). $^{31}P\{^1H\}$ NMR (202.17 MHz; $CDCl_3$): δ 93.13 (d, $^3J_{P\text{-}F}$ = 14.96 Hz). ^{19}F NMR

(469.93 MHz; $CDCl_3$): -20.67 (d, 1F, $^2J_{F\text{-}F}$ 31.49 Hz), -147.32 (dt, 1F, $^2J_{F\text{-}F}$ = 31.49 Hz, $^3J_{F\text{-}P}$ = 14.96 Hz). $^{13}C\{^1H\}$ NMR (125.58 MHz, $CDCl_3$): δ 161.06 (s), 154.33 (s), 139.60 (s), 135.57 (pseudo-t, $J_{C\text{-}P}$ = 9.22 Hz), 133.21 (s), 133.00 (s), 131.29 (br), 129.01 (br), 128.74 (s), 127.96 (s), 29.00 (pseudo-t, $J_{C\text{-}P}$ = 14.45 Hz), 26.88 (pseudo-t, $J_{C\text{-}P}$ = 14.45 Hz), 19.38 (s; $CH_{3i\text{-}Pr}$), 19.17 (s; $CH_{3i\text{-}Pr}$) , 18.82 (s; $CH_{3i\text{-}Pr}$), 18.53 (s; $CH_{3i\text{-}Pr}$). Elemental analysis calcd (%) for $C_{30}H_{41}AuClF_2P_2Sb$: C 42.10, H 4.83; found: C 42.08, H 4.95.

Synthesis of [37][PF_6]. A solution of $TlPF_6$ (16 mg, 0.046 mmol) in CH_2Cl_2 (1 mL) was added to a solution of **37** (40 mg, 0.046 mmol) in CH_2Cl_2 (3 mL) and stirred at ambient temperature for 30 min. resulting in the precipitation of a white TlCl salt. The resulting mixture was filtered over Celite and concentrated to *ca.* 1 mL. Addition of pentane (5 mL) resulted in precipitation of a white powder that was filtered, washed with pentane (3 × 3 mL), and dried *in vacuo* to afford 36 mg (80%) of [**37**][PF_6]. Single crystals of [**37**][PF_6] suitable for X-ray diffraction were obtained by vapor diffusion of Et_2O into a solution of the compound in CH_3CN. ^1H NMR (499.43 MHz, $CDCl_3$): δ 7.89 (d, 2H, $^3J_{H\text{-}H}$ = 7.62 Hz, *o*-P(Sb)C_6H_4), 7.77 (m, 2H, P(Sb)C_6H_4), 7.66 (pseudo-t, 2H, $^3J_{H\text{-}H}$ = 7.62 Hz, SbPh-C*H*), 7.61 (m, 2H, P(Sb)C_6H_4), 7.53 (d, 2H, $^3J_{H\text{-}H}$ = 7.62 Hz, *o*-P(Sb)C_6H_4), 7.44 (pseudo-t, 2H, $^3J_{H\text{-}H}$ = 7.62 Hz, SbPh-C*H*), 3.29 (m, 4H, C*H*CH_3), 1.47 (dd, 12H, $^3J_{H\text{-}H}$ = 7.59 Hz, $^3J_{H\text{-}P}$ = 19.58 Hz, CHC*H*$_3$), 1.32 (dd, 12H, $^3J_{H\text{-}H}$ = 7.59 Hz, $^3J_{H\text{-}P}$ = 19.58 Hz, CHC*H*$_3$). $^{31}P\{^1H\}$ NMR (202.17 MHz; $CDCl_3$): δ 78.79 (s, 2P, P*i*Pr_2), -144.23 (sept, 1P, $^1J_{P\text{-}F}$ = 712.73 Hz, PF_6^-). ^{19}F NMR (469.93 MHz; $CDCl_3$): -73.30 (d, 6F, $^2J_{F\text{-}P}$ 712.73 Hz, PF_6^-), -96.86 (s, 2F, SbF_2). $^{13}C\{^1H\}$ NMR (125.58 MHz, $CDCl_3$): δ 158.68 (br), 136.09 (s), 135.51 (pseudo-t, $J_{C\text{-}P}$ = 6.94 Hz), 135.07 (s), 134.04 (s), 132.82

(s), 132.27 (s), 131.59 (pseudo-t, $J_{C\text{-}P}$ = 3.50 Hz), 130.93 (pseudo-t, $J_{C\text{-}P}$ = 29.25 Hz), 130.18 (s), 26.88 (pseudo-t, $J_{C\text{-}P}$ = 14.95 Hz), 20.62 (s; $CH_{3i\text{-}Pr}$), 19.03 (s; $CH_{3i\text{-}Pr}$). Elemental analysis calcd (%) for $C_{30}H_{41}AuF_8P_3Sb$: C 37.33, H 4.28; found: C 36.99, H 4.28.

Synthesis of 38. A solution of TBAF (8 mg, 0.03 mmol) in CH_2Cl_2 (2 mL) was added to a solution of [**37**][PF_6] (25 mg, 0.026 mmol) in CH_2Cl_2 (3 mL) and stirred at ambient temperature for 12 hours resulting in the precipitation of a white solid. The solvent was removed in vacuo, and the residue extracted with CH_2Cl_2 (5 mL). The resulting mixture was filtered over Celite and concentrated to ca. 1 mL. Addition of pentane (5 mL) resulted in precipitation of a white powder that was filtered, washed with MeOH (3 × 3 mL), and dried in vacuo to afford 15 mg (67%) of **38**. Single crystals of **38** suitable for X-ray diff fraction were obtained by slow evaporation of the compound in CH_2Cl_2/Et_2O (1/1). ^{1}H NMR (499.43 MHz, $CDCl_3$): δ 9.11 (d, 2H, $^3J_{H\text{-}H}$ = 8.37 Hz, *o*-P(Sb)C_6H_4), 7.88 (d, 2H, *o*-P(Sb)C_6H_4, $^3J_{H\text{-}H}$ = 8.85 Hz), 7.69 (pseudo-t, 2H, $^3J_{H\text{-}H}$ = 7.28 Hz, *m*-P(Sb)C_6H_4), 7.49 (pseudo-t, 2H, $^3J_{H\text{-}H}$ = 7.28 Hz, *m*-P(Sb)C_6H_4), 7.41 (d, 2H, $^3J_{H\text{-}H}$ = 8.32 Hz, *o*-SbPh-C*H*), 7.33 (pseudo-t, 2H, $^3J_{H\text{-}H}$ = 8.32 Hz, *m*-SbPh-C*H*), 7.10 (pseudo-t, 1H, $^3J_{H\text{-}H}$ = 8.32 Hz, *p*-SbPh-C*H*), 3.45 (m, 4H, C*H*CH_3), 1.17 (dd, 12H, $^3J_{H\text{-}H}$ = 8.22 Hz, $^3J_{H\text{-}P}$ = 18.62 Hz, CHC*H*$_3$), 0.87 (dd, 12H, $^3J_{H\text{-}H}$ = 8.22 Hz, $^3J_{H\text{-}P}$ = 18.62 Hz, CHC*H*$_3$). ^{31}P{^{1}H} NMR (202.17 MHz; $CDCl_3$): δ 107.31 (d, $^3J_{P\text{-}F}$ = 18.82 Hz). ^{19}F NMR (469.93 MHz; $CDCl_3$): -83.89 (d, 2F, $^2J_{F\text{-}F}$ 20.61 Hz), -121.62 (dt, 1F, $^2J_{F\text{-}F}$ = 20.61 Hz, $^3J_{F\text{-}P}$ = 18.82 Hz). ^{13}C{^{1}H} NMR (125.58 MHz, $CDCl_3$): δ 139.31 (s), 136.89 (s), 136.81 (s), 133.19 (s), 133.00 (s), 130.11 (s), 129.28 (s), 129.19 (s), 125.87 (s), 123.96 (s), 27.09

(pseudo-t, $J_{C\text{-}P}$ = 16.63 Hz), 18.43 (s; $CH_{3i\text{-}Pr}$), 18.10 (s; $CH_{3i\text{-}Pr}$). Elemental analysis calcd (%) for $C_{30}H_{41}AuF_3P_2Sb$: C 42.93, H 4.92; found: C 42.81, H 4.91.

Crystallography. All crystallographic measurements were performed at 110(2) K using a Bruker SMART APEX II diffractometer with a CCD area detector (graphite monochromated Mo Kα radiation, λ = 0.71073 Å, ω-scans with a 0.5° step in ω) at 110 K. In each case, a specimen of suitable size and quality was selected and mounted onto a nylon loop. The semi-empirical method SADABS was applied for absorption correction. The structures were solved by direct methods and refined by the full-matrix least-square technique against F^2 with the anisotropic temperature parameters for all non-hydrogen atoms. All H atoms were geometrically placed and refined in riding model approximation. Data reduction and further calculations were performed using the Bruker SAINT+ and SHELXTL NT program packages.

Theoretical calculations. Density functional theory (DFT) calculations (full geometry optimization) were carried out on **36**, **37**, [**37**]$^+$ and **38** starting from the crystal structure geometries with Gaussian09[122] program (BP86[80,81] with 6-31g(d) for H, C, F; 6-311+g(d) for P, Cl; Stuttgart relativistic small core (RSC) 1997 ECP for Au[179]; Stuttgart relativistic large core (RLC) 1997 ECP for Sb[180]). Frequency calculations were also carried out on the optimized geometry, showing no imaginary frequencies. The optimized structures, which are in excellent agreement with the solid-state structures, were subjected to a NBO analysis.[125] The resulting Natural Localized Molecular Orbitals (NLMOs) were visualized and plotted in Jimp 2 program.[126]

Table 17. Crystal data, data collections, and structure refinements for **36** and **37**

Crystal data	**36**·$CHCl_3$	**37**
Formula	$C_{30}H_{41}AuCl_3P_2Sb \cdot CHCl_3$	$C_{30}H_{41}AuClF_2P_2Sb$
Mr	1008.00	855.73
Crystal size (mm^3)	0.42 x 0.35 x 0.30	0.44 x 0.32 x 0.29
Crystal system	Monoclinic	Monoclinic
Space group	P2(1)/c	P2(1)/n
a (Å)	20.977(3)	11.571(9)
b (Å)	12.512(2)	17.799(13)
c (Å)	14.563(2)	15.330(11)
α (°)	90	90
β (°)	107.171(2)	101.679(8)
γ (°)	90	90
V ($Å^3$)	3651.9(9)	3092(4)
Z	4	4
ρ_{calc} (g cm^{-3})	1.833	1.838
μ (mm^{-1})	5.300	5.833
F(000)	1960	1664
T/K	110(2)	110(2)
Scan mode	ω, φ	ω, φ
hkl Range	-28 → +27	-15 → +15
	-16 → +16	-23 → +23
	-19 → +19	-20 → +20
Measd reflns	44239	36364
Unique reflns [R_{int}]	9129 [0.0481]	7615 [0.0515]
Reflns used for refinement	9129	7615
Refined parameters	370	334
GooF	1.036	1.165
*R*1,[a] *wR*2[b] (all data)	0.0297, 0.0560	0.0379, 0.0747
ρ_{fin} (max/min.) ($eÅ^{-3}$)	1.032, -0.837	1.647, -1.191

[a] $R_1 = \Sigma||Fo| - |Fc||/\Sigma|Fo|$. [b] $wR_2 = [[\Sigma w(Fo^2 - Fc^2)^2]/[\Sigma w(Fo^2)^2]]^{1/2}$.

Table 18. Crystal data, data collections, and structure refinements for [**37**][PF_6] and **38**

Crystal data	[**37**][PF_6]	**38**
Formula	$C_{30}H_{41}AuF_2P_2Sb$, F_6P	$C_{30}H_{41}AuF_3P_2Sb$
Mr	965.16	839.28
Crystal size (mm^3)	0.21 x 0.18 x 0.17	0.21 x 0.15 x 0.11
Crystal system	Triclinic	Rhombic
Space group	P -1	R -3
a (Å)	8.739(3)	26.570(4)
b (Å)	13.935(5)	26.570(4)
c (Å)	14.336(5)	23.545(7)
α (°)	90.334(5)	90
β (°)	91.788(5)	90
γ (°)	93.837(5)	120
V ($Å^3$)	1741.1(10)	14395(5)
Z	2	18
ρ_{calc} (g cm^{-3})	1.841	1.743
μ (mm^{-1})	5.183	5.560
F(000)	936	7344
T/K	253(2)	110(2)
Scan mode	ω, φ	ω, φ
hkl Range	-10 → +10	-35 → +34
	-17 → +17	-35 → +34
	-17 → +17	-31 → +30
Measd reflns	18038	55830
Unique reflns [R_{int}]	6819 [0.0703]	7755 [0.0740]
Reflns used for refinement	6819	7755
Refined parameters	388	334
GooF	1.033	1.109
$R1$,[a] $wR2$[b] (all data)	0.0818, 0.1537	0.0495, 0.0971
ρ_{fin} (max/min.) ($eÅ^{-3}$)	1.154, -1.670	1.507, -4.932

[a] $R_1 = \Sigma||Fo| - |Fc||/\Sigma|Fo|$. [b] $wR_2 = [[\Sigma w(Fo^2 - Fc^2)^2]/[\Sigma w(Fo^2)^2]]^{1/2}$.

CHAPTER VIII

SYNTHESIS OF TRINUCLEAR CU(I) AND AG(I) COMPLEXES SUPPORTED BY A TETRADENTATE SB AND BI LIGANDS

8.1 Introduction

When compared to phosphines and arsines, the coordination chemistry of stibine[33,90] and bismuthine ligands[201-203] appears relatively underdeveloped. This situation reflects the increasing s-character and decreased donicity of the pnictine lone pair observed as the group is descended. In the case of bismuth, the 6s lone pair is further contracted by relativistic effects, a factor that adds further limitation to the coordination of these ligands to metal centers. A strategy that has been employed in the past consists of incorporating the heavy group 15 elements in a polydentate scaffold where coordination of a metal is assisted by the presence of ancillary ligands. Examples of such ligands include the trisphosphino-stibines of general formula ((*o*-$(R_2P)C_6H_4)_3Sb$ which have been incorporated in a broad range of metal complexes.[35,71,204-207] Much less is known about the corresponding trisphosphino-bismuthine ligands of general formula (*o*-$(R_2P)C_6H_4)_3Bi$ which, until recently, had not been described.[166,208]

As part of our contribution to this area of research, we have recently investigated the coordination chemistry of such ligands to gold(I) ion. We observed that ((*o*-$(Ph_2P)C_6H_4)_3Sb$ reacts with AuCl(tht) to afford a stibine-gold complex (**A**) featuring a weak Sb→Au interaction of 2.8374(4) Å (Figure 89).[35] When the same reaction was carried out with the corresponding bismuth ligand ((*o*-$(R_2P)C_6H_4)_3Bi$ (R = Ph or *i*-Pr), a

ligand exchange reaction took place leading to the isolation of the corresponding chlorobismuthine complexes **B** and **C** (Figure 89).[166] To our surprise, a bonding analysis of these bismuth gold complexes revealed the presence of a weak Au→Bi donor-acceptor interaction. Intrigued by the diverse reactivity that these ligands display toward gold(I) chloride, we have now decided to extend the scope of our studies to other group 11 metal ions. In this paper, we report that the reaction of the tetradentate stibine and bismuthine ligands ((*o*-(*i*Pr$_2$P)C$_6$H$_4$)$_3$Sb ($\mathbf{L}_{Sb}^{P3}$) and (*o*-(*i*Pr$_2$P)C$_6$H$_4$)$_3$Bi ($\mathbf{L}_{Bi}^{P3}$)[209] with Cu(I) and Ag(I) halides leads to the unanticipated formation of complexes featuring a M$_3$(μ_2-Cl)$_3$ cluster (M = Cu or Ag) supported by the $\mathbf{L}_{Sb}^{P3}$ or $\mathbf{L}_{Bi}^{P3}$ ligand. We also show that the heavy group 15 element of the ligands interacts concomitantly with all three group 11 metal ions.

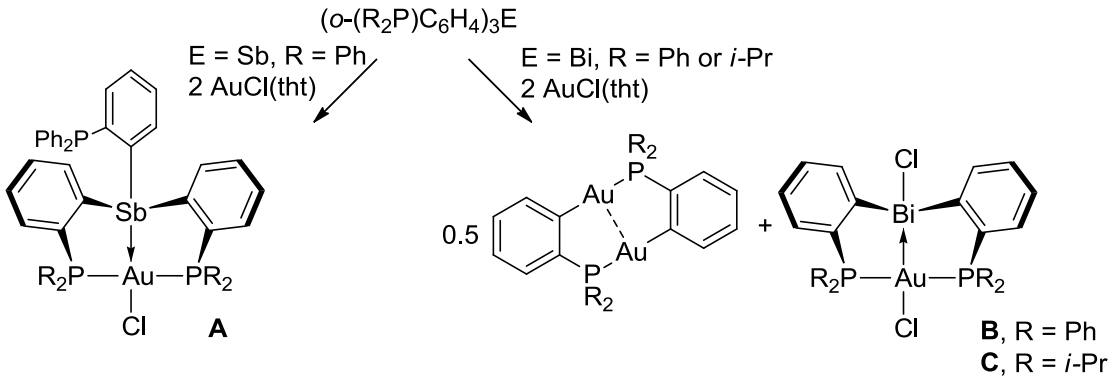

Figure 89. Illustration of complexes **A**, **B** and **C**.

8.2 Synthesis and characterization of **39**, **40**, **41** and **42**.

As a starting point for this study, we chose to investigate the synthesis of stibine complexes. To this end, the ligand $\mathbf{L}_{Sb}^{P3}$ was mixed with 3 equiv. of CuCl in THF to afford a yellow solution. After 12 hours of stirring at room temperature, the trinuclear complex (*o*-(*i*Pr$_2$P)C$_6$H$_4$)$_3$SbCu$_3$(μ_2-Cl)$_3$ (**39**) was isolated in 84% yield as a light yellow solid. Using a similar protocol, reaction of $\mathbf{L}_{Sb}^{P3}$ with 3 equiv. of AgCl in THF afforded the trinuclear silver complex (*o*-(*i*Pr$_2$P)C$_6$H$_4$)$_3$SbAg$_3$(μ_2-Cl)$_3$ (**40**) as a white solid in 75% yield (Figure 90). Interestingly, we found that the reaction of CuCl and AgCl with $\mathbf{L}_{Bi}^{P3}$ follows a similar course and affords (*o*-(*i*Pr$_2$P)C$_6$H$_4$)$_3$BiCu$_3$(μ_2-Cl)$_3$ (**41**) and (*o*-(*i*Pr$_2$P)C$_6$H$_4$)$_3$BiAg$_3$(μ_2-Cl)$_3$ (**42**) in 71% and 82% yield, respectively. It is interesting to note that adjusting the ligand/metal stoichiometry of these reactions to 1/1 did not lead to the formation of the corresponding mononuclear complexes. Instead, the formation of the trinuclear complexes **39-42** was observed, albeit in lower yields. These complexes are air-stable solids which, in the case of copper, display a light yellow color. They show no apparent luminescence when placed under hand-held UV lamp, even at 77 K. They have been fully characterized and their molecular structures determined using single crystal X-ray diffraction. The ^{31}P NMR spectra of the copper complexes **39** and **41** display a single resonance at 36.2 ppm and 37.3 ppm, respectively. In the case of **40** and **42**, the ^{31}P NMR resonance at 39.25 ppm and 42.51 ppm, respectively, is split into a doublet (J = 549 Hz for **40** and 560 Hz for **42**) because of coupling with the $^{107/109}$Ag nuclei. The detection of a single ^{31}P NMR resonance for these four complexes suggests a C_3 symmetrical core with all phosphorus nuclei in the same magnetic environment.

These complexes can be recrystallized by slow diffusion of Et_2O into a solution of the compounds in CH_2Cl_2 or $CHCl_3$.

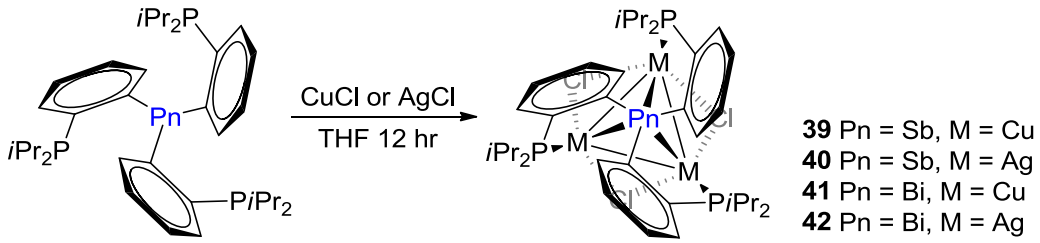

Figure 90. Synthesis of **39, 40, 41** and **42**.

To gain a greater insight into their precise molecular structures, single crystals of these group 11 metal complexes were subjected to a X-ray diffraction analysis. All four complexes feature very similar structures. The structures of **39-42** are shown in Figure 91, Figure 94, Figure 93 and Figure 94. All four compounds feature a $M_3(\mu_2\text{-}Cl)_3$ cyclic unit in which the three coinage metal atoms are arranged in an equilateral triangle crowned by three bridging chloride anions (see Table 19 for metrical parameters). This triangular unit is supported by the coordination of an ancillary phosphino arm of the ligand to each group 11 metal ion. As a result of this arrangement, the core of the complex adopts a three-fold symmetry which is in agreement with the detection of a single ^{31}P NMR resonance for these complexes.

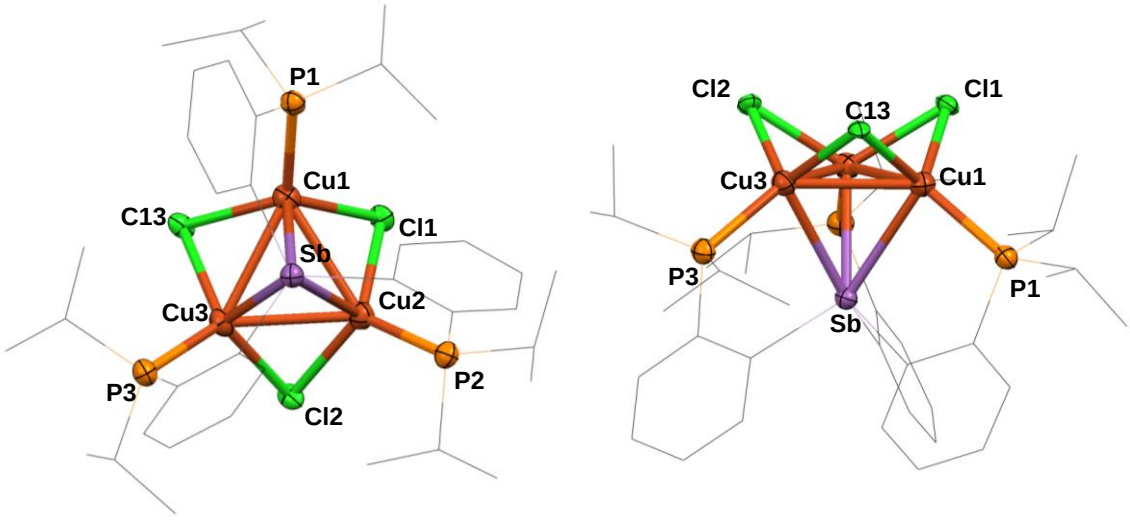

Figure 91. Solid-state structure of **39** (left: bottom view, right: side view). Ellipsoids are set at 50 % probability; hydrogen atoms and non-coordinated solvent molecules are omitted for clarity. Pertinent metrical parameters can be found in the text.

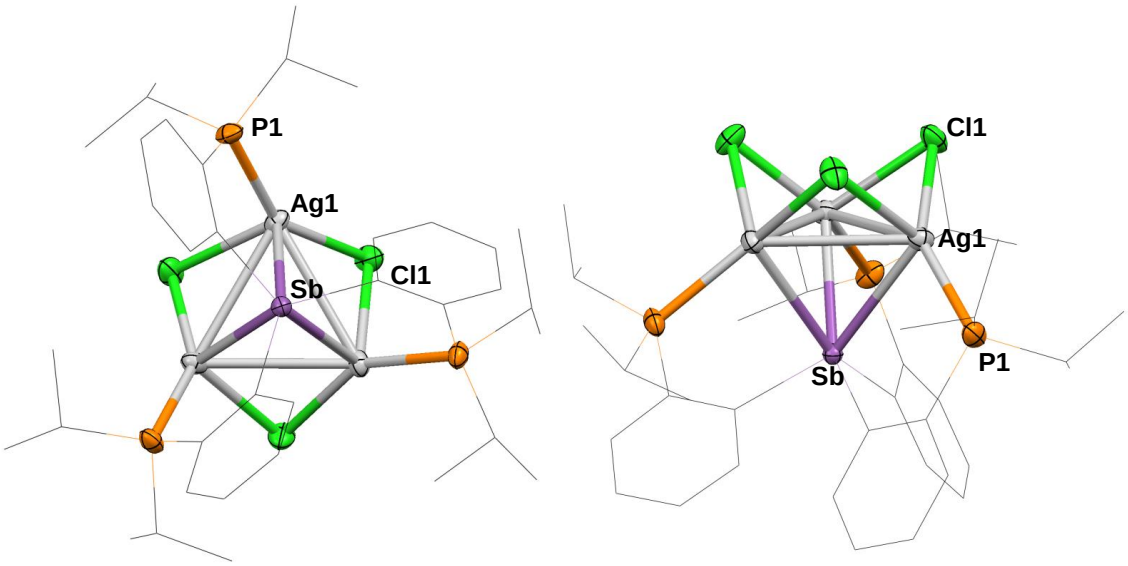

Figure 92. Solid-state structure of **40** (left: bottom view, right: side view). Ellipsoids are set at 50 % probability; hydrogen atoms and non-coordinated solvent molecules are omitted for clarity. Pertinent metrical parameters can be found in the text.

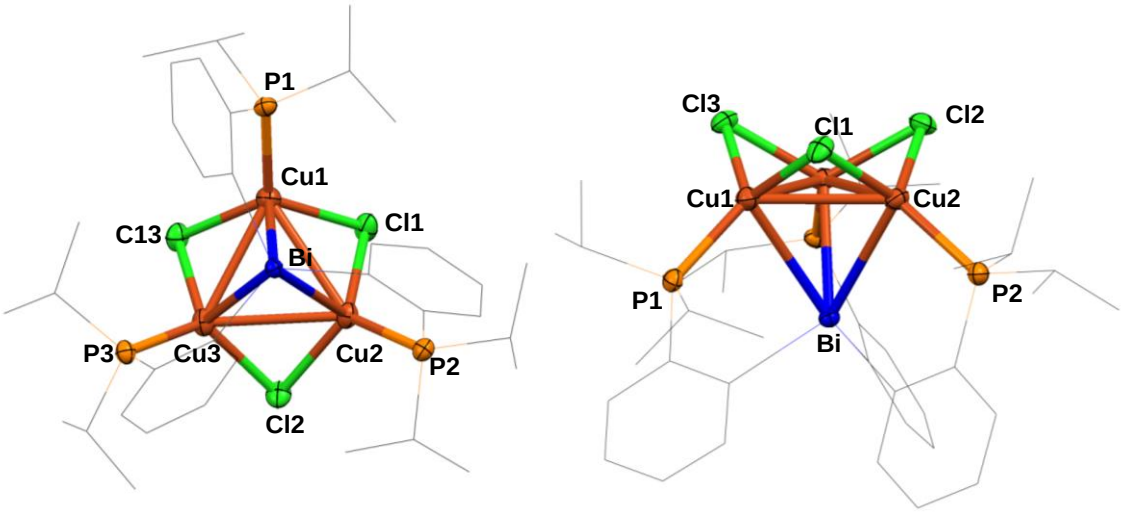

Figure 93. Solid-state structure of **41** (left: bottom view, right: side view). Ellipsoids are set at 50 % probability; hydrogen atoms and non-coordinated solvent molecules are omitted for clarity. Pertinent metrical parameters can be found in the text.

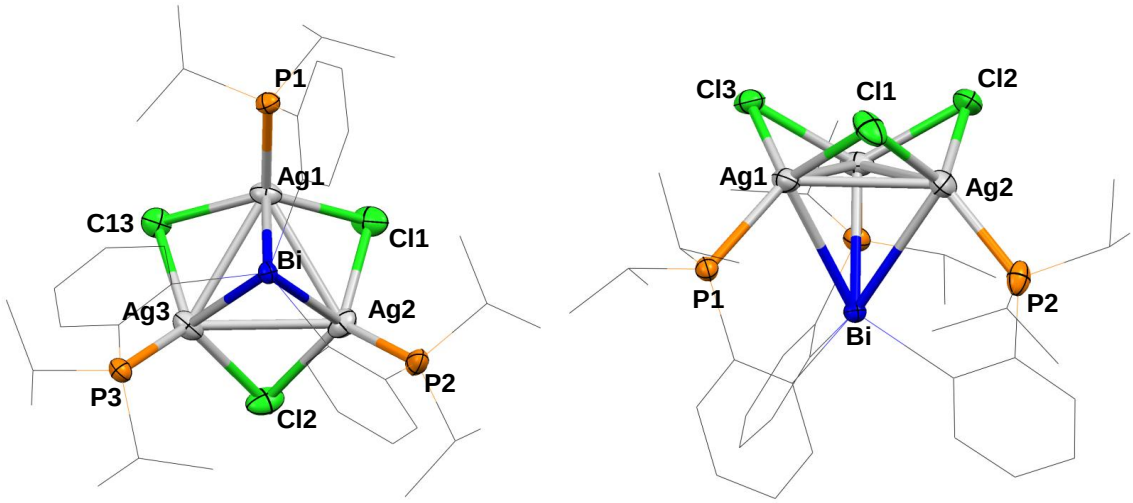

Figure 94. Solid-state structure of **42** (left: bottom view, right: side view). Ellipsoids are set at 50 % probability; hydrogen atoms and non-coordinated solvent molecules are omitted for clarity. Pertinent metrical parameters can be found in the text.

Table 19. Selected metrical parameters for complexes **39-42** as determined by X-ray diffraction.

	39	**40**	**41**	**42**
d(Pn-M_1) (Å)	2.7933(10)	2.9731(8)	2.9778(10)	3.1358(4)
d(Pn-M_2) (Å)	2.8729(10)	-	2.8855(10)	3.1932(4)
d(Pn-M_3) (Å)	2.7384(9)	-	2.9406(11)	3.1805(5)
d(M_1-M_2) (Å)	2.6488(12)	3.1560(9)	2.8475(14)	3.0135(6)
d(M_1-M_3) (Å)	2.6767(12)	-	2.8244(14)	3.0738(5)
d(M_2-M_3) (Å)	2.6558(12)	-	2.8869(14)	3.0776(6)
d(P_1-M_1) (Å)	2.2038(19)	2.3900(18)	2.203(2)	2.3992(12)
d(P_2-M_2) (Å)	2.1924(19)	-	2.208(2)	2.3876(14)
d(P_3-M_3) (Å)	2.2096(18)	-	2.213(2)	2.4005(13)
M_1-Pn-M_2 (^{o})	55.72(3)	64.11(2)	58.08(3)	56.859(11)
M_1-Pn-M_3 (^{o})	57.87(2)	-	57.00(3)	58.236(10)
M_2-Pn-M_3 (^{o})	56.43(3)	-	59.40(3)	57.743(11)
M_1-X_1-M_2 (^{o})	69.39(5)	76.30(5)	76.96(7)	73.66(4)
M_1-X_3-M_3 (^{o})	69.14(5)	-	76.22(7)	74.75(3)
M_2-X_2-M_3 (^{o})	69.43(5)	-	77.63(7)	75.38(4)
X_1-M_2-X_2 (^{o})	110.56(6)	96.59(10)	111.71(8)	112.51(5)
X_1-M_1-X_3 (^{o})	109.60(6)	-	111.28(8)	115.68(5)
X_2-M_3-X_3 (^{o})	110.43(6)	-	111.35(8)	112.11(4)

The $Cu_3(\mu_2\text{-}Cl)_3$ and $Ag_3(\mu_2\text{-}Cl)_3$ units observed in these complexes are reminiscent of the gas phase structure of these coinage metal chlorides. Gas phase electron diffraction experiments have served to confirm that cyclotrimers are one of the main oligomers present in vapors of CuCl.[210] In a recent study, Hargittai concluded that the $Cu_3(\mu_2\text{-}Cl)_3$ cluster present in the gas phase at 689 K have D_{3h} symmetry.[211] The Cu-Cu distance of 2.627±0.012 Å derived from this gas phase study is shorter than the average Cu-Cu distance found in **39** (2.66 Å) and **41** (2.85 Å), a factor that we assign to the geometrical constraints imposed by the tripodal ligand. Coordination of the phosphine ligands to each metal atom is also held responsible for the fact that the Cu-Cl

bonds observed in **39** (av. 2.34 Å) and **41** (av. 2.29 Å) are longer than in the gas phase $Cu_3(\mu_2\text{-}Cl)_3$ cluster (Cu-Cl 2.166±0.008 Å).[212] To our knowledge, there is no gas phase structure available for the $Ag_3(\mu_2\text{-}Cl)_3$ cluster. However, mass spectrometry and matrix IR measurement suggest a structure that resembles that of the copper analog,[213] a conclusion supported by recent calculations which predict a cluster of D_{3h} symmetry with Ag-Ag and Ag-Cl distances of 3.282 Å and 2.442 Å, respectively.[214] Theses calculated Ag-Ag and Ag-Cl distances are in good agreement with those observed in **40** (Ag-Ag 3.16 Å, Ag-Cl av. 2.55 Å) and **42** (Ag-Ag av. 3.05 Å, Ag-Cl av. 2.52 Å). The slight elongation observed in the Ag-Cl distances could again be assigned to coordination of the phosphine ligands. For all four compounds, it should be emphasized that, unlike in the gas phase, the $M_3(\mu_2\text{-}Cl)_3$ is not planar but rather triply folded with the three chloride anions projecting above the M_3 plane.

Last but not least, we observe the concomitant coordination of the heavy pnictogen atom to all three group 11 metal atoms leading to formation of a PnM_3 tetrahedron (Pn = Sb or Bi, M = Cu or Ag, Figure 95). The observation of a triply bridging stibine or bismuthine unit as in the structure of these complexes is, to our knowledge, unprecedented.[34] The Cu-Sb bonds of **39** (av. 2.80 Å) can be compared to those in known stibine-copper complexes such as $CuCl(SbPh_3)_3$ (2.548-2.564 Å),[173] $[Cu(SbPh_3)_4][ClO_4]$ (2.572-2.577 Å)[215] and $[(Ph_3Sb)_2Cu(\mu_2\text{-}Cl)_2Cu(SbPh_3)_2]$ (2.528-2.539 Å).[216] It can also be compared to sum of the covalent radii of the two elements (2.68-2.84 Å)[112,113] that it exceeds by only 4.7%-10.9%. The moderately elongated Cu-Sb distances observed in **39** can be assigned to the triply bridging nature of the antimony

atom and are consistent with the presence of a Sb→Cu_3 interaction. A similar situation is encountered in the case of **40** which displays a longer Ag-Sb separation (2.9731(8) Å) than in complexes such as $AgCl(SbPh_3)_3$ (2.705-2.786 Å)[174], $[Ag(SbPh_3)_4][BF_4]$ (2.720-2.730 Å)[217] and $[(Ph_3Sb)_2Ag(\mu_2\text{-}Cl)_2Ag(SbPh_3)_2]$ (2.702-2.735 Å).[218] Hence, by analogy with **39**, a Sb→Ag_3 interaction can be proposed. The bismuthine complexes **41** and **42**, are, to our knowledge, the first structurally characterized examples of complexes involving a bismuthine and a copper or silver metal ion. For this reason, the M-Bi bonds (M = Cu, Ag) of **41** and **42** can only be compared to the sum of the covalent radii of the elements (2.63-2.80 Å for Bi-Cu; 2.79-2.93 Å for Bi-Ag)[112,113] that they exceeds by 4.8%-11.6% and 8.2%-13.6%, respectively. Because the noted elongations are moderate and also comparable to those observed for the M-Sb bond in **39** and **40**, we also propose that **41** and **42** are stabilized by Bi→M_3 interactions.

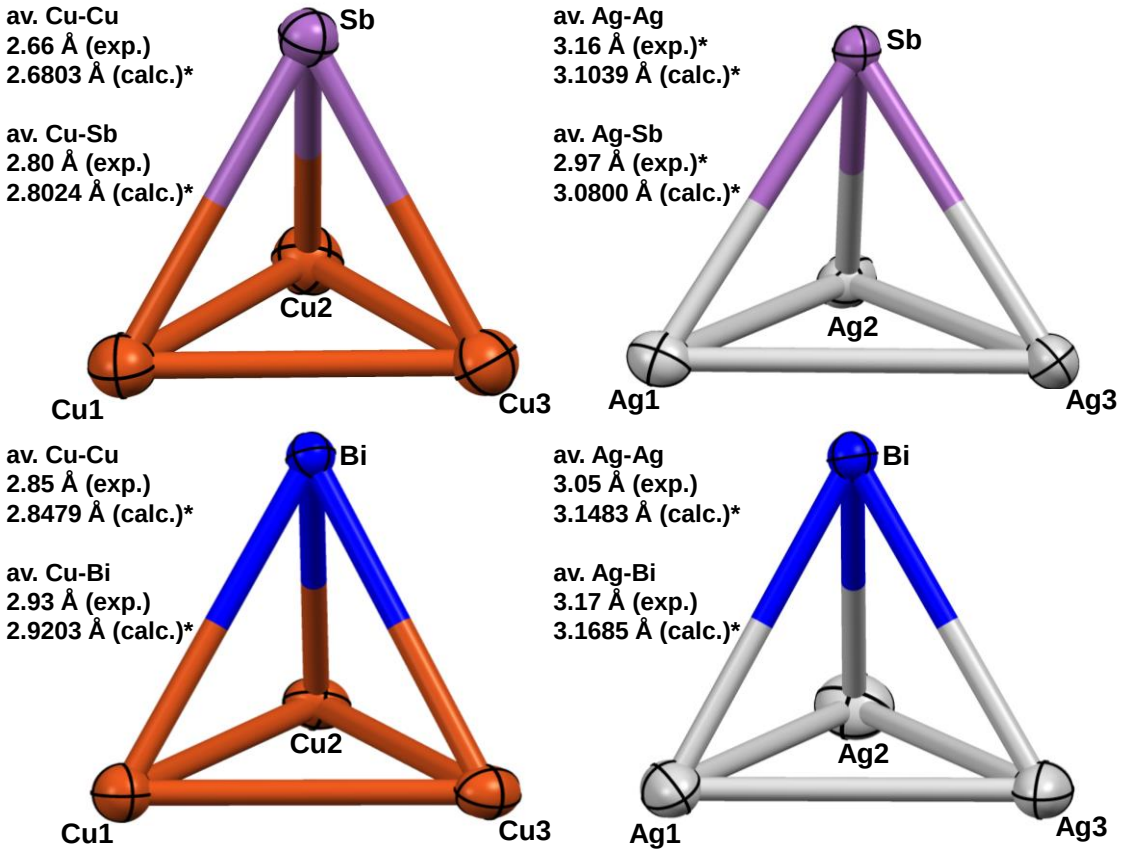

Figure 95. Tetrahedral core of **39-42**. Ellipsoids are set at 50 % probability. Experimental and calculated average M-Pn and M-M distances are also listed. The distances marked by a * do not correspond to averages.

8.3 Computational studies

The structures of **39-42** have been optimized using Density Functional Theory as implemented in the Gaussian09 program. The optimized geometries are in good agreement with those determined experimentally thus suggesting that the level of theory chosen for these calculations is appropriate. To shed light on the bonding interaction occurring at the core of these complexes, the optimized structures were subjected to a Natural Bond Orbital analysis (NBO).[219] For complex **39**, the NBO analysis treats the

$\mathbf{L}_{Sb}^{P3}$ as an independent unit that interacts with the trinuclear copper cluster $Cu_3(\mu_2\text{-}Cl)_3$. In addition to interactions involving the phosphine ligands, the NBO analysis identifies three strong 5s(Sb)→4s(Cu) interactions (Figure 96). Collectively, these interactions may be viewed as a 4-center 2-electron interaction resulting from the donation of an antimony 5s lone pair into three vacant copper 4s orbitals. A deletion calculation[220] carried out by concomitantly zeroing the Kohn–Sham matrix elements corresponding to the three 5s(Sb)→4s(Cu) interactions affords a stabilization energy, E_{del}, of 70.3 kcal mol^{-1}. A similar situation is found in complex **40**, in which the three 5s(Sb)→5s(Ag) interactions account for E_{del} = 42.3 kcal mol^{-1}. A comparison of the two stabilization energies shows that the trinuclear $Cu_3(\mu_2\text{-}Cl)_3$ cluster is a better acceptor, an observation that can be rationalized by invoking the lower energy of the accepting 4s orbitals as well as the higher charge/size ratio of the Cu(I) ion. For **41** and **42**, the stabilization energies calculated for the 6s(Bi)→4s(Cu) and 6s(Bi)→5s(Ag) interactions are lower (E_{del} = 40.7 kcal mol^{-1} for **41** and 26.9 kcal mol^{-1} for **42**) as expected from the inert character of bismuth 6s lone pair which is contracted by relativistic effects. The lower basicity of bismuthines is a known phenomenon which is illustrated by the stability of adducts such $Et_3Al\text{-}E(SiMe_3)_3$ and $t\text{-}Bu_3Al\text{-}E(i\text{-}Pr)_3$ (E = P, As, Sb, Bi).[221,222]

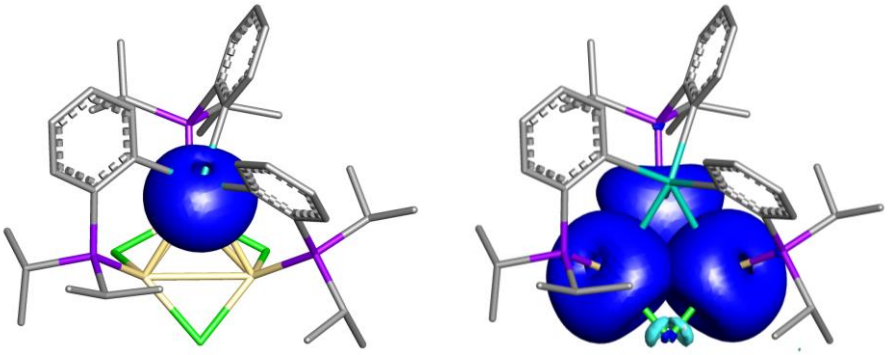

Donor **Acceptor**

	39	**40**	**41**	**42**
E_{del} (kcal/mol)	70.3	42.3	40.7	26.9

Figure 96. NBO plot showing the orbitals involved in the 5s(Sb)→4s(Cu) in complex **39**. The 5s(Sb) donor orbital is shown on the left; . The three 4s(Cu) acceptor orbitals are shown on the right (isovalue=0.05; hydrogen atoms are omitted for clarity). Analogous NBOs are involved in the Pn→M_3 of **40-42**.

8.4 Conclusions

In conclusion, we report that the trisphosphino-stibine and -bismuthine ligands $\mathbf{L}_{Sb}^{P3}$ and $\mathbf{L}_{Bi}^{P3}$ may be used to nucleate and stabilize $M_3(\mu_2\text{-}Cl)_3$ cluster which had thus far only been observed in the gas phase. Coordination of the ligands to the trinuclear cluster pushes the chloride anions out of the plane defined by the three metals, leading to a crown structure. Another important outcome of this work is the observation that the stibine or bismuthine ligands coordinate concomitantly to the three metal atoms of the cluster. This is, to our knowledge, the first observation of stibine or bismuthine ligands in triply bridging situations. Another unique character of this work is the first structural characterization of bismuthine copper and silver complexes.

8.5 Experimental

General considerations. $\mathbf{L}_{Sb}^{P3}$ and $\mathbf{L}_{Bi}^{P3}$ were prepared according to the reported procedures. Solvents were dried by passing through an alumina column (n-pentane and CH_2Cl_2) or by reflux under N_2 over Na/K (Et_2O and THF). All other solvents were used as received. CuCl and AgCl were purchased from Aldrich and used as received. All air and moisture sensitive manipulations were carried out under an atmosphere of dry N_2 employing either a glove box or standard Schlenk techniques. Ambient temperature NMR spectra were recorded on a Varian Unity Inova 400 FT NMR (399.59 MHz for ^{1}H, 100.45 MHz for ^{13}C, 161.74 MHz for ^{31}P) spectrometer. Chemical shifts (δ) are given in ppm and are referenced against residual solvent signals (^{1}H, ^{13}C) or external H_3PO_4(^{31}P). Elemental analyses were performed at Atlantic Microlab (Norcross, GA).

Crystallography. All crystallographic measurements were performed at 110(2) K using a Bruker SMART APEX II diffractometer with a CCD area detector (graphite monochromated Mo K_α radiation, λ = 0.71073 Å) at 110 K. In each case, a specimen of suitable size and quality was selected and mounted onto a nylon loop. The semi-empirical method SADABS was applied for absorption correction. The structures were solved by direct methods and refined by the full-matrix least-square technique against F^2 with the anisotropic temperature parameters for all non-hydrogen atoms. All H atoms were geometrically placed and refined in riding model approximation. Data reduction and further calculations were performed using the Bruker SAINT+ and SHELXTL NT program packages.[78]

Theoretical calculations. Density functional theory (DFT) calculations (full geometry optimization) were carried out on **39-42** starting from the crystal structure geometries with Gaussian09[122] program (BP86[80,81] with 6-31G for H, C; 6-311+g(d) for P, Cl; Stuttgart relativistic small core (RSC) 1997 ECP for Cu[179] and Ag[179]; Stuttgart relativistic large core (RLC) ECP for Sb[180] and Bi[180]). Frequency calculations were also carried out on the optimized geometry, showing no imaginary frequencies. The optimized structures, which are in excellent agreement with the solid-state structures, were subjected to a NBO analysis.[219] The resulting NBO of donor-acceptor interactions were visualized and plotted in Jimp 2 program.[126]

Synthesis of 39. To a suspension of CuCl (21.2 mg, 0.21 mmol) in THF (2 mL) was added a solution of (*o*-(*i*Pr$_2$P)C$_6$H$_4$)$_3$Sb (50 mg, 0.071 mmol) in THF (2 mL) at room temperature. The solution turned yellow immediately. After subsequent stirring for 12 hr, volatiles were removed and the residue was washed with pentane (10 mL). Removal of the residual solvent afforded **39** (59.5 mg, 84% yield) as a yellow powder. X-ray quality crystals were obtained by slow diffusion of Et_2O into a solution of the compound in CH_2Cl_2. ^{1}H NMR (499.43 MHz, $CDCl_3$): δ 7.62 (pseudo-t, 3H, *o*-P(Sb)C$_6$H$_4$, $^3J_{H\text{-}H}$ = 5.58 Hz), 7.45 (pseudo-t, 3H, *m*-P(Sb)C$_6$H$_4$, $^3J_{H\text{-}H}$ = 7.67 Hz), 7.33 (pseudo-t, 3H, *m*-P(Sb)C$_6$H$_4$, $^3J_{H\text{-}H}$ = 7.67 Hz), 7.19 (d, 3H, *o*-P(Sb)C$_6$H$_4$, $^3J_{H\text{-}H}$ = 7.67 Hz), 2.52 (m, 3H, C*H*CH$_3$), 2.09 (m, 3H, C*H*CH$_3$), 1.45 (dd, 9H, $^3J_{H\text{-}H}$ = 6.72 Hz, $^3J_{H\text{-}P}$ = 18.46 Hz, CHC*H*$_3$), 0.98 (dd, 9H, $^3J_{H\text{-}H}$ = 6.72 Hz, $^3J_{H\text{-}P}$ = 18.46 Hz, CHC*H*$_3$), 0.80 (dd, 9H, $^3J_{H\text{-}H}$ = 6.72 Hz, $^3J_{H\text{-}P}$ = 18.46 Hz, CHC*H*$_3$), 0.51 (dd, 9H, $^3J_{H\text{-}H}$ = 6.72 Hz, $^3J_{H\text{-}P}$ = 18.46 Hz, CHC*H*$_3$). ^{31}P{^{1}H} NMR (202.16 MHz; $CDCl_3$): δ 36.16 (s). ^{13}C{^{1}H} NMR (125.58 MHz,

$CDCl_3$): δ 149.59 (s), 136.69 (d, $^1J_{C\text{-}P}$ = 14.18 Hz), 135.37 (d, $^1J_{C\text{-}P}$ = 29.35 Hz), 134.21 (s), 130.23 (s), 129.04 (d, $^1J_{C\text{-}P}$ = 4.22 Hz), 25.92 (d, $^1J_{C\text{-}P}$ = 17.12 Hz, $C(CH_3)_2$), 24.49 (d, $^1J_{C\text{-}P}$ = 17.12 Hz, $C(CH_3)_2$), 20.01 (d, $^1J_{C\text{-}P}$ = 7.63 Hz, $CH_{3i\text{-}Pr}$), 19.23 (d, $^1J_{C\text{-}P}$ = 13.09 Hz, $CH_{3i\text{-}Pr}$), 18.29 (d, $^1J_{C\text{-}P}$ = 5.49 Hz, $CH_{3i\text{-}Pr}$) , 17.01 (s, $CH_{3i\text{-}Pr}$). Elemental analysis calculated (%) for $C_{36}H_{54}Cl_3Cu_3P_3Sb$: C, 43.30; H, 5.45. Found: C, 43.04; H, 5.36.

Synthesis of 40. The synthesis of **40** is same as **39**. Complex **40** (60.2 mg, 75% yield) is a white powder. X-ray quality crystals were obtained by slow diffusion of Et_2O into a solution of the compound in $CHCl_3$. ^{1}H NMR (499.43 MHz, $CDCl_3$): δ 7.69 (pseudo-t, 3H, *o*-P(Sb)C_6H_4, $^3J_{H\text{-}H}$ = 7.94 Hz), 7.49 (pseudo-t, 3H, *m*-P(Sb)C_6H_4, $^3J_{H\text{-}H}$ = 6.89 Hz), 7.31 (pseudo-t, 3H, *m*-P(Sb)C_6H_4, $^3J_{H\text{-}H}$ = 6.89 Hz), 7.01 (d, 3H, *o*-P(Sb)C_6H_4, $^3J_{H\text{-}H}$ = 6.89 Hz), 2.53 (br, 3H, C*H*CH_3), 1.96 (br, 3H, C*H*CH_3), 1.39 (d, 9H, $^3J_{H\text{-}P}$ = 20.08 Hz, CHC*H*$_3$), 1.02 (d, 9H, $^3J_{H\text{-}P}$ = 20.08 Hz, CHC*H*$_3$), 0.79 (br, 9H, CHC*H*$_3$), 0.72 (br, 9H, CHC*H*$_3$). ^{31}P{^{1}H} NMR (202.16 MHz; $CDCl_3$): δ 39.25 (d, $^1J_{Ag\text{-}P}$ = 549.45 Hz). ^{13}C{^{1}H} NMR (125.58 MHz, $CDCl_3$): δ 148.12 (s), 138.01 (d, $^1J_{C\text{-}P}$ = 12.74 Hz), 136.88 (d, $^1J_{C\text{-}P}$ = 25.03 Hz), 134.43 (s), 130.61 (s), 129.51 (d, $^1J_{C\text{-}P}$ = 3.64 Hz), 26.89 (d, $^1J_{C\text{-}P}$ = 13.40 Hz, $C(CH_3)_2$), 24.90 (br, $C(CH_3)_2$), 20.16 (s, $CH_{3i\text{-}Pr}$), 20.06 (s, $CH_{3i\text{-}Pr}$), 19.05 (s, $CH_{3i\text{-}Pr}$), 18.57 (s, $CH_{3i\text{-}Pr}$). Elemental analysis calculated (%) for $C_{36}H_{54}Cl_3Ag_3P_3Sb{\cdot}CHCl_3$: C, 35.53; H, 4.43. Found: C, 35.54; H, 4.48.

Synthesis of 41. The synthesis of **41** is same as **39**. Complex **41** (48.6 mg, 71% yield) is a yellow powder. X-ray quality crystals were obtained by slow diffusion of Et_2O into a solution of the compound in CH_2Cl_2. ^{1}H NMR (499.43 MHz, $CDCl_3$): δ 7.75 (d, 3H, *o*-P(Sb)C_6H_4, $^3J_{H\text{-}H}$ = 7.34 Hz), 7.61 (pseudo-t, 3H, *m*-P(Sb)C_6H_4, $^3J_{H\text{-}H}$ = 6.50

Hz), 7.45 (m, 6H, *m*-P(Sb)C_6H_4 + *o*-P(Sb)C_6H_4), 2.32 (br, 6H, C*H*CH_3), 0.90 (m, 36H, CHC*H*$_3$). $^{31}P\{^1H\}$ NMR (202.16 MHz; $CDCl_3$): δ 37.31 (s). $^{13}C\{^1H\}$ NMR (125.58 MHz, $CDCl_3$): δ 165.58 (s), 137.62 (d, $^1J_{C\text{-}P}$ = 14.81 Hz), 135.16 (d, $^1J_{C\text{-}P}$ = 32.99 Hz), 134.91 (s), 132.06 (s), 128.01 (d, $^1J_{C\text{-}P}$ = 4.57 Hz), 25.07 (d, $^1J_{C\text{-}P}$ = 18.14 Hz, *C*$(CH_3)_2$), 19.67 (d, $^1J_{C\text{-}P}$ = 10.77 Hz, *C*$(CH_3)_2$), 17.48 (s, *C*$H_{3i\text{-}Pr}$). Elemental analysis calculated (%) for $C_{36}H_{54}BiCl_3Cu_3P_3$: C, 39.83; H, 5.01. Found: C, 39.80; H, 5.01.

Synthesis of 42. The synthesis of **42** is same as **39**. Complex **42** (60.9 mg, 82% yield) is a white powder. X-ray quality crystals were obtained by slow diffusion of Et_2O into a solution of the compound in CH_2Cl_2. ^1H NMR (499.43 MHz, $CDCl_3$): δ 7.68 (pseudo-t, 3H, *o*-P(Bi)C_6H_4, $^3J_{H\text{-}H}$ = 6.16 Hz), 7.61 (d, 3H, o- P(Bi)C_6H_4, $^3J_{H\text{-}H}$ = 7.26 Hz), 7.49 (pseudo-t, 3H, *m*-P(Bi)C_6H_4, $^3J_{H\text{-}H}$ = 7.26 Hz), 7.38 (pseudo-t, 3H, *m*-P(Bi)C_6H_4, $^3J_{H\text{-}H}$ = 7.26 Hz), 2.29 (br, 6H, C*H*CH_3), 0.93 (br, 36H, CHC*H*$_3$). $^{31}P\{^1H\}$ NMR (202.16 MHz; $CDCl_3$): δ 42.51 (d, $^1J_{Ag\text{-}P}$ = 559.97 Hz). $^{13}C\{^1H\}$ NMR (125.58 MHz, $CDCl_3$): δ 166.91 (s), 139.13 (d, $^1J_{C\text{-}P}$ = 13.95 Hz), 136.74 (d, $^1J_{C\text{-}P}$ = 26.41 Hz), 134.87 (s), 132.73 (s), 128.47 (d, $^1J_{C\text{-}P}$ = 3.65 Hz), 25.77 (br, *C*$H_{3i\text{-}Pr}$), 20.23 (d, $^1J_{C\text{-}P}$ = 13.39 Hz, *C*$(CH_3)_2$), 18.50 (s; $CH_{3i\text{-}Pr}$). Elemental analysis calculated (%) for $C_{36}H_{54}Ag_3BiCl_3P_3$: C, 35.48; H, 4.47. Found: C, 35.78; H, 4.45.

Table 20. Crystal data, data collections, and structure refinements for **39** and **40**

Crystal data	**39**	**40**·3/2($CHCl_3$)
Formula	$C_{36}H_{54}Cl_3Cu_3P_3Sb$	$C_{36}H_{54}Cl_3Ag_3P_3Sb$·3/2($CHCl_3$)
Mr	998.42	2620.93
Crystal size (mm^3)	0.10 x 0.10 x 0.19	0.15 x 0.14 x 0.14
Crystal system	Monoclinic	Cubic
Space group	P2(1)/n	P 21 3
a (Å)	11.632(3)	21.5232(12)
b (Å)	16.257(4)	21.5232(12)
c (Å)	21.873(6)	21.5232(12)
α (°)	90	90
β (°)	97.847(3)	90
γ (°)	90	90
V ($Å^3$)	4097.5(18)	9970.6(10)
Z	4	4
ρ_{calc} (g cm^{-3})	1.618	1.746
μ (mm^{-1})	2.526	2.221
F(000)	2016	5160
T/K	110(2)	110(2)
Scan mode	ω, φ	ω, φ
hkl Range	-13 → +13	-26 → +26
	-18 → +18	-26 → +26
	-25 → +25	-26 → +26
Measd reflns	35386	105133
Unique reflns [R_{int}]	6437 [0.0697]	6539 [0.0635]
Reflns used for Refined	6437	6539
parameters	415	311
GooF	1.047	1.166
*R*1,[a] *wR*2[b] (all data)	0.0604, 0.1081	0.0422, 0.1183
ρ_{fin} (max/min.) ($eÅ^{-3}$)	1.137, -0.616	5.341, -1.293

[a] $R_1 = \Sigma||Fo| - |Fc||/\Sigma|Fo|$. [b] $wR_2 = [[\Sigma w(Fo^2 - Fc^2)^2]/[\Sigma w(Fo^2)^2]]^{1/2}$.

Table 21. Crystal data, data collections, and structure refinements for **41** and **42**

Crystal data	**41**	**42**
Formula	$C_{36}H_{54}Cl_3Cu_3P_3Bi$	$C_{36}H_{54}Cl_3Ag_3P_3Bi$
Mr	1085.65	1218.64
Crystal size (mm^3)	0.22 x 0.14 x 0.14	0.21 x 0.15 x 0.12
Crystal system	Monoclinic	Monoclinic
Space group	P2(1)/c	P2(1)/n
a (Å)	11.653(2)	11.7899(11)
b (Å)	16.302(3)	16.5980(16)
c (Å)	23.344(4)	22.239(2)
α (°)	90	90
β (°)	111.019(7)	98.4260(10)
γ (°)	90	90
V ($Å^3$)	4139.5(13)	2384.1(15)
Z	4	4
ρ_{calc} (g cm^{-3})	1.742	1.880
μ (mm^{-1})	6.093	5.741
F(000)	2144	2360
T/K	110(2)	110(2)
Scan mode	ω, φ	ω, φ
hkl Range	-14 → +14	-14 → +14
	-20 → +20	-20 → +20
	-28 → +28	-27 → +27
Measd reflns	42497	44155
Unique reflns [R_{int}]	8127 [0.1021]	8463 [0.0488]
Reflns used for refinement	8127	8463
Refined parameters	415	415
GooF	1.024	1.082
*R*1,[a] *wR*2[b] (all data)	0.0616, 0.1201	0.0329, 0.0654
ρ_{fin} (max/min.) ($eÅ^{-3}$)	0.824, -0.848	1.458, -1.135

[a] $R_1 = \Sigma||Fo| - |Fc||/\Sigma|Fo|$. [b] $wR_2 = [[\Sigma w(Fo^2 - Fc^2)^2]/[\Sigma w(Fo^2)^2]]^{1/2}$.

CHAPTER IX

SUMMARY

9.1 Lewis acidity of a stibonium ion

In order to investigate the Lewis acidity of the pnictonium ions, the initial studies of fluoride affinity for $[Ph_4Pn]^+$ and the computational results of competition reactions between $[Ph_4Pn]^+$ and Ph_4Pn-F have been performed. Inspired by these results, stibonium ions exhibited exceptional acidity in the group 15 elements. Incorporating with fluorescence reporter, 9-anthryltriphenylstibonium ion $[\mathbf{17}]^+$ has been synthesized, and its fluoride binding properties have been investigated. $[\mathbf{17}]^+$ reacts with fluoride in MeOH to afford **17**-F. Supporting this results, the X-ray crystal structures of $[\mathbf{17}]^+$ and **17**-F have been isolated. The Lewis acidity of this stibonium $[\mathbf{17}]^+$ has been investigated in aqueous solutions (H_2O/DMSO, 9:1 vol.) containing CTAB (10 mM) and sodium phosphate (10 mM) by monitoring the absorbance of the anthryl group on Sb atom as a function of pH, which affords pK_{R+} = 7.07(±0.05). The fluoride affinity of $[\mathbf{17}]^+$ has also been studied under the same conditions. This cation exhibits a high affinity for fluoride in aqueous solution, giving binding constant of 12000(±1100) M^{-1} for $[\mathbf{17}]^+$. Having this high binding constant, this studying makes the stibonium $[\mathbf{17}]^+$ compatible for the detection of fluoride in the part per million ranges.

Interestingly, $[\mathbf{17}]^+$ is only weakly fluorescent with a quantum yield of Φ = 0.7%. Conversion of $[\mathbf{17}]^+$ into **17**-F by addition of fluoride induced a blue shift of the anthryl-based absorption as well as a drastic increase in the fluorescence intensity with a

quantum yield of Φ = 9.5% for **17**-F. Using this fluorescence turn-on response, we can selectively detect fluoride in both tap and bottled water in ppm level.

9.2 Cationic stibine-palladium complex for fluoride anion sensing

In an extension of our fluoride binding studies with the stibonium, we proposed an analogy between a tetraorganostibonium cation and triarylstibine coordinated to a cationic transition metal. With this idea in mind, cationic stibine-palladium complex [**19**]BPh_4 which was supported by bisphosphanylphenyl analog (*o*-$(Ph_2P)C_6H_4)_2PhSb$ (referred to as L^2) has been synthesized and fully characterized. The geometry of Pd atom features a distorted square planar. [**19**]BPh_4 can react with fluoride to afford corresponding **19**-F in 9/1 vol. MeOH/CH_2Cl_2 with large binding constants, 12000(±2000) M^{-1} for [**19**]BPh_4.

9.3 Anion-induced internal redox switching of a heterobimetallic complex

Having successfully isolated Sb-Pd complex [**19**]BPh_4 in previous section, we decided to synthesized Sb-Pt analog [**20**][Cl] (Sb(IV)-Pt(I)). Additionally, complex [**20**][Cl] is chemically robust and undergoes a clean two-electron oxidation reaction in the presence of *o*-chloranil (*o*-$O_2C_6Cl_4$) to afford Sb(IV)-Pt(III) complex **21**, a complex combining a hypervalent five-coordinate antimony atom and an octahedral platinum center. In order to understand the fluoride affinity of this complex, complex **21** reacts with KF in MeOH resulting in the formation of the fluoride-bridged complex **22** (Sb(V)-Pt(II)). Fluoride titration experiments monitored by UV-vis indicated that the first

fluoride binding constant (K_1) is greater than 10^6 M^{-1} while the second (K_2) equals 4500 (± 200) M^{-1}. The oxidation states of Pt were also confirmed by both DFT calculations and Pt L3-X-ray Absorption Near Edge Structure (XANES) spectrum. This internal redox process, however, is chemically reversible by adding the TMSCl to complex **22**. Finally, the fluoride affinity of complex **21** is also investigated by layering the ppm level of aqueous fluoride solutions.

9.4 A redox active PtSb platform with differential chloride anion affinity

The results presented in this study show that the chloride affinity of the antimony atom in platinum stibine complexes is controlled by the redox state of the metal center. When such complexes are oxidized as in **23**-Cl, the Lewis acidity of the antimony atom increases, leading to a tighter coordination of the anion bound to antimony. Conversely, in [**20**][Cl], the chloride is loosely bound and readily liberated to the medium.

9.5 σ-Donor/acceptor-confused ligands: The case of a chlorostibine

In search for new examples of σ-acceptor ligands, we have investigated the tridentate ligands (*o*-(*i*Pr_2P)$C_6H_4)_2$SbPh) (L^{Ph}) and (*o*-(*i*Pr_2P)$C_6H_4)_2$SbCl) (L^{Cl}) which react with (tht)AuCl (tht = tetrahydrothiophene) to afford L^{Ph}AuCl (**26**) and L^{Cl}AuCl (**27**), respectively. As suggested by the structure of these complexes, which confirm complexation of SbP_2 ligands to the gold chloride fragment, and in agreement with the results of the DFT and NBO calculations, the gold and antimony atom of **26** and **27** are involved in a Au→Sb donor acceptor interaction. The magnitude of this interaction is

higher in complex **27** which possess a chlorinated and thus more Lewis acidic antimony center. We have also compared the strength of the Au→Sb interaction present in **27** with the Au→Bi interaction observed in the newly prepared bismuth analog [(*o*-(*i*Pr$_2$P)C$_6$H$_4$)$_2$BiCl]AuCl (**28**). This comparison reveals that **27** possesses a stronger Au→Pn bond (Pn = pnictogen), an observation reconciled by invoking the greater Lewis acidity of antimony(III) halides. Finally, complexes **26** and **27** undergo a clean antimony-centered oxidation when treated with *ortho*-chloranil. These oxidation reactions afford complexes [(*o*-(*i*Pr$_2$P)C$_6$H$_4$)$_2$(*o*-C$_6$Cl$_4$O$_2$)SbPh]AuCl (**30**) and [(*o*-(*i*Pr$_2$P)C$_6$H$_4$)$_2$(*o*-C$_6$Cl$_4$O$_2$)SbCl]AuCl (**31**). Structural and computational studies of **30** showed that the Au→Sb bond becomes shorter and more covalent upon oxidation of the antimony atom. Although the structure of **31** has not been experimentally determined, spectroscopic and computational results show a similar effect in this complex. Complex **30** and **31** constitute rare examples of metallated six coordinate antimony compounds.

9.6 Synthesis, structure and reactivity of a cationic Sb-Au complex

As part of our developing interest in metal stiborane complexes, we recognized that stibonium and six coordinate antimony compounds can act a strong Lewis acid toward the transition metal center as we mentioned in earlier section. To continue this study, Sb-Au complex **36** can be synthesized via two electron oxidation by PhICl$_2$. Two chlorine atoms were added across the Sb center. Upon addition of KF in MeOH, halides exchange reaction results in the formation of complex **37** with a shorter Sb-Au separation of 2.7450(14) Å. The chlorine atom on Au can be removed by adding 1 eq. of

$TlPF_6$ to afford the cationic Sb-Au complex [**37**][PF_6]. DFT studies of **36**, **37** and [**37**][PF_6] suggest an Au→Sb interactions. NBO analysis identified a relatively strong d(Au)→σ*(Sb) donor-acceptor interactions (E_{del} = 15.6 kcal/mol for **36**, E_{del} = 53.7 kcal/mol for **37** and E_{del} = 2.4 kcal/mol for [**37**][PF_6]) whereas the deletion energy of [**37**][PF_6] drops significantly upon cationization. The reaction of [**37**][PF_6] with TBAF in the CH_2Cl_2 afforded an unexpected isomerization complex **38** which was confirmed by the single crystal structure.

9.7 Synthesis of trinuclear Cu(I) and Ag(I) complexes

As part of our interest in the weak interactions between heavier pnictogen and cyclic trinuclear copper and silver complexes, we have synthesized the corresponding adducts of (*o*-(*i*Pr_2P)C_6H_4)$_3$SbCu$_3$(μ_2-Cl)$_3$ (**39**), (*o*-(*i*Pr_2P)C_6H_4)$_3$SbAg$_3$(μ_2-Cl)$_3$ (**40**), (*o*-(*i*Pr_2P)C_6H_4)$_3$BiCu$_3$(μ_2-Cl)$_3$ (**41**) and (*o*-(*i*Pr_2P)C_6H_4)$_3$BiAg$_3$(μ_2-Cl)$_3$ (**42**), respectively. Adducts of **39**-**42** have been fully characterized by ^{1}H, ^{31}P NMR, elemental analysis as well as the X-ray crystallography. In the solid state, the *c*-M$_3$(μ_2-Cl)$_3$ clusters are close to planar involving bridging halide ligands which form bend isosceles triangles. The intermetallic Cu-Cu and Ag-Ag distances are 2.6604(12)-2.8529(14) Å and 3.0550(6)-3.1560(9) Å, respectively, indicating weak closed-shell metal-metal interactions (cuprophilic and argentophilic interactions). Sb and Bi are located above these trinuclear clusters suggesting the presence and magnitude of the E→*c*-M$_3$(μ_2-Cl)$_3$ (E = Sb, Bi; M = Cu, Ag) interactions which have been assessed theoretically.

9.8 Conclusions

Our efforts in studying the Lewis acidity in group 15 elements have led to the discovery of several interesting Lewis acidic properties, especially for antimony atom. Firstly, the cation 9-anthryltriphenylstibonium ([**17**]$^+$) which has a surpringly high fluoride binding constant in 90% water, is competent for the detection of fluoride at part per million concentrations. Stimulated by this result, we chose to design fluoride sensors that incorporate antimony and a late transition metal. The cationic bisphosphanylstibine-palladium complex [**19**]BPh_4 was found to react with fluoride to afford the corresponding fluoride complex **19**-F. This complexation occurs in 9/1 vol. MeOH/CH_2Cl_2 indicating that [**19**]$^+$ had a high affinity for fluoride anions. After this, we turned our attention to the case of bimetallic systems containing antimony and a group 10 or 11 metal. The SbPt complex [**20**][Cl] was successfully synthesized. It can be easily oxidized with *o*-chloranil or $PhICl_2$ to afford the corresponding complexes **21** and **23**-Cl, respectively. Complex **21** also showed a strong affinity for fluoride. Finally, a series of SbAu complexes have been synthesized. The bonding interactions between the two atoms have been elucidated by computational studies which suggest Sb→Au as well as Au→Sb donor-acceptor interactions.

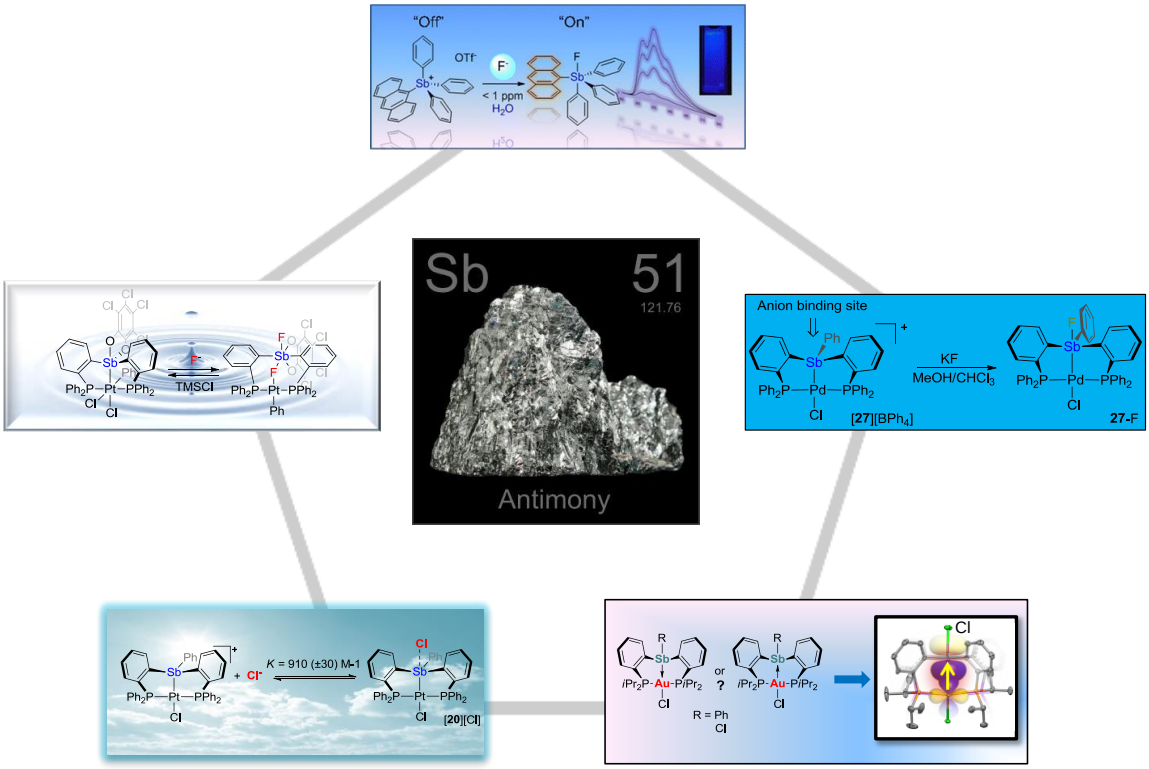

Figure 97. The summary of the antimony chemistry

REFERENCES

(1) Carton, R. J. *Fluoride* **2006**, *39*, 163-172.

(2) Kleerekoper, M. *Endocrinology and metabolism clinics of North America* **1998**, *27*, 441-452.

(3) Owais, W. M.; Zarowitz, M. A.; Gunovich, R. A.; Hodgdon, A. L.; Kleinhofs, A.; Nilan, R. A. *Mutation Research* **1978**, *53*, 355-358.

(4) Lehn, J. M.; Sonveaux, E.; Willard, A. K. *J. Am. Chem. Soc.* **1978**, *100*, 4914-4916.

(5) Dhara, K.; Saha, U. C.; Dan, A.; Sarkar, S.; Manassero, M.; Chattopadhyay, P. *Chem. Commun.* **2010**, *46*, 1754-1756.

(6) Yamaguchi, S.; Akiyama, S.; Tamao, K. *J. Am. Chem. Soc.* **2001**, *123*, 11372-11375.

(7) Kubo, Y.; Yamamoto, M.; Ikeda, M.; Takeuchi, M.; Shinkai, S.; Yamaguchi, S.; Tamao, K. *Angew. Chem. Int. Ed.* **2003**, *42*, 2036-2040.

(8) Hoefelmeyer, J. D.; Sole, S.; Gabbai, F. P. *Dalton Trans.* **2004**, 1254-1258.

(9) Agou, T.; Kobayashi, J.; Kawashima, T. *Org. Lett.* **2005**, *7*, 4373-4376.

(10) Kawai, H.; Takeda, T.; Fujiwara, K.; Suzuki, T. *J. Am. Chem. Soc.* **2005**, *127*, 12172-12173.

(11) Liu, X. Y.; Bai, D. R.; Wang, S. N. *Angew. Chem. Int. Ed.* **2006**, *45*, 5475-5478.

(12) Parab, K.; Venkatasubbaiah, K.; Jakle, F. *J. Am. Chem. Soc.* **2006**, *128*, 12879-12885.

(13) Bai, D. R.; Liu, X. Y.; Wang, S. I. *Chem. Eur. J.* **2007**, *13*, 5713-5723.

(14) Yuan, M. S.; Liu, Z. Q.; Fang, Q. *J. Org. Chem.* **2007**, *72*, 7915-7922.

(15) Zhou, Z. G.; Li, F. Y.; Yi, T.; Huang, C. H. *Tetrahedron Lett.* **2007**, *48*, 6633-6636.

(16) Lee, M. H.; Agou, T.; Kobayashi, J.; Kawashima, T.; Gabbai, F. P. *Chem. Commun.* **2007**, 1133-1135.

(17) Hudnall, T. W.; Kim, Y.-M.; Bebbington, M. W. P.; Bourissou, D.; Gabbai, F. P. *J. Am. Chem. Soc.* **2008**, *130*, 10890-10891.

(18) Wade, C. R.; Gabbaï, F. P. *Organometallics* **2011**, *30*, 4479-4481.

(19) Lebedev, V. A.; Bochkova, R. I.; Kuz'min, E. A.; Sharutin, V. V.; Osanova, N. A.; Belov, N. V. *Dokl. Akad. Nauk SSSR* **1981**, *261*, 91-94 [Crystallogr].

(20) Beauchamp, A. L.; Bennett, M. J.; Cotton, F. A. *J. Am. Chem. Soc.* **1969**, *91*, 297-301.

(21) Shen, K.-W.; McEwen, W. E.; La Placa, S. J.; Hamilton, W. C.; Wolf, A. P. *J. Amer. Chem. Soc.* **1968**, *90*, 1718-1723.

(22) Ferguson, G.; Hawley, D. M. *Acta Crystallogr., Sect. B* **1974**, *B 30*, 103-111.

(23) Ferguson, G.; Glidewell, C.; Lloyd, D.; Metcalfe, S. *J. Chem. Soc., Perkin Trans. 2* **1988**, 731-735.

(24) Knop, O.; Vincent, B. R.; Cameron, T. S. *Can. J. Chem.* **1989**, *67*, 63-70.

(25) Arvanitis, G. M.; Berardini, M. E.; Acton, T. B.; Dumas, P. E. *Phosphorus Sulfur* **1993**, *82*, 127-135.

(26) Haiges, R.; Schroer, T.; Yousufuddin, M.; Christe, K. O. *Z. Anorg. Allg. Chem.* **2005**, *631*, 2691-2695.

(27) Sharutin, V. V.; Sharutina, O. K.; Pakusina, A. P.; Smirnova, S. A.; Pushilin, M. A. *Russ. J. Coord. Chem.* **2005**, *31*, 108-114.

(28) Bowen, L. H.; Rood, R. T. *J. Inorg. Nucl. Chem.* **1966**, *28*, 1985-1990.

(29) Jean, M. *Anal. Chim. Acta* **1971**, *57*, 438-439.

(30) Champness, N. R.; Levason, W. *Coord. Chem. Rev.* **1994**, *133*, 115-217.

(31) Jimenez-Tenorio, M.; Puerta, M. C.; Salcedo, I.; Valerga, P.; Rios, I. D.; Mereiter, K. *Dalton Trans.* **2009**, 1842-1852.

(32) Levason, W.; Reid, G. *Coord. Chem. Rev.* **2006**, *250*, 2565-2594.

(33) Levason, W.; McAuliffe, C. A. *Acc. Chem. Res.* **1978**, *11*, 363-368.

(34) Werner, H. *Angew. Chem., Int. Edit.* **2004**, *43*, 938-954.

(35) Wade, C. R.; Gabbaï, F. P. *Angew. Chem., Int. Edit.* **2011**, *50*, 7369-7372.

(36) Malisch, W.; Kaul, H.-A.; Gross, E.; Thewalt, U. *Angew. Chem., Int. Edit.* **1982**, *21*, 549-550.

(37) Malisch, W.; Panster, P. *Angew. Chem., Int. Edit.* **1974**, *13*, 670-672.

(38) Yamamoto, Y.; Okazaki, M.; Wakisaka, Y.; Akiba, K.-Y. *Organometallics* **1995**, *14*, 3364-3369.

(39) Toyota, K.; Yamamoto, Y.; Akiba, K.-Y. *Chem. Lett.* **1999**, 783-784.

(40) Toyota, K.; Yamamoto, Y.; Akiba, K.-Y. *Organometallics* **2000**, *19*, 5134-5142.

(41) Toyota, K.; Wakisaka, Y.; Yamamoto, Y.; Akiba, K.-y. *Organometallics* **2000**, *19*, 5122-5133.

(42) Lin, T.-P.; Wade, C. R.; Pérez, L. M.; Gabbaï, F. P. *Angew. Chem., 2010, 122, 6501-6504;* **2010**, *49*, 6357-6360.

(43) Wade, C. R.; Lin, T.-P.; Nelson, R. C.; Mader, E. A.; Miller, J. T.; Gabbaï, F. P. *J. Am. Chem. Soc.* **2011**, *133*, 8948-8955.

(44) Lin, T.-P.; Nelson, R. C.; Wu, T.; Miller, J. T.; Gabbaï, F. P. *Chem. Sci.* **2012**, *3*, 1128-1136.

(45) Lin, T.-P.; Ke, I.-S.; Gabbaï, F. P. *Angew. Chem. Int. Ed.* **2012**, *51*, 4985–4988.

(46) Lin, T.-P.; Gabbaï, F. P. *Angew. Chem. Int. Ed.* **2013**, *52*, 3864–3868.

(47) Lin, T.-P.; Gabbaï, F. P. *J. Am. Chem. Soc.* **2012**, *134*, 12230-12238.

(48) Sebelius, K. *Fed. Regist.* **2011**, *76*, 2383-2388.

(49) Badr, I. H. A.; Meyerhoff, M. E. *J. Am. Chem. Soc.* **2005**, *127*, 5318-5319.

(50) Chaniotakis, N.; Jurkschat, K.; Müller, D.; Perdikaki, K.; Reeske, G. *Eur. J. Inorg. Chem.* **2004**, *2004*, 2283-2288.

(51) De Vries, T. S.; Prokofjevs, A.; Vedejs, E. *Chem. Rev.* **2012**, *112*, 4246-4282.

(52) Wade, C. R.; Broomsgrove, A. E. J.; Aldridge, S.; Gabbaï, F. P. *Chem. Rev.* **2010**, *110*, 3958-3984.

(53) Hudson, Z. M.; Wang, S. *Acc. Chem. Res.* **2009**, *42*, 1584-1596.

(54) Hudnall, T. W.; Chiu, C.-W.; Gabbaï, F. P. *Acc. Chem. Res.* **2009**, *42*, 388-397.

(55) Agou, T.; Sekine, M.; Kobayashi, J.; Kawashima, T. *Chem. Eur. J.* **2009**, *15*, 5056-5062.

(56) Bonnier, C.; Piers, W. E.; Parvez, M.; Sorensen, T. S. *Chem. Commun.* **2008**, *0*, 4593-4595.

(57) Venkatasubbaiah, K.; Nowik, I.; Herber, R. H.; Jakle, F. *Chem. Commun.* **2007**, *0*, 2154-2156.

(58) Badugu, R.; Lakowicz, J. R.; Geddes, C. D. *Sens. Actuators, B* **2005**, *104*, 103-110.

(59) Dusemund, C.; Sandanayake, K. R. A. S.; Shinkai, S. *Chem. Commmun.* **1995**, 333-334.

(60) Kim, Y.; Gabbaï, F. o. P. *J. Am. Chem. Soc.* **2009**, *131*, 3363-3369.

(61) Lee, M. H.; Agou, T.; Kobayashi, J.; Kawashima, T.; Gabbaï, F. P. *Chem. Commun.* **2007**, *0*, 1133-1135.

(62) Hounjet, L. J.; Caputo, C. B.; Stephan, D. W. *Angew. Chem., Int. Edit.* **2012**, *51*, 4714-4717.

(63) Tschersich, C.; Limberg, C.; Roggan, S.; Herwig, C.; Ernsting, N.; Kovalenko, S.; Mebs, S. *Angew. Chem., Int. Edit.* **2012**, *51*, 4989-4992.

(64) Wade, C. R.; Lin, T.-P.; Nelson, R. C.; Mader, E. A.; Miller, J. T.; Gabbaï, F. P. *J. Am. Chem. Soc.* **2011**, *133*, 8948-8955.

(65) Conrad, E.; Burford, N.; McDonald, R.; Ferguson, M. J. *J. Am. Chem. Soc.* **2009**, *131*, 17000-17008.

(66) Schmidbaur, H.; Mitschke, K.-H.; Weidlein, J. *Angew. Chem., Int. Edit.* **1972**, *11*, 144-145.

(67) Schmidbaur, H.; Stühler, H. *Angew. Chem., Int. Edit.* **1972**, *11*, 145-146.

(68) Schmidbaur, H.; Mitschke, K.-H.; Buchner, W.; Stühler, H.; Weidlein, J. *Chem. Ber.* **1973**, *106*, 1226-1237.

(69) Hudnall, T. W.; Kim, Y.-M.; Bebbington, M. W. P.; Bourissou, D.; Gabbaï, F. o. P. *J. Am. Chem. Soc.* **2008**, *130*, 10890-10891.

(70) Lin, T.-P.; Nelson, R. C.; Wu, T.; Miller, J. T.; Gabbaï, F. P. *Chem. Sci.* **2012**, *3*, 1128-1136.

(71) Wade, C. R.; Ke, I.-S.; Gabbaï, F. P. *Angew. Chem., Int. Edit.* **2012**, *51*, 478-481.

(72) Sharutin, V. V.; Sharutina, O. K.; Pakusina, A. P.; Smirnova, S. A.; Pushilin, M. A. *Russ. J. Coord. Chem.* **2005**, *31*, 108-114.

(73) Ooi, T.; Goto, R.; Maruoka, K. *J. Am. Chem. Soc.* **2003**, *125*, 10494-10495.

(74) Yamaguchi, S.; Akiyama, S.; Tamao, K. *J. Am. Chem. Soc.* **2000**, *122*, 6793-6794.

(75) Yamaguchi, S.; Akiyama, S.; Tamao, K. *J. Organomet. Chem.* **2002**, *652*, 3-9.

(76) Kimura, M.; Iwata, A.; Itoh, M.; Yamada, K.; Kimura, T.; Sugiura, N.; Ishida, M.; Kato, S. *Helv. Chim. Acta* **2006**, *89*, 747-783.

(77) Ryan, D. K.; Weber, J. H. *Anal. Chem.* **1982**, *54*, 986-990.

(78) Bruker, SAINTPlus. Data Reduction and Correction Program v. 6.2, Bruker AXS, Madison, Wisconsin, USA, 2001.

(79) M. J. Frisch; G. W. Trucks; H. B. Schlegel; G. E. Scuseria; M. A. Robb; J. R. Cheeseman; V. G. Zakrzewski; J. A. Montgomery; R. E. Stratman; J. C. Burant; S. Dapprich; J. M. Millam; A. D. Daniels; K. N. Kudin; M. C. Strain; O. Farkas; J. Tomasi; V. Barone; M. Cossi; R. Cammi; B. Mennucci; C. Pomelli; C. Adamo; S. Clifford; J. Ochterski; G. A. Petersson; P. Y. Ayala; Q. Cui; K. Morokuma; D. K. Malick; A. D. Rabuck; K. Raghavachari; J. B. Foresman; J. Cioslowswi; J. V. Ortiz; A. G. Baboul; B. B. Stefanov; G. Liu; A. Liashenko; P. Piskorz; I. Komaromi; R. Gomperts; R. Martin; D. J. Fox; T. Keith; M. A. Al-Laham; C. Y.

Peng; A. Nanayakkara; C. Gonzalez; M. Challacombe; P. M. W. Gill; B. Jonhson; W. Chen; M. W. Wong; J. L. Andres; M. Head-Gordon; E. S. Replogle; J. A. Pople; Gaussian 03; C.02 ed. Pittsburgh PA, 2006.

(80) Becke, A. D. *Phys. Rev. A* **1988**, *38*, 3098-3100.

(81) Perdew, J. P. *Phys. Rev. B* **1986**, *33*, 8822-8824.

(82) Feller, D. *J. Comput. Chem.* **1996**, *17*, 1571-1586.

(83) Schuchardt, K. L.; Didier, B. T.; Elsethagen, T.; Sun, L.; Gurumoorthi, V.; Chase, J.; Li, J.; Windus, T. L. *J. Chem. Inf. Model.* **2007**, *47*, 1045-1052.

(84) Bergner, A.; Dolg, M.; Kuchle, W.; Stoll, H.; Preuss, H. *Mol. Phys.* **1993**, *80*, 1431-1441.

(85) IgelMann, G.; Stoll, H.; Preuss, H. *Mol. Phys.* **1988**, *65*, 1321-1328.

(86) Yamaguchi, S.; Wakamiya, A. *Pure Appl. Chem.* **2006**, *78*, 1413-1424.

(87) J kle, F. *Chem. Rev.* **2010**, *110*, 3985-4022.

(88) Tagne Kuate, A. C.; Reeske, G.; Schurmann, M.; Costisella, B.; Jurkschat, K. *Organometallics* **2008**, *27*, 5577-5587.

(89) Zhao, H.; Gabbaï, F. P. *Nat. Chem.* **2010**, *2*, 984-990.

(90) Levason, W.; Reid, G. *Coord. Chem. Rev.* **2006**, *250*, 2565-2594.

(91) Parkin, G. *Organometallics* **2006**, *25*, 4744-4747.

(92) Hill, A. F. *Organometallics* **2006**, *25*, 4741-4743.

(93) Fontaine, F. G.; Boudreau, J.; Thibault, M. H. *Eur. J. Inorg. Chem.* **2008**, 5439-5454.

(94) Braunschweig, H.; Dewhurst, R. D.; Schneider, A. *Chem. Rev.* **2010**, *110*, 3924–3957.

(95) Amgoune, A.; Bourissou, D. *Chem. Commun.* **2011**, *47*, 859-871.

(96) Bouhadir, G.; Amgoune, A.; Bourissou, D. *Adv. Organomet. Chem.* **2010**, *58*, 1-107.

(97) Tsay, C.; Mankad, N. P.; Peters, J. C. *J. Am. Chem. Soc.* **2010**, *132*, 13975-13977.

(98) Wagler, J.; Brendler, E. *Angew. Chem., 2010, 122, 6501-6504;* **2010**, *49*, 624-627.

(99) Wagler, J.; Hill, A. F.; Heine, T. *Eur. J. Inorg. Chem.* **2008**, 4225-4229.

(100) Gualco, P.; Mercy, M.; Ladeira, S.; Coppel, Y.; Maron, L.; Amgoune, A.; Bourissou, D. *Chem. Eur. J.* **2010**, *16*, 10808-10817.

(101) Gualco, P.; Lin, T.-P.; Sircoglou, M.; Mercy, M.; Ladeira, S.; Bouhadir, G.; Pérez, L. M.; Amgoune, A.; Maron, L.; Gabbaï, F. P.; Bourissou, D. *Angew. Chem., 2010, 122, 6501-6504;* **2009**, *48*, 9892-9895.

(102) Grobe, J.; Krummen, N.; Wehmschulte, R.; Krebs, B.; Lage, M. *Z. Anorg. Allg. Chem.* **1994**, *620*, 1645-1658.

(103) Solar, J. M.; Ozkan, M. A.; Isci, H.; Mason, W. R. *Inorg. Chem.* **1984**, *23*, 758-764.

(104) Roberts, D. A.; Mason, W. R.; Geoffroy, G. L. *Inorg. Chem.* **1981**, *20*, 789-796.

(105) Drew, D.; Doyle, J. R. *Inorg. Synth.* **1990**, *28*, 346-349.

(106) Ni, Z. P.; Fiedler, S. R.; Shores, M. P. *Dalton Trans.* **2011**, *40*, 944-950.

(107) Ni, Z. P.; McDaniel, A. M.; Shores, M. P. *Chem. Sci.* **2010**, *1*, 615-621.

(108) Ni, Z.; Shores, M. P. *Inorg. Chem.* **2010**, *49*, 10727-10735.

(109) Chao, S. T.; Lara, N. C.; Lin, S. B.; Day, M. W.; Agapie, T. *Angew. Chem., Int. Edit.* **2011**, *50*, 7529-7532.

(110) Cao, D.; Zhao, H.; Gabbaï, F. P. *New J. Chem.* **2011**, *35*, 2299-2305.

(111) Wendt, O. F.; Scodinu, A.; Elding, L. I. *Inorg. Chim. Acta* **1998**, *277*, 237-241.

(112) Cordero, B.; Gomez, V.; Platero-Prats, A. E.; Reves, M.; Echeverria, J.; Cremades, E.; Barragan, F.; Alvarez, S. *Dalton Trans.* **2008**, 2832-2838.

(113) Pyykkö, P.; Atsumi, M. *Chem. Eur. J.* **2009**, *15*, 186-197.

(114) Lebedev, V. A.; Bochkova, R. I.; Kuzmin, E. A.; Sharutin, V. V.; Belov, N. V. *Dokl. Akad. Nauk. SSR* **1981**, *260*, 1124-1127.

(115) Sharutin, V. V.; Sharutina, O. K.; Pakusina, A. P.; Platonova, T. P.; Zadachina, O. P.; Gerasimenko, A. V. *Russ. J. Coord. Chem.* **2003**, *29*, 89-92.

(116) Hope, E. G.; Levason, W.; Powell, N. A. *Inorg. Chim. Acta* **1986**, *115*, 187-192.

(117) Oberhauser, W.; Bachmann, C.; Stampfl, T.; Bruggeller, P. *Inorg. Chim. Acta* **1997**, *256*, 223-234.

(118) Oberhauser, W.; Stampfl, T.; Bachmann, C.; Haid, R.; Langes, C.; Kopacka, H.; Ongania, K. H.; Bruggeller, P. *Polyhedron* **2000**, *19*, 913-923.

(119) Hall, M. D.; Foran, G. J.; Zhang, M.; Beale, P. J.; Hambley, T. W. *J. Am. Chem. Soc.* **2003**, *125*, 7524-7525.

(120) De Crisci, A. G.; Lough, A. J.; Multani, K.; Fekl, U. *Organometallics* **2008**, *27*, 1765-1779.

(121) Zhao, X.-F.; Zhang, C. *Synthesis* **2007**, 551-557.

(122) Frisch, M. J.; Trucks, G. W.; Schlegel, H. B.; Scuseria, G. E.; Robb, M. A.; Cheeseman, J. R.; Scalmani, G.; Barone, V.; Mennucci, B.; Petersson, G. A.; Nakatsuji, H.; Caricato, M.; Li, X.; Hratchian, H. P.; Izmaylov, A. F.; Bloino, J.; Zheng, G.; Sonnenberg, J. L.; Hada, M.; Ehara, M.; Toyota, K.; Fukuda, R.; Hasegawa, J.; Ishida, M.; Nakajima, T.; Honda, Y.; Kitao, O.; Nakai, H.; Vreven, T.; Montgomery, J., J. A.; ; Peralta, J. E.; Ogliaro, F.; Bearpark, M.; Heyd, J. J.; Brothers, E.; Kudin, K. N.; Staroverov, V. N.; Kobayashi, R.; Normand, J.; Raghavachari, K.; Rendell, A.; Burant, J. C.; Iyengar, S. S.; Tomasi, J.; Cossi, M.; Rega, N.; Millam, J. M.; Klene, M.; Knox, J. E.; Cross, J. B.; Bakken, V.; Adamo, C.; Jaramillo, J.; Gomperts, R.; Stratmann, R. E.; Yazyev, O.; Austin, A. J.; Cammi, R.; Pomelli, C.; Ochterski, J. W.; Martin, R. L.; Morokuma, K.; Zakrzewski, V. G.; Voth, G. A.; Salvador, P.; Dannenberg, J. J.; Dapprich, S.; Daniels, A. D.; Farkas, Ö.; Foresman, J. B.; Ortiz, J. V.; Cioslowski, J.; Fox, D. J. *Gaussian09*; *Gaussian 09*, Revision B.01, Gaussian, Inc.: Wallingford, CT, 2009.

(123) Figgen, D.; Peterson, K. A.; Dolg, M.; Stoll, H. *J. Chem. Phys.* **2009**, *130*, 164108-164112.

(124) Metz, B.; Stoll, H.; Dolg, M. *J. Chem. Phys.* **2000**, *113*, 2563-2569.

(125) Beez, V.; Greiwe, P.; Pritzkow, H.; Hofmann, M.; v. R. Schleyer, P.; Siebert, W. *Eur. J. Inorg. Chem.* **1998**, *1998*, 1775-1779.

(126) Manson, J.; Webster, C. E.; Pérez, L. M.; Hall, M. B., http://www.chem.tamu.edu/jimp2/index.html.

(127) Klan, P.; Solomek, T.; Bochet, C. G.; Blanc, A.; Givens, R.; Rubina, M.; Popik, V.; Kostikov, A.; Wirz, J. *Chem. Rev.* **2013**, *113*, 119-191.

(128) Shinkai, S. In *Molecular switches*; Feringa, B. L., Ed.; Wiley-VCH: Weinheim, 2001.

(129) Ciesienski, K. L.; Franz, K. J. *Angew. Chem. Int. Ed.* **2011**, *50*, 814-824.

(130) Ellis-Davies, G. C. R. *Chem. Rev.* **2008**, *108*, 1603-1613.

(131) Kaplan, J. H.; Ellis-Davies, G. C. *Proceedings of the National Academy of Sciences* **1988**, *85*, 6571-6575.

(132) McCray, J. A.; Trentham, D. R. *Annual Review of Biophysics and Biophysical Chemistry* **1989**, *18*, 239-270.

(133) Kaplan, J. H. *Annual Review of Physiology* **1990**, *52*, 897-914.

(134) Adams, S. R.; Tsien, R. Y. *Annual Review of Physiology* **1993**, *55*, 755-784.

(135) Ellis-Davies, G. C. R. *Biophotonics, Pt A* **2003**, *360*, 226-238.

(136) Mayer, G.; Heckel, A. *Angew. Chem.-Int. Edit.* **2006**, *45*, 4900-4921.

(137) Ellis-Davies, G. C. R. *Nature Methods* **2007**, *4*, 619-628.

(138) Zucker, R. In *Calcium in Living Cells*; Whitaker, M., Ed. 2010; Vol. 99, p 27-66.

(139) Grell, E.; Warmuth, R. *Pure Appl. Chem.* **1993**, *65*, 373-379.

(140) Shinkai, S.; Ogawa, T.; Nakaji, T.; Kusano, Y.; Nanabe, O. *Tetrahedron Lett.* **1979**, *20*, 4569-4572.

(141) Adams, S. R.; Kao, J. P. Y.; Grynkiewicz, G.; Minta, A.; Tsien, R. Y. *J. Am. Chem. Soc.* **1988**, *110*, 3212-3220.

(142) Tsien, R. Y.; Zucker, R. S. *Biophys. J.* **1986**, *50*, 843-853.

(143) Ellis-Davies, G. C. R.; Barsotti, R. J. *Cell Calcium* **2006**, *39*, 75-83.

(144) Ciesienski, K. L.; Haas, K. L.; Dickens, M. G.; Tesema, Y. T.; Franz, K. J. *J. Am. Chem. Soc.* **2008**, *130*, 12246-12247.

(145) Park, C.-H.; Givens, R. S. *J. Am. Chem. Soc.* **1997**, *119*, 2453-2463.

(146) Bencini, A.; Bianchi, A.; Giorgi, C.; Romagnoli, E.; Lodeiro, C.; Saint-Maurice, A.; Pina, F.; Valtancoli, B. *Supramol. Chem.* **2001**, *13*, 277-285.

(147) Wang, Y.; Bie, F.; Jiang, H. *Org. Lett.* **2010**, *12*, 3630-3633.

(148) Hua, Y.; Flood, A. H. *J. Am. Chem. Soc.* **2010**, *132*, 12838-12840.

(149) Shimasaki, T.; Kato, S.-I.; Ideta, K.; Goto, K.; Shinmyozu, T. *J. Org. Chem.* **2007**, *72*, 1073-1087.

(150) Li, Z.; Zhang, C.; Ren, Y.; Yin, J.; Liu, S. H. *Org. Lett.* **2011**, *13*, 6022-6025.

(151) Lee, S.; Flood, A. H. *J. Phys. Org. Chem.* **2013**, *26*, 79-86.

(152) Verkman, A. S.; Galietta, L. J. V. *Nature Reviews. Drug Discovery* **2009**, *8*, 153-171.

(153) Ke, I.-S.; Myahkostupov, M.; Castellano, F. N.; Gabbaï, F. P. *J. Am. Chem. Soc.* **2012**, *134*, 15309-15311.

(154) Lin, T. P.; Gabbai, F. P. *J. Am. Chem. Soc.* **2012**, *134*, 12230-12238.

(155) Ke, I. S.; Myahkostupov, M.; Castellano, F. N.; Gabbaï, F. P. *J. Am. Chem. Soc.* **2012**, *134*, 15309-15311.

(156) Hatchard, C. G.; Parker, C. A. *Proc. R. Soc. A* **1956**, *235*, 518-536.

(157) Parker, C. A. *Proc. R. Soc. A* **1953**, *220*, 104-116.

(158) Kuhn, H. J.; Braslavsky, S. E.; Schmidt, R. *Pure Appl. Chem.* **2004**, *76*, 2105-2146.

(159) Braunschweig, H.; Dewhurst, R. D. *Dalton Trans.* **2011**, *40*, 549-558.

(160) Rudd, P. A.; Liu, S.; Gagliardi, L.; Young, V. G.; Lu, C. C. *J. Am. Chem. Soc.* **2011**, *133*, 20724-20727.

(161) Bauer, J.; Braunschweig, H.; Dewhurst, R. D. *Chem. Rev.* **2012**, *112*, 4329-4346.

(162) Anderson, J. S.; Moret, M.-E.; Peters, J. C. *J. Am. Chem. Soc.* **2012**, *135*, 534-537.

(163) Ohkata, K.; Takemoto, S.; Ohnishi, M.; Akiba, K.-y. *Tetrahedron Lett.* **1989**, *30*, 4841-4844.

(164) Yi, W.; Tan, N. *Acta Crystallogr., Sect. E: Struct. Rep. Online* **2011**, *67*, m917.

(165) Benjamin, S. L.; Levason, W.; Reid, G.; Warr, R. P. *Organometallics* **2012**, *31*, 1025-1034.

(166) Lin, T.-P.; Ke, I.-S.; Gabbaï, F. P. *Angew. Chem., Int. Edit.* **2012**, *51*, 4985-4988.

(167) Jones, P. G. *Acta Crystallogr., Sect. C: Cryst. Struct. Commun.* **1992**, *48*, 1487-1488.

(168) Becker, G.; Mundt, O.; Sachs, M.; Breunig, H. J.; Lork, E.; Probst, J.; Silvestru, A. *Z. Anorg. Allg. Chem.* **2001**, *627*, 699-714.

(169) Hall, M.; Sowerby, D. B. *J. Organomet. Chem.* **1988**, *347*, 59-70.

(170) Milićev, S.; Hadži, D. *Inorg. Chim. Acta* **1977**, *21*, 201-207.

(171) Sircoglou, M.; Bontemps, S.; Mercy, M.; Saffon, N.; Takahashi, M.; Bouhadir, G.; Maron, L.; Bourissou, D. *Angew. Chem., Int. Edit.* **2007**, *46*, 8583-8586.

(172) N. Gibbons, M.; J. Begley, M.; J. Blake, A.; Bryan Sowerby, D. *J. Chem. Soc., Dalton Trans.* **1997**, *0*, 2419-2426.

(173) Rheingold, A.; Fountain, M. *J. Crystallogr. Spectrosc. Res.* **1984**, *14*, 549-557.

(174) Effendy; Kildea, J. D.; White, A. H. *Aust. J. Chem.* **1997**, *50*, 587-604.

(175) Uson, R.; Laguna, A.; Laguna, M.; Briggs, D. A.; Murray, H. H.; Fackler, J. P. *Inorg. Synth.* **1989**, *26*, 85-91.

(176) Korshin, E. E.; Leitus, G.; Shimon, L. J. W.; Konstantinovski, L.; Milstein, D. *Inorg. Chem.* **2008**, *47*, 7177-7189.

(177) Chan, K. H.; Leong, W. K.; Mak, K. H. G. *Organometallics* **2006**, *25*, 250-259.

(178) Nunn, M.; Sowerby, D. B.; Wesolek, D. M. *J. Organomet. Chem.* **1983**, *251*, C45-C46.

(179) Figgen, D.; Rauhut, G.; Dolg, M.; Stoll, H. *Chem. Phys.* **2005**, *311*, 227-244.

(180) Stoll, H.; Metz, B.; Dolg, M. *J. Comput. Chem.* **2002**, *23*, 767-778.

(181) Akrivos, P. D.; Katsikis, H. J.; Koumoutsi, A. *Coord. Chem. Rev.* **1997**, *167*, 95-204.

(182) Gimeno, M. C.; Laguna, A. *Chem. Rev.* **1997**, *97*, 511-522.

(183) Fernandez, E. J.; Laguna, A.; Olmos, M. E. *Adv. Organomet. Chem.* **2005**, *52*, 77-141.

(184) Fenske, D.; Rothenberger, A.; Wieber, S. *Eur. J. Inorg. Chem.* **2007**, 3469-3471.

(185) Bojan, V. R.; Fernandez, E. J.; Laguna, A.; Lopez-De-Luzuriaga, J. M.; Monge, M.; Olmos, M. E.; Silvestru, C. *J. Am. Chem. Soc.* **2005**, *127*, 11564-11565.

(186) Vicente, J.; Arcas, A.; Jones, P. G.; Lautner, J. *J. Chem. Soc., Dalton Trans.* **1990**, 451-456.

(187) Jones, P. G. *Z. Naturforsch., B: Chem. Sci.* **1982**, *37*, 937-940.

(188) Bojan, V. R.; Fern ndez, E. J.; Laguna, A.; L pe z-de-Luzuriaga, J. M.; Monge, M.; Olmos, M. E.; Puelles, R. C.; Silvestru, C. *Inorg. Chem.* **2010**, *49*, 5530-5541.

(189) Coates, G. E.; Parkin, C. *J. Chem. Soc.* **1962**, 3220-3226.

(190) Tokunaga, T.; Seki, H.; Yasuike, S.; Ikoma, M.; Kurita, J.; Yamaguchi, K. *Tetrahedron* **2000**, *56*, 8833-8839.

(191) Batsanov, S. S. *Inorg. Mater.* **2001**, *37*, 871-885.

(192) Chekhlov, A. N. *Dokl. Akad. Nauk* **1993**, *328*, 205-208.

(193) Sharutin, V. V.; Sharutina, O. K.; Egorova, I. V.; Senchurin, V. S.; Zakharova, A. N.; Bel'skii, V. K. *Russ. J. Gen. Chem.* **1999**, *69*, 1414-1417.

(194) Schwarz, W.; Guder, H. J. *Z. Anorg. Allg. Chem.* **1978**, *444*, 105-111.

(195) Pearson, R. G. *J. Am. Chem. Soc.* **1963**, *85*, 3533-3539.

(196) Laitar, D. S.; Muller, P.; Gray, T. G.; Sadighi, J. P. *Organometallics* **2005**, *24*, 4503-4505.

(197) Melgarejo, D. Y.; Chiarella, G. M.; Fackler, J. P.; Perez, L. M.; Rodrigue-Witchel, A.; Reber, C. *Inorg. Chem.* **2011**, *50*, 4238-4240.

(198) Mankad, N. P.; Toste, F. D. *J. Am. Chem. Soc.* **2010**, *132*, 12859-12861.

(199) Sladek, A.; Hofreiter, S.; Paul, M.; Schmidbaur, H. *J. Organomet. Chem.* **1995**, *501*, 47-51.

(200) Lu, P. F.; Boorman, T. C.; Slawin, A. M. Z.; Larrosa, I. *J. Am. Chem. Soc.* **2010**, *132*, 5580-5581.

(201) Compton, N. A.; Errington, R. J.; Norman, N. C. In *Adv. Organomet. Chem.*; Stone, F. G. A., Robert, W., Eds.; Academic Press: 1990; Vol. Volume 31, p 91-182.

(202) Silvestru, C.; Breunig, H. J.; Althaus, H. *Chem. Rev.* **1999**, *99*, 3277-3328.

(203) Mehring, M. *Coord. Chem. Rev.* **2007**, *251*, 974-1006.

(204) Levason, W.; McAuliffe, C. A.; Murray, S. G. *J. Organomet. Chem.* **1975**, *88*, 171-174.

(205) Baracco, L.; McAuliffe, C. A. *J. Chem. Soc., Dalton Trans.* **1972**, 948-951.

(206) Higginson, B. R.; McAuliffe, C. A.; Venanzi, L. M. *Inorg. Chim. Acta* **1971**, *5*, 37-40.

(207) Dawson, J. W.; Venanzi, L. M. *J. Amer. Chem. Soc.* **1968**, *90*, 7229-7233.

(208) Tschersich, C.; Limberg, C.; Roggan, S.; Herwig, C.; Ernsting, N.; Kovalenko, S.; Mebs, S. *Angew. Chem., Int. Edit.* **2012**, *51*, 4989-4992.

(209) Ke, I.-S.; Gabbai, F. P. *Inorg. Chem.* **2013**, in press.

(210) Wong, C.-h.; Schomaker, V. *The Journal of Physical Chemistry* **1957**, *61*, 358-360.

(211) Hargittai, M.; Schwerdtfeger, P.; Réffy, B.; Brown, R. *Chem. Eur. J.* **2003**, *9*, 327-333.

(212) Anderson, K. M.; Orpen, A. G. *Chem. Commun.* **2001**, *0*, 2682-2683.

(213) Martin, T. P.; Schaber, H. *J. Chem. Phys.* **1980**, *73*, 3541-3546.

(214) Tsipis, A. C.; Stalikas, A. V. *Inorg. Chem.* **2012**, *51*, 2541-2559.

(215) Bowmaker, G. A.; Effendy; Hart, R. D.; Kildea, J. D.; Skelton, B. W.; Silva, E. N. d.; White, A. H. *Aust. J. Chem.* **1997**, *50*, 539-552.

(216) Hart, R. D.; Bowmaker, G. A.; Silva, E. N. d.; Skelton, B. W.; White, A. H. *Aust. J. Chem.* **1997**, *50*, 621-626.

(217) Hill, A. M.; Levason, W.; Webster, M. *Inorg. Chem.* **1996**, *35*, 3428-3430.

(218) Bowmaker, G. A.; Effendy; Silva, E. N. d.; White, A. H. *Aust. J. Chem.* **1997**, *50*, 641-652.

(219) Glendening, E. D. B., J. K.; Reed, A. E.; Carpenter, J. E.; Bohmann, J. A.; Morales, C. M.; Weinhold, F., *NBO 5.9*; Theoretical Chemistry Institute, University of Wisconsin, Madison, WI, 2011.

(220) Reed, A. E.; Curtiss, L. A.; Weinhold, F. *Chem. Rev.* **1988**, *88*, 899-926.

(221) Kuczkowski, A.; Schulz, S.; Nieger, M.; Schreiner, P. R. *Organometallics* **2002**, *21*, 1408-1419.

(222) Kuczkowski, A.; Fahrenholz, S.; Schulz, S.; Nieger, M. *Organometallics* **2004**, *23*, 3615-3621.